FERMILAB-THESIS-2010-54

A Search for Neutrino Induced Coherent NC(π^0) Production in the MINOS Near Detector

A dissertation

submitted by

Daniel David Cherdack

In partial fulfillment of the requirements

for the degree of

Doctor of Philosophy

in

Physics

TUFTS UNIVERSITY

February, 2011

ADVISER: William Anthony Mann

Abstract

The production of single, highly forward π^0 mesons by NC coherent neutrino-nucleus interactions ($\nu_\mu + N \rightarrow \nu_\mu + N + \pi^0$) is a process which probes fundamental aspects of the weak interaction. This reaction may also pose as a limiting background for long baseline searches for $\nu_\mu \rightarrow \nu_e$ oscillations if the neutrino mixing angle θ_{13} is very small. The high-statistics sample of neutrino interactions recorded by the MINOS Near Detector provides an opportunity to measure the cross section of this coherent reaction on a relatively large-A nucleus at an average $E_\nu = 4.9$ GeV. A major challenge for this measurement is the isolation of forward-going electromagnetic (EM) showers produced by the relatively rare coherent NC(π^0) process amidst an abundant rate of incoherently produced EM showers. The backgrounds arise from single π^0 dominated NC events and also from quasi-elastic-like CC scattering of electron neutrinos. In this Thesis the theory of coherent interactions is summarized, and previous measurements of the coherent NC(π^0) cross section are reviewed. Then, methods for selecting a sample of coherent NC(π^0) like events, extracting the coherent NC(π^0) event rate from that sample, estimating the analysis uncertainties, and calculating a cross section, are presented. A signal for neutrino-induced NC(π^0) production is observed in the relevant kinematic regime as an excess of events of three standard deviations above background. The reaction cross section, averaged over an energy window of $2.4 \leqslant E_\nu \leqslant 9.0$ GeV is determined to be $(31.6 \pm 10.5) \times 10^{-40}$ cm^2/nucleus. The result is the first evidence obtained for neutrino-nucleus coherent NC(π^0) scattering on iron, and is the first measurement on an average nuclear target above $A = 30$. The cross section measurement is in agreement with NEUGEN3 implementation of the model by Rein and Sehgal which is motivated by the PCAC hypothesis.

Contents

List of Tables

List of Figures

Acknowledgments

I would like to dedicate this Thesis to my parents. Without their love, and support (especially of the financial variety) I would never have made been able to make it this far. To my Father, thank you for your patience in dealing with my juvenile temper, and the countless hours of conversation on various physics topics and the gory details of this analysis. You always made yourself available so I could talk through whatever issue was holding me back at the time. Many a problem was solved through your thoughtfulness, your attention to detail, and your knack for asking just the right question. To my Mother, you have always been my biggest supporter. Whenever I was in need you were there, with a new hand-knitted hat, a check to get me through the month, or news from home. Thank you both.

I would also like to thank my adviser, Tony, and the rest of the neutrino group at Tufts, Hugh, Jack, and Tomas. With your guidance I have gone from an enthusiastic student, to a contributing member of the high energy physics community. You have inspired me with your knowledge, your work ethic, and your love of physics. Also, a huge heartfelt thanks to Jacki, Jean, and Gayle. Without your kindness and constant assistance I would be lost.

To all of the people on MINOS I would like to extend my sincerest thanks.

It has been a pleasure to work with all of you over the years. The conveners of the Near Detector Working Group have provided constant guidance and feedback, that kept the analysis on track and moving forward. Also much thanks to everyone in the ν_e Working Group, the MC group, and everyone else whose work I borrowed, who made efforts on my behalf, and who took the time to answer my questions, to teach me physics, or to help me conquer ROOT. Of course, I would also like to thank all of my friends and colleagues in Young MINOS. We have shared a lot of long nights working, and, well, not working.

I am truly grateful for all of my friends who have helped me over the years. You have all been there, either to help me with a coding conundrum, to lend me your laptop for a few minutes so I could be working even when I wasn't working, or to help me out of a jam. Most of all, thank you for putting up with me.

Lastly, I would like to thank *you*, Dear Reader, for you are about to embark on a long and arduous journey. I wish you luck.

Synopsis

The production of single, highly forward π^0 mesons by neutral current (NC) coherent neutrino-nucleus interactions ($\nu_\mu + A \rightarrow \nu_\mu + A + \pi^0$) is thought to involve fundamental aspects of the weak interaction. The reaction is also recognized as one which may pose a limiting background for long baseline searches for $\nu_\mu \rightarrow \nu_e$ oscillations if θ_{13} is very small. This Thesis describes the analysis methods and results of a measurement of the reaction rate and cross section for neutrino NC(π^0) coherent scattering in iron using the MINOS Run I and II Near Detector data sample.

Measurement Motivation and Means: Coherent NC(π^0) interaction theory and measurements of the coherent NC(π^0) cross section by previous experiments are discussed in **Chapters 1 and 2**. Descriptions of the MINOS Near Detector and the NuMI neutrino beam, and a discussion of how the cross section is calculated from the coherent NC(π^0) event rate measured by the MINOS experiment is given in **Chapter 3**. An overview of the analysis procedures is given, and useful physics and analysis terms are introduced and defined in **Chapter 4**.

Signature of the Coherent NC(π^0) Reaction: Coherent NC(π^0) events initiated by the NuMI low energy neutrino beam will produce single neutral

pions within distinctive ranges of visible energy and of shower angle with respect to the beam; the coherent NC(π^0) reaction produces no other visible final-state particles. Backgrounds are comprised of reactions whose final-states contain dominant electromagnetic-shower-inducing particles; additional final-state particles are, for the most part, unresolved. The number of predicted background reactions is relatively modest, however their total rate is still large in comparison with the expected coherent NC(π^0) signal rate. A detailed description of the coherent process and the relevant backgrounds is presented in **Chapter 5**.

Event Selection: Event selection utilizes a multivariate classification algorithm which is implemented via a Support Vector Machine (SVM). Topological information concerning the final-state electromagnetic shower, which distinguishes signal events from background events, comprises the essential input to the SVM. Estimates based upon the Monte Carlo (MC) indicate the selected sample will be composed of roughly 17% of coherent NC(π^0) signal events together with three categories of backgrounds: 68% NC, 7% CC-ν_μ, and 8% CC-ν_e. The event selection process is detailed in **Chapter 6**.

Fitting for the Background Contour: Reliable separation of the signal from the abundant background requires that the agreement between the selected Monte Carlo and data samples be significantly refined, and that all relevant systematic uncertainties be accounted for. To this end, a fitting procedure is used to develop a unified description of event rates for all backgrounds in conjunction with the signal. The description is in terms of an event rate contour over a plane defined by the two most relevant kinematic variables, namely *i*) the event visible energy (Energy) and; *ii*) the cosine of the angle of the outgoing final-state electromagnetic-shower with respect to the neutrino

beam direction (Angle). As may be expected with a cutting-edge measurement, the modeling of the signal here has uncertainties which exceed those which characterize the backgrounds, and so the fitting is constrained to regions of the Angle-vs-Energy plane where the backgrounds dominate and the signal must be weak. A full description of the fitting procedure is given in **Chapter 9**.

Systematic Uncertainties: The fitting procedure utilizes effective parameters that vary the normalizations for three background categories: *i*) NC and CC-ν_μ DIS; *ii*) NC and CC-ν_μ resonance production and; *iii*) CC-ν_e. Additional fit parameters to account for individual systematic errors are also included. The relative importance of each systematic has been gauged using studies of simulated experiments. In particular, these studies are the basis for an evaluation, for each and every systematic source, as to whether the effective normalization fit parameters adequately account for the fluctuations induced in the Angle-vs-Energy distribution, or else whether an additional fit parameter for the systematic source in question needs to be included in the fitting. Details concerning the studies carried out for the individual systematic error sources are given in **Chapter 10**. Note that the outcome of the systematics treatment is an error band which encompasses the observed data-vs-MC disagreement for the unblinded data sample.

Mock Data Studies and Error Estimates: Mock data is created by subjecting the MC to random fluctuations which may arise as the result of all the systematic error sources and from finite sample statistics. Thousands of mock data experiments are conducted, each producing a measured signal event rate, N_{fit}, to be compared to the event rate implicit in the mock data sample, N_{true}. The fractional error distribution, $(N_{true} - N_{fit})/N_{true}$, for a set of mock data

experiments is plotted, and the overall systematic+statistical error is taken to be the width of this distribution. Additional uncertainties that are not accounted for in mock data generation are added in quadrature to this error.

The overall uncertainty (statistical plus systematic) on the coherent NC event rate, based on the mock data experiments, is 30%. An additional 10% uncertainty from other sources increases the uncertainty on the event rate to 32%. Conversion to a cross section measurement introduces additional errors, mostly from uncertainties in the neutrino flux. These are estimated to be 7.9%. Thus the total uncertainty to be associated with MINOS measurement of the coherent NC cross section is 33%. A detailed description of the mock data studies and the total uncertainties on the cross section measurement is presented in **Chapter 11**.

Results and Discussion: The cross section for neutrino-induced NC(π^0) production is observed in the relevant kinematic regime as an excess of events of three standard deviations above background. The total coherent NC(π^0) event rate in the MINOS Run I + Run II data sample is 9241 events. This represents a 16% excess over the Monte Carlo prediction of 7971 events. The reaction cross section, averaged over a ± 1 σ energy window of $2.4 \leqslant E_\nu \leqslant 9.0$ GeV is determined to be $(31.6 \pm 10.5) \times 10^{-40}$ cm^2/nucleus. The result is the first evidence obtained for neutrino-nucleus coherent NC(π^0) scattering on iron, and is the first result on an average nuclear target above $A = 30$. The cross section is in agreement with NEUGEN3 implementation of the model put forth by Rein and Sehgal which is motivated by the PCAC hypothesis. A more detailed description of the results and a discussion of their implications can be found in **Chapter 12**.

A Search for Neutrino Induced Coherent NC(π^0) Production in the MINOS Near Detector

A dissertation

submitted by

Daniel David Cherdack

In partial fulfillment of the requirements

for the degree of

Doctor of Philosophy

in

Physics

TUFTS UNIVERSITY

February, 2011

ADVISER: William Anthony Mann

Part I

Measurement Motivation and Means

Chapter 1

Theory of the Coherent Neutrino-Nucleus Interaction

1.1 Nuclear Coherence

In depicting the interaction of a quantum particle with a nucleus the amplitude for scattering from the entire nucleus, $\mathcal{A}$ (with A nucleons, $\mathcal{N}$), is constructed as the sum of the amplitudes from the A individual nucleons. Consequently the covariant scattering matrix element is the sum

$$M(\mathcal{A}) = \sum_{A} M(\mathcal{N}) \ . \tag{1.1}$$

In most nuclear scattering reactions the relative phases among the individual nucleon scattering amplitudes are independent of each other. The transition probability is therefore constructed from the sum over the squares of the scattering amplitudes from the individual nucleons. For such incoherent reactions the cross section, which is proportional to the the square of the amplitude via

Fermi's Golden Rule for scattering, goes as:

$$\sigma \propto |M(\mathcal{A})|^2 = |\sum_A M(\mathcal{N})|^2 \approx |\sqrt{A \times M(\mathcal{N})^2}|^2 = A|M(\mathcal{N})|^2 \ . \qquad (1.2)$$

However, in the case of coherent nuclear interactions scattering from the individual nucleons of the target nucleus interferes constructively, and the total scattering amplitude, $M(\mathcal{A})$, is the sum over the individual nucleon amplitudes. The transition probability, which determines the cross section, is then

$$\sigma \propto |M(\mathcal{A})|^2 = |\sum_A M(\mathcal{N})|^2 = |A \times M(\mathcal{N})|^2 = A^2|M(\mathcal{N})|^2 \ . \qquad (1.3)$$

Coherent nuclear interactions are such that no property of the interaction can distinguish any of the nucleons from one another. Several conditions must be met in order to ensure that coherence prevails [1]:

1) The wavelength of the virtual exchange particle must be compatible with the dimensions of the entire nucleus. A relatively large wavelength (roughly the size of the nucleus) is required, which implies a diffractive scattering process, and a small momentum transfer, Q^2. In essence the incident wave must be large enough such that all the nucleons can interact with it in phase with each other.

2) The nucleus must recoil as a whole, without breakup. The momentum transferred to any nucleon must be small enough that it remains bound to the nucleus.

2) The nucleus remains unchanged and in the ground state. Any excitation would require a nucleon to change state, via a spin flip for example, and hence differentiate that nucleon from the others.

3) There is no transfer of quantum numbers, as that would single out individual nucleons. Spin, charge, and isospin transfer all require differentiation between nucleons. Both isospin and charge transfer may distinguish protons from neutrons, and spin transfer may identify nucleons in differing spin states.

1.2 Coherent Neutrino-Nucleus Scattering

Coherent neutrino-nucleus scattering can occur in either of two interaction channels via the exchange of a weak vector boson. The two reaction channels are *i*) neutral current (NC) via Z^0 exchange, or *ii*) charged current (CC) via $W^{\pm}$ exchange:

$$\nu(\overline{\nu}) + \mathcal{A} \rightarrow \nu + \mathcal{A} + \pi^0 \tag{1.4}$$

$$\nu(\overline{\nu}) + \mathcal{A} \rightarrow \mu^{\mp} + \mathcal{A} + \pi^{\pm} \tag{1.5}$$

In either channel the reaction is characterized by emission of a single forward-going pion, with the final-state nucleus remaining in its original ground state. Neither the nucleus nor any constituent nucleons are excited, nor is there any nuclear breakup. No quantum numbers (charge, spin, isospin) are transferred to the nucleus, as this would require different amplitudes for the various nucleons, destroying the coherence. Thus the NC channel produces a single π^0 as the only detectable final state product of the interaction, while the CC interaction produces only a charged lepton paired with an oppositely charged pion.

1.3 The Reaction Differential Cross Section

Coherent neutrino-nucleus scattering is described as a current-current interaction mediated by the weak force. The relevant Feynman diagram for the NC channel is shown in Fig. 1.1. The leptonic current, l^μ annihilates the incoming neutrino, $\nu(q)$, via $\psi_\nu(q)$ and creates the outgoing lepton $l(q')$ via $\bar{\psi}_l(q')$. The hadronic current is denoted by H_μ. The four-momentum-squared, q^2, and the energy, ν, transferred from the leptonic to the hadronic system are $q^2 = (p - p')^2 \equiv -Q^2$ and $\nu = (p^0 - p'^0) = E - E'$. The currents are related to the amplitude of the cross section by

$$M = \frac{G_F}{\sqrt{2}} l^\mu H_\mu = \frac{G_F}{\sqrt{2}} \bar{l}(q')\gamma^\mu(1-\gamma_5)\nu(q)H_\mu \ . \tag{1.6}$$

where G_F is the Fermi coupling constant for weak interactions. For the NC case the outgoing lepton is a neutrino, $\psi_\nu(q)$. The hadronic current can be broken up into its vector V_μ and axial-vector A_μ components and the covariant scattering amplitude can be written as,

$$M = \frac{G_F}{\sqrt{2}} \bar{\nu}(q')\gamma^\mu(1-\gamma_5)\nu(q)(V_\mu + A_\mu) \ . \tag{1.7}$$

The square of the amplitude can then be written

$$|M|^2 = \frac{G_F^2}{2} L^{\mu\nu}(V_{\mu\nu} + A_{\mu\nu} + I_{\mu\nu}) \ , \tag{1.8}$$

where $I_{\mu\nu}$ is the interference between the vector and axial-vector terms. Coherent interactions are low Q^2 processes. As $Q^2 \to 0$, the leptonic(neutrino)

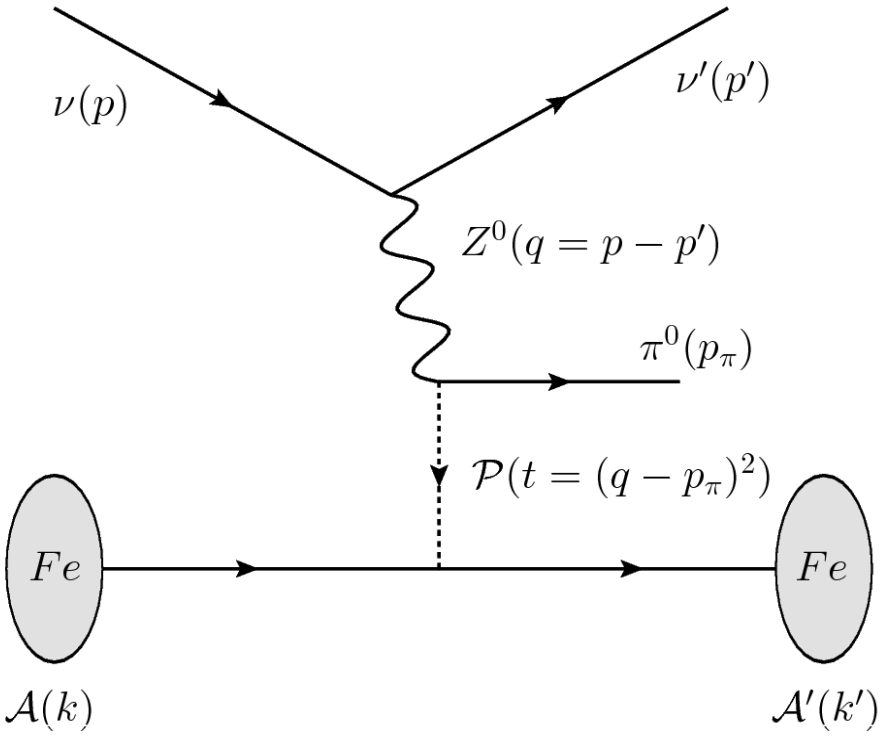

Figure 1.1: Feynman diagram for the coherent NC(π^0) reaction. The Z^0 exchange boson decays to a final-state π^0, and a pomeron, $\mathcal{P}$, which carries the momentum to the nucleus.

tensor for the NC channel reduces to

$$L_{\mu\nu} = 2\frac{EE'}{\nu^2} q_\mu q_\nu \ , \tag{1.9}$$

where q_μ is the covariant form of the four-momentum transfer. This allows the amplitude to be expressed as:

$$\begin{aligned} |M|^2 &= G_F^2 \frac{EE'}{\nu^2} q_\mu q_\nu (V_{\mu\nu} + A_{\mu\nu} + I_{\mu\nu}) \\ &= G_F^2 \frac{EE'}{\nu^2} (q_\mu V^{\mu\nu} q_\nu + q_\mu A^{\mu\nu} q_\nu + q_\mu I^{\mu\nu} q_\nu) \ . \end{aligned} \tag{1.10}$$

The CC channel requires an additional factor of 4 in $L_{\mu\nu}$ to account for the helicity states of the outgoing charged lepton. Note that the neutrino tensor is built from the four-momentum transfer of the contributing neutrino, q_μ, the only four-vector available to this weak process. Each of the three hadronic tensor terms can be related to the divergence of their constituent four-vectors. The vector tensor term thus can be expressed as

$$q_\mu V^{\mu\nu} q_\nu = q_\mu V^\mu V^{\nu *} q_\nu = (-i\partial_\mu V^\mu)\,(i\partial_\nu V^\mu) = |\partial_\mu V^\mu|^2 \ , \tag{1.11}$$

which is proportional to Q^2. As $Q^2 \to 0$ the divergence of the vector current must go to zero, thus eliminating the contribution of the vector component of the weak current. Kopelavich. et. al. [1] show that the Conserved Vector Current (CVC) hypothesis prevents a pion-pole term from appearing which would be non-zero in the limit of $Q^2 \to 0$, and dominate at low Q^2. The interference term, $q_\mu I^{\mu\nu} q_\nu$, vanishes in the case of coherent interactions in the limit that $Q^2 \to 0$, as it can only contribute if the final state can be produced by either a vector or axial-vector current.

The Partially Conserved Axial Current (PCAC) hypothesis relates the divergence of the axial-vector current to the amplitude of the pion field, $\phi_\pi(x)$

$$q_\mu A^\mu = \langle -i\partial_\mu A^\mu \rangle = f_\pi m_\pi^2 \phi_\pi(x) \ , \tag{1.12}$$

and the matrix element for the divergence of the axial current is consequently [2]

$$\langle \mathcal{A}' | \partial_\mu A^\mu | \mathcal{A} \rangle = f_\pi \frac{m_\pi^2}{Q^2 + m_\pi^2} \langle \mathcal{A}' | \mathcal{A} + \pi \rangle \ . \tag{1.13}$$

In the limit of $Q^2 \to 0$ this relation can be extended to the axial-vector tensor to yield

$$\begin{aligned} q_\mu A^{\mu\nu} q_\nu &= q_\mu \langle A^\mu \rangle \langle A^\nu \rangle^* q_\nu \\ &= -i f_\pi \langle \mathcal{A}' | \mathcal{A} + \pi \rangle \times i f_\pi \langle \mathcal{A}' | \mathcal{A} + \pi \rangle \\ &= f_\pi^2 |A(\mathcal{A} + \pi \to \mathcal{A}')|^2 \ , \end{aligned} \tag{1.14}$$

which has a term that is not proportional to Q^2, and remains in the $Q^2 \to 0$ limit. For the NC case an extra factor of 2 is introduced to account for the fact that $f_{\pi^0} = f_{\pi^\pm}/\sqrt{2}$. Only the axial-vector component of the hadronic tensor remains and the resulting amplitude can be used to construct the cross section via Fermi's Golden Rule for scattering

$$\begin{aligned} \sigma(\nu + \mathcal{A} \to \nu' + \mathcal{A}' + \pi^0) = G_F^2 \frac{EE'}{4EM\nu^2} 2 f_\pi^2 |A(\mathcal{A} + \pi \to \mathcal{A}')|^2 \\ \times (2\pi)^4 \ \delta^4(p_\mu + k_\mu - p'_\mu - k'_\mu) \\ \times \frac{1}{(2\pi)^3} \frac{d^3p'}{2E'} \frac{1}{(2\pi)^3} \frac{d^3k'}{2k'_0} \ . \end{aligned} \tag{1.15}$$

The cross section for the reaction $A + \pi \to A'$ expressed as a function of the

amplitude is

$$\sigma(\mathcal{A}+\pi\rightarrow\mathcal{A}')=\frac{|A(\mathcal{A}+\pi\rightarrow\mathcal{A}')|^2}{4\nu M} \times(2\pi)^4\delta^4(p_\mu+k_\mu-p'_\mu-k'_\mu)\frac{1}{(2\pi)^3}\frac{d^3k'}{2k'_0}\ . \tag{1.16}$$

Expressing Eq. (1.16) in terms of $\frac{d^3k'}{2k'_0}$ and substituting into Eq. (1.15) yields

$$\sigma(\nu+\mathcal{A}\rightarrow\nu'+\mathcal{A}'+\pi^0)=\frac{G_F^2f_\pi^2}{4\pi^3\nu}\sigma(\mathcal{A}+\pi\rightarrow\mathcal{A}')d^3p'\ . \tag{1.17}$$

Using the fact that $d^3p=|\vec{p}|^2dpd\Omega=|\vec{p}|^2dp2\pi d\cos\theta$ and that for massless particles $|\vec{p}|=E$, $Q^2=2EE'(1-\cos\theta)$ (along with their differential forms $d|\vec{p}|=dE$, $dQ^2=-2EE'd\cos\theta$, and $d\nu=-dE'$), the change of variables

$$d^3p'=E'^2dE'2\pi d\cos\theta=2\pi E'^2\left(\frac{-dQ^2}{2EE'}\right)(-d\nu)=\pi\frac{E'}{E}dQ^2d\nu \tag{1.18}$$

can be made. The doubly differential cross section can thus be written

$$\frac{d\sigma(\nu+\mathcal{A}\rightarrow\nu'+\mathcal{A}'+\pi^0)}{dQ^2d\nu}=\frac{G_F^2f_\pi^2}{4\pi^2\nu}\frac{E'}{E}\sigma(\mathcal{A}+\pi\rightarrow\mathcal{A}')\ . \tag{1.19}$$

This expression is known as Adler's theorem; it relates the weak neutrino-nucleus cross section to that of the strong pion-nucleus cross section. Pion pole terms arising from Eq. (1.14) have been negelected for the NC case, as they are proportional to the outgoing neutrino mass.

To account for small, non-zero values of Q^2 (and allow for a small contribution from the vector current) a propagator term is included of the form

$$G_A^2=\left(\frac{M_A^2}{Q^2+M_A^2}\right)^2\ , \tag{1.20}$$

where M_A is the axial mass for coherent interactions.

The value for M_A can be understood through a generalization of Vector Meson Dominance (VMD) applied to weak interaction theory known as Hadron Dominance (HD). HD postulates that a weak current can fluctuate into virtual hadrons, and can thus be characterized as a linear superposition of the weak vector boson and various mesons carrying the appropriate quantum numbers. Since the weak current can have both vector and axial-vector components, the mesons used in the HD based calculations include both vector and axial-vector mesons. The lightest mesons to have the appropriate quantum numbers and parity state are the a^1 meson (or the non-resonant $\pi\rho$ state) and the ρ meson; these are used for the axial-vector and vector component, respectively, of the weak current. The Feynman diagrams describing these processes are shown in Fig. 1.2. The cross section can be calculated in terms of the dominant a^1 scattering, diagram (a), plus corrections from the other diagrams. These corrections include contributions from the *i*) ρ, diagram (b), which introduces a small contribution from the vector current, contributions from *ii*) the π, diagram (c), which is proportional to the lepton mass and can be neglected for NC scattering, or contributions from *iii*) the $a^1-\rho$ interference term corresponding to the $I_{\mu\nu}$ tensor. The exchange particle mass, M_A, therefore becomes an effective parameter that represents the weighted average mass of the contributing mesons.

To check that the mass term used in the propagator is reasonable, uncertainty principle arguments can be used to estimate the coherence length, or distance travelled by the exchange meson. This distance should be compatible with the

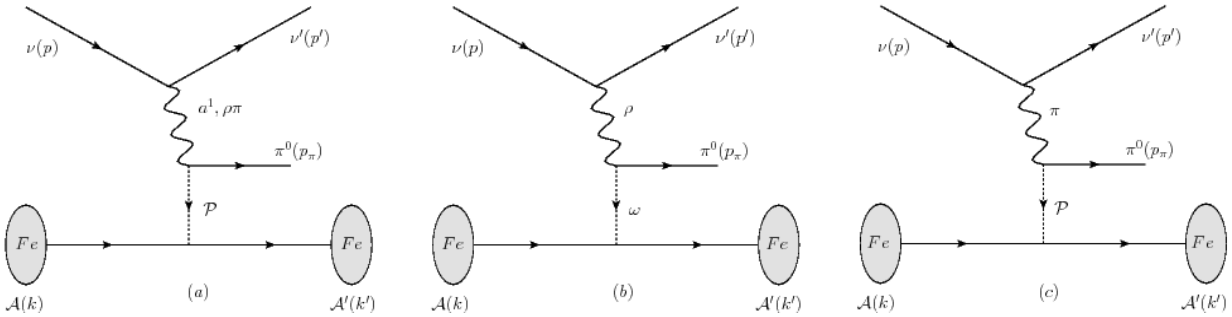

Figure 1.2: Feynman diagram for the HD terms of the coherent NC(π^0) cross section that contribute to M_A. The a^1 meson of diagram (a) provides the largest contribution to the amplitude.

interaction length; it is determined by (using natural units, $\hbar = c = 1$)

$$\begin{aligned} l_c = \Delta t_c \leqslant \frac{1}{\Delta E} &= \frac{1}{\nu - E_A} \\ &= \frac{1}{\nu - \sqrt{|\vec{q}|^2 + M_A^2}} \\ &= \frac{1}{\nu - \sqrt{\nu^2 + Q^2 + M_A^2}} \\ &\simeq \frac{2\nu}{Q^2 + M_A^2} \quad \text{for} \quad \nu \gg \sqrt{Q^2 + M_A^2}\ . \end{aligned} \tag{1.21}$$

A range of M_A values have been considered in the literature. An upper bound for M_A was set by early experiments at 1.35 GeV [1], however values as low as 0.95 GeV [3] have been used. Note that these values bracket the mass of the a^1 (1.26 GeV [4]). The Rein-Sehgal model uses a value of 1.0 GeV [5]. Figure 1.3 displays the value of G_A^2 over the relevant ranges for M_A and Q^2. The value of the propagator term only changes by few percent for low values of Q^2 (< 0.25 GeV^2) where about 80% of the interactions occur. It can, however change by as much as 20% for Q^2 values from 0.25 to 0.50 GeV^2, where the Rein-Sehgal model predicts the remaining $\sim$20% of the interactions to occur.

In addition to the propagator term, the cross section expressed in Eq. (1.19), needs to be corrected for the assumption of $Q^2 = 0$ which is used in deriving the

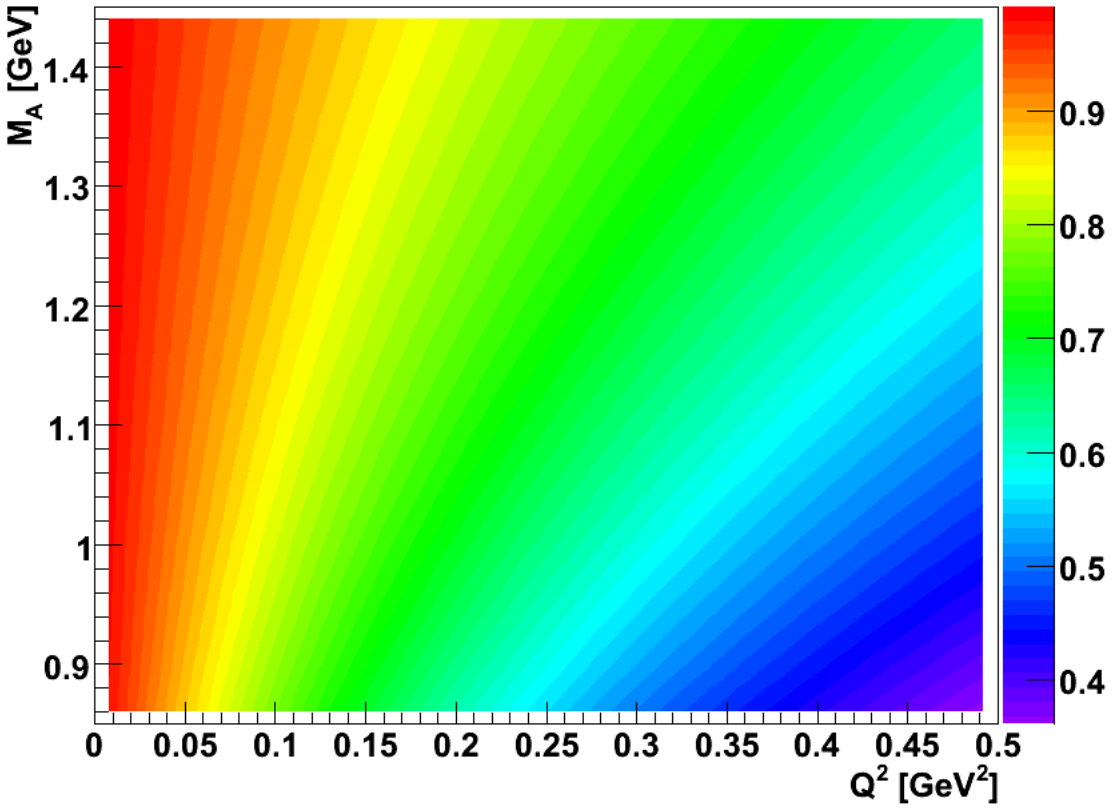

Figure 1.3: The value of the propagator term, G_A^2, as a function of M_A and Q^2. The change to the propagator term, and hence the overall cross section is relatively small across the relevant range of M_A for constant values of Q^2. The effect becomes more pronounced at values of $Q^2 > 0.25$ GeV^2, where the cross section is relatively small.

kinematic terms. Adding the propagator term, and correcting the kinematic term results in the following expression for the differential cross section for $Q^2 \geqslant 0$:

$$\frac{d\sigma(\nu + \mathcal{A} \to \nu' + \mathcal{A}' + \pi^0)}{dQ^2 d\nu} = \frac{G_F^2 f_\pi^2}{4\pi^2} \frac{4EE' - Q^2}{4E^2\sqrt{Q^2+\nu^2}} G_A^2 \; \sigma(\mathcal{A} + \pi \to \mathcal{A}') \; . \tag{1.22}$$

This expression is generally accepted by theorists exploring coherent neutrino-nucleus interactions though PCAC. The main difference between the various models is the treatment of the pion-nucleus scattering cross section. To elaborate on the differences between models, the Rein-Sehgal model [5], which is implemented in the NEUGEN3 [6] based Monte Carlo (MC) used in the MINOS experiment, will be elucidated. The differences between the Rein-Sehgal model and several competing models will then be discussed.

In addition to the PCAC-based models, a class of dynamical models, in which the interaction is modeled as the coherent sum of neutrino-nucleon interactions producing the appropriate final state, have been developed to explain the discrepancies between data from low-energy ($E_\nu \lesssim 1.0$ GeV) CC interactions and the predictions of the PCAC based models. As the NuMI beam produces neutrinos with energies almost exclusively above 1.0 GeV, and this investigation explores the NC channel, the rest of this discussion will focus on the coherent interaction models which are based upon PCAC.

1.4 The Rein-Sehgal Formulation

The first step of the Rein-Sehgal calculation for coherent NC(π^0) scattering is to take the derivative of Eq. (1.22) with respect to the (absolute value)

momentum transfer from the exchange particle to the nucleus, $|t| = |-(q - p_\pi)^2|$. This allows the pion-nucleus interaction to be expressed as a differential cross section in terms of the relevant kinematic variable. The only contribution to the cross section that is a function of $|t|$ is the pion-nucleus cross section, so the rest of the expression remains unchanged. The result is the triply differential cross section,

$$\frac{d\sigma(\nu + \mathcal{A} \to \nu' + \mathcal{A}' + \pi^0)}{dQ^2 d\nu d|t|} = \frac{G_F^2 f_\pi^2}{4\pi^2 \nu} \frac{E'}{E} G_A^2 \frac{d\sigma(\mathcal{A} + \pi \to \mathcal{A}' + \pi)}{d|t|} \ . \qquad (1.23)$$

The kinematic term here has been reset to the $Q^2 = 0$ form used by Rein and Sehgal. The differential pion-nucleus cross section can be expressed as a function of the differential pion-nucleon cross section in the forward direction ($|t| = 0$),

$$\frac{d\sigma(\mathcal{A} + \pi \to \mathcal{A} + \pi)}{d|t|} = A^2 |F(t)|^2 \left| \frac{d\sigma(\mathcal{N} + \pi \to \mathcal{N} + \pi)}{d|t|} \right|_{|t|=0} \ . \qquad (1.24)$$

Here $F(t)$ is the nuclear form factor, and the A^2 factor arises from the coherent nature of the scattering. Since the scattering is in the very forward direction and the imaginary part of the scattering amplitude gives the dominant contribution, the optical theorem can be used to express the differential pion-nucleon cross section in terms of the total pion-nucleon cross section, $\sigma_{tot}^{\pi^0 \mathcal{N}}$,

$$\left| \frac{d\sigma(\mathcal{N} + \pi \to \mathcal{N} + \pi)}{d|t|} \right|_{t=0} = \frac{1}{16\pi} \left[\sigma_{tot}^{\pi^0 \mathcal{N}} \right]^2 \ . \qquad (1.25)$$

A correction of the form $1 + r^2$, where $r = \mathrm{Re}\{f_{\pi\mathcal{N}}(0)\} / \mathrm{Im}\{f_{\pi\mathcal{N}}(0)\}$, and $f_{\pi\mathcal{N}(0)}$ is the forward scattering amplitude, is applied to account for the contribution from the real part of the scattering amplitude. Rein and Sehgal incorporate this correction factor, but the possible real part of the scattering

amplitude is small and this correction factor can be neglected. The total pion-nucleon cross section is determined numerically from pion-deuterium scattering data

$$\sigma_{tot}^{\pi^0\mathcal{N}} = \frac{1}{4}\left[\sigma_{tot}^{\pi^+\mathcal{D}} + \sigma_{tot}^{\pi^-\mathcal{D}}\right] \ , \tag{1.26}$$

or an approximate empirical relation to photon-nucleon (Compton) scattering

$$\sigma_{tot}^{\pi^0\mathcal{N}} = 200\sigma_{tot}^{\gamma\mathcal{N}} \ , \tag{1.27}$$

which yields a similar result. The nuclear form factor is expressed as

$$|F(t)|^2 = e^{-\frac{1}{3}R_{\mathcal{N}}^2 A^{\frac{2}{3}}|t|}F_{abs} \ , \tag{1.28}$$

where $R_{\mathcal{N}}$ is the radius of a nucleon and F_{abs} accounts for pion absorption in the nucleus, which in this model is assumed to be independent of $|t|$. An estimate for F_{abs} results from a simple model of the nucleus, treating it as a homogeneous sphere. This model takes into account the average path length of a pion in the nucleus as a function of the inelastic pion-nucleon cross section $\sigma_{inel}^{\pi^0\mathcal{N}} = \sigma_{tot}^{\pi^0\mathcal{N}} - \sigma_{el}^{\pi^0\mathcal{N}}$, and the estimated size and density of the nucleus, using the expression,

$$F_{abs} = \exp\left\{-\frac{9A^{\frac{1}{3}}}{16\pi R_{\mathcal{N}}^2}\sigma_{inel}^{\pi^0\mathcal{N}}\right\} \ . \tag{1.29}$$

The final expression for the Rein-Sehgal model of the differential cross cross section is thus,

$$\begin{aligned}\frac{d\sigma(\nu + \mathcal{A} \to \nu' + \mathcal{A}' + \pi^0)}{dQ^2 d\nu d|t|} = \frac{G_F^2 f_\pi^2}{4\pi^2\nu}\frac{E'}{E}G_A^2\frac{A^2}{16\pi}\left[\sigma_{tot}^{\pi^0\mathcal{N}}\right]^2 \\ \times\ e^{-\frac{1}{3}R_{\mathcal{N}}^2 A^{\frac{2}{3}}|t|}\ e^{-\frac{9A^{\frac{1}{3}}}{16\pi R_{\mathcal{N}}^2}\sigma_{inel}^{\pi^0\mathcal{N}}} \ .\end{aligned} \tag{1.30}$$

The cross section expression can be factored into four component parts. The HD based extention to finite Q^2 though the use of the propagator G_A has already been discussed. The weak NC interaction and the associated kinematics are represented by

$$\frac{G_F^2}{4\pi^2}\frac{(4EE'-Q^2)^2}{4E^2\sqrt{Q^2+\nu^2}} = \frac{G_F^2}{4\pi^2}\frac{E'}{\nu E} \quad \text{in the limit} \quad Q^2 \to 0 \ . \tag{1.31}$$

The PCAC term

$$f_\pi^2 \frac{A^2}{16\pi}\left[\sigma_{tot}^{\pi^0\mathcal{N}}\right]^2 e^{-\frac{1}{3}R_{\mathcal{N}}^2 A^{\frac{2}{3}}|t|}\ e^{-\frac{9A^{\frac{1}{3}}}{16\pi R_{\mathcal{N}}^2}\sigma_{inel}^{\pi^0\mathcal{N}}} \ . \tag{1.32}$$

can be factored into two distinct parts. These are the pion-nucleon cross section,

$$\left[\sigma_{tot}^{\pi^0\mathcal{N}}\right]^2 \ , \tag{1.33}$$

and the nuclear model expression,

$$\frac{A^2}{16\pi} e^{-\frac{1}{3}R_{\mathcal{N}}^2 A^{\frac{2}{3}}|t|}\ e^{-\frac{9A^{\frac{1}{3}}}{16\pi R_{\mathcal{N}}^2}\sigma_{inel}^{\pi^0\mathcal{N}}} \ . \tag{1.34}$$

The latter includes A^2 to account for the coherent state of the nucleus, a factor for the size of the nucleus, and a factor related to the effects of pion absorption. The final step in the Rein-Sehgal model is to change and/or to integrate over the differential kinematic variables. This is done in order to either calculate the total cross section, or the cross section as a function of other kinematic variables such as neutrino energy, or the angle of the pion with respect to the incoming neutrino. The integration over the variable $|t|$ is fairly involved, and beyond the scope of this summary. When making comparisons with other models, one should note Rein and Sehgal assume an infinitely heavy nucleus (i.e. no nuclear recoil), which allows the calculation to be performed

analytically.

1.5 Other PCAC Based Models

There are several alternatives to the original Rein-Sehgal model. The first of these is the Kopeliovich-Marage [1] model. The largest difference between the Kopeliovich-Marage model and the Rein-Sehgal model comes from the difference in the nuclear models. Kopeliovich and Marage note that the absorption factor used in the Rein-Sehgal nuclear model is not consistent with the diffractive nature of pion-nucleon scattering, and instead use a nuclear model based on Glauber theory. In addition the kinematic term used in the Kopeliovich-Marage model is not simplified by the $Q^2 = 0$ assumption, and the values of 1.35 GeV and 1.05 GeV are used for M_A, both of which are justified experimentally, based on the data available at the time.

In the model by Paschos et. al. [7], the pion-nucleus scattering is parametrized in much the same way as in the Rein-Sehgal model, however pion-carbon scattering data, instead of pion-deuterium or photon-nucleon data is used. Instead of altering the value of M_A, the Paschos et. al. model varies the value of the entire propagator term ($G_A^2 = 0.2$, 0.5, 1.0, and 4.0). Paschos et. al. also uses the full form of the kinematic term.

The model by Hernandez et. al. [8] follows that of Rein-Sehgal, aside from a few corrections made to help improve the CC predictions at low neutrino energy. Hernandez et. al. use the $Q^2 \to 0$ assumption for the kinematic terms, noting that the choice is somewhat arbitrary. Hernandez et. al. also suggest some improvements to the pion-nucleon cross section, and to the pion-absorption term, but admit that effects of the corrections become small for

larger nuclei and at higher neutrino energies. As the investigation of this Thesis relies on the relatively high energy neutrinos produced by the NuMI beam, and an iron detector, the improvements to the Rein-Sehgal model suggested by Hernandez et. al. should have little effect on the MINOS Monte Carlo predictions used in this Thesis.

The Berger-Sehgal [3] model is built from the Rein-Sehgal model with a few changes. The value used for M_A is 0.95 GeV, and the full form of the kinematic term is used. The model of the nucleus and the nuclear pion absorption is the same, but updated pion-nucleon cross sections are estimated differently in that linearly interpolated pion-carbon scattering data is used. In addition the Berger-Sehgal model is the only model not to assume an infinitely heavy nucleus for the integration over $|t|$. Instead values of $|t|$ are calculated in the interaction center-of-mass, and are then boosted to the lab frame.

There are several implementations of the Rein-Sehgal model in various neutrino generators. Each of these implementations yields somewhat different predictions for the neutrino cross section as a function *i*) of the neutrino energy, *ii*) of the nuclear target, and *iii*) of the outgoing final-state pion kinetic energy, (T_π). There is an alternative class of coherent neutrino interaction models based on nuclear physics that moderate the interaction. The latter class of models has been more successful in replicating experimental results obtained using low energy neutrinos (with $E_\nu \lesssim 1.0$ GeV), while the PCAC-based models agree better with data from experiments using neutrinos of energies above 3 GeV. There is also a paper by Rein and Sehgal that offers an update to their model that includes a lepton mass term [9]. A comparison of these models (including alternative implementations of the Rein-Sehgal model) for the prediction of T_π at a few specific neutrino energies (incident on carbon) is

shown in Fig. 1.4.

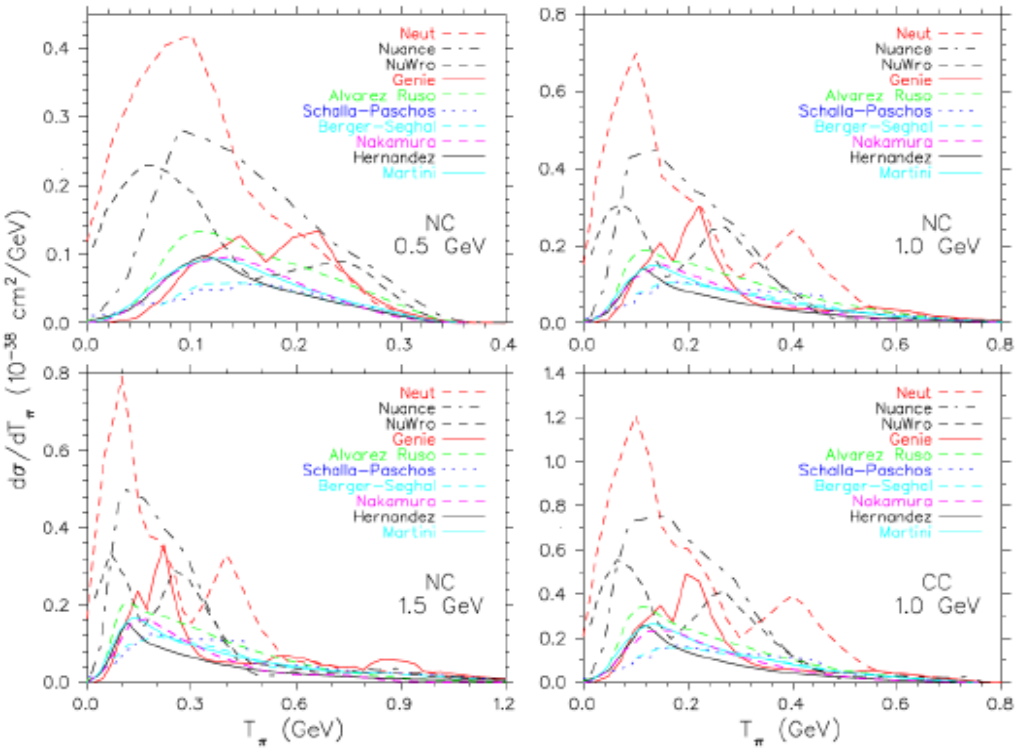

Figure 1.4: Differential cross sections as a function of the pion final state kinetic energy (T_π) on carbon, for various neutrino coherent scattering models. At the neutrino energies plotted, the predicted cross sections for the models vary significantly in both shape and rate [10].

NEUGEN3 [6] is the neutrino event generator used in MINOS. For coherent interactions NEUGEN3 is equivalent to the GENIE [11] event generator referenced in the plots of Fig. 1.4. The Rein-Sehgal model for coherent interactions and the coherent NC(π^0) cross sections calculated by NEUGEN3 do not necessarily agree over all kinematic regimes. However, throughout the rest of this Thesis, the results of the NEUGEN3 event generator, propagated though the MINOS MC, are assumed to be synonymous with the Rein-Sehgal model. All reference to the predictions of the Rein-Sehgal model, or the Rein-Sehgal cross section, are in fact, the NEUGEN3 implementation of the Rein-Sehgal model.

Chapter 2

Measurements by Previous Experiments

The first evidence for coherent neutrino-nucleus scattering was obtained by the Aachen-Padova collaboration who analyzed neutrino interactions producing single neutral pions in the final state [12]. The Aachen-Padova spark chamber detector contained a longitudinal stack of 282 aluminum ($A = 27$) plates, each of which were 1.0 cm thick and 2.0 m x 2.0 m across. The plates were spaced 1.0 cm apart, and the gaps were filled with a gas mixture comprised of 70% neon and 30% helium. The spark chamber detector was deployed in the CERN-PS wide-band low energy neutrino (antineutrino) beam. The neutrino beam incident on the 30 ton detector was obtained using 26 GeV protons. The neutrino flux peaked at an E_ν of 1.4 GeV. A total exposure of 1.7×10^{19} POT was obtained, resulting in roughly one million neutrino (and antineutrino) events being recorded.

An analysis of resonantly produced neutral pions from NC interactions uncov-

ered an excess of events at small angles. The excess was comprised of events described by the authors as "naked" π^0s, where no recoil nucleon (nor any other activity) was observed. The π^0 search required the events to have two EM showers (from the two converted photons) for which the combined transverse momentum was consistent with the beam direction, and the invariant mass was consistent with the π^0 mass. A sample of single π^0 events where the recoil nucleon could be identified was used to constrain the resonant π^0 sample, which now comprised the largest background. The fraction of resonant events where the recoil nucleon could be identified was determined from charged current resonance production interactions producing neutral pions, and was used to estimate the contribution from resonance production to the "naked" π^0 sample. An independent cross check of the "naked" pion event rate resulting from resonance production was calculated based on theoretical predictions which were normalized to the event rate at high angles. Although the latter method suffered from systematic uncertainty, while the former method suffered from statistical uncertainty, the two methods produced consistent results.

The small angle of the excess "naked" pions with respect to the beam suggested a small momentum transfer from the incoming neutrino to the nuclear system which was recognized as consistent with coherent NC(π^0) interactions. The number of measured neutrino (antineutrino) interactions led to a cross section estimate of $\sigma = (29 \pm 10) \times 10^{-40}\text{cm}^2/\text{Al nucleus}$ ($\sigma = (25 \pm 7) \times 10^{-40}\text{cm}^2/\text{Al nucleus}$). The two cross sections are consistent with each other, and with the Rein-Sehgal prediction of $\sigma = 33 \times 10^{-40}\text{cm}^2/\text{Al nucleus}$.

Over the next several years the experiments of Gargamelle (CERN-PS) [13], CHARM (CERN-SPS) [14], SKAT (IHEP Serpukhov) [15], and the 15-ft. Bubble Chamber (FNAL) [16], made similar measurements although with differ-

ent neutrino energy spectra and using other nuclear targets. Like the Aachen-Padova result, all four of the measurements provided high-resolution event-by-event reconstruction, but were only able to collect low-statistics event samples. The four results were consistent with the Rein-Sehgal predictions within experimental uncertainties. The coherent NC(π^0) cross sections measured by these experiments, along with more recent experiments, are displayed in Fig. 2.1. All of the data points have been scaled to a titanium target. Scaling of the cross sections was done using cross section ratios calculated by the NEUGEN3 implementation of the Rein-Sehgal model. Also shown in Fig. 2.1 is the coherent NC(π^0) cross section on titanium calculated from NEUGEN3. Aside from the differing target nuclei and beam spectra, the detectors also differed in their threshold for neutral pion detection. The pion detection threshold essentially defines a minimum value for the energy transfer to the hadronic system, ν, for the events used in the analysis, and therefore sets a minimum for the limit of integration used when calculating the total cross section to be compared with experimentally obtained values. For most experiments, however, the full cross sections are calculated with the use of acceptance corrections to account for the events lost to the pion energy threshold.

More recently, the NOMAD [17], MiniBooNE [18], and SciBooNE [19] experiments have measured the coherent NC(π^0) cross section on carbon. These experiments have compiled large statistics event samples, but with relatively higher systematic errors. The cross sections measured by these experiments, along with those from the previously generation of experiments are shown in Table 2.1. The recent high-statistics measurements have increased the World data set of neutrino-nucleus coherent NC(π^0) reactions, have tested the coherent models at visible energies near 1.0 GeV, and along with recent coherent CC($\pi^{\pm}$) measurements (K2K [20][21], MiniBooNE [22], SciBooNE [22]),

have inspired new theoretical work on the subject. In particular, the coherent CC($\pi^{\pm}$) cross section measured at $E_\nu \lesssim 1$ GeV is much lower than that predicted by the Rein-Sehgal model.

Experiment	Year	Average Neutrino Energy, $\bar{E}_\nu$ [GeV]	Average Nucleus $\mathcal{A}$ [nucleons]	Minimum π^0 Energy, $E_{\pi^0}^{min}$ [GeV]	Coherent Cross Section, σ^{coh} $\nu/(\bar{\nu})$ $[10^{-40}\mathrm{cm}^2/A]$	Rein-Sehgal (NEUGEN3) Cross Section $[10^{-40}\mathrm{cm}^2/A]$
Aachen-Padova [12]	1983	2	Aluminum 27	0.0	29±10 (25±7)	19.0
Gargamelle [13]	1984	2	Freon CF_3Br - 30	0.0	31±20 (45±24)	27.7
CHARM [14]	1985	31 24	Marble $CaCO_3$ - 20	6.0	96±42 (79±26)	84.5
SKAT [15]	1986	7	Freon CF_3Br - 30	0.0	52±19	44.4
15' BC [16]	1986	20	Neon NeH_2 - 20	2.0	RSx0.98±0.24	66.0
MiniBooNE [18]	2008	0.8	Mineral Oil C_XH_Y - 12	0.0	RSx0.65±0.14 RSx0.65±0.14	4.4
NOMAD [17]	2009	24.8	Carbon+ 12.8	0.5	72.6±10.6	52.1
SciBooNE [19]	2010	0.8	Polystyrene C_8H_8 - 12	0.0	RSx0.96±0.20	4.4

Table 2.1: Summary of previous coherent NC(π^0) searches. Several experiments only provide a ratio to the Rein-Sehgal prediction for the coherent NC(π^0) cross section. These results are displayed as RSx the fractional cross section. Coherent scattering off hydrogen is not defined, as a single nucleon cannot be in a coherent state. Hydrogen nuclei, therefore, do not contribute to the event rate, and are not included in the calculation of A.

The Rein-Sehgal model is predicated on assumptions which are justified for higher E_ν, and for larger target nuclei. These assumptions are not valid, however, at lower neutrino energies ($E_\nu \lesssim 1.0$ GeV), and for relatively small target nuclei. Corrections to the older PCAC based models have been offered and a new approach to describing coherent interactions has been developed to help explain the dearth of low energy events in recent experiments. The newer PCAC based models of Rein and Sehgal [9], Berger and Sehgal [3],

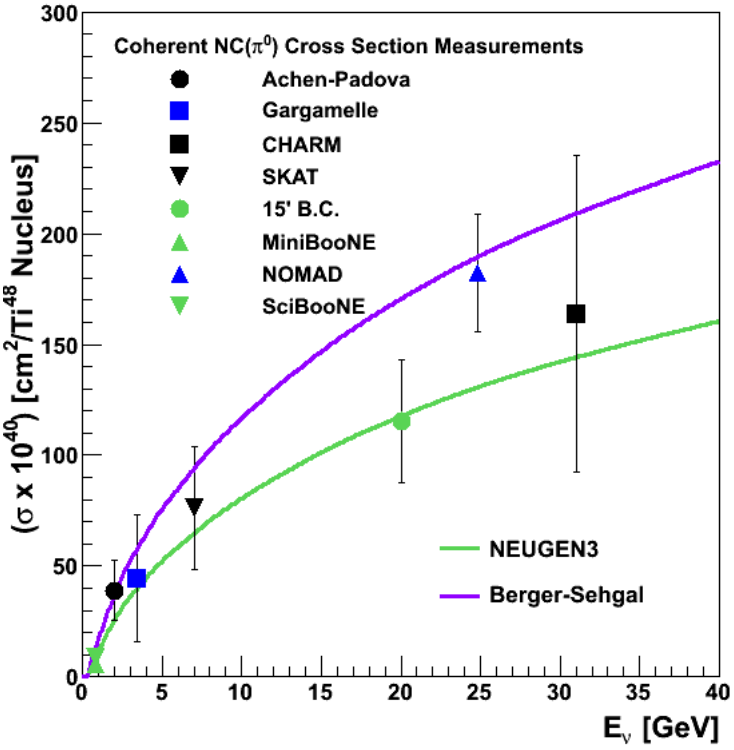

Figure 2.1: Selected cross section measurements for neutrino-induced coherent NC(π^0) scattering, scaled to titanium, as a function of neutrino energy, E_ν. Titanium is used because the average nuclear mass in the MINOS detector is 48 amu, the atomic weight if titanium. The green line is the NEUGEN3 prediction for the neutrino-titanium coherent NC(π^0) scattering cross section as a function of neutrino energy. The MiniBooNE, SciBooNE, and the 15-ft. Bubble Chamber experiments do not provide absolute cross sections. Instead they report cross sections as fractions of the Rein-Sehgal predictions at the appropriate values of A and E_ν. The relative cross sections, shown in green, have been scaled to the relevant NEUGEN3 cross section predictions. The purple line is an estimate of the Berger-Sehgal cross section, which agrees with the Rein-Sehgal cross section reported in reference [5] for Aluminum at 2.0 GeV, and with the MC cross section reported by NOMAD.

Paschos et. al. [7], and Hernandez et. al. [8] include updated nuclear models, more precise pion-nucleon scattering data, and/or the inclusion of the terms proportional to the lepton mass. In some cases the newer models no longer assume an infinitely heavy nucleus, and in turn take into account the dependence of the pion-nucleon scattering cross section on the momentum transfer to the nucleus, $|t|$, rather than evaluate it at $|t| = 0$. These corrections lead to improved agreement with data, however, there are several assumptions intrinsic to a PCAC based model that can affect the prediction of the coherent cross section.

A new class of "dynamical" models uses a microscopic approach where the possible reactions with individual nucleons are considered. The PCAC models evaluate reactions with the nucleus as a whole, and employ a nuclear model that enforces the coherence condition. The reactions must preserve the nuclear coherence and produce the relevant final states. The dynamical models, on the other hand, begin with neutrino-nucleon interactions that produce a single pion in the final state, and add the amplitudes for those interactions coherently over the nucleus. These reactions are not predicted by the PCAC hypothesis, but still contribute to the coherent scattering amplitude; their contribution only having a significant effect at low neutrino energies. The largest contribution to the scattering amplitude comes from virtual Δ-hole excitations. These models also elucidate the dependence of the cross section on the angle of the outgoing pion with respect to the incident neutrino direction, which, again, becomes more pronounced at low energies. The dynamical models have had success in reproducing the behavior of coherent interactions at low energies, but fail to do so at higher energies ($E_\nu > 3$ GeV), where the PCAC models have been shown to be in good agreement with data.

Several of the recent experiments use the Rein-Sehgal prediction for coherent scattering as a template with which to fit the data. This technique assumes the shape of the Rein-Sehgal distributions are correct, but not the overall normalizations. These analyses are model-dependent, and it has been suggested that the use of an alternate model could affect the results obtained. Although the analysis presented in this Thesis does not make use of a relatively light nuclear target, nor neutrinos with an $E_\nu \lesssim 1.0$ GeV, every effort has been made to ensure that the result is independent of the coherent model used in the MINOS Monte Carlo simulations.

Chapter 3

The Coherent NC(π^0) Cross Section Measurement in MINOS

3.1 Motivation for a MINOS Measurement

New measurements of single π^0 coherent scattering are desirable for three reasons: *i*) Additional data are needed with which to compare current models of the interaction; *ii*) clarification of the fundamental physics is needed, for example, the applicability of PCAC-based approximations, and *iii*) more accurate delination is needed of the cross section of the process, in as much as coherent NC(π^0) scattering may pose a significant background for future $\nu_\mu \rightarrow \nu_e$ oscillation experiments. The latter situation is especially relevant if the value of θ_{13} is in fact significantly below the CHOOZ limit, where uncertainties in the rate of coherent NC(π^0) events could overwhelm the ν_e oscillation appearance

signal. Obviously, these objectives go hand-in-hand: Better determination of the cross section for a range of neutrino energies and for a variety of nuclear targets, necessarily involving a range of outgoing pion energies, is needed to fully explore the phenomenology. Such measurements will be prerequisites for reducing the systematic errors in the measurement of θ_{13}, Δm^2_{13}, and δ_{CP} in future accelerator-based neutrino oscillation measurements using long baselines.

3.2 The NuMI Beam

The NuMI beam, which stands for "Neutrinos at the Main Injector", was designed as a neutrino source for the MINOS experiment, and is now also used by the MINERνA and the NOνA experiments. To create the NuMI beam, protons are accelerated, first up to 400 MeV by the Linac linear accelerator, then up to 8.0 GeV by the Booster synchrotron, and then to 120 GeV by the Main Injector (MI) synchrotron. The Main Injector accelerates an 8.7 μs pulse of protons every 2.0 s. The majority of the protons are either used to create antiprotons to be used in the Tevatron, or are extracted to NuMI. The beam proton intensity is measured in units of Protons-On-Target (POT) by toroids placed along the beamline upstream of the target.

The protons are directed so as to strike a graphite target, producing hadronic final states consisting mostly of charged pions and kaons. These secondary particles are focused by two magnetic horns. The relative position of the target and horns, and the current in the horns, can be adjusted to provide different beam energy spectra. The current in the horns can be reversed to focus oppositely charged hadrons and create an anti-neutrino beam. The majority

of MINOS running was taken with the beam configured in neutrino-focusing mode and in the low energy configuration (LE-10). The focused pions and kaons are directed though a 675 m long decay pipe where the pions and kaons decay to neutrinos and charged leptons. At the end of the decay pipe is a hadron monitor followed by the absorber, which consists of five meters of concrete used to absorb the remaining (undecayed) hadrons. Between the absorber and the MINOS Near Detector lies 240 m of rock which stops most of the remaining muons. Along the first 40 m of rock there are three alcoves dug into the rock which contain muon monitors. The monitors are used to measure the muon flux, and are used to help constrain and measure the neutrino flux [23]. With the LE-10 configuration (in neutrino mode) the beam spectrum peaks at roughly 3.0 GeV, and is comprised of 92.9% ν_μ, 5.8% $\bar{\nu}_\mu$, 1.0% ν_e, and 0.3% $\bar{\nu}_e$.

Determining the neutrino flux of the NuMI beam with good precision is essential to performing a direct cross section measurement. The most precise measurement of the NuMI neutrino flux comes from the measurement of the inclusive CC cross section [24]. The flux is calculated as a function of the detector live time, measured in POT, and is given in the units of neutrinos/m^2/10^9 POT. For the Run I + Run II data sample in the MINOS Near Detector, the live time is 2.8×10^{20} POT. The error on the POT counting is estimated at 1.0% [25]. The integrated flux, which is used to calculate the cross section, is determined to be 291,000$\pm$7.8% neutrinos/m^2/10^9 POT using the numbers displayed in Table 3.1.

Energy Range	Flux	Uncertainty	Flux	Uncertainty	Uncertainty
[GeV]	$[\frac{\nu/\mathrm{GeV}/\mathrm{m}^2}{10^9\mathrm{POT}}]$	$[\frac{\nu/\mathrm{GeV}/\mathrm{m}^2}{10^9\mathrm{POT}}]$	$[\nu/\mathrm{m}^2/10^9$ POT]	$[\nu/\mathrm{m}^2/10^9$ POT]	[%]
0.0-0.6†	3.92×10^3	520	2.35×10^3	310	13.3
0.6-1.2†	2.09×10^4	2.2×10^3	1.26×10^4	1.3×10^3	10.4
1.2-1.8†	4.38×10^4	4.4×10^3	2.63×10^4	2.6×10^3	10.1
1.8-2.4†	6.21×10^4	5.9×10^3	3.73×10^4	3.5×10^3	9.6
2.4-3.0†	8.39×10^4	6.8×10^3	5.03×10^4	4.1×10^3	8.2
3.0-4.0	8.05×10^4	5.2×10^3	8.05×10^4	5.2×10^3	6.5
4.0-5.0	3.06×10^4	2.4×10^3	3.06×10^4	2.4×10^3	7.8
5.0-7.0	9.07×10^3	530	1.81×10^4	1.1×10^3	5.8
7.0-9.0	5.18×10^3	350	1.04×10^4	700	6.8
9.0-12	3.21×10^3	220	9.63×10^3	660	6.9
12-15	1.94×10^3	100	5.82×10^3	300	5.2
15-18	1.09×10^3	65	3.27×10^3	200	6.0
18-22	629	37	2.52×10^3	150	5.9
22-26	348	20	1.39×10^3	80	5.7
26-30	200	13	800	52	6.5
30-36	119	6.8	714	41	5.7
36-42	72.2	3.9	433	23	5.4
42-50	51.6	2.8	413	22	5.4
Total	-	-	2.93×10^5	2.3×10^4	7.8

Table 3.1: NuMI flux as a function of neutrino energy presented in the inclusive CC cross section paper [24]. † Flux data is not provided by the inclusive CC cross section paper for $E_\nu < 3.0$ GeV, and must be obtained from the muon monitor based flux measurement [23]. The two measurements are consistent within uncertainties for the neutrino energy ranges where the measurements overlap. The average E_ν, taking into account the small contribution from neutrinos with an energy above 50 GeV, is 4.9 GeV. The range of neutrinos energies about the average that contains 68% of the flux is $2.4 \leq E_\nu \leq 9.0$ GeV

3.3 The MINOS Near Detector

The MINOS Near Detector (ND) was designed as a muon tracking spectrometer used to measure the muon neutrino energy spectra of the NuMI beam before any the neutrinos have a chance to oscillate into one of the other two neutrino species. The unoscillated energy spectrum can then be compared to the oscillated energy spectrum measured in the MINOS Far Detector (FD) and the oscillation parameters θ_{23} and Δm^2_{23} can be extracted [26]. Because it was designed for near-to-far spectral comparisons, the Near Detector mimics the structure of the FD as much as possible. For the purpose of a neutrino cross section analysis, however, the Near Detector functions as an iron tracking calorimeter, measuring the energy of the charged leptons and hadronic showers produced by neutrino interactions.

The 980 ton Near Dector is made up of 282 planes. Each plane consists of a 2.54 cm (1 in.) thick steel plane, followed by a 1 cm thick plane of scintillator-doped (1% PPO, and 0.030% POPOP fluors) polystyrene. Each scintillator plane consists of 4.1 cm wide strips, each co-extruded with a reflective TiO_2 sheath, and contains an embedded wavelength-shifting optical fiber. The strips are oriented 45° from horizontal, with each alternating plane rotated 90° from the previous plane. The two orthogonal configurations are labeled as U planes and V planes. The planes are spaced 6 cm apart, with the remaining volume (2.46 cm/plane) filled by air. The cross section of the planes resembles a "squashed octagonal prism" 4.8 m across, and 3.8 m high.

One end of each of the optical fibers is covered with a piece of reflective aluminum mylar tape, while the other end is attached to a Hamamatsu M64 photomultiplier tube (PMT). Each PMT, which converts the signal from the

scintillation light to an electrical signal, has 64 channels; each channel is connected to a single optical fiber. The PMTs read out through a 53 MHz continuous analog processing chip known as a QIE or charge to current encoder. The MENU modules, which contain the QIE chips, also house an ADC and a FIFO for data storage. A MINDER provides interface, control, and power to groups of 16 MENU modules and applies a 19 ns time stamp to the data. The ND electronics have to read out faster than the FD electronics because the event rate is greater by 5-6 orders of magnitude. The 19 ns time stamp gives the ND output the same data format as the Far Detector output.

The starting point for the energy calibration in MINOS is the measurements obtained with the MINOS Calibration Detector (CalDet) [27]. CalDet was constructed to have the same planar structure of the MINOS Near and Far Detectors and wasinstrumented with the same electronics. It was exposed to two particle beams at the CERN-PS. Incident upon the CalDet were hadrons and leptons of known energies at various settings from 0.2 to 10.0 GeV. The response of the detector was calibrated to the input energies of the incident beam particles. Electromagnetic showering particles such as electrons and neutral pions elicit a different response than do track-producing particles such as muons, protons and charged pions. The induced signal from EM showers establishes the electromagnetic energy scale, while the light output and the associated electronic response to (non-π^0) hadrons sets the hadronic energy scale. The muon energy scale was also measured. Coherent NC(π^0) interactions only produce neutral pions, and for the purpose of this analysis all showers are calibrated to the electromagnetic energy scale.

The responses of the MINOS Near and Far Detectors will differ from the CalDet, and from each other due to the differences in their sizes, relative

lifetimes, and in the individual scintillator strips and PMTs. To account for these differences, a calibration scheme was designed to account for spacial and temporal differences in the detector responses. A light injection system together with the detector response to cosmic muons are used in calibrate the detectors. There are five steps in the calibration chain. They are *i*) the change in the response over time (*drift*) due to PMT and scintillator degradation, *ii*) differences in the *attenuation* of the light as it travels through the optical fiber to the PMT, *iii*) differences between strips (*strip to strip*), *iv*) the *linearity* of the of the PMT response over the range of light input, and *v*) the ratio of the output (signal) PMT electrons, to the input (photo) electrons (*gains*), which differs for each pixel of each PMT.

The calibrated detector response is input into the reconstruction software. Raw hit information is used by the reconstruction software to identify tracks and showers and to calculate kinematic quantities, such as the event energy and the angle of the tracks and showers with respect to the beam direction. The output of the reconstruction is used as an input to the $\nu_\mu \rightarrow \nu_e$ analysis software, where further calculations related to identification of events containing EM showers are performed. The final EM energy scale is set using a comparison of the reconstructed energy in GeV and the calibrated detector response measured in ADCs for MC events. The relationship between the two is found to be linear with small uncertainty, and the resulting correction to the reconstructed energy is applied to the data. The output of the $\nu_\mu \rightarrow \nu_e$ software is in turn is used as an input to the coherent NC(π^0) search software.

The Near Detector is comprised of four sections. The first 20 planes act as a veto section, used to reject events originating in front of the detector, such as rock muons and rock neutrons. The next section, referred to as the target

region, consists of 40 planes. Events with interaction vertices in this region are used to compare with the FD. The next 60 planes make up the third region, known as the hadron shower region. This region is used to fully contain the hadronic activity produced by showers originating in the target region. The final 160 planes of the Near Detector are used as a muon spectrometer.

The center of the beam spot on the Near Detector is 50 cm to the left of the detector's vertical midpoint. A 40 kA-turn magnetic coil runs through the Near Detector 50 cm from the vertical midpoint on the other side, such that the magnetic field where the beam strikes the detector is comparable to the FD magnetic field. Only one out of every five planes is fully instrumented (containing scintillator, and the related electronics). The first three regions are partially instrumented about the beam spot, with the scintillator covering at least a 1.0 m radius. The muon spectrometer has no instrumentation for four out of five planes. The fiducial volume defined for the coherent NC(π^0) analysis was chosen to maximize the sensitivity of the measurement, and does not employ the conventional detector sections. The analysis of this Thesis is based only on Near Detector data; obviously the comparison of ND and FD spectra has no bearing on the result. The fiducial volume is defined by a 0.8 m radius, 4.0 m long cylinder concentric with the beam spot, starting at plane 17 (1.0 m) and running parallel to the Near Detector z-axis for 67 (4.0 m) planes. The 0.8 m radius gives a cross sectional area of 2.0 m^2 and, together with a length of 4.0 m, a total volume of 8.0 m^3.

The direct calculation of a cross section requires a detailed study of the number of nuclei of each element in the Near Detector fiducial volume. The majority of the mass in the Near Detector comes from the steel plates. Less than 5.0% of the detector mass comes from scintillator strips and the remainder of the

components. There are 3.57×10^{29} nuclei in the Near Detector fiducial volume, with an average molecular weight of 48 amu. The main contribution to the uncertainty of the number of nuclei is the uncertainty on the mass of the steel. The MINOS NIM paper [28] estimates this to be roughly 3 kg in 10,000, or 0.03%. Propagated to the total number of nuclei in the fiducial volume gives an uncertainty of 1.27×10^{26} nuclei. Table 3.2 shows the makeup of the Near Detector by component.

3.4 Cross Section Measurement

There are a number of aspects of the NuMI beam flux and the MINOS Near Detector which must be taken into account in order to measure the coherent NC(π^0) cross section. The relationship between the total number of coherent NC(π^0) events and the energy-dependent reaction cross section is succinctly expressed as:

$$N^{Coh} = \mathcal{E}\mathcal{M}_T \int \phi\left(E_\nu\right)\sigma^{Coh}\left(E_\nu\right)dE_\nu \ . \tag{3.1}$$

In this equation the neutrino flux of the NuMI beam is given by ϕ, and σ denotes the cross section; both are functions of the neutrino energy E_ν. The mass of the Near Detector target fiducial volume, $\mathcal{M}_T$, and the neutrino exposure, $\mathcal{E}$, measured in POT, are energy-independent.

The coherent NC(π^0) event rate, N^{Coh}, represents the total number of coherent NC(π^0) interactions in the Near Detector fiducial volume, over the exposure period. A fraction of the neutrino interactions in the Near Detector will not be reconstructed, either because they do not impart enough energy to the

Detector Component	Element	Mass Fraction [%]	Atomic Weight [g/mole]	Mass [g]	Number of Nuclei [Nuclei]
Steel AISI 1006 Hot Rolled	Iron (Fe^{56})	99.46	56	4.02×10^{5}	4.32×10^{27}
	Manganese (Mn^{55})	0.38	55	1535	1.68×10^{25}
	Carbon (C^{12})	0.04	12	242	1.21×10^{25}
	Sulfur (S^{32})	0.05	32	202	3.80×10^{24}
	Phosphorus (P^{31})	0.04	31	162	3.15×10^{24}
	Silicon (S^{28})	0.01	28	40	8.60×10^{23}
Scintillator Strips Polystyrene(C_8H_8) 98% TiO_2 1% PPO 1.0%, POPOP 0.03%	Carbon (C^{12})	91.35	12	1.93×10^{4}	9.68×10^{26}
	Hydrogen (H^{1})	7.59	1	1.60×10^{3}	9.65×10^{26}
	Titanium (Ti^{48})	0.55	48	120	1.47×10^{24}
	Oxygen (O^{16})	0.45	16	94	3.54×10^{24}
	Nitrogen (N^{14})	0.06	14	13	5.59×10^{23}
Air	Nitrogen (N^{14})	78.08	14	50	2.15×10^{24}
	Oxygen (0^{16})	20.95	16	13	4.89×10^{23}
	Argon (Ar^{40})	0.93	40	1	1.51×10^{22}
Total	Plane	-	48	4.26×10^{5}	5.33×10^{27}
	Fiducial Volume	-	48	2.85×10^{7}	3.57×10^{29}

Table 3.2: The constituent elements of MINOS Near Detector fiducial volume by plane. The final columns shows the number of nuclei for each element in each detector component. The air also contains a negligible amount of water vapor. The molecular weight displayed for the total is determined as a weighted average over all components. The totals shown in the second to last row refer to a single plane while the totals in the last row refer to the entire fiducial volume. The uncertainty on the number of nuclei is roughly 0.03% [28]. The contribution from hydrogen nuclei are neglected in computing the total number of nuclei and the average nuclear weight.

active detector, or they overlap in space and time with a more energetic event. Also, most coherent NC(π^0) interactions will not provide a clear enough signal in the Near Detector to be clearly identified as a signal event, and selected for analysis. Monte Carlo simulations are used to estimate the fraction of coherent NC(π^0) that are actually measured as compared to the total number of generated events, and these *detection* and *selection* efficiencies are used to correct the measured event rate. The coherent NC(π^0) event rate is the neutrino flux times the coherent NC(π^0) cross section, which is equivalent to the number of interactions in the Near Detector fiducial volume during an exposure to the NuMI beam.

The detection, ϵ_d, and selection, ϵ_s, efficiencies are expected to be functions of the final-state visible shower energy, E_{vis}. To avoid propagating model dependence to the result, the efficiencies should therefore be applied as a function of E_{vis}. There may be visible energies where the selection efficiency is functionally zero, and a correction cannot be applied as a function of E_{vis}. To account for these events, an overall efficiency correction ϵ_o is also applied giving,

$$N^{Coh} = \frac{1}{\epsilon_o} \int \frac{\mathcal{N}^{Coh}\left(E_{vis}\right)}{\epsilon_d\left(E_{vis}\right)\epsilon_s\left(E_{vis}\right)} dE_{vis} \ , \tag{3.2}$$

where $\mathcal{N}^{Coh}$ is the uncorrected event rate as a function of the visible event energy.

Studies of MINOS Monte Carlo show that the detection efficiency, defined as the fraction of neutrino interactions in the ND to result in a reconstructed event, is very close to one across all visible energies. The detection efficiency can therefore be moved outside the integral, and absorbed into ϵ_o. These studies were performed by comparing a sample of generated MC to the corresponding reconstructed MC. Events that are not reconstructed are not included in

the reconstructed sample. The detection efficiency inferred from the number of MC shower events which survive reconstruction is 99.97%. For the purposes of this analysis the detection efficiency is assumed to be 1.0 with an error of 0.05%, which is accounted for in the uncertainty assigned to ϵ_o. Application of the efficiency corrections, along with the propagation of associated errors, is done as part of the fitting procedure detailed in Chapter 9.4.

As with any NC process, the final-state energy recorded by the ND (visible energy) is only a fraction of true neutrino energy. Therefore, without prior knowledge of the energy dependence of the coherent NC(π^0) cross section, it is difficult to extract the cross section as a function of energy. One can, however, measure a flux-averaged, energy-averaged cross section $\langle\sigma\rangle$ which is defined in the following way (here, subscripts and energy-dependence labels are suppressed):

$$N^{Coh} = \mathcal{E}\mathcal{M}_T \int \phi\ \sigma\ dE_\nu\ \simeq\ \langle\sigma\rangle \mathcal{E}\mathcal{M}_T \int \phi\ dE_\nu\ . \tag{3.3}$$

Taking Φ to be the integrated flux $\int \phi dE_\nu$, and substituting into Eq. (3.3) the form for the numerator implied by Eq. (3.1), the flux-averaged, energy-averaged cross section is,

$$\langle\sigma\rangle = \frac{N^{Coh}}{\mathcal{E}\mathcal{M}_T\Phi}\ . \tag{3.4}$$

The constants $\mathcal{E}$, $\mathcal{M}_T$, and Φ, are determined by the specific experimental running conditions of MINOS. Consequently, a measurement of $\langle\sigma\rangle$ is effectively a measurement of the coherent NC(π^0) event rate, N^{Coh}. Estimates for these quantities and for their errors are given in Table 3.3.

Maximizing the precision of the measurement requires minimizing the frac-

tional error $\frac{\delta\sigma}{\sigma}$. The uncertainties on $\mathcal{E}$, $\mathcal{M}_T$, and Φ are essentially independent of how the measurement is performed. Therefore, to determine the coherent NC(π^0) cross section for the ND exposure, the value of N^{Coh} and its fractional uncertainty, $\frac{\delta N^{Coh}}{N^{Coh}}$ are the essential quantities to be measured.

Constant	Value	Error	Description
$\mathcal{E}$	2.8×10^{20}	1.0%	Neutrino exposure in POT
$\mathcal{M}_T$	3.57×10^{29}	0.03%	Number of nuclei in the ND fiducial volume
Φ	2.93×10^{-8}	7.8%	Neutrinos/POT/cm^2

Table 3.3: Parameters used to calculate the energy-averaged cross section in Eq.(3.4) and their fractional uncertainties. These parameters characterize the MINOS Near Detector and the NuMI beamline exposure of this analysis. The uncertainty on the flux is the dominant contribution to the overall uncertainty associated with the conversion of the coherent NC(π^0) event rate to a cross section.

The flux in Table 3.3 corresponds to the total flux calculated in Table 3.1 converted to units of ν/POT/cm^2. The Near Detector exposure measured in POT is the sum of the POT associated with the data files used in the analysis. The uncertainty of 1.0% on the POT counting is established from the calibration error on the toroids [25]. The number of nuclei in the Near Detector fiducial volume is based upon the information summarized in the Table 3.2, with the uncertainty of 0.03% resulting from the uncertainty in the mass of the steel. The cross section, in the standard units of cm^2/nucleus, is the measured event rate divided by the product of these three numbers. The uncertainties on the exposure, the fiducial mass, and the flux combine to give a total uncertainty of 7.9% on the conversion from an event rate to a cross section.

3.5 Performing a Blind Analysis

It is easy for experimenters to allow their personal biases to affect the results of an experiment if the experimenters have any preconceived notion of the experimental outcome. To prevent this bias, blind analysis techniques have been developed. These techniques as applied in HEP use simulations, in the form of Monte Carlo, to design the analysis procedures. Portions of the data (where, according to MC, the information about the quantities to be measured cannot be extracted) are used to calibrate and cross-check the MC simulations. Blinding techniques were applied at each step of the coherent NC(π^0) analysis, and many precautions were taken so as not to influence the result with a priori expectations of the nature of coherent interactions.

Monte Carlo distributions were plotted before investigating data distributions, or making data-vs-MC comparisons. The regions where a coherent NC(π^0) signal is expected to make a significant contribution to the distribution were identified. Those regions were treated as blinded, and the data from those regions was not explored. It is important to note that single events are not blinded or unblinded. Blinding is defined as a function of the distributions in question. The use of the terms *blinded* and *unblinded* can be ambiguous, so they will be defined here for use in the rest of this document. *Blinded* refers to regions in a distribution where the data is expected, according to the MC, to contain a significant fraction of signal. These data points are not displayed or investigated until the analysis procedure is defined. Once this data has been viewed the analysis procedure cannot be changed without justification, and detailed explanation. *Unblinded* refers to regions of data distributions that, according to MC, can be viewed. If the region of the data distribution is not expected to contain a significant portion of the signal it will be unblinded

for use in designing the analysis procedure. After the analysis procedure is finalized, the blinded data becomes unblinded, and can be viewed, and used in the analysis. The unbinding of the data is referred to as a "box opening".

The coherent NC(π^0) analysis was designed so that much of the procedure could be completed without unblinding the blinded sample. This allowed cross checks to be performed as the analysis unfolded. The box opening procedure is outlined in Chapter 12.1 after a full description of the analysis procedure. Here the cross-checks are laid out in detail, and specific portions of blinded data are defined such that they could be unblinded as they were needed. This reduced the chance that the analysis would have to be changed after the full results were revealed.

3.6 The Data Sample

The data used for the coherent NC(π^0) analysis is obtained from MINOS Run I + Run II of the Near Detector. The data were collected from May 2005 through July 2007, and correspond to 2.8×10^{20} protons-on-target. The data corresponds to that analyzed for the first ν_e oscillation search in MINOS, reported in Ref. [29]. Figure 3.1 shows the NuMI proton beam intensity over the first two run periods (and extends into the beginning of Run III).

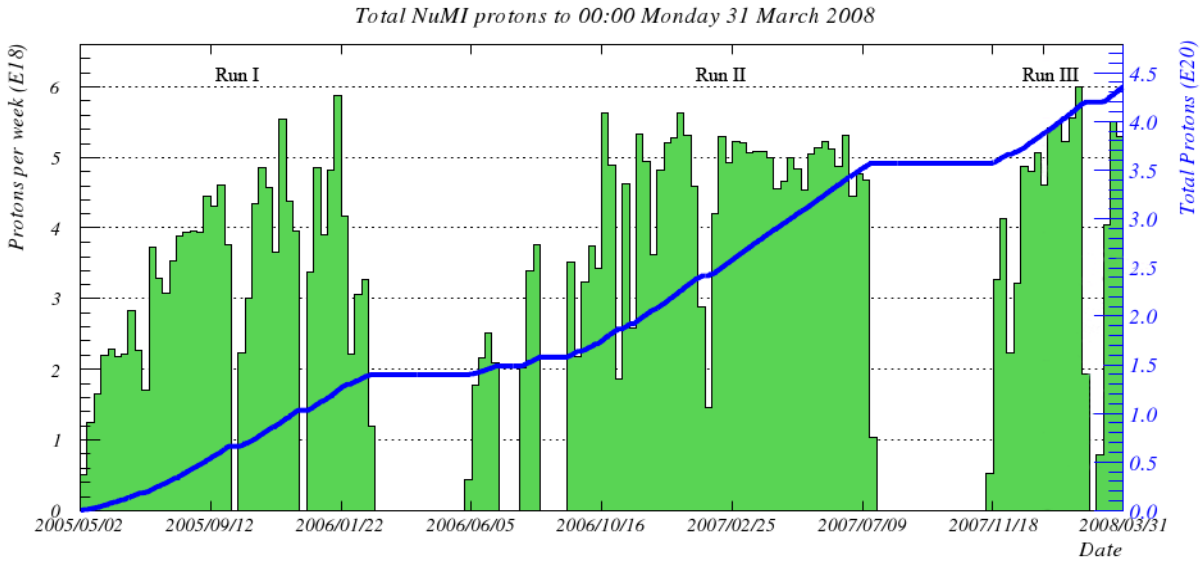

Figure 3.1: The NuMI proton beam intensity as a function of time for the Run I + Run II data sample as well as the beginning of the Run III sample [30].

Chapter 4

Analysis Overview

The following chapters in this Thesis describe the MINOS coherent NC(π^0) analysis in detail. An overview of the analysis is presented here, prior to proceeding to the full description. In addition, several key quantities are defined for readers unfamiliar with experimental particle and neutrino physics.

The coherent NC(π^0) signal events produce a distinct final state. Two types of information about that final state are available in the reconstructed event output: *i*) topological information and *ii*) kinematic information. The raw topological information refers to the pattern of energy deposition in the detector. The kinematic information, on the other hand, are reconstructed estimates of the energies and momenta of the particles of the reaction. The reconstructed kinematic information is gleaned from the raw topological information, and has an associated uncertainty.

Monte Carlo (MC) simulations were used to determine the topologies of coherent NC(π^0) reactions in the MINOS Near Detector along with those of background interactions that produce similar final states and detector responses.

The agreement between the unblinded data and the MC was also investigated, and data-based reweighting techniques were used to help improve the data-vs-MC agreement. Next, a series of cuts were developed to remove any backgrounds with topologies that are wholly distinct from the signal. The remaining background events, which produce similar topologies to the signal, were examined to determine the interactions involved, and to identify more subtle topological differences that might be exploited in selecting a sample with a large fraction of coherent NC(π^0) events.

Information on the topological differences was fed to a multivariate analysis technique known as a Support Vector Machine (SVM). The output of the SVM is a distribution that separates background-like topologies from signal-like topologies. The SVM output was used to select a subsample of the data and MC samples that produce a final-state energy deposition pattern similar to coherent NC(π^0) events. Based solely on the topological information used in the SVM, there is a set of irreducible backgrounds. These backgrounds produce energy deposition patterns in the detector which are practically indistinguishable from signal events. The kinematic information was reserved to separate the signal from these irreducible background events. There are large uncertainties on this background sample, which would propagate to the result if the kinematic information were to be used in the SVM event selection process. The kinematic information was used to remove the backgrounds in such a way as to reduce the effect of the uncertainties on the selected background event samples.

The selected sample is defined using the output variable given by the SVM by requiring selected events to have values above or below some threshold. Estimates for the sensitivity of the analysis can be expressed via the purity, ρ,

and efficiency, ϵ_s, of the selected sample (see Chapter 9.1 for details). These quantities, and thus the sensitivity, can be adjusted by varying the SVM output threshold used in defining the selected sample. The purity of the selected sample is defined as the fraction of the selected sample, $N_{sel} = N_{sel}^{Coh} + N_{sel}^{Bkg}$, that is comprised of coherent NC(π^0) events, N_{sel}^{Coh},

$$\rho = \frac{N_{sel}^{Coh}}{N_{sel}^{Coh} + N_{sel}^{Bkg}} \ . \tag{4.1}$$

The selection efficiency, ϵ_s, is also referred to as the acceptance. It is the fraction of the total coherent NC(π^0) sample, $N^{coh} = N_{sel}^{Coh} + N_{unsel}^{Coh}$, that is accepted into the selected sample, N_{sel}^{Coh},

$$\epsilon = \frac{N_{sel}^{Coh}}{N^{Coh}} \ . \tag{4.2}$$

Once the selected sample has been optimized to give the best sensitivity, the makeup of the selected subsample is evaluated. First the subsample is broken out into reaction categories and subcategories in order to determine exactly which interactions have been selected, and the uncertainty in the modeling of those interactions is evaluated. The true kinematic distributions were also investigated and compared with their reconstructed counterparts. Investigating the kinematic variables gave insight into the nature of the selected interactions, while comparing the true and reconstructed quantities revealed whether the reconstructed versions were accurate enough for use in the analysis. The true kinematic quantities investigated were:

- **Visible Energy,** E_{vis}

  The energy deposited in the detector. For NC events, including the coherent NC(π^0) signal, this is the energy of the hadronic shower. For

CC events E_{vis} includes the energy of the charged lepton as well. For events in the selected sample this quantity essentially gives the energy of the EM shower. This reconstructed quantity is used widely in the analysis, and is referred to as the Energy.

- **Shower Angle,** $\cos\theta_{shw}$

  The cosine of the angle of the event shower with respect to the beam direction. In the case of the selected sample the shower is most often an EM shower resulting from a final-state π^0 or an electron. Again, the reconstructed form of this variable is used very often in the analysis; it is referred to as the Angle.

- **Energy Weighted Shower Angle,** $\eta = E_{vis}(1.0 - \cos\theta_{shw})$

  The visible energy multiplied by one minus the shower angle is used widely in coherent analyses. The distribution of events as a function of η has a distinct shape for coherent interactions, as compared to the most common backgrounds. The reconstructed form of this variable is used in optimizing the selected sample, and in displaying results.

- **Square of the 4-momentum transfer to the hadronic system,** Q^2

  This Lorentz invariant quantity characterizes the 4-momentum transfer from the neutrino to the hadronic system. If the 4-momentum of the incoming (outgoing) neutrino is p (p') then $Q^2 = -q^2 = -(p - p')^2$. For NC neutrino interactions, where the mass of incoming and outgoing leptons are negligible $Q^2 = -(p^2 + p'^2 - 2pp') = 2EE'(1 - \cos\theta)$, where θ is the angle of the outgoing neutrino with respect to the beam direction.

- **The square of the invariant mass of the hadronic system,** W^2

  This Lorentz invariant quantity represents the square of the invariant mass of the hadronic system. In coherent interactions the minimum value

for W^2 is the sum of the pion mass and the nuclear mass, $(m_\pi + Am_\mathcal{N})^2$. The full expression for W^2 in a coherent interaction is $W^2 = m_\pi^2 - Q^2 + 2yE_\nu Am_\mathcal{N}$, where y is the Bjorken y described below.

- **Square of the 4-momentum transfer to the nucleus, $|t|$**

  The square of the 4-momentum transferred to the nucleus is calculated as $|t| = -(q - p_\pi)^2$, where p_π is the 4-momentum of the final-state pion. Assuming an infinitely heavy nucleus, the target nucleus does not recoil, and so $|t| = 2E_\pi^2 + Q^2 - m_\pi^2 - 2E_\pi\sqrt{E_\pi^2 + Q^2}\sqrt{E_\pi^2 + m_\pi^2}$.

- **Bjorken x**

  This scaling variable was created to quantify the fraction of the nucleon momentum carried by the struck quark in Deep Inelastic Scattering (DIS) interactions. This interpretation, of course, must be adjusted for coherent interactions, where the interaction takes place with the nucleus as a whole. Using the same notation as above x is defined as $x = -(p - p')/(2q \cdot k) = Q^2/(2m_\mathcal{N}\nu)$, where k is the 4-momentum of the target, and $\nu = E - E'$.

- **Bjorken y**

  A second scaling variable, y, is the fraction of the incoming neutrino energy transferred to the hadronic system. Bjorken y is defined as $y = (k \cdot q)/(k \cdot p) = \nu/E$.

- **EM shower fraction**

  The fraction of the visible energy resulting from EM shower producing particles (π^0, e^-).

- **Charged Pion Energy Fraction**

  The fraction of the visible energy associated with charged pions.

Of these variables only the visible shower energy and the shower angle are reconstructed well enough to be useful. Fortunately the signal and the backgrounds distribute differently in the Energy and Angle. The selected MC sample is plotted as a function of these two variables and regions where the signal is predicted to be small are compared with data. The background MC is then adjusted, within uncertainties, to match the data in these regions. The adjustments are extrapolated to the entire background sample and the estimated background is then subtracted from the data. What is left is the measured selected signal event rate. The selected signal is then corrected by the acceptance to retrieve the total event rate, which is then converted to a cross section.

The matching of the data and MC is done using a fitting package developed for the analysis presented in this Thesis. This fitting package was also used to estimate the systematic uncertainties and to determine the overall sensitivity of the measurement based on the combined statistical and systematic uncertainties. The overall sensitivity was greatly enhanced by use of the fitting package, which utilized the information from the reconstructed kinematic variables. The full analysis involves additional complications not mentioned in this section; full descriptions are provided in Chapters to follow.

Part II

Selection of Coherent NC(π^0)-Like Events

Chapter 5

Signal and Background Interactions in the Near Detector

While theoretical models represent an understanding of the physical processes involved in the neutrino interactions we observe in MINOS, it is the realization of physical processes in our experimental apparatus which defines how analyses can be performed. It is necessary to understand how the neutrino events being investigated, both signal and background, appear in the MINOS Near Detector. The patterns of energy deposition in the Near Detector produced by final state particles must be understood, and that information used to classify events. Also, the physical quantities that can be accurately reconstructed must be identified, and the precision to which they can measured must be evaluated. In the MINOS experiment, realistic MC simulations are used to explore the properties of signal and background interactions in the Near Detector.

5.1 Coherent NC(π^0) Interactions in the Near Detector

As indicated by Eq.(1.4), a coherent NC(π^0) interaction with an iron nucleus within the MINOS Near Detector will produce a single π^0 meson. In NEUGEN3, the MINOS neutrino interaction Monte Carlo (MC), this reaction is modelled via an implementation of the Rein-Sehgal model, from which some general features of produced events can be inferred. Simulations for the MINOS Near Detector exposed to the low-energy (LE-10) NuMI neutrino beam indicate that the expected energy distribution for the produced neutral pions is peaked below 1.0 GeV. The distribution falls with increasing π^0 energy, as shown in Fig. 5.1. Approximately half of the events will deposit more than 1.0 GeV in the ND, while less than 10% of the events will have visible energy exceeding 4.0 GeV. The distribution of the cosine of the production angle of the final-state pion with respect to the beam direction ($\cos\theta_{shw}$), shown in Fig. 5.2, is expected to be sharply peaked as well, with the majority of the neutral-pion showers developing along, or very close to, the neutrino beam direction. More than 75% of the signal events have $\cos\theta_{shw}$ greater than 0.97, corresponding to a production angle of less than 14 degrees.

As a consequence of the coarse sampling afforded by the scintillator planes of the iron tracking calorimeter, the opening angle of the two γ's produced by the π^0 decay cannot be resolved, consequently the event appears as a single electromagnetic shower. An example of a coherent NC(π^0) event in the ND is shown in Fig. 5.3. The topology is similar to that produced by a single electron of comparable energy.

It is possible to differentiate the characteristic electromagnetic showers pro-

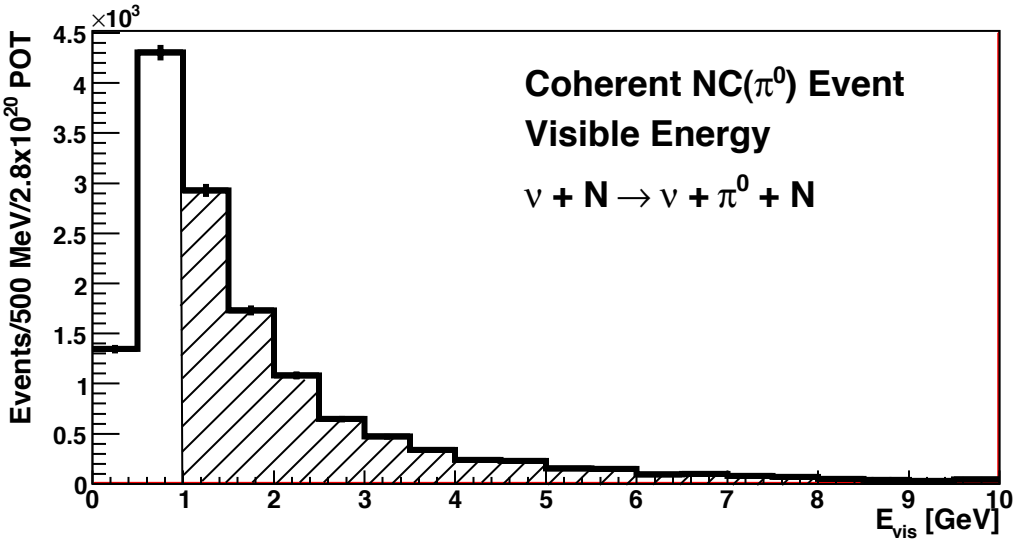

Figure 5.1: Reconstructed visible energy spectrum for coherent NC(π^0) events based on the NEUGEN3 Monte Carlo. Events with deposited energy below 1.0 GeV cannot be reliably identified as EM shower structures in the MINOS Near Detector.

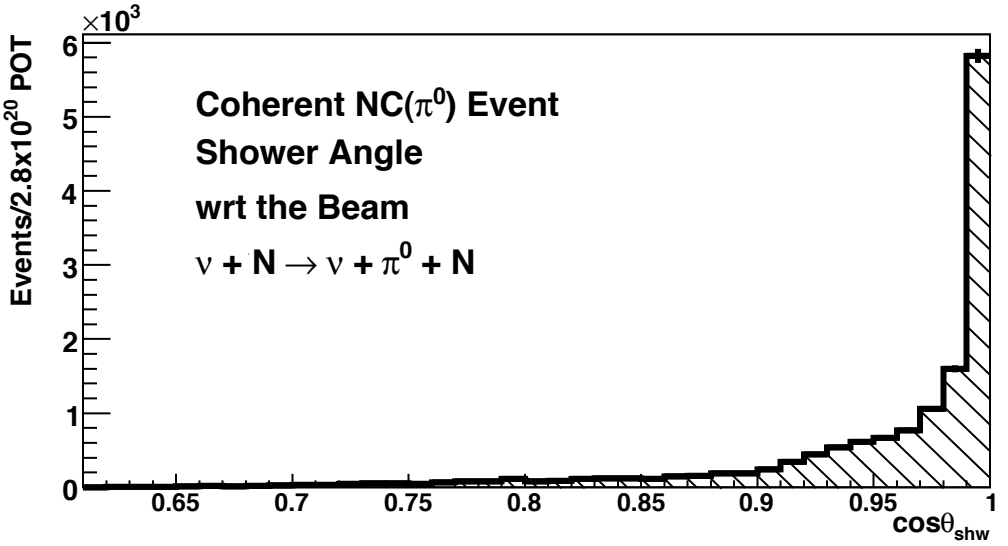

Figure 5.2: Reconstructed angular ($\cos\theta_{shw}$) distribution for showers produced by coherent NC(π^0) reactions based on the MINOS Monte Carlo. The steep peak in the forward direction is characteristic of coherent scattering.

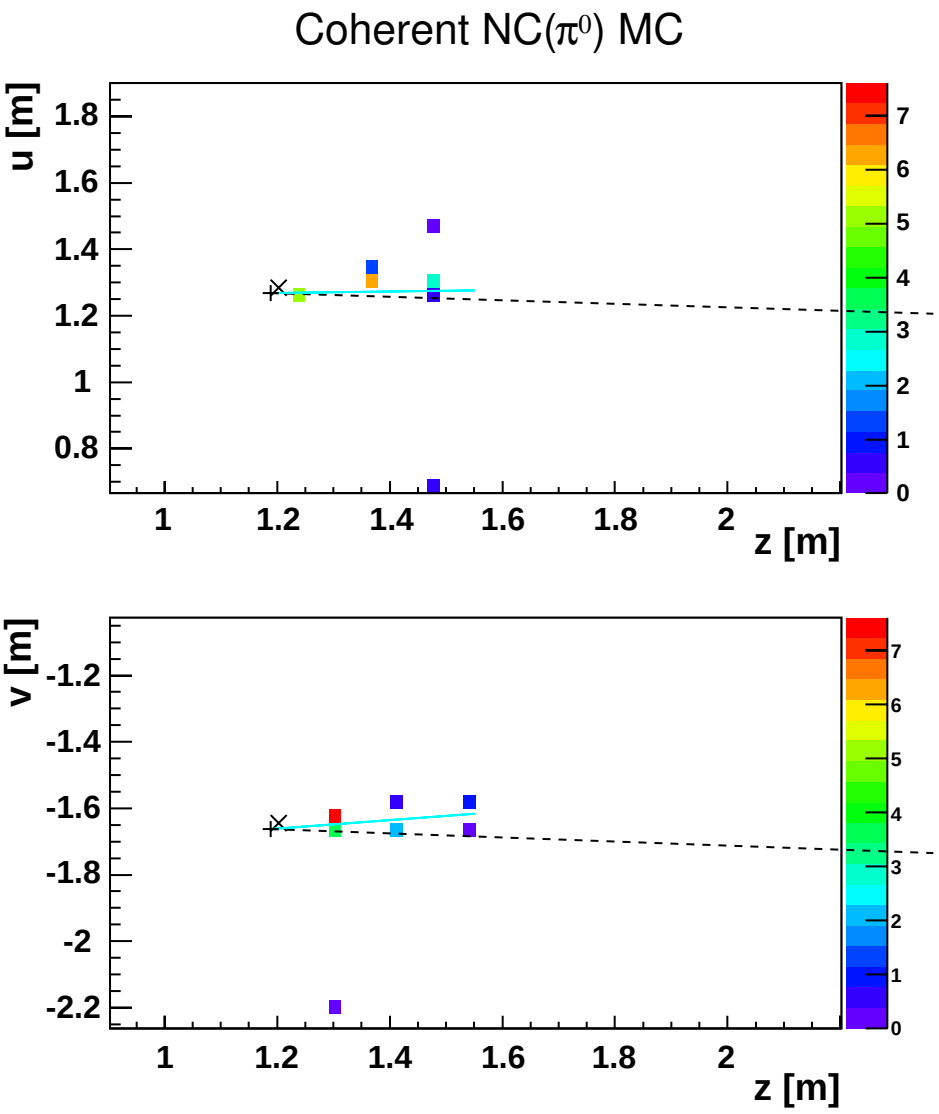

Figure 5.3: Monte Carlo simulation of the coherent NC(π^0) reaction ($\nu + Fe \rightarrow \nu + Fe + \pi^0$) in the MINOS Near Detector. The vertical axes show the transverse position of hits in the u and v projections of the event in the ND, and the horizontal axes show the longitudinal position of hits along the ND. The color axes depict the energy deposited in mips (minimum ionizing particle) in the ND. The dashed line shows the trajectory of the outgoing neutrino, and the solid (cyan) line shows the trajectory of the outgoing π^0.

duced by the signal from shower structures which are comprised of both charged and neutral hadrons by using various shower shape and size parameters. These differences are generally more readily distinguished at higher final state visible energies. The MINOS Near Detector, a muon tracking spectrometer by design, has relatively limited sensitivity in both its hadronic and electromagnetic calorimetric response at relatively low visible energies ($E_{vis} < 1 - 2$ GeV).

However, with the use of advanced pattern recognition software it is possible to isolate samples of predominantly electromagnetic events in the 1.0 to 8.0 GeV range as required for a measurement of the coherent NC(π^0) cross section. As will be described below, pattern recognition software has been developed which both selects for electromagnetic (EM) shower topologies and mitigates against events that exhibit hadronic activity. The latter activity may, for example, consist of extra vertex activity due to the presence of a recoil proton, or of downstream hits extraneous to the EM shower which may result from final-state neutrons. It may also consist of hadronic tracks aligned with the EM shower, but extending beyond the downstream end of the shower.

5.2 Background Processes for the Coherent NC(π^0) Search

Background interactions for the coherent NC(π^0) reaction originate from one of three general reaction categories. It is, of course, a characteristic of these background processes that their visible final state energies are dominated by electromagnetically showering particles.

NC resonance production and low-multiplicity NC DIS events

The predominant background comes from low-multiplicity NC events that produce final state π^0's which initiate the bulk of the detectable shower energy. At lower energies, where the signature of an EM shower cannot be unambiguously determined, a hadronic shower may also mimic the EM shower topology. The majority of these neutral-current induced background events come from resonance production and deep inelastic scattering (DIS) reactions. An example of a NC background event from the MC is shown in Fig. 5.4.

CC-ν_μ high-y resonance production and CC-ν_μ high-y DIS events

As with the NC backgrounds, high-y CC-ν_μ events which contain an energetic π^0 in the hadronic shower and have no visible muon track, can contribute to the background. The quantity, y, refers to the Bjorken y defined in Chapter 4. The large energy transfers to the hadronic system implied by a high value for y go hand-in-hand with relatively low muon energies, such that the muons are not detected. An illustrative MC event representing this type of background is shown in Fig. 5.5.

While both the NC and CC-ν_μ backgrounds have visible energy distributions which are similar to those produced by coherent NC(π^0) reactions, the angles of the hadronic showers with respect to the beam produced by these events generally distribute more broadly than do the production angles of signal events. The latter effect is especially notable at lower final-state energies.

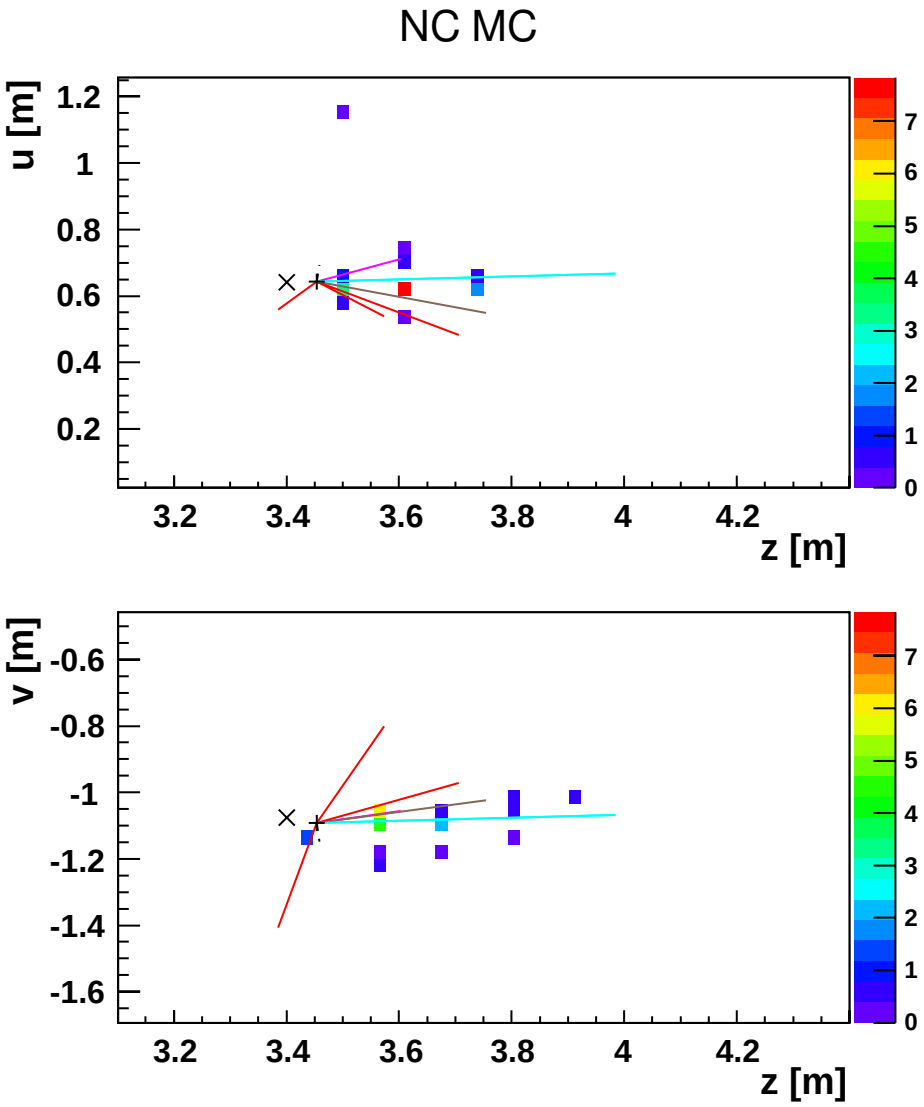

Figure 5.4: Simulated NC DIS interaction ($\nu_\mu + Fe \rightarrow \nu'_\mu + Fe' + \pi^0 + \pi^+ + 3p + n$) in the Near Detector. The horizontal axes show the transverse position of hits in the u and v projections of the event in the ND, and the horizontal axes shows the longitudinal position of hits along the ND. The color axes depict the energy deposited in mips in the ND. The solid lines show the trajectories of the outgoing final-state hadrons, including the dominant π^0 in cyan.

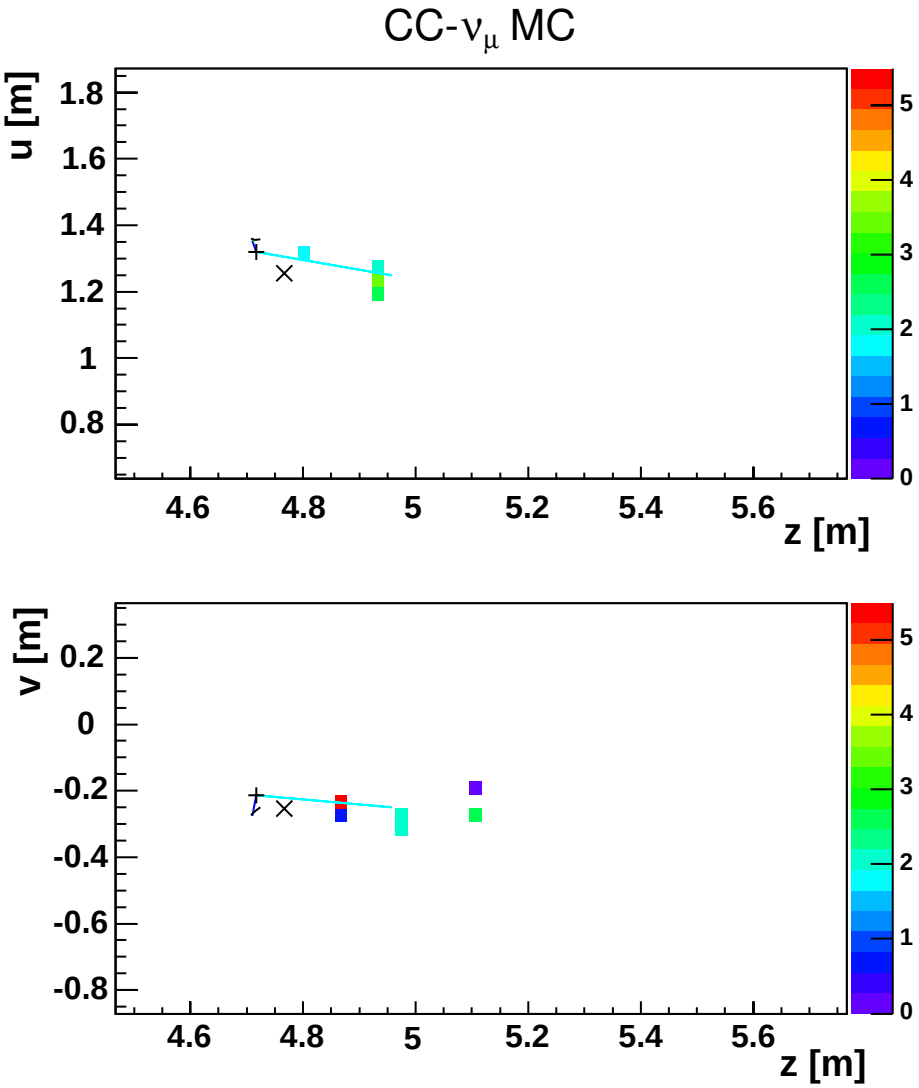

Figure 5.5: Simulation of a high-y CC-ν_μ DIS interaction ($\nu_\mu + Fe \rightarrow \mu^- + Fe' + \pi^0$). The vertical axes show the transverse position of hits in the u and v projections of the event in the ND, and the horizontal axes show the longitudinal position of hits along the ND. The lengths of the colored lines are proportional to the momenta of the particles they represent. The short dark blue line extending from the true vertex (denoted by a "+") shows the trajectory of the outgoing muon, while the dominant π^0 is in cyan.

Quasi-elastic-like CC-ν_e events

The third major background category arises from quasi-elastic-like CC-ν_e events (i.e. true quasi-elastic reactions, plus resonance and DIS production) in which a single prompt electron is detected. The energy distribution of these events is peaked in the vicinity of 2.0 GeV in final-state visible energy, and extends to higher visible energies than does that of the signal. The angular distribution with respect to the neutrino beam on the other hand, is as sharply-peaked as the signal, consequently the shower production angle is not especially helpful with distinguishing this type of background from the signal. An example of a quasi-elastic-like CC-ν_e event is shown in Fig. 5.6.

Taken together the three background processes represent several orders-of-magnitude more in event rate than is estimated for the signal. An event selection, based on the pattern recognition software, greatly reduces the amount of background. The resulting sample is a small fraction (less than 0.1%) of the total number of neutrino events produced in the MINOS Near Detector, as can be seen in Fig. 5.7. Unfortunately, the selected sample size for each of the three processes is similar in size with the estimated number of signal events. Consequently a successful extraction of the coherent NC(π^0) signal hinges upon reliable background subtraction. To this end a detailed fitting procedure has been developed to extract the signal from the copious Near Detector event rate and to accurately ascertain the errors on the signal amount.

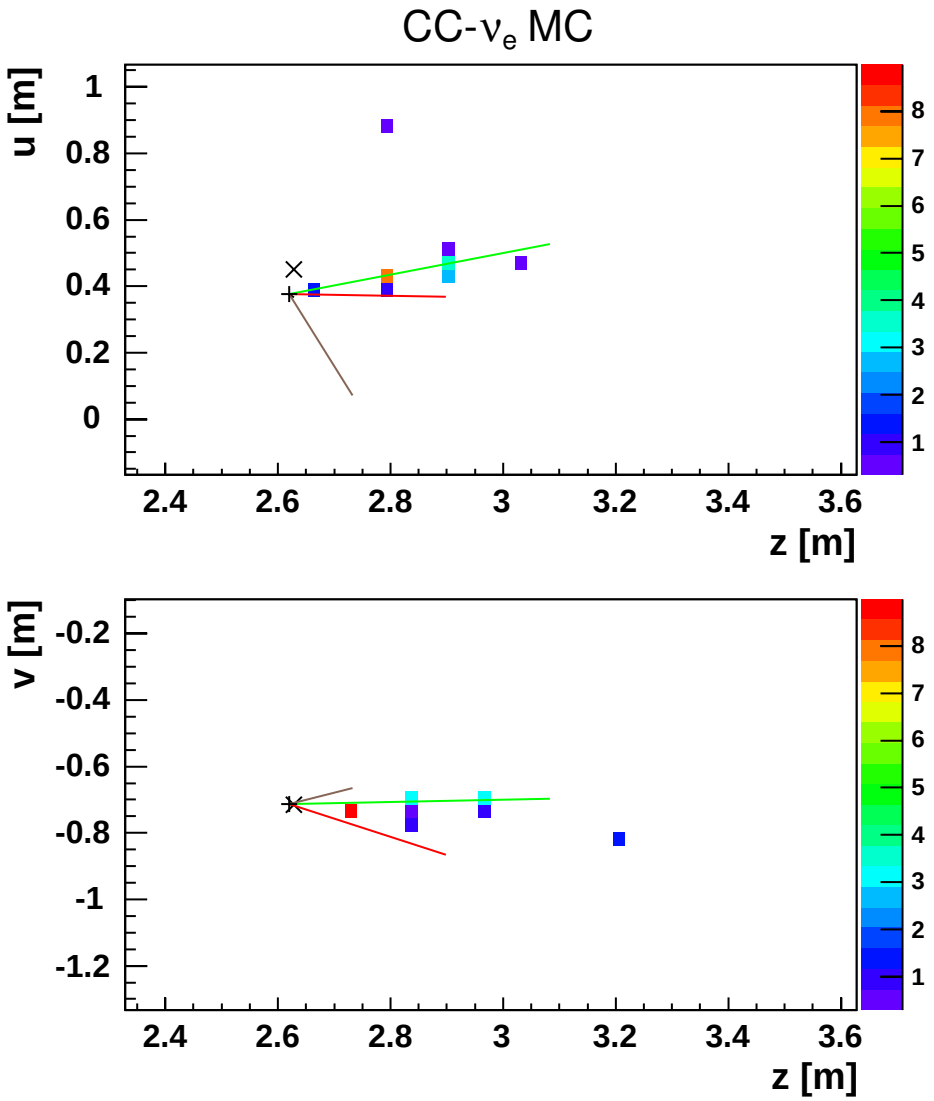

Figure 5.6: Simulated CC-ν_e quasi-elastic interaction ($\nu_e + Fe \rightarrow e^- + Fe' + p + n$). The vertical axes show the transverse position hits in the u and v projections of the event in the ND, and the horizontal axes shows the longitudinal of hits position along the ND. The color axes depict the energy deposited in mips in the ND. The green line shows the trajectory of the final-state electron which gives rise to the EM shower. The red line represents the recoil proton, which also contributes a few hits. A recoil neutron (undetected) is indicated by the brown line.

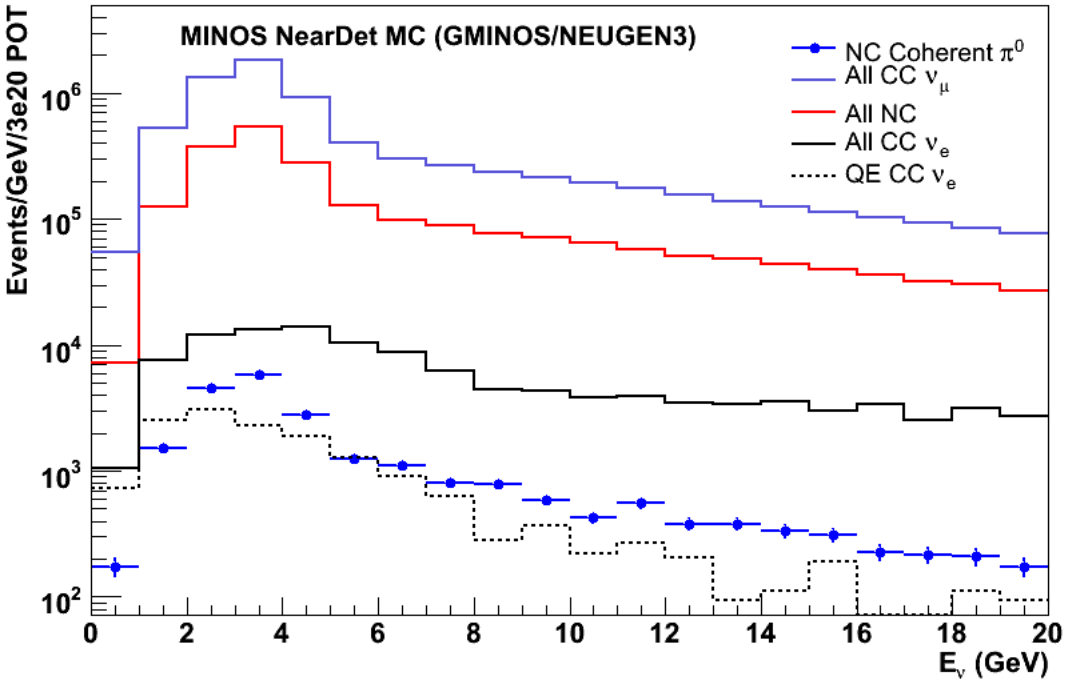

Figure 5.7: The event rate as a functions of true neutrino energy in the MINOS Near Detector for the signal and for the reaction categories relevant to the coherent NC(π^0) analysis. The estimated signal (solid circles) is of sub-percent relative rate at all energies. Note, however, that no pre-selection or selection cuts have been applied.

Chapter 6

Event Selection

An event selection procedure has been developed to extract coherent NC(π^0) from the abundant backgrounds. This procedure, which was developed using simulations afforded by the MINOS Daikon04 Monte Carlo, has several steps. The first is to re-weight the standard MC, using data-based corrections. The effect is to improve the initial data-vs-MC agreement. Second, a set of initial cuts, referred to as pre-selection cuts, are applied. These cuts are intended to exclude as much background as possible while retaining the entire signal sample. Next a set of variables (attributes) that separate signal from background are identified. The subset of these variables that, when taken together, have the most power to separate signal from background are chosen for use in a multivariate classification algorithm (MVA). The MVA used in the analysis presented in the Thesis is a Support Vector Machine (SVM). The output of the SVM is a single variable, known as the signal selection parameter, or the PID (particle ID). This variable is a numerical parameter whose value represents all of the signal-vs-background separation information contained in the input variables. A set of cuts on the PID is used to select a sample that contains a

high fraction of signal events. This "selected sample" is the input to the fitting procedure, which is used to extract the total number of coherent NC(π^0) events in the data sample.

6.1 Initial Reweighting of Monte Carlo Events

Several weighting factors are applied at the outset to the standard Monte Carlo event sample for the purpose of enhancing its agreement with the data. The first weight merely sets the normalization of the MC sample to the data based upon protons-on-target (POT). The second weight is based on neutrino beam properties as characterized by the SKZP beam parameters [31]. The third weight is based upon the Muon Removed Charge Current (MRCC) sample. That is, for the MRCC data set, CC-ν_μ events are used but with the track produced by the final-state muons removed from the event prior to reconstruction [32]. The result is an event sample which simulates NC events to good approximation with respect to most inclusive distributions.

For MC event samples, the CC-ν_μ content can be tuned to the data using the high energy portion of the event visible energy distribution, where it is feasible to isolate pure CC-ν_μ samples both in data and in MC. However, with respect to tuning the NC content of MC samples, no such control region exists; with the event resolutions afforded by MINOS, there is no straightforward way, using event selections, to avoid contamination from CC-ν_μ events. However, in the MRCC sample a pure CC-ν_μ event sample is 'converted' to a clean NC sample through the muon removal process. The converted sample can then be compared to a similarly created MC sample, and the desired data-based correction to the standard MC can then be inferred. The prerequisite weighting

factor is constructed as summarized below in Eqs. (6.1), (6.2), and (6.3).

In an analysis of shower-dominated events in MINOS, the following relationship is observed to be valid to good approximation:

$$\frac{NC_{data}(E_{vis}, PID)}{NC_{MC}(E_{vis}, PID)} \simeq \frac{MRCC_{data}(E_{vis}, PID)}{MRCC_{MC}(E_{vis}, PID)} \ . \tag{6.1}$$

With the above assumption, the NC_{data} sample can be simulated according to

$$NC_{data}(E_{vis}, PID) \simeq NC_{MC}(E_{vis}, PID)\frac{MRCC_{data}(E_{vis}, PID)}{MRCC_{MC}(E_{vis}, PID)} \ . \tag{6.2}$$

Consequently NC_{MC} events are to be multiplied by a weight factor,

$$Weight(E_{vis}, PID) = \frac{MRCC_{data}(E_{vis}, PID)}{MRCC_{MC}(E_{vis}, PID)} \ , \tag{6.3}$$

in order that their distributions better approximate the data.

The weight is applied as a function of visible energy and PID. The net result of this MRCC weighting is to lower the background NC content in the selected sample and to increase the number of true NC events that fail the PID cut. There is marked improvement of the data-versus-MC agreement in the unblinded portion of the PID distribution, and of data-versus-MC agreement in the unblinded regions of the visible energy and $\cos\theta_{shw}$ distributions as well.

The effect of the MRCC weights was more pronounced for the Daikon00 MC set where the hadronization model was less refined. The correction however, still produced the same level of data-versus-MC agreement. In moving to the Daikon04 MC several issues related to the hadronic shower production were improved. The verity of the implemented MC upgrades is supported by the reduced impact of the MRCC weighting and the maintenance of the same level

of data-vs-MC agreement.

After the application of the SKZP and MRCC weights, the data-vs-MC agreement for signal-like events is improved, but the data is still 10% to 15% lower than the MC predictions. The MRCC reweighting improves data-vs-MC agreement in the unblinded regions of all spectra investigated for the pre-selected NC sample. The SKZP weights, on the other hand, improve the data-vs-MC agreement for the majority of the MC, but push the MC predictions away from the data for more signal-like events. Moreover, both the SKZP and MRCC weights have less pronounced effects for events that appear to be more signal-like, with the caveat that at some point the sample distributions become blinded and cannot be compared with data.

The effects of the SKZP and MRCC weights on the selected MC sample can be seen in several plots in Chapter 6.6 once the selected sample has been defined. Plots showing various kinematic truth distributions (Figures 6.11 and 6.12) provide comparisons between the fully weighted (solid) and the unweighted (dashed) curves. Differences between the weighted and unweighted distributions show the effect of all three weights as a function of the each kinematic truth variable. For example, the upper right hand plot of Fig. 6.11 shows that the NC events are weighted downward at high y-values more than they are at low-y. Figures 6.8 and 6.9 display the number of events as a function of the Energy and the Angle, respectively, for the MC with and without the MRCC weights applied. The MRCC decreases the weight of events with a visible shower energy below 1.5 GeV while increasing the weight of events with visible energies above 3.0 GeV, as well as events with small angles between the shower and the beam.

6.2 Pre-selection Cuts

The first pre-selection consists of data quality cuts applied to the data sample. These cuts remove data events for which there were problems along the beamline, with the MINOS Near Detector, with the timing system, or with the online data acquisition software. These data quality cuts are identical to those used by the $\nu_\mu \rightarrow \nu_e$ oscillation analysis of the 3.5×10^{20} POT exposure [29]. Since the latter analysis also seeks to identify EM showers it has many aspects in common with the coherent NC(π^0) analysis.

The next type of pre-selection removes events that are outside the scope of the analysis. This may include signal events, but ones which would not be useful in extracting a cross section. The first of these selections requires that events are fully contained within a specified fiducial volume of the MINOS Near Detector, as defined in Chapter 3.3. The fiducial volume requirement prevents the inclusion of incomplete events, in which either an interaction occurred outside the detector but its final state particles still reached the detector, or an interaction occurred close to the edge of the detector, where final state particles may exit the detector without depositing all of their energy.

Another cut removes events having visible energy below 1.0 GeV. These events do not contain enough information to allow for reliable topological classification. This is unfortunate because the MC predicts that as much as 50% of the remaining (reweighted) signal events have final state EM showers with less than 1.0 GeV in visible energy. However, inclusion of these events would require a disproportionally large increase in the size of the selected background sample and would thus detract from the sensitivity of the measurement.

The data and MC samples which survive the pre-selection cuts contain many

events that are clearly not coherent NC(π^0) events. Irrelevant events are readily removed using a few additional straightforward cuts. The most obvious cut is to remove events which do not contain a reconstructed shower. Next is a cut on events with long tracks which represent obvious muons. If the reconstruction were perfect all events with tracks could be excluded. However, the centroid of a well-formed EM shower in the MINOS Near Detector is quite track-like, and will be identified as a "track" by the reconstruction software. An inclusive pre-selection cut includes all of the events with tracks arising from the EM shower topology while rejecting events that have a clear muon or hadronic track. This is accomplished by removing events with tracks longer than 2.0 meters, which is longer than any reconstructed "track" in the coherent NC(π^0) MC sample. The results of these cuts on the data and MC samples is shown in Table 6.1.

Pre-selection Cut	Coherent NC(π^0) Monte Carlo Events	Background Monte Carlo Events	Data Events
Total Events	100%	100%	100%
Data Quality	100%	100%	98.7%
Fiducial Volume	15.5%	7.24%	7.06%
$E_{vis} > 1.0$ GeV	8.30%	6.53%	6.44%
One Shower	8.25%	5.37%	5.29%
One Track < 2.0 m	8.17%	2.00%	1.90%

Table 6.1: Event sample survival fractions upon successive application of the various pre-selection cuts. The apparent difference in the fiducial volume cut between the signal and background/data is a result of muon events with a vertex outside of the detector. These events occur in both the background MC sample and the data sample, but not in the signal MC.

6.3 Variable (Attribute) Selection

A set of variables (or in the parlance of MVA, "attributes") was chosen that best separate coherent NC(π^0) signal events from the various backgrounds.

These variables take advantage of the specific nature of the signal events, especially of their topologies. Coherent NC(π^0) events produce a single final state EM shower, with no muon or hadronic activity. The variables considered all take advantage of this fact in some way. A description of the general categories for these variables is indicated below; the full list of variables is presented in Appendix A.

Shower Size Variables:

These variables use shower size to distinguish EM showers from hadronic activity. The size refers to the length, width, and total energy deposition. Several of the quantities look specifically at the strips and planes which receive the greatest amount of energy deposition.

Shower Shape Variables:

The shapes of hadronic versus EM showers can differ greatly. These variables look at the distribution of shower energy in both the transverse and longitudinal profiles. Several geometry and physics-based quantities are calculated, such as the longitudinal distance between shower vertex and the point at which the shower has deposited half of its energy, and the fraction of the energy deposited within the Moliere radius for iron. The Moliere radius is a characteristic constant of a material giving the radius of a cylinder containing, on average, 90% of the energy deposited by an EM shower.

Shower Fit Variables:

Fits to shower transverse and longitudinal energy profiles are also useful in distinguishing showers. Gaussian fits are applied to the transverse profiles; a good fit and a narrow distribution are indicative of a forward-going EM shower. A Maxwell distribution and a Landau distribution are fit to the longitudinal energy profile, as both provide approximate descriptions for the expected shape of longitudinal energy deposition of an EM shower in the MINOS Near Detector.

Hadronic Activity Variables:

Coherent NC(π^0) interactions do not produce recoil nucleons or nuclear breakup. Several variables look for excess activity near the vertex indicative of hadronic activity produced by such nucleons. Other variables attempt to distinguish events with hadronic activity around the shower. In essence, these variables identify strips with high energy deposition outside the EM shower core.

Track Variables:

Two variables are used to help reject events with tracks. These identify events where the "track" is unlikely to be the result of a well-formed EM shower.

Quantities which directly measure final-state shower visible energy or direction have not been included in the attributes discussed above. These quantities

comprise the only two kinematic handles on the signal, and have been reserved for use in the background subtraction. The shape differences between the selected signal and backgrounds in these two variables are indispensable for accurately predicting the backgrounds using the fitting procedure.

6.4 Support Vector Machines and the PID

Support Vector Machines (SVM) represent a strategy among those comprising Multivariate Analysis (MVA) classification algorithms. Most of these algorithms utilize the same general principles, but differ greatly in implementation. Classification algorithms work to separate mixed samples into their constituent groups (classes) based upon measureable characteristics. The first step is to identify measureable characteristics that differ, to at least some degree, between the classes. The set of attributes associated with these characteristics is selected such that each additional attribute adds separation information. The attribute must not only separate, but have some independent information that is "orthogonal" to the information contained in all of the other attributes.

In the next step, known as training, a data sample of known class is used to map out a Probability Distribution Function (PDF). In the application of MVA, the PDF is a function of the selected attributes that returns the probability that an event with the attributes x_i is of class y. Training data usually consists of samples of "hand-classified" events. In high energy physics, a "hand-classification" is not always reliable and therefore training samples are built from Monte Carlo simulations where truth information about the event class is available.

The purpose of the MVA algorithm is to define a function of the attributes

that returns a classification by approximating the PDF implied by the training data. The output of the MVA approximation of the PDF can be an integer (0 for class A, 1 for class B) or a decimal (lower is more like class A, higher is closer to class B). To define the approximate PDF, most MVA algorithms plot the training sample in an N-dimensional attribute space, where N is the number of attributes. An artificial neural network (aNN) approximates the PDF with an analytic function of the attributes. A k-nearest neighbor (kNN) algorithm determines the return value of the PDF for a point in attribute x_i space by calculating the fraction of events in each class for the k-nearest training events to point x_i. Other methods quantize attribute space and approximate the PDF with the fractions of each event class in each quantum of attribute space.

In SVM algorithms, such as the one used in the present analysis, border surfaces between regions (in attribute space) of high class density are determined. Support vectors represent points (in attribute space) in the training sample at the edges of the class dense regions, where the return value for the PDF is ambiguous (i.e. approximately 50%-50%). The algorithm uses the support vectors to optimize the positions of the borders such that each region contains a large fraction of events from a single class. A point in attribute space is thus classified by the region in attribute space in which it resides. Functionally, this is performed by calculating the distance to the nearest border. The SVM can simply return an integer, referring to the region, and thus the class, y, of a point, x_i, or else, return the distance to the nearest border.

For the purposes of the analysis presented here, the number of events is plotted as a function of the distance to the nearest SVM border, as shown in Fig. 6.1. The MC sample, which must be different from the MC sample used to train the SVM, is broken out by true class. The total MC sample is also shown, and

can be compared with the unblinded data sample. This distribution is used to select a sample of events that contains a large fraction of coherent NC(π^0) events, and is referred to as the signal selection parameter, or the particle-ID (PID). The border between signal-like event region and the background-like event region occurs at a PID value of -1.0. Events at the negative end of the spectrum are in the region of background-like events, while the positive end of the PID spectrum contains signal-like events. The events in the middle are close to the border between the signal-like and background-like regions, and their class distinction, based on their attributes, is less definite. The SVM classifies everything to the right of the border (PID $>$ -1.0) as signal, and everything to the left of the border (PID $<$ -1.0) as background. The purity of the signal-like sample selected by the SVM is too low, and the distance information in the PID must be used to select a sample that, according to the MC, has a higher purity.

The output distribution of this particular SVM is not a typical result in that the peaks of the distributions for all of the classes appear near the border. Support vector machines are considered to be among the most powerful MVA techniques available, and have been shown to separate classes very well. A typical result would have the peak of the distribution for each class at a different SVM output value, while the border regions would be occupied by a small set of ambiguous events. The relatively poor performance of this SVM is indicative of the difficulty in separating EM shower topologies from hadronic shower topologies in the MINOS Near Detector. The coarse sampling of the ND, and the large fraction of dense, inactive detector limit the amount of topological information available, especially for events with an $E_{shw} < 1 - 2$ GeV, and result in a large fraction of ambiguous topologies.

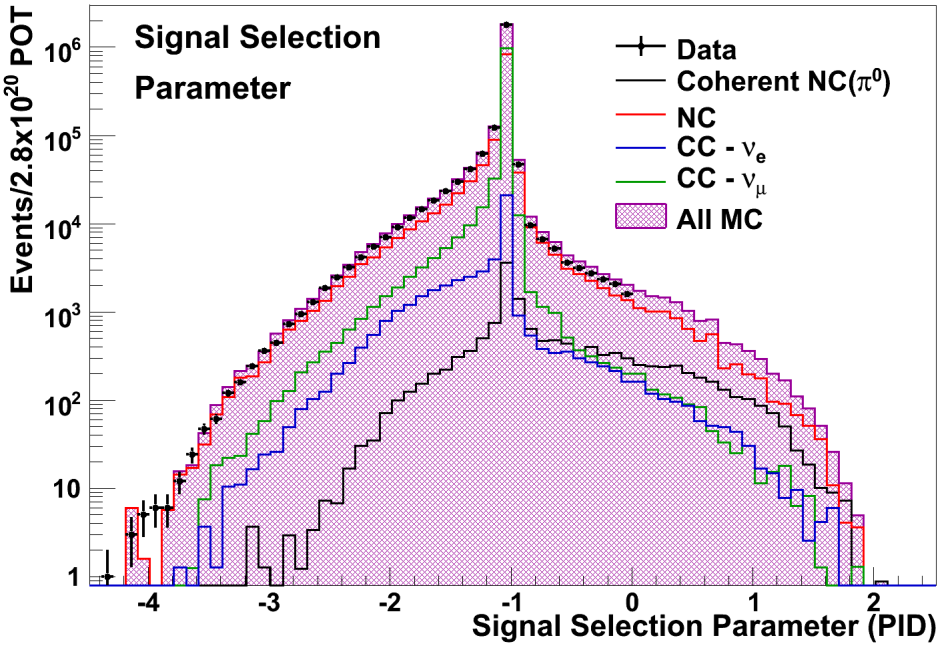

Figure 6.1: The number of events as a functions of the signal selection parameter. The PID is used to select a sample with a relatively large proportion of coherent NC(π^0) events (black dots) as compared to backgrounds (NC - red, CC-ν_μ - green, CC-ν_e - blue). Data (black histogram with statistical errors) is compared with the total MC spectrum (purple) in the unblinded, low PID region, where the coherent NC(π^0) content is comparatively small.

Also atypical for an SVM problem is the level of inseparable background. The ultimate goal of the event selection procedure is to identify a sample based on the physical processes involved. However, only topological information is available, and several interaction categories produce final state topologies identical to those in the signal event sample. Hence the large contamination of background events in the signal region. Further investigation of the signal-like event sample shows that these event classes are topologically identical, and inseparable. The SVM presented here provides the best possible result with the information available. Much time was invested in identifying the SVM as the best performing MVA technique available for this analysis. Furthermore, as with most MVA, the SVM requires customization and has several tunable parameters. A formal discussion of SVMs can be found in reference [33], and a description of the training techniques used for this analysis are provided in Appendix B.

6.5 Efficiency, Purity, and the PID Cut

The PID variable gives the best available separation between signal and background events. The sample of events used in the analysis is selected based on the PID values of the events. This "selected sample" still contains a large fraction of signal-like backgrounds which cannot be distinguished from true signal events by pattern recognition methods. These events can however be accounted for by a background subtraction method. In a simple analysis the number of events subtracted from the selected sample is based on MC predictions of the backgrounds, and the uncertainty on the remaining signal is a function of the uncertainties on the total selected backgrounds. Due to large

uncertainties in the physics models, the overall errors from such a method would necessarily be large, hence this simple approach would not produce a useful result. In the present analysis however, the MC is fit to the data, taking into account all uncertainties in the physics and detector modeling. Such a procedure greatly reduces the overall systematic error. The details of the fitting procedure used in the analysis are discussed in Chapter 9.

The fractional uncertainties in the physics models used to generate the background MC, although large, are small relative to the uncertainties in the coherent interaction model used in NEUGEN3. The large uncertainties on the coherent model reflect the dearth of high-precision data and the existence of competing models with large variations in the predicted cross sections. In order to lower the overall uncertainty on the measurement of the coherent NC(π^0) cross section the influence of the Rein-Sehgal model must be minimized. This is accomplished by fitting the "Angle-vs-Energy" distribution of the selected MC sample to that of the selected data sample, where "Angle" refers to the cosine of the angle of the final state shower with respect to the beam, and "Energy" refers to the event final-state visible energy. The signal and the three backgrounds distribute differently in the Angle-vs-Energy plane. The region of predicted high signal concentration is referred to as the "signal region" and the regions of low signal concentration are referred to as the "sideband". The fits only compare data to MC in sideband bins, where the signal concentration is predicted to be low relative to the backgrounds. This helps to limit the influence of the signal model on the result, and hence limit the effect of the uncertainty on the signal model when propagated through to the cross section measurement.

A second sample of events, those which fail the PID cut, but pass a second cut

in the PID variable, is also defined. This sample, referred to as the "near-PID" sample, is used to increase the amount of information about the background MC samples available to the fitting procedure. The PID cut values used to determine the near-PID sample are chosen such that the near-PID sample contains events with similar final states to the background events in the selected sample. The near-PID selected events are still very signal-like, but contain a lower proportion of signal events than the selected sample, allowing a larger portion of the Angle-vs-Energy plane to be used in the fits.

Optimization of the PID cut value used to define the selected and near-PID samples for the analysis is non-trivial. In general, methods for optimizing PID cuts require the maximization of a metric tied to the overall sensitivity of the measurement. This metric is referred to as a figure of merit (FOM). There are several different FOMs and the best one for a particular analysis is the one that best reflects the sensitivity. FOMs are usually defined as functions of purity, ρ, and efficiency (or acceptance), ϵ, as defined in Chapter 4.

For a simple background-subtraction-based analysis, a FOM based on the sensitivity is sufficient. However, for the fit-based method it is important to maximize the purity in the signal region, while minimizing the signal content in the sideband. For this reason a good PID cut will provide subsamples of low purity in addition to a subsample of high purity containing most of the signal. In addition, a minimum efficiency of approximately 10% must be maintained to ensure that the selected signal contains a representative event sample. The efficiency here is defined in relation to the total reconstructed signal sample in the fiducial volume.

These requirements cannot be met by the application of a single PID cut. Instead, the PID cut values are defined as a function of the variable η =

$E_{vis}(1-\cos\theta_{shw})$. This variable has proven useful in published coherent analyses because of its distinct shape for coherent processes as compared to backgrounds. Coherent reactions produce a more sharply peaked η spectrum with most events occurring at low values. The signal region of the selected sample can therefore be approximated by a cut in η, and the PID and near-PID cut values can be adjusted to give samples of the desired purities and efficiencies. The cut value in the signal region ($\eta \lesssim 0.1$ GeV), must produce a high purity, while maintaining a minimum efficiency. On the other hand, in the sideband region ($\eta \gtrsim 0.2$ GeV) the purity should be low. To find a smooth function of η which could accommodate these two requirements the purity and efficiency were plotted, in Fig. 6.2, as functions of η and the PID cut value.

Each two-dimensional bin in these plots represents the purity or efficiency in a bin of η for a particular cut value on the PID. For example, placing the PID cut at -0.5 will yield an efficiency of close to 50% for events with an η value of 0.0 to 0.02, and about 25% for event with a η value of around 0.35. This same cut will select a sample with a purity of roughly 20% for the first η bin, and close to zero at $\eta = 0.35$. This cut obviously does not meet the requirements for a successful analysis. Overlaid on Fig. 6.2 are two stepwise functions that define the selected and near-PID samples. The selected sample is defined by the following PID cut, cut_{ss}, as a function of η,

$$cut_{ss} = \begin{cases} 0.6 - 3.0\eta & : \eta < 0.5 \\ -0.9 & : \eta \geq 0.5 \end{cases} \tag{6.4}$$

Similarly, the near-PID sample is defined as the events that fail the selected sample PID cut, but pass the cuts defined by the function, cut_{np}, of η,

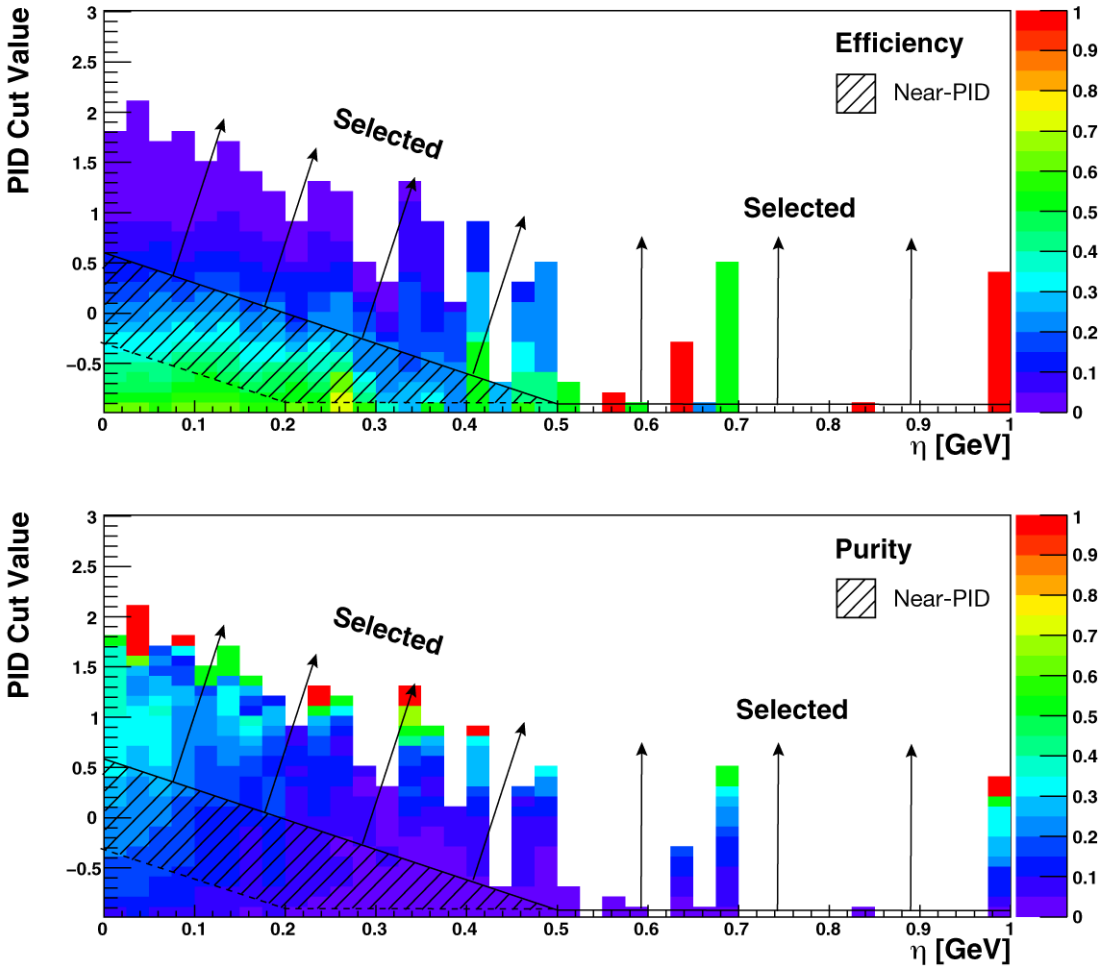

Figure 6.2: The efficiency and purity of the selected sample (color-axes) as a function of $\eta = E_{vis}(1 - \cos\theta_{shw})$ (horizontal axis) and the PID cut value (vertical axis). The PID cuts as a function of η are determined using these plots. The solid line depicts the PID cut function for the selected sample, while the dashed line depicts the PID cut function for the near-PID. A viable analysis requires a purity of at least 20% to 30% inside the signal region ($\eta < 0.1$ GeV), and a purity below 5% outside the signal region ($\eta > 0.2$ GeV). A minimum efficiency of roughly 10% is also required.

$$cut_{np} = \begin{cases} -0.3 - 3.0\eta & : \eta < 0.2 \\ -0.9 & : \eta \geq 0.2 \end{cases} \quad (6.5)$$

The background samples in the low purity sideband regions, through the fitting procedure, will be used to estimate the amount of background in the signal region. The extrapolation from the sideband to the signal region requires that the types of events in the two sub-samples be similar, and that the background sample in the sideband is representative of the background sample in the signal region. Figure 6.3 compares the shape of the MC event rate in the signal region to the shape of the MC event rate in the sideband as a function of Q^2. The event rates are scaled to contain the same number of events so that the shapes can be compared. The error bars reflect the fractional errors from statistical uncertainty. In general the distributions do not match very closely, nor are they expected to. The sideband region does however, include at least some events at each Q^2 value present in the signal region and the shapes are similar enough for the sideband to be useful in extrapolating to the signal region. The largest differences occur in the coherent NC(π^0) distribution. This is expected because the signal region is defined to contain most of the signal and limit the number of signal events in the sideband region. The small size of the coherent sideband sample is reflected by the large statistical errors bars as compared to those of the coherent NC(π^0) sample in the signal region. Similar plots for the invariant mass (W^2), Bjorken x, and Bjorken y can be found in Appendix C. Further discussion of the selected sample event rate distributions as a function of kinematic variables is given at the end of Chapter 6.6.

Similar plots have been made to compare the selected sample and the near-

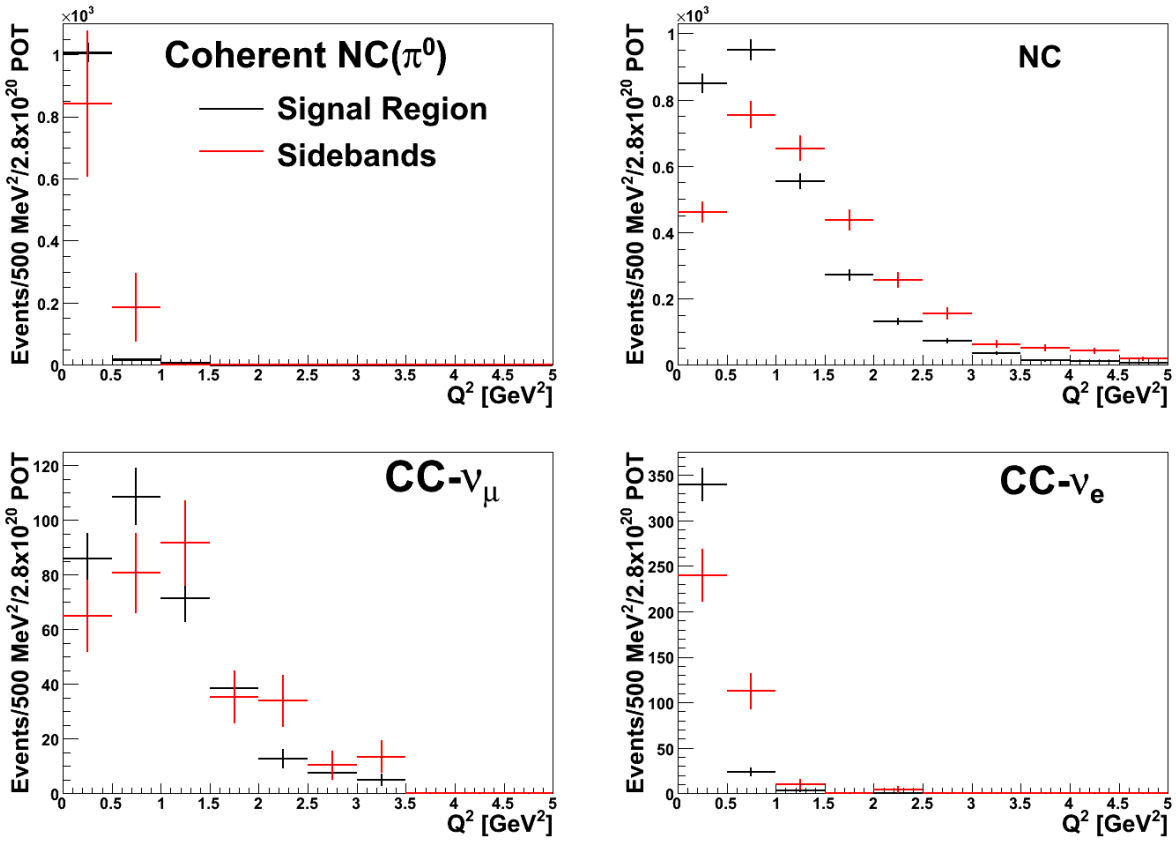

Figure 6.3: The event rate distribution as a function of true Q^2 for selected MC events. The plots show the number of events in the signal region (black) area-normalized to the number of events in the sideband region (red). The sideband distributions are peaked at higher values of Q^2 than those in the signal region. This reflects the fact that the signal region consists of events having relatively lower final-state visible energies.

PID sample. The event rate shapes as functions of Q^2 are displayed in Fig. 6.4. These plots show closer matches in most cases than do the signal region versus sideband comparisons, and demonstrate the usefulness of the near-PID sample in extrapolating the background event rates into the signal region. Similar plots for the invariant mass (W^2), Bjorken x, and Bjorken y can be found in Appendix D.

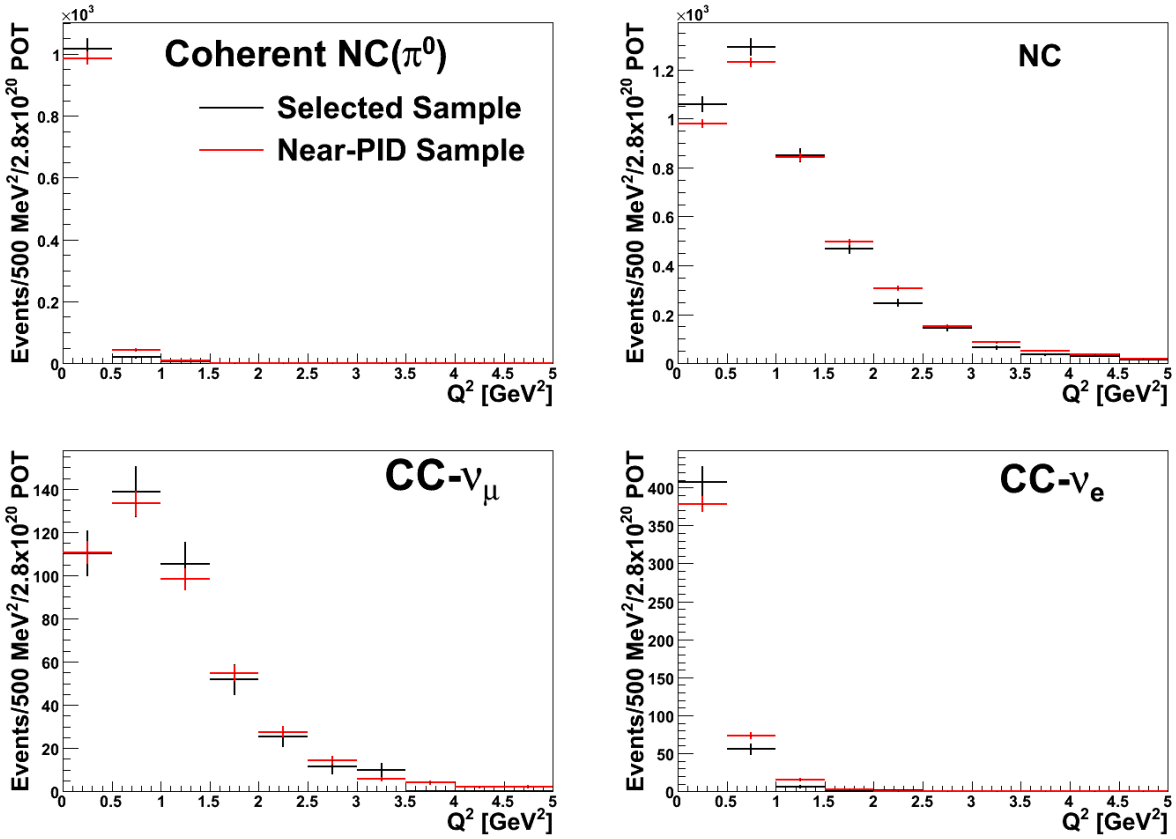

Figure 6.4: The event rate distribution as a function of true Q^2 for the selected sample (black) and the near-PID sample (red) MC events. The plots show the number of events in the signal region area-normalized to the number of events in the near-PID sample. The level of agreement between the Q^2 event rate distributions suggests that events in the two samples are produced by the same physical processes.

6.6 The Selected Sample

The final-state visible energy (Energy), and the angle of the final state shower prong with respect to the beam (Angle), are the only kinematic handles available for coherent NC(π^0) reactions in the MINOS Near Detector, and are therefore heavily relied upon. Figure 6.5 displays the energy spectrum of the selected sample. The coherent NC(π^0) component is similar in shape to that of the non-coherent NC events. The CC-ν_e spectrum however, is quite different. This difference is exploited by the fitting procedure to isolate CC-ν_e events in the sideband and match them to the data. The angular spectrum of the selected sample, shown in Fig. 6.6, can be used to separate coherent and non-coherent NC events in a similar manner. Fig. 6.7 displays η for the selected sample. The coherent NC(π^0) component is highly peaked at zero, and a cut on η can be used to approximate the signal region for the purpose of optimizing the PID cut functions.

The first $\nu_\mu \rightarrow \nu_e$ oscillation analysis reported a discrepancy of greater than 15% between the data and MC event rates for events containing EM showers in the ND [32]. The coherent NC(π^0) selected sample is a more limited sample, and an increase in this discrepancy is not unexpected. It is clear that the MC overestimates the rate of EM shower dominated events in the ND. The sole purpose of the fitting procedure developed for this analysis, and described in detail in Chapter 9, is to rectify this data-vs-MC discrepancy by ensuring that the MC estimates of the background in the signal region reflect the data in the sideband region and the near-PID sample.

The data-versus-MC agreement, although still discrepant by 30%, is improved by the MRCC reweighting. Figure 6.8 shows that the MRCC reweighting

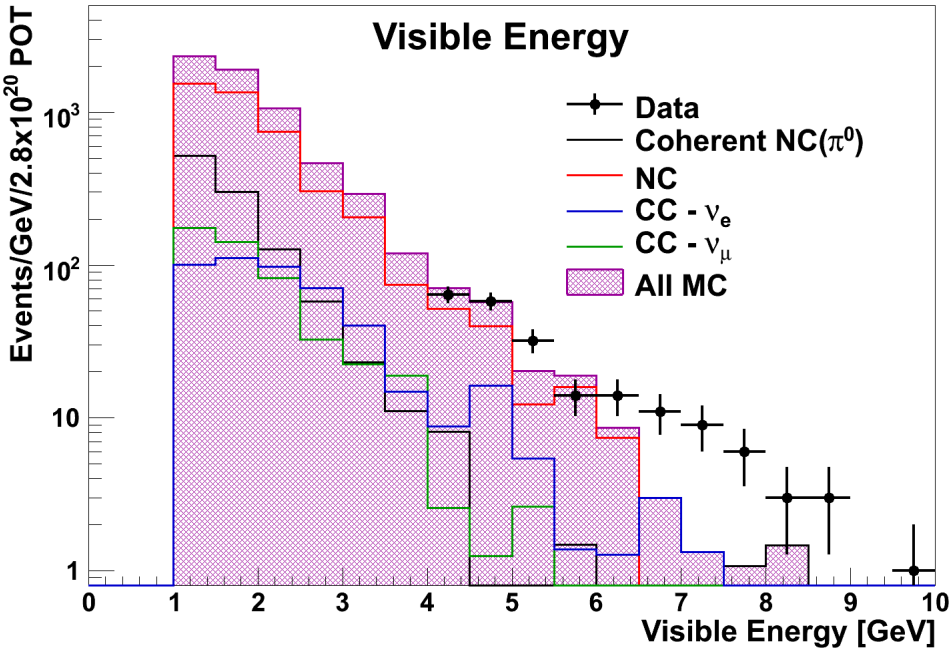

Figure 6.5: The number of events as a function of the reconstructed visible energy for the selected sample. The data (black points) are shown for the unblinded region only. The visible energy distribution of the data below 4.0 GeV was blinded from the analysis. The signal (black histogram) is concentrated at low visible energies.

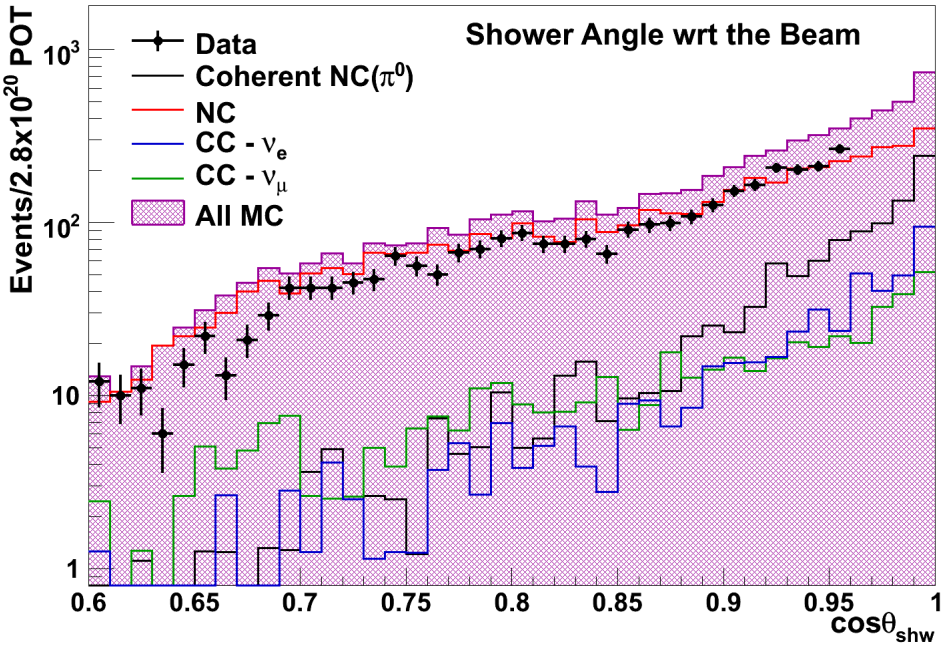

Figure 6.6: Distribution of selected events as a function of the cosine of the reconstructed shower angle with respect to the beam direction, $\cos\theta_{shw}$. The data is shown for the unblinded region below a $\cos\theta_{shw}$ value of 0.97 and indicates a normalization overestimate of roughly 30% by the MC predictions. The shape of the data distribution and the total MC distribution however, are fairly similar.

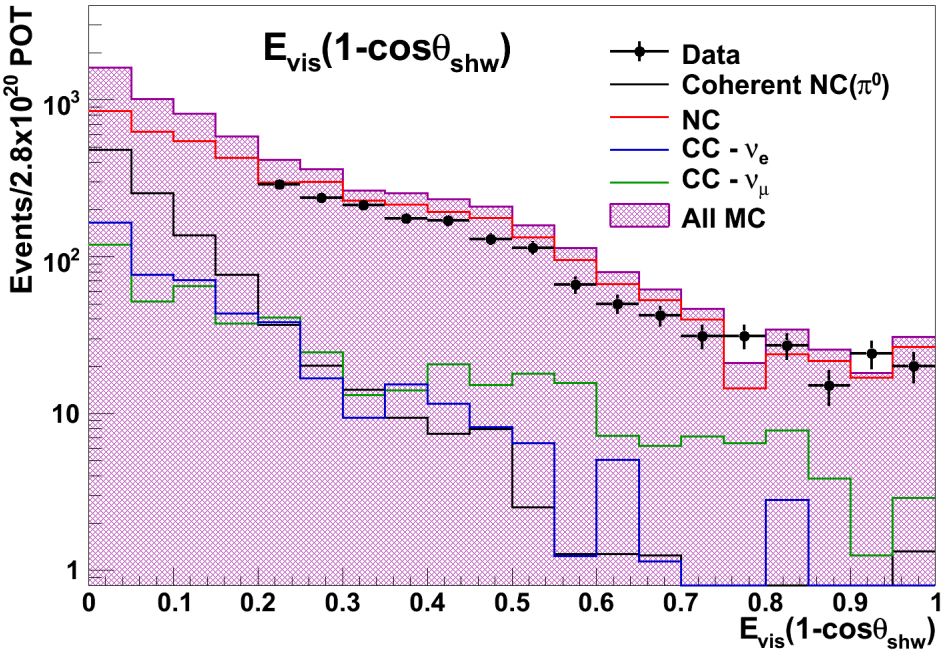

Figure 6.7: The number of selected events as a function of $\eta = E_{vis}\,(1 - \cos\theta_{shw})$. The data is shown for the unblinded region, defined by $\eta < 0.2$ GeV, indicates a normalization overestimate of 30% by the MC predictions. The shape of the unblinded data distribution and the total MC distribution are in good agreement.

increases the weights of high energy events where the MC prediction is well below the data. Figure 6.9 shows the effect of the MRCC weights on the event rate distribution as a function of the cosine of the shower angle with respect to the beam. The increased background rate at small values of Angle is difficult to evaluate since the data there were blinded.

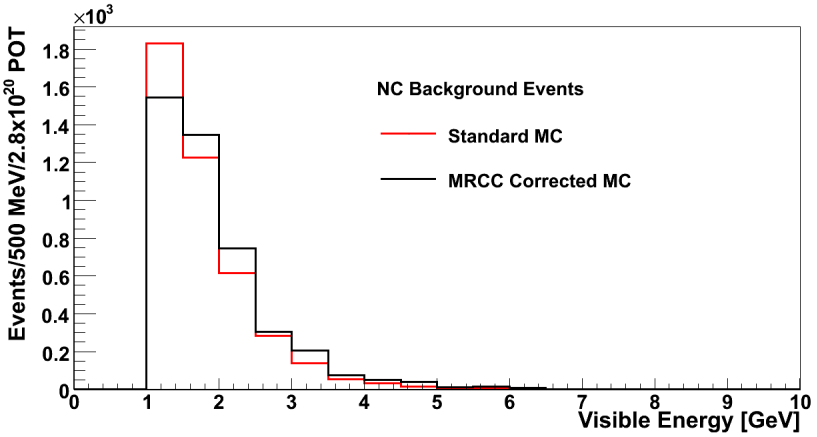

Figure 6.8: The number of NC events in the selected sample as a function of the visible shower energy for MC with (black) and without (red) the MRCC reweighting applied. Events below 1.5 GeV are weighted down by roughly 70%, while events above 3.0 GeV are weighted up by as much as 100%.

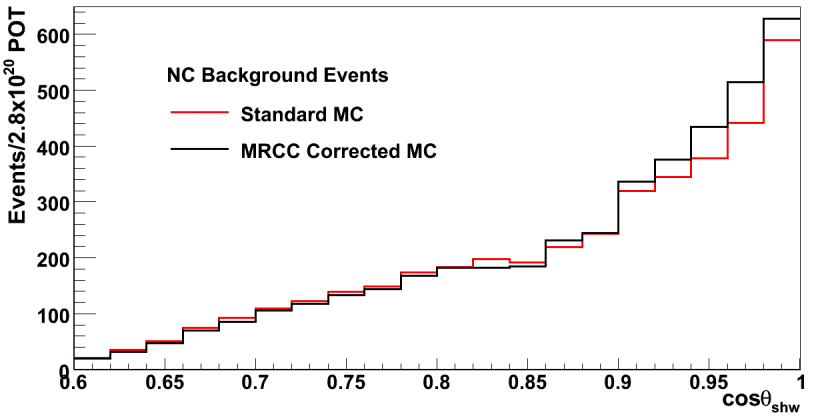

Figure 6.9: The number of events in the selected sample as a function of the cosine of the shower angle with respect to the beam for MC with (black) and for MC without (red) the MRCC reweighting applied. The increased number of events at small angles is a reflection of the fact that higher energy events, which are weighted up the most, occur at smaller values of Angle.

A complete error analysis requires a detailed understanding of the background components. Fig. 6.10 shows the energy spectrum of the three background categories broken out by interaction type, (quasi-)elastic, resonance production, and deep inelastic scattering (DIS). Neutral Current and CC-ν_μ events are mostly of the DIS variety, but with a significant contribution from resonance production below 2.0 GeV. Charged Current ν_e events are mostly comprised of quasi-elastic reactions, with a contribution from resonance production up to a visible energy of 3.0 GeV, and an additional small contribution from low multiplicity ν_e DIS events extending to higher Energy.

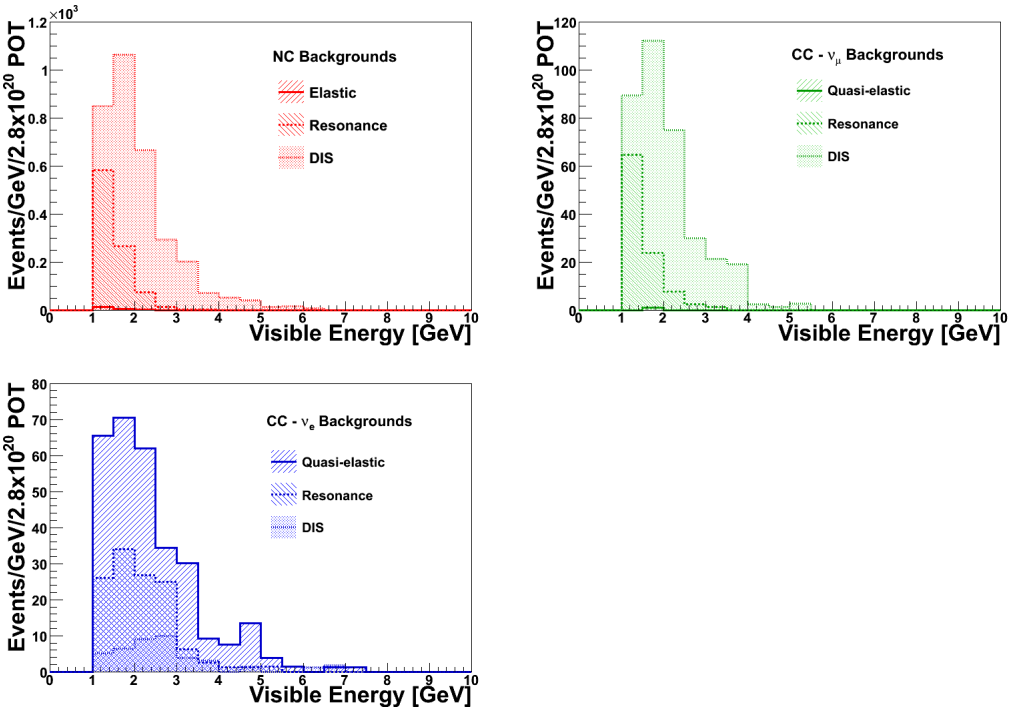

Figure 6.10: The visible energy of selected MC background events categorized by neutrino interaction type (NC, CC-ν_μ, CC-ν_e). Each distribution is further broken out into its component contributions from (quasi)-elastic, resonance production, and DIS reaction types.

Tables 6.2, 6.3, and 6.4 display the MC event multiplicities for the most common background events. The Tables indicate the number of outgoing charged and neutral pions, and whether an event produces a recoil proton or a recoil

neutron. Additionally, the Tables indicate whether or not an event was accompanied by nuclear breakup. As expected, the majority of selected background events contain only a neutral pion or an electron, or else a neutral pion or an electron accompanied by an additional charged or neutral pion. The energy of these secondary pions is usually small compared to the energy of the EM shower-producing particle.

Final State Nucleon	**Final State Charged π's**	**Final State π^0's**			
		0	1	2	3
Proton	**None**	0.76% 1.15%	**30.90%** **22.07%**	2.01% 0.05%	0.00% 0.22%
	π^-	1.92% 0.60%	2.06% 0.28%	0.00 0.00	0.00% 0.00%
	π^+	0.15% 0.83%	0.00% 0.33%	0.00% 0.00%	0.00% 0.00%
	π^+ & π^-	0.85% 0.43%	0.00% 0.26%	0.00% 0.00%	0.00% 0.00%
Neutron	**None**	0.35% 0.00%	**21.36%** 0.33%	0.38% 0.15%	0.00% 0.00%
	π^-	0.00% 0.00%	0.00% 0.00%	0.00% 0.00%	0.00% 0.00%
	π^+	0.64% 0.00%	1.14% 0.00%	0.38% 0.00%	0.00% 0.00%
	π^+ & π^-	0.31% 0.00%	0.18% 0.00%	0.00% 0.00%	0.00% 0.00%

Table 6.2: Sample percentages for the selected NC resonance production background MC events broken out according to final-state multiplicities. Each entry indicates the relative number of events which have a particular combination of final-state particles emerging from the nucleus. Upper entries in each cell summarize events devoid of nuclear breakup, while lower entries summarize events for which nuclear breakup is present. The nuclear breakup is indicated in the stdhep record by the presence of additional low energy (undetectable) nucleons in the final state.

The nuclear breakup may result from nucleon or pion absorption, and is an indication that the intranuclear re-scattering model has been invoked. For example, of the selected NC DIS background events 7.7% produce a proton, a π^-, and a π^0 in the final state, while an additional 12.2% produce a single

Final State Nucleon	**Final State Charged π's**	**Final State π^0's**			
		0	1	2	3
Proton	**None**	0.00%	3.32%	**4.71%**	1.23%
		0.36%	**12.22%**	**4.55%**	1.19%
	π^-	1.50%	**7.65%**	**4.77%**	0.05%
		1.00%	3.58%	**4.60%**	0.13%
	π^+	0.00%	0.19%	0.10%	0.00%
		0.55%	**4.28%**	0.55%	0.10%
	π^+ & π^-	1.13%	1.50%	0.22%	0.02%
		0.65%	1.07%	0.34%	0.20%
Neutron	**None**	0.00%	**8.66%**	2.81%	1.09%
		0.02%	1.81%	0.32%	0.02%
	π^-	0.02%	0.20%	0.05%	0.02%
		0.05%	0.10%	0.02%	0.00%
	π^+	0.34%	**6.48%**	0.84%	0.22%
		0.14%	0.41%	0.10%	0.00%
	π^+ & π^-	0.31%	0.72%	0.20%	0.00%
		0.10%	0.10%	0.03%	0.00%

Table 6.3: Sample percentages for the selected NC DIS background MC events broken out according to final-state multiplicities. Each entry indicates the relative number of events which have a particular combination of final-state particles emerging from the nucleus. Upper entries in each cell summarize events devoid of nuclear breakup, while lower entries summarize events for which nuclear breakup is present. The nuclear breakup is indicated in the stdhep record by the presence of additional low energy (undetectable) nucleons in the final state.

π^0, a recoil proton, and several other nucleons. The majority of the 5,866 NC DIS events contain a single π^0, or a π^0 in addition to a second charged or neutral pion. The final-state categories listed account for 87.0% of the NC DIS background events. The remaining 13.0% are distributed over a variety of lightly-populated categories including those which contain kaons, or other combinations of pions. Each of the later multiplicity based categories account for less than 1.0% (per category) of the NC DIS background sample.

Final State Nucleon	**Final State Charged π's**	**Final State π^0's**			
		Quasi-elastic		**Resonance**	
		0	1	0	1
Proton	**None**	**42.88%** **43.90%**	0.00% 0.00%	0.00% **8.90%**	**7.98%** 4.31%
	π^-	0.00% 0.00%	0.00% 0.00%	0.00% 1.23%	0.00% 0.00%
	π^+	0.00% 0.00%	0.00% 0.00%	**25.77%** **19.94%**	0.00% 0.92%
	π^+ & π^-	0.00% 0.00%	0.00% 0.00%	1.23% 0.31%	0.00% 0.00%
Neutron	**None**	2.54% 0.00%	0.00% 0.00%	0.00% 1.23%	0.92% 0.00%
	π^-	0.00% 0.00%	0.00% 0.00%	2.45% 0.00%	0.00% 0.00%
	π^+	0.00% 0.00%	0.17% 0.00%	4.60% 0.31%	0.00% 0.00%
	π^+ & π^-	0.00% 0.00%	0.00% 0.00%	0.00% 0.00%	0.00% 0.00%

Table 6.4: Percentages of selected quasi-elastic and resonance production CC-ν_e background events of various final-state multiplicities. Each entry indicates the relative number of events which have a particular combination of final-state particles emerging from the nucleus. Upper entries summarize events devoid of nuclear breakup, while lower entries summarize events for which nuclear breakup is present. Nuclear breakup is indicated by the presence of additional low energy (undetectable) nucleons in the final state.

In the case of CC-ν_e interactions, 25.8% of the selected CC-ν_e resonance background events produce an electron, a recoil proton, and a π^+ in the final state, and 43.9% of the quasi-elastic CC-ν_e events produce an electron, recoil proton,

and several other nucleons. Most of the 590 quasi-elastic events contain an electron and a recoil proton, and roughly half include nuclear breakup. Selected resonance production events, of which there are 326, most commonly result in an electron, a recoil proton, and a π^+ in the final state. The quasi-elastic final-state categories listed account for 90% of the selected background events, while the resonance production events listed account for 80% of the selected sample. Other final-state categories, which may contain kaons, or other combinations of pions, account for less than 1.0% (per category) of the CC-ν_e background sample. The relative absence of events with a recoil neutron reflects the ratio of electron neutrinos to electron anti-neutrinos in the NuMI beam.

Distributions of Bjorken x, Bjorken y, Q^2, and W^2 for the selected sample are shown in Fig. 6.11. The Bjorken x distribution for the selected signal is peaked at zero and falls off rapidly. The selected backgrounds on the other hand peak above zero, and are more broadly distributed. The shapes of the distributions can be better understood through the Q^2 and y distributions as x is defined (see Chapter 4) as a function of those variables.

Coherent scattering is a low Q^2 process, which is reflected in the Q^2 distribution of the selected signal. The selected CC-ν_e Q^2 spectrum is similarly sharply peaked, although slightly broader. The selected NC and CC-ν_μ events come from a higher Q^2 region, consistent with the shape of the corresponding pre-selected samples. The invariant hadronic mass, W^2, is close to zero for coherent reactions and near 1.0 for (quasi)-elastic processes. The distributions for resonance production and DIS NC and CC-ν_μ events are similar in shape to their respective pre-selected samples. The Bjorken y distribution for CC-ν_e events is peaked at zero. This is expected because the EM shower produc-

ing particle in these interactions is the charged lepton, not a dominant π^0 in the hadronic shower. In the case of CC-ν_e events, the presence of a visible hadronic shower would likely qualify the event as background. The CC-ν_μ y distribution peaks at 1.0, which is also expected, as the CC-ν_μ events selected do not contain a visible final-state muon, and most of the energy is transferred to the hadronic system. The NC processes have y-values spread across the allowed range, although the coherent channel peaks at a relatively lower value of y.

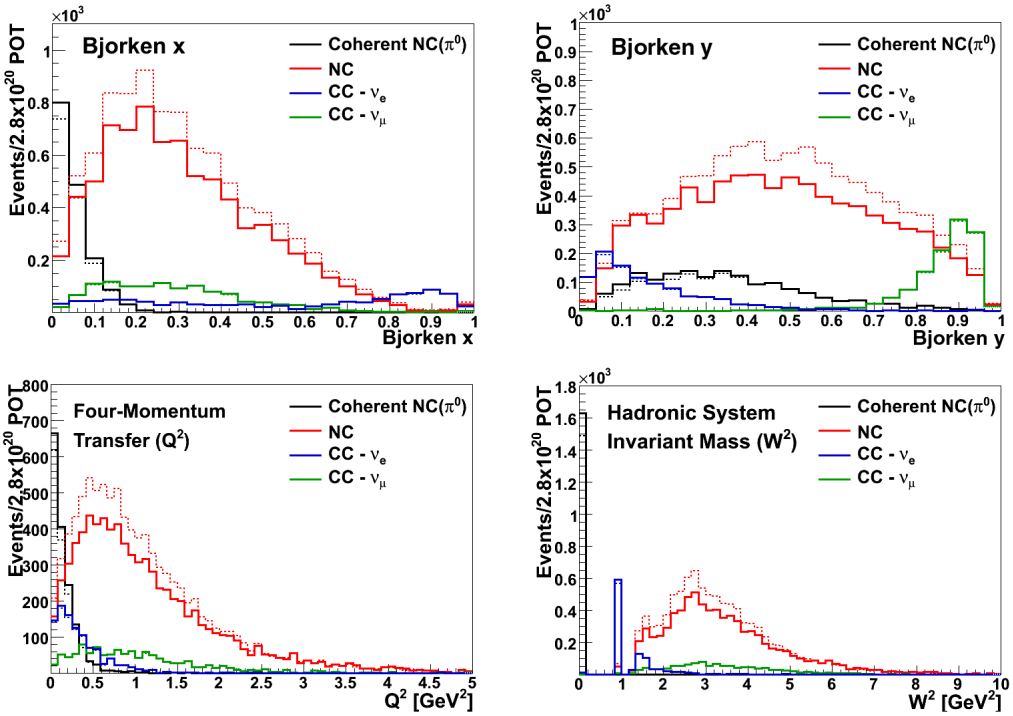

Figure 6.11: The number of selected Monte Carlo events as a function of true Bjorken x (top left), true Bjorken y (top right), true Q^2 (bottom left), and true W^2 (bottom right). Included are the distributions for the unweighted MC predictions (dashed) and distributions which show the effects of reweighting with respect to the MRCC and SKZP data based corrections to the MC (solid).

Distributions of the final-state EM shower fraction, the final-state charged pion energy fraction, true visible energy, and true values of η for the selected sample are shown in Fig. 6.12. The EM shower fraction for coherent NC(π^0)

events is 1.0 as the outgoing neutral pion is the only final state particle. The background events, for the most part, have a large fraction of their final-state energy in EM shower producing particles. The events with an EM shower fraction of, or close to, zero have visible energies less than 2.0 GeV, where the structure of the EM shower is more diffuse. The apparent structure of the hadronic shower in these events is coincidentally EM-like in its characteristics. The charged pion energy fraction is, as expected, zero for a large fraction of the selected events. For events with non-zero values, a relatively small fraction of the final-state event energy is in charged pions. The true visible energy, and η distributions for the selected signal and backgrounds are more sharply peaked than the corresponding reconstructed quantities. Several selected signal events have a true visible energy less than 1.0 GeV. These are taken into account by an acceptance correction detailed in Chapter 9.4.

There are a variety of events that contain healthy electromagnetic showers, for example high energy quasi-elastic CC-ν_e events, but are not in the selected sample. In Fig. 6.13 the MC predictions for the true transverse, and longitudinal momenta of the most energetic EM shower producing particle in each reaction is shown for the signal and for the three background categories. The color axis displays all pre-selected events, and the boxes show the EM shower momenta for selected events. From this plot it can be seen that the coherent NC(π^0) reaction produces neutral pions in a certain momentum range. Electromagnetic shower producing particles with momenta outside of that range are not selected.

It is also clear from Fig. 6.13 that the coherent NC(π^0) selection does not represent a viable alternative for selecting ν_e events. The PID has been designed to take advantage of the lack of vertex hadronic activity produced by

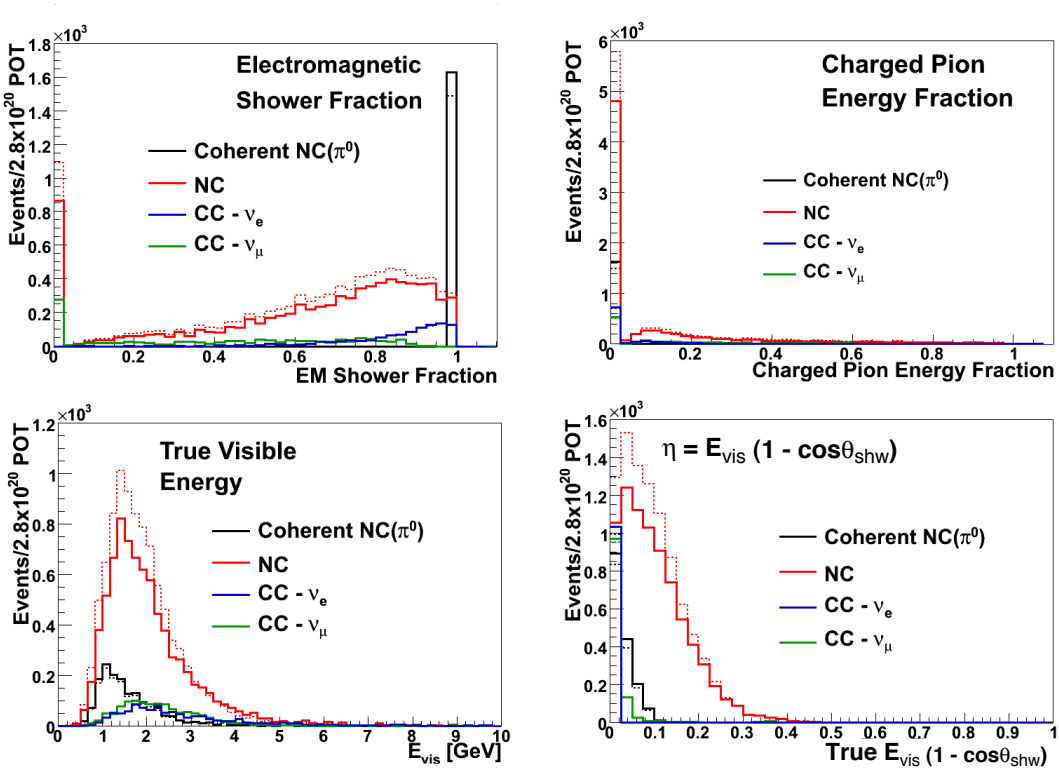

Figure 6.12: The Monte Carlo predicted event rates for the true electromagnetic shower fraction (top, left), the true charged pion energy fraction (top, right), the true visible energy (bottom, left) and true η (bottom, right). Included are the distributions for the unweighted MC predictions (dashed) and distributions which show the effects of the MRCC and SKZP data based corrections to the MC (solid).

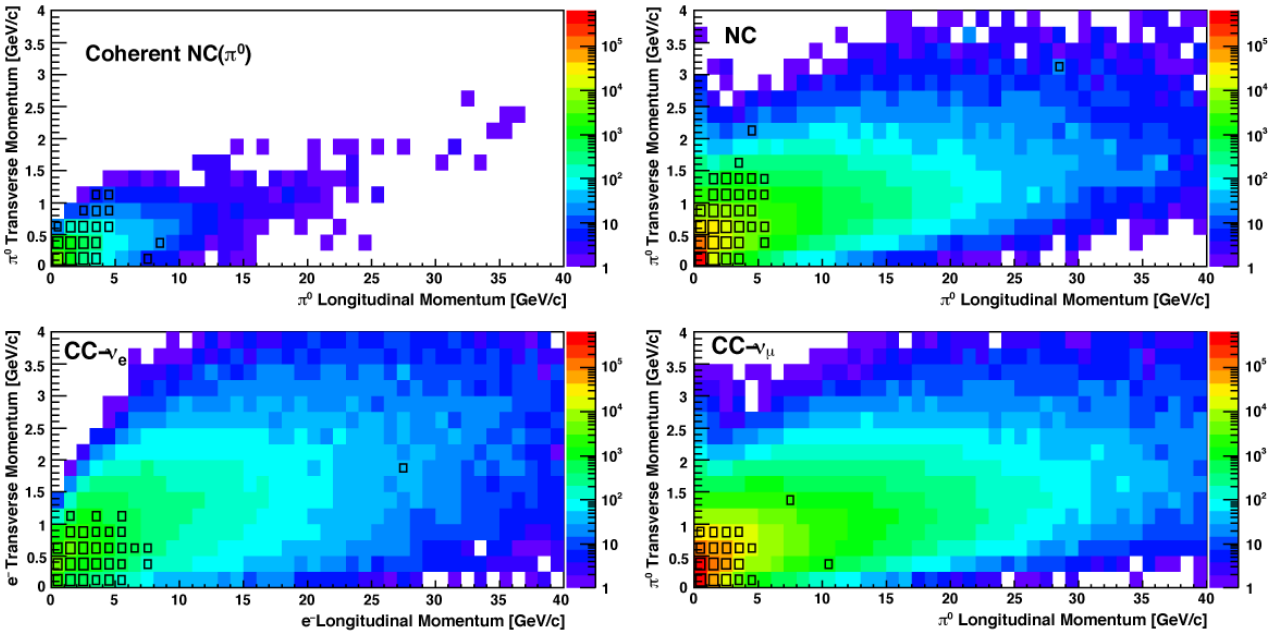

Figure 6.13: Monte Carlo predictions for the transverse and longitudinal momenta of the most energetic EM shower producing particle in each event. The color axes display the number of pre-selected events in each bin. The size of the boxes reflect the number of selected events in each bin (a.u.). Coherent events rarely produce events with an EM shower energy greater than 5 GeV/c, which is reflected in the momentum range of EM shower producing particles for events in the selected sample.

CC-ν_e reactions, and also keys on the momentum of resulting electromagnetic showers. This results in the exclusion of many CC-ν_e events that a successful PID would be required to select.

6.7 Utilization of ν_e Working Group Analysis Tools

Much of the event selection procedure used here, as well as other key aspects of the coherent NC(π^0) analysis, utilize tools developed by the MINOS $\nu_\mu \rightarrow \nu_e$ oscillation analysis (ν_e) Working Group. Their charge requires the identification and selection of events with EM showers. It is therefore sensible to begin the search for coherent NC(π^0) events by building on work already done. Many of the selection variables were developed by members of the ν_e Working Group. The SVM and other coherent NC(π^0) analysis software use the ν_e Group's analysis ntuples as input files, and utilize the same ND fiducial volume and data quality cuts as well. The MRCC reweighting scheme, although modified for this analysis, was developed by the ν_e Group. In addition the ν_e Working Group developed software to explore systematic error sources relevant to the production of EM shower-producing events. The analysis reported here has benefitted from all of the ν_e Working Group's foundational work [34].

Chapter 7

Neutrino-Electron Scattering

The elastic (NC) channel of muon (anti)neutrino-electron scattering,

$$\begin{aligned} \nu_\mu + e^- &\rightarrow \nu_\mu + e^- \quad (NC) \\ \bar{\nu}_\mu + e^- &\rightarrow \bar{\nu}_\mu + e^- \quad (NC) \end{aligned} \tag{7.1}$$

was not included in the Monte Carlo, nor was electron neutrino-electron scattering,

$$\begin{aligned} \nu_e + e^- &\rightarrow e^- + \nu_e \quad (CC) \\ \nu_e + e^- &\rightarrow \nu_e + e^- \quad (NC) \\ \bar{\nu}_e + e^- &\rightarrow e^- + \bar{\nu}_e \quad (CC) \\ \bar{\nu}_e + e^- &\rightarrow \bar{\nu}_e + e^- \quad (NC) \end{aligned} \tag{7.2}$$

These processes are not expected to contribute a significant background to any other MINOS analyses. However, these events produce a pure EM shower resulting from the production of an electron as the only detectable final-state particle. The coherent NC(π^0) PID is designed to select pure EM showers, so

even the modest event rate produced by this interaction could have an effect. For this reason a special MC sample was generated to estimate the number of elastic neutrino-electron scattering events expected in the Run I + Run II data sample, and to estimate the number of such events in the selected sample. A sample corresponding to 30×10^{21} POT using the proper ratio of the Run I + Run II neutrino fluxes was generated, reconstructed, and processed in the same way as the standard MC. The resulting files were used to generate Angle-vs-Energy histograms which were scaled to 2.8×10^{20} POT. Figure 7.1 shows the result of the study. The contribution from this interaction is small but must be accounted for in the analysis. The physics of this interaction is well understood, and the cross section and final-state kinematics are well constrained by data. The contribution from elastic neutrino-electron scattering can therefore be subtracted directly from the data with little uncertainty.

Additional electron scattering channels that produce final-state electrons come from elastic anti-muon neutrino interactions and from the CC and NC channels of $(\nu_e + e^-)$ and $(\bar{\nu}_e + e^-)$ scattering. These interactions are complicated by interference terms resulting from the identical initial and final states for the NC and CC channels. Generator level estimates of these subdominant interactions are used to reweight the full simulation of NC muon neutrino scattering as a function of true final-state electron energy. The result is a 25% increase in total event rate, mostly at higher energies. Figure 7.2 displays the expected event rate as a function of true final-state electron energy, scaled to $2.8{\times}10^{20}$ POT, for all four relevant $\nu{+}e^-$ scattering processes. The reweighted reconstructed Angle-vs-Energy distribution, accounting for all four neutrino-electron scattering processes, is subtracted from the data Angle-vs-Energy histogram before proceding to the fit procedure.

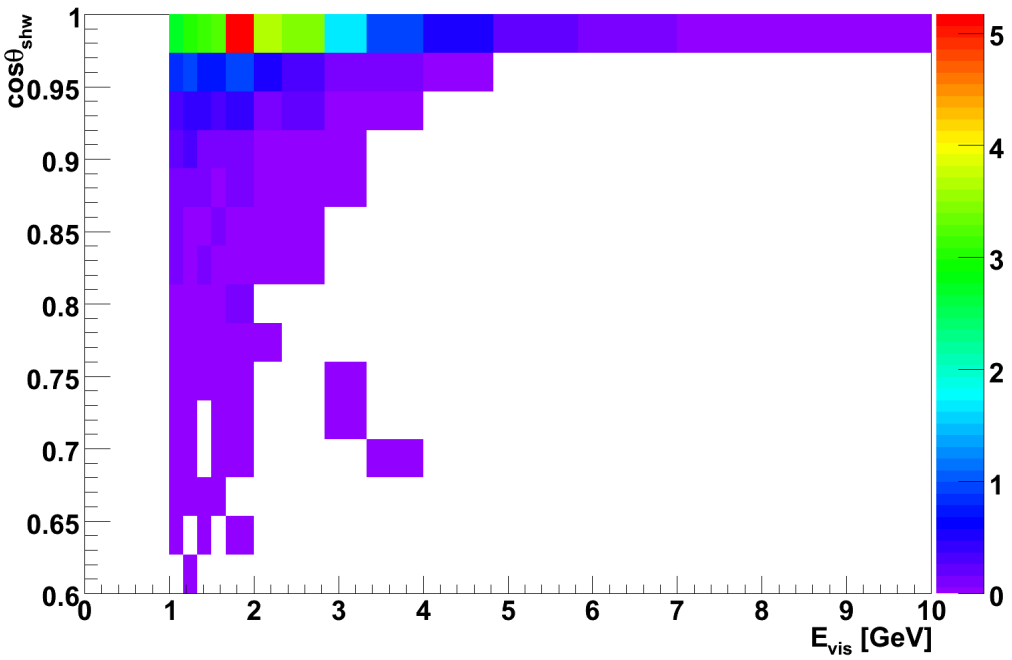

Figure 7.1: Full Monte Carlo simulations for the selected event rate for elastic neutrino-electron scattering in the MINOS Near Detector as a function of visible shower energy, and the cosine of the shower angle with respect to the beam. The events are concentrated at the same Angles and Energies as the coherent NC(π^0) sample, although the relative event rate is <5% per bin.

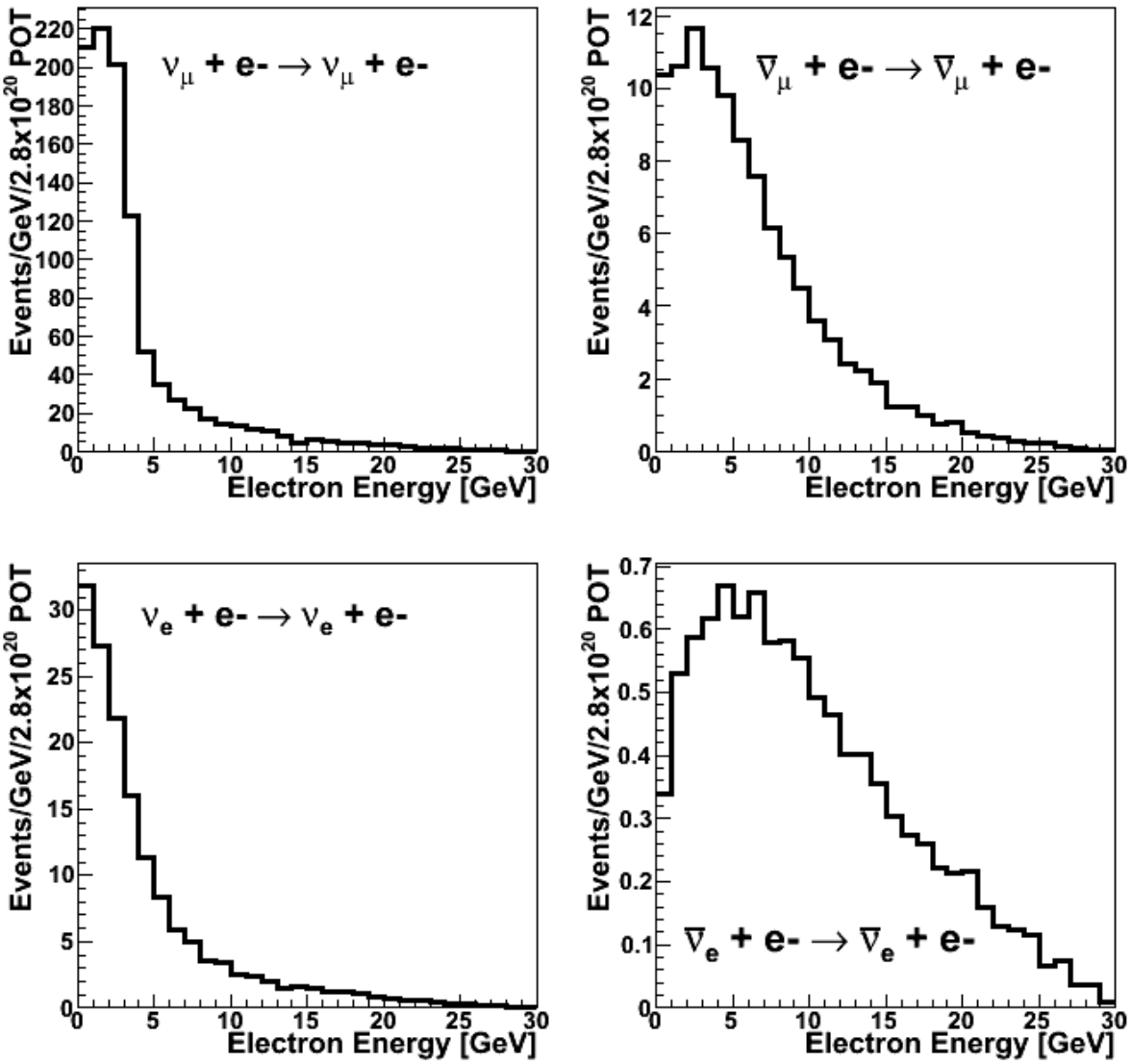

Figure 7.2: Generator level Monte Carlo predictions for event rates of the various neutrino-electron scattering processes found in the MINOS Near Detector. The main contribution comes from the $\nu_\mu + e^-$ interactions. The other three reaction categories contribute an additional 25% to the total event rate.

Part III

The Fitting Procedure

Chapter 8

Overview

The selected MC sample consists of 16.8% coherent NC(π^0) signal events while the remaining 83.2% is comprised of a combination of the three background event types (68.3% NC, 7.3% CC-ν_μ, 7.6% CC-ν_e). The uncertainties relating to the number of selected background events are large, so a straightforward background subtraction would result in a low precision measurement. Fortunately, the signal and backgrounds distribute differently in the two measurable kinematic variables: *i*) the event visible energy (Energy) and *ii*) the cosine of the angular orientation of the event shower with respect to the neutrino beam direction (Angle). That is, the backgrounds distribute in such a way that they can be isolated in regions of a plane which is defined by two axes, one for each of the two kinematic variables.

In this Angle-vs-Energy plane, events of the signal will cluster at low visible energies and at small production angles (the signal region) whereas the various backgrounds will tend to also populate the outlying "sideband" region. This additional information enables the use of a more sophisticated background subtraction method, namely fitting the various background com-

ponents to the data in the sideband region of the Angle-vs-Energy plane prior to performing the background subtraction. A software package was developed to enable the fitting of MC background Angle-vs-Energy histograms to the background regions of the data Angle-vs-Energy plane. This "fitting package" inputs Angle-vs-Energy histograms, as well as a list of fit parameters. In addition, the fitting package accepts arguments that determine the set of values used for each fit parameter.

The systematic uncertainties on the background samples are large, but the sources of these uncertainties are well studied and the uncertainties can therefore be incorporated into the fitting procedure. The coherent NC(π^0) model on the other hand, has large uncertainties that are difficult to study and constrain due to the large disagreement between the predictions made by current models, and the lack of high precision data. The PCAC formulations and the dynamical models differ in their characterization of the underlying interaction, and there is much disagreement among predictions made by the models. Furthermore, cross section calculations made by NEUGEN3 used in the MINOS MC differs greatly from other implementations of the Rein-Sehgal model used by the neutrino event generators of other experiments (NUANCE, NUINT, etc) [10]. It is therefore prudent to limit the influence of the Rein-Sehgal model, and thus reduce the uncertainty propagated to the result. To this end, bins of the Angle-vs-Energy histograms with a large fraction of coherent NC(π^0) events, as predicted by the MC, are excluded from the fit. Bins where the expected contribution from the signal is limited to 5% of the total bin contents are included in the fit. This 5% limit thus defines the cutoff between the signal region and the sideband region.

A measurement of the coherent NC(π^0) event rate in MINOS suffers from a

multitude of systematic error sources. Fitting for each of these systematic error sources individually is impractical. Instead a set of "effective fit parameters" was developed. These parameters scale the total number of events in each relevant background category. The background categories used in the fits are, *i*) NC and CC-ν_μ resonance events, *ii*) NC and CC-ν_μ DIS events, and *iii*) all CC-ν_e events. In principle the NC and CC-ν_μ samples could be fit for separately, but the two samples occupy the same regions of the Angle-vs-Energy plane as shown in Fig. 9.3, and the selected background events have similar kinematics (except, of course, for y), as shown in Figures 6.11 and 6.12. The latter reflects the fact that the events selected are susceptible to the same errors in the modelling. Furthermore, it is observed that the χ^2 variation in response to reasonable changes in the CC-ν_μ normalization parameter is negligible.

If a systematic error causes the total number of events (normalization) of one of the background categories to change, but not the shape of the Energy-vs-Angle distribution for that category, then that systematic can be absorbed into the effective fit parameters, and does not need to be fit for individually. However, each systematic error source that gives rise to distortion of the Energy-vs-Angle distribution must be fit for independently, and therefore requires an additional "systematic" fit parameter.

The fitting package has three distinct modes of operation:

1) **Single systematic error fits**. The purpose of these fits is to evaluate each of the systematic error sources individually; it is necessary to understand how fluctuations in each systematic affect the selected sample, and to decide how to treat each systematic in the next round of fits. The Monte Carlo is reweighted to reflect a ± 1 σ fluctuation in a single systematic error source.

An Angle-vs-Energy histogram produced from the selected event sample of the reweighted MC sample is used as data. The normalizations of the five background samples (NC DIS, NC resonance, CC-ν_μ DIS, CC-ν_μ, resonance, and CC-ν_e) are adjusted via the three effective fit parameters so as to match the systematic reweighted MC Angle-vs-Energy distribution. The results of the fits are used to evaluate the effect of the systematic error source on the analysis.

2) **Mock data fits**. The purpose of this second round of fits is to propagate the combined systematic uncertainties through the fitting procedure to determine the uncertainty on the measurement of the coherent NC(π^0) event rate. In this mode additional fit parameters corresponding to possible shape changes to the background Angle-vs-Energy distributions induced by single systematic error sources are included based on the results of the single-systematic-error fits. Mock data for these studies is created by reweighting each subsample of the standard Monte Carlo. A random coherent NC(π^0) event rate is chosen and random variations to the background MC include contributions from all of the systematic error sources, with strengths randomly varied based on probability distribution functions (pdfs) from external data. Fits to thousands of mock data experiments are performed. Each fit returns a measured coherent NC(π^0) event rate. Comparisons of the measured event rate with the mock data event rate yield an error for that mock data experiment. These errors combine to determine the overall systematic error.

3) **Data fits**. The results of the mock data studies are used to estimate the sensitivity of the measurement from the overall systematic+statistical uncertainty. The fitting procedure is then applied to Near Detector data to measure the coherent NC(π^0) event rate, and to produce a cross section measurement.

In all three modes the basic procedure for the fits is the same. Finely binned Angle-vs-Energy histograms of the standard MC signal and backgrounds are loaded. The resolutions for the Energy and the Angle are calculated and are used to determine the proper histogram bin sizes. The bin contents of the input histograms are then redistributed into histograms with the new binning scheme. "Data" is then either constructed based on the MC (mock data), or loaded and rebinned (real data). Fits are then performed using a χ^2 derived from a Poisson-distribution based likelihood ratio.

Each fit parameter is assigned a minimum and maximum value, and number of steps over the allowed range at which individual χ^2 values are to be calculated. As the number of steps (for a given range) increases, the distance between two fit parameter values decreases. A "fit parameter space" can be defined as an N dimensional space where N is the number of fit parameters. Each axis corresponds to one fit parameter and each point in fit parameter space corresponds to a particular combination of fit parameter values. The quantized nature of the fitting procedure selects a set of discrete points in fit parameter space. The χ^2 is used to select the point in this set that produces the best match between MC and data. A finer sampling of fit parameter space requires an increase in the number of fit steps for each of the fit parameters. The number of points sampled is the number of fit steps to the Nth power.

The implementation of fitting is done in one of two ways: *i*) A 'brute force' and compute-intensive grid search is performed over the fit parameters, or else *ii*) A minimization algorithm is used which searches out the fit parameters that produce the minimum χ^2. The first method grinds through each of the possible permutations of the sampled set of values for each of the fit parameters and calculates the χ^2 for each permutation. The benefit of this

approach is that the fit delivers a complete set of $\Delta\chi^2$ curves and surfaces, from which confidence intervals and contours can readily be extracted. The down-side is the processing time required, which grows quickly with additional fit parameters or with increases to the number of values sampled for each fit parameter. In order to process thousands of mock data experiments quickly, or to constrain the search region (in the case of real data) the minimization algorithm method is used.

The fit parameter values associated with the lowest χ^2 value, known as the best-fit values, are then used to predict the background Angle-vs-Energy distributions in both the signal region and the sideband region. The backgrounds are then subtracted from the data, bin-by-bin. The resulting bin contents are acceptance-corrected (also bin-by-bin to remove as much of the coherent model-dependence as possible). Finally, an overall acceptance correction is applied to account for any bins with an acceptance of 0.0. The result is a count of the number of coherent NC(π^0) events in the ND over the Run I + Run II exposure. The measured event rate can be compared to the number of signal events in a mock data sample, or in the case of real data, converted into a cross section measurement.

There are several inputs to the fitting procedure that determine the details of how the fits are to be performed. These include the number and identity of the systematic fit parameters and the values of the fit parameters to be sampled. A set of inputs constitutes a fit configuration. For each configuration a set of mock data studies is performed. Each set of mock data studies is used to evaluate the measurement sensitivity for that configuration. The fit configuration that gives the best sensitivity (i.e. the lowest uncertainty) is used to fit the data and produce the cross section measurement.

Chapter 9

The Fitting Procedure

9.1 Definitions of Signal and Sideband Regions, and of the Near-PID Sample

The success of the MINOS coherent NC(π^0) measurement hinges on the ability of the analysis to limit the effect of the uncertainties on the backgrounds. In a simple background subtraction scheme the systematic error from the background is multiplied by a factor of

$$\frac{1}{\rho} - 1 = \frac{N_{sel}^{bkg}}{N_{sel}^{coh}} \ , \tag{9.1}$$

where ρ is the purity of the selected sample, and N_{sel}^{bkg} and N_{sel}^{coh} are the number of background and signal events in the selected sample, respectively. The error arising from the uncertainty on the modelling of the signal, on the other hand, increases linearly with that uncertainty. The precision attainable with a simple background subtraction technique, derived through error propagation, is given

by

$$\left(\frac{\delta N^{coh}}{N^{coh}}\right)^2 = \left(\frac{1}{\epsilon\rho\ N^{coh}}\right) + \left(\left(\frac{1}{\rho} - 1\right) f_b\right)^2 + f_e^2\ . \tag{9.2}$$

Here $\left(\frac{\delta N^{coh}}{N^{coh}}\right)^2$ is the square of the factional error on the number of coherent NC(π^0) events in the data sample, N^{coh}, ϵ and ρ are the efficiency and the purity, and f_b and f_e are the fractional uncertainties on the number of background events and on the signal efficiency.

By fitting for all of the systematic error sources through a combination of effective and single systematic fit parameters, the overall systematic uncertainty can be reduced. All of the sources of possible uncertainty on the background samples have been well studied, and detailed analyses of the effects of these uncertainties on the MINOS MC are available [35] [36] [37] [38]. On the other hand, the model for the signal is much more uncertain, as there are several alternative models and implementations of the Rein-Sehgal model, which produce varied cross section predictions. Measurements of the coherent process to date do not explicitly exclude any of these models.

Error propagation through the fitting procedure is more complex, but to first order, the same relationships apply. The largest contribution to the reduction in the magnitude of the overall uncertainty results from the fact that the fitting procedure reduces the fractional uncertainties on the backgrounds. The reduction is consistent with the amount to which the background predictions from the sideband region can successfully be extrapolated to the background content in the signal region.

The ability to accurately extrapolate the background event rates into the signal region is a function of both the uncertainties on the shape of the background

Angle-vs-Energy distributions, and of the "signal contamination" in the sideband region and near-PID sample. The uncertainties on the signal are relatively large and a small contribution from the signal in an Angle-vs-Energy bin can increase the uncertainty on the background significantly. The effect of the signal contamination is a result-dependent bias where the measured number of coherent NC(π^0) events is biased toward the Rein-Sehgal prediction of the MC. The strength of the bias is a function of the measured number of coherent NC(π^0) interactions in the data set, and the level of signal contamination. For this reason it is important to define the sideband such that the influence from the signal model is minimal. This is done by defining the sideband as the bins with a low signal purity. However, having fewer bins in the sideband region reduces the amount of information available to the fits, and therefore increases the overall uncertainty on the number of signal events. Optimization of the signal region must balance these two factors, and to that end, the signal region is defined such that the signal purity of bins in the sideband, based on the standard MC predictions, is less than 5.0%.

The resulting sideband is composed of a combination of the three backgrounds, with the NC sample being fairly isolated at low values of Angle, and the CC-ν_e background accounting for the largest portion of the high Energy tail. A cutoff on event visible energy is imposed at 8.0 GeV. For the low-energy beam configuration (LE010-185kA), the CC-ν_e events with a neutrino energy below 8.0 GeV are produced, for the most part, by the decay of muons. The majority of the CC-ν_e events with a neutrino energy above 8.0 GeV are produced by kaon decay [31]. This effect is illustrated by the upper right plot in Fig 9.1. Above visible energies of 8.0 GeV contributions from the other background sources are negligible.

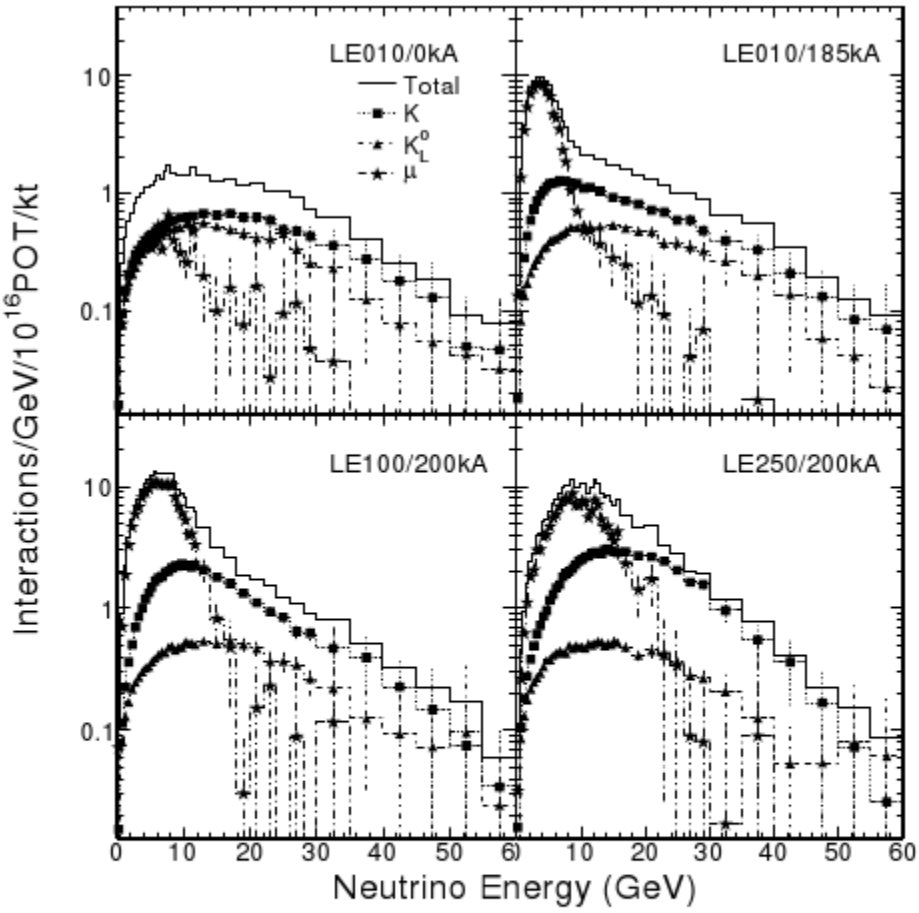

Figure 9.1: The energy spectrum of CC-ν_e interactions in the MINOS Near Detector for four different beam configurations, broken out by the contributions from each type of neutrino parent particle whose decay yields a neutrino. The upper right plot shows the standard low energy beam configuration used to produce the data sets for this analysis. At 8.0 GeV there is a transition from muon-produced neutrinos to kaon-produced neutrinos [31].

The sideband region is mostly composed of signal-like background events that are used to fit the backgrounds for the purpose of extrapolation into the signal region. A larger sample of signal-like background events would improve the accuracy of the extrapolation by providing more information about the signal-like background events. Such a sample exists, and can be isolated using the PID variable. To this end a near-PID sample has also been defined. This sample consists of events that fail the PID cut, but pass a second, near-PID cut defined as cut_{np} in Eq (6.5).

The near-PID sample is comprised of signal-like background events, similar to those in the selected sample. The near-PID cut was designed to *i*) select background events that have similar kinematics to those in the selected sample, and to *ii*) select a sample with a lower fraction of signal events as compared to the selected sample. The second goal is to insure that a greater portion of the Angle-vs-Energy plane is outside the signal region (as defined by those bins in the Angle-vs-Energy plane where the signal purity is less than 5.0%), and can be accessed by the fits. Unfortunately, there is still a region of the near-PID Angle-vs-Energy plane where a large contribution from the signal is predicted, and consequently it must be defined as "signal region" and cannot be used in the fits. Table 9.1 displays the number of selected and near-PID MC events in each of the three background categories. Figures 9.3 and 9.4 of the following Section show the MC Angle-vs-Energy distributions of the selected sample and of the near-PID sample with the signal regions outlined in black.

Reliable extrapolation of the background content of the signal region from the sideband and near-PID samples hinges on the extent to which the signal region, the sideband region, and the near-PID sample are congruent. The level of congruence is demonstrated by comparing true kinematic variables

Event Type	Selected Sample	Near-PID Sample
Coherent NC(π^0)	1044	2146
NC	4233	12257
CC-ν_μ	454	1740
CC-ν_e	470	1642

Table 9.1: Numbers of signal and background events in the selected sample and in the near-PID sample.

for the two regions. Fig. 6.3 and the Figures of Appendix C display the true Q^2, the true W^2, the true Bjorken x, and the true Bjorken y for selected events in the signal and sideband regions. Plots comparing the selected sample to the near-PID sample in the same manner are shown in Fig. 6.4 and the Figures of Appendix D. The distributions, for the most part, do not match very closely, but the sideband region does contain events that encompass the entire kinematic range of the events in the signal region. Furthermore, the kinematic distributions for the selected sample and the near-PID sample match fairly well.

9.2 Binning of Shower Angle Versus Visible Energy

The χ^2 used in the fitting procedure is computed bin-by-bin in the Angle-vs-Energy plane, and, as will be explained in Chapter 9.3, is formulated based on Poisson statistics. Therefore, there is no need to choose bins based on ensuring a minimum bin content needed for a Gaussian approximation. Instead, the sizes of the Energy and Angle bins can be chosen to reflect the resolutions of the two kinematic variables which are estimated by comparing the Monte Carlo truth and reconstructed quantities. For the Energy, the ratio

$(E_{vis}^{true} - E_{vis}^{reco})/E_{vis}^{true}$ is plotted, while for the Angle, the difference between the truth and reconstructed values is used. Representative distributions for these quantities are displayed in Fig. 9.2.

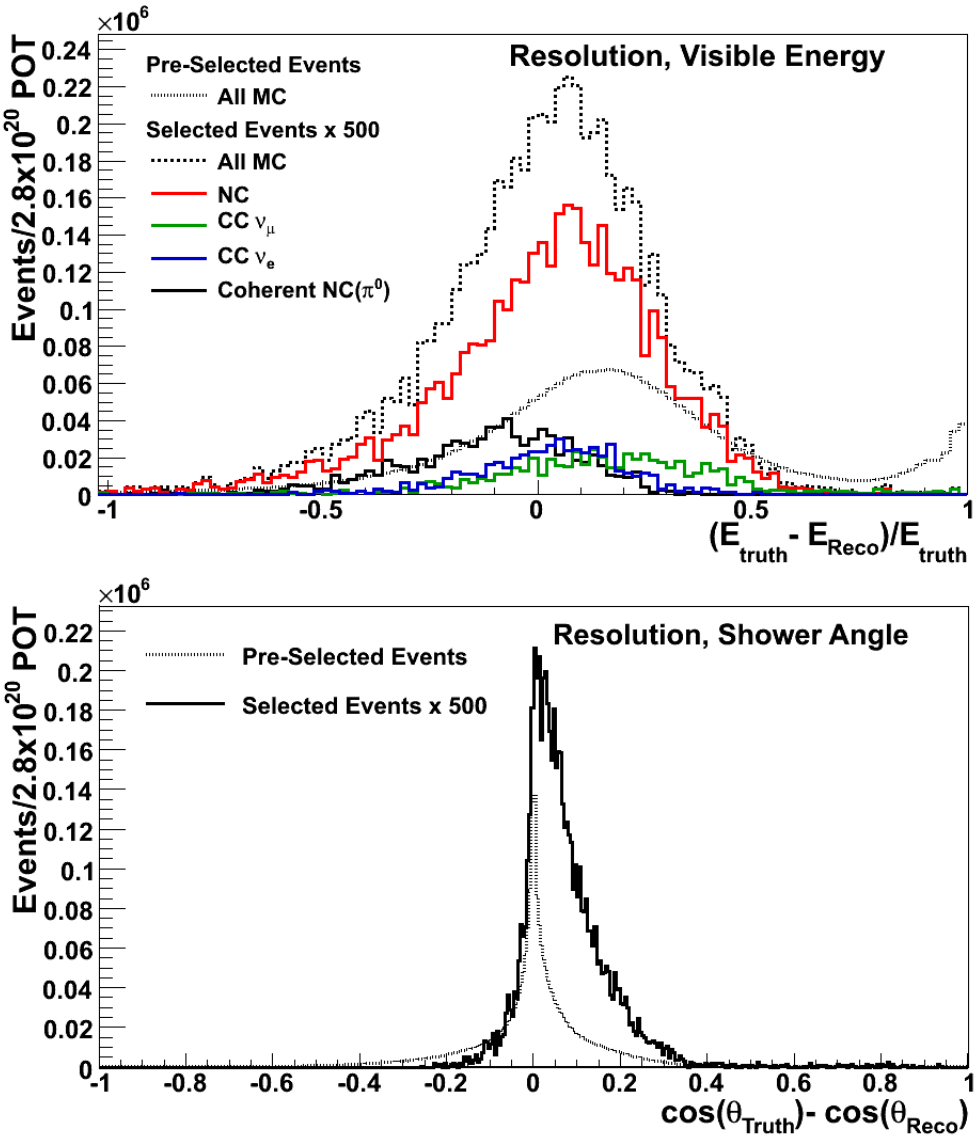

Figure 9.2: Distributions used to specify the resolutions of the reconstructed visible energy and the cosine of the shower angle with respect to the beam. The distributions are functions of the true Energy (Angle) and reconstructed Energy (Angle). The pre-selected sample and selected sample are both displayed for comparison. The resolutions used for re-binning are defined to be the widths of Gaussian fits to the total selected event distributions shown by the dotted black (upper) and solid black (lower) histograms.

The distributions are fitted using Gaussian functions; the widths of the Gaussians are used to determine the resolutions which then dictate the bin size. The two-dimensional Angle-vs-Energy distributions which comprise the input information to the fitting procedure, are finely binned histograms ($0.0 \leq E_{vis} <$ 10.0 GeV in 60 bins and $0.6 \leq \cos\theta_{shw} < 1.0$ in 120 bins). These histograms are then re-binned to reflect the measured resolutions. The Angle variable is observed to have a resolution of roughly 0.04 and bins of constant width are used. The Energy has a resolution of roughly 20%, and a bin size which is proportional to Energy is used. The minimum bin-size is 0.167 GeV reflecting the binning used in the input histogram. The bin width used in fitting increases to about 1.0 GeV for events having visible energy of roughly 5.0 GeV. Illustrative rebinned Angle-vs-Energy distributions are shown in Fig. 9.3 for the selected sample, and Fig. 9.4 for the near-PID sample.

9.3 Formulation of χ^2 and the Penalty Terms

The χ^2 statistic is defined in terms of a likelihood ratio [39], Λ, as

$$\chi^2 = -2\ln(\Lambda) \quad . \tag{9.3}$$

The likelihood ratio used in this analysis is computed based on the Poisson probability distribution which correctly describes the statistical uncertainty for low event rates. When the χ^2 is constructed from a Poisson-statistics-based likelihood ratio, the bin sizes can reflect the resolutions of the parameters being displayed instead of some minimum bin content as required for the Gaussian error approximation. (As the event rates per bin increase above roughly 10, Gaussian errors become a reasonable approximation to Poisson errors.) How-

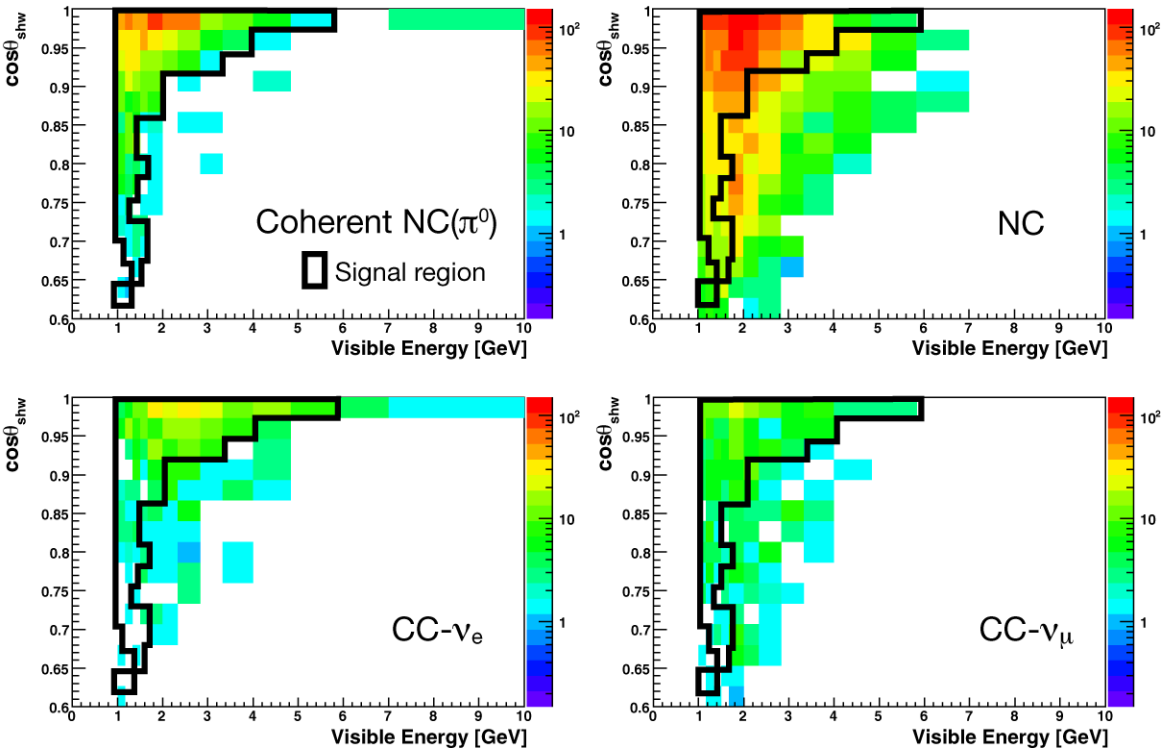

Figure 9.3: The rebinned Angle-vs-Energy selected event rate distributions for the coherent NC(π^0) channel and for each of the three background reaction categories. The color axes represent the number of events in each bin. The solid line border encloses the signal region.

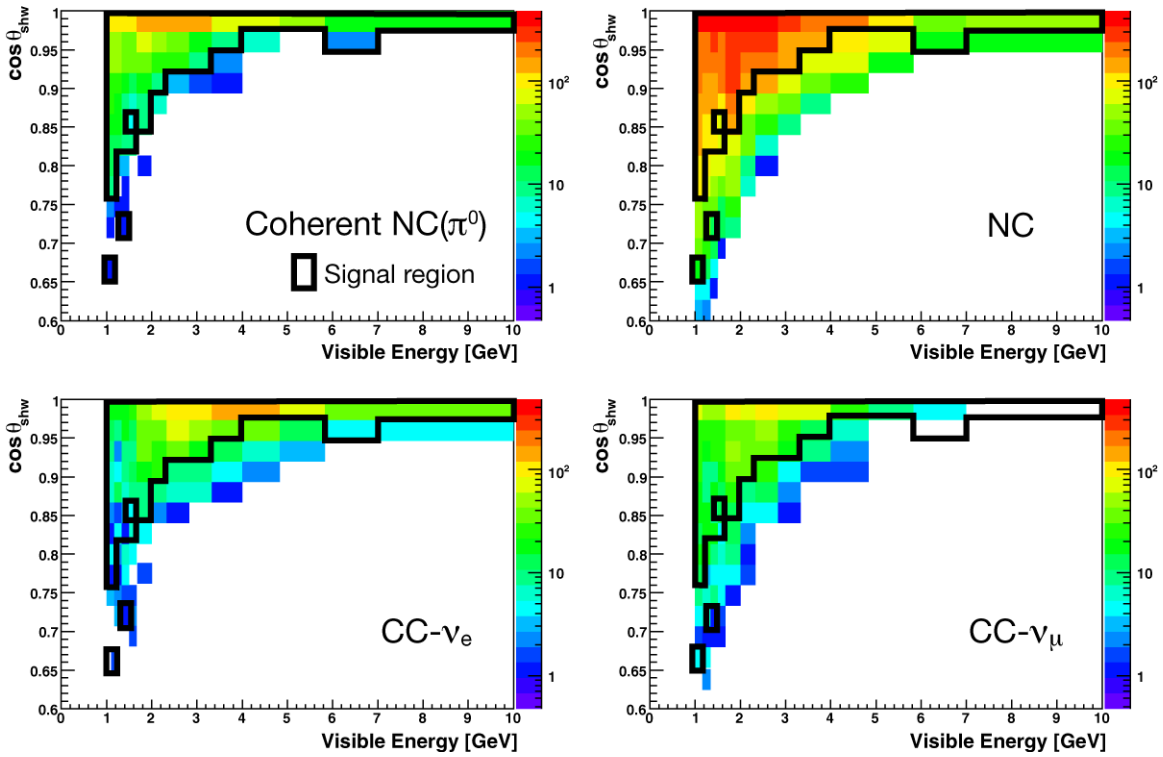

Figure 9.4: The "re-binned" Angle-vs-Energy near-PID sample event rate distributions for the coherent NC(π^0) channel and for each of the three background reaction categories. The color axes represent the number of events in each bin. The signal region is bounded by the solid line.

ever, resolution-based bins in the high Energy and low Angle regions of the Angle-vs-Energy plane are sparsely populated. The final form of the χ^2, including penalty terms, is derived in Eqs. (9.4) through (9.16) below. The number of degrees-of-freedom used in calculating the reduced χ^2 (i.e. χ^2/ndf) is the number of non-zero bins in the sideband region minus the number of fit parameters.

Likelihood Ratio

The probability that the observed number of data events, N_{obs}^{ij}, in bin ij resulted from the MC expectation, N_{exp}^{ij}, in bin ij is calculated from the Poisson probability mass function

$$P_{ij}\left(N_{obs}, N_{exp}\right) \;=\; \frac{{N_{exp}^{ij}}^{N_{obs}^{ij}}}{N_{obs}^{ij}!} e^{-N_{exp}^{ij}} \;. \tag{9.4}$$

The values for N_{exp}^{ij} are the sums of the various signal/background components, b, each of which is adjusted separately by the fit parameters,

$$N_{exp}^{ij} = \sum_{b} N_{exp}^{ijb} \;. \tag{9.5}$$

The likelihood, $\mathcal{L}$, that the data arises from the physics represented by the MC is calculated as the product of these probabilities over the sideband bins ij of the Angle-vs-Energy plane, for both the selected and near-PID samples,

$$\mathcal{L} = \prod_{ij} P_{ij}\left(N_{obs}, N_{exp}\right) = \prod_{ij} \frac{{N_{exp}^{ij}}^{N_{obs}^{ij}}}{N_{obs}^{ij}!} e^{-N_{exp}^{ij}} \;. \tag{9.6}$$

This likelihood is compared to the maximum likelihood, which occurs when

the expectation is observed, i.e. $N_{exp} = N_{obs}$, via a likelihood ratio

$$\Lambda = \prod_{ij} \frac{P_{ij}\left(N_{obs}, N_{exp}\right)}{P_{ij}\left(N_{exp} = N_{obs}\right)} = \prod_{ij} \frac{\frac{{N_{exp}^{ij}}^{N_{obs}^{ij}}}{N_{obs}^{ij}!} e^{-N_{exp}^{ij}}}{\frac{{N_{obs}^{ij}}^{N_{obs}^{ij}}}{N_{obs}^{ij}!} e^{-N_{obs}^{ij}}} \ , \tag{9.7}$$

which reduces to

$$\Lambda \ = \ \prod_{ij} \left(\frac{N_{exp}^{ij}}{N_{obs}^{ij}} \right)^{N_{obs}^{ij}} e^{N_{obs}^{ij} - N_{exp}^{ij}} \ . \tag{9.8}$$

Finite MC Statistics

The above construction of Λ assumes that the statistical error on the MC is negligible. Unfortunately, this is not the case for this analysis since the MC sample is similar in size to the data sample, and they have comparable statistical uncertainties. Techniques to address the problem of limited MC statistics have been documented [40]. Essentially, the MC in each bin is allowed to vary within its Possion-based statistical uncertainty in such a way as to maximize Eq. (9.8) with the addition of a penalty which accounts for the amount of deviation from the MC expectation. The form of this penalty term is another likelihood ratio, Λ_{FMC} based on the probability that the adjusted MC expectation is consistent with the expectation of the standard MC sample, leading to the equation:

$$\Lambda_{FMC} = \prod_{ij} \frac{P_{ij}\left(N_{exp}, N_{adj}\right)}{P_{ij}\left(N_{adj} = N_{exp}\right)} = \prod_{ij} \left(\frac{N_{adj}^{ij}}{N_{exp}^{ij}} \right)^{N_{exp}^{ij}} e^{N_{exp}^{ij} - N_{adj}^{ij}} \ , \tag{9.9}$$

where N_{exp}^{ij} is still the MC expectation for the set of fit parameters in question, and N_{adj}^{ij} is the adjusted expectation value. Equation (9.8) now becomes

$$\Lambda = \prod_{ij} \left(\left(\frac{N_{exp}^{ij}}{N_{obs}^{ij}} \right)^{N_{obs}^{ij}} e^{N_{obs}^{ij} - N_{exp}^{ij}} \times \left(\frac{N_{adj}^{ij}}{N_{exp}^{ij}} \right)^{N_{exp}^{ij}} e^{N_{exp}^{ij} - N_{adj}^{ij}} \right) . \tag{9.10}$$

Just as the values values N_{exp}^{ij} are the sum of the background components, so are those of N_{adj}^{ij}, and each component is adjusted individually in maximizing the product of likelihood ratios of Eq. (9.10). This technique also allows for adjustments to bins that have an expectation of zero events. The Poisson probability for observing any number of events with an expectation of zero, is zero. However, in the case of a limited-statistics MC sample, the expectation value of zero may be the result of a statistical fluctuation, and the probability of observing an event is actually non-zero.

The inclusion of the limited-statistics MC sample correction requires the MC to be adjusted to maximize the likelihood in each bin for each set of fit parameters. This added level of complexity is reduced by the fact the bin-to-bin statistical fluctuations are decoupled from all other bins, such that

$$N_{adj}^{ij} = \sum_{b} N_{adj}^{ijb} \tag{9.11}$$

can be calculated on a bin-by-bin basis for a given N_{obs}^{ij} and set of N_{exp}^{ijb}. This is accomplished by finding the N_{adj}^{ij}'s that maximize each bin in Eq. (9.10) by using Newton's Method, before calculating the product.

Penalty Terms

Fit parameter values correspond to physical quantities that are constrained by external data. Penalty terms are used to incorporate the constraints of the external data into the χ^2 calculation. The external data for each fit parameter, p, is usually described by a Gaussian function with a mean p_0 determined from the World's data and a width, σ_p, reflecting the associated uncertainty. The likelihood that a deviation $\delta_p = |p - p_0|$ in parameter p from the mean, p_0, is consistent with the uncertainty, σ_p, in p is given by the expression

$$\mathcal{L} = P_p\left(\delta_p, \sigma_p\right) = Ae^{-\frac{1}{2}\left(\frac{\delta_p}{\sigma_p}\right)^2} \ . \tag{9.12}$$

The likelihood ratio, Λ_{PT}, compares this probability to the maximum probability, which occurs when $\delta_p = 0$. The likelihood ratio for all fit parameters agreeing with external data is then

$$\Lambda_{PT} = \prod_p \frac{P_p\left(\delta_p, \sigma_p\right)}{P_p\left(\delta_p = 0, \sigma_p\right)} = \prod_p \frac{Ae^{-\frac{1}{2}\left(\frac{\delta_p}{\sigma_p}\right)^2}}{Ae^{-0}} = \prod_p e^{-\frac{1}{2}\left(\frac{\delta_p}{\sigma_p}\right)^2} \ . \tag{9.13}$$

Thus the likelihood ratio for the observed data resulting from a given set of fit parameters, p, applied to the MC is

$$\begin{aligned} \Lambda = \prod_{ij} \Bigg(\left(\frac{N_{exp}^{ij}}{N_{obs}^{ij}}\right)^{N_{obs}^{ij}} e^{N_{obs}^{ij} - N_{exp}^{ij}} \\ \times \left(\frac{N_{adj}^{ij}}{N_{exp}^{ij}}\right)^{N_{exp}^{ij}} e^{N_{exp}^{ij} - N_{adj}^{ij}} \Bigg) \times \prod_p e^{-\frac{1}{2}\left(\frac{\delta_p}{\sigma_p}\right)^2} \ . \end{aligned} \tag{9.14}$$

The χ^2 Function

The χ^2 is calculated as a function of the likelihood ratio via Eq. (9.3). This expression must be minimized to find the corresponding maximum of the likelihood ratio. The expression for Λ from Eq. (9.13) is substituted back into Eq. (9.3) and the following expression is obtained:

$$\chi^2 = -2\ln\left[\prod_{ij}\left(\left(\frac{N_{exp}^{ij}}{N_{obs}^{ij}}\right)^{N_{obs}^{ij}} e^{N_{obs}^{ij}-N_{exp}^{ij}} \times \left(\frac{N_{adj}^{ij}}{N_{exp}^{ij}}\right)^{N_{exp}^{ij}} e^{N_{exp}^{ij}-N_{adj}^{ij}}\right) \times \prod_p e^{-\frac{1}{2}\left(\frac{\delta_p}{\sigma_p}\right)^2}\right] . \tag{9.15}$$

After propagating the natural log through Eq. (9.15) the final expression for the χ^2 is

$$\chi^2 = 2\sum_{ij}\left[\left(\ln\frac{N_{obs}^{ij}}{N_{exp}^{ij}} - 1\right)N_{obs}^{ij} + N_{exp}^{ij} + \left(\ln\frac{N_{exp}^{ij}}{N_{adj}^{ij}} - 1\right)N_{exp}^{ij} + N_{adj}^{ij}\right] + \sum_p\left(\frac{\delta_p}{\sigma_p}\right)^2 . \tag{9.16}$$

Covariance Matrix

Relation (9.16) assumes the fit parameters to be uncorrelated. That is not necessarily the case, and a more general formulation, which can be derived in a similar fashion, is required. In the χ^2 expression above, the last term is to be modified according to

$$\sum_p\left(\frac{\delta_p}{\sigma_p}\right)^2 \rightarrow \sum_{p_i,p_j}\epsilon_{ij}\frac{\delta_i\delta_j}{\sigma_i^2\sigma_j^2}\sigma_{ij} , \tag{9.17}$$

where the covariance matrix is constructed such that

$$\sigma_{ij} \;=\; \sigma_i \sigma_j \;, \tag{9.18}$$

and ϵ_{ij} is defined as

$$\epsilon_{ij} \;=\; \begin{cases} 1 & : i = j \\ -1 & : i \neq j \end{cases} \;, \tag{9.19}$$

such that diagonal terms are positive and off-diagonal terms have a negative sign.

9.4 Extraction of the Coherent NC(π^0) Event Rate

The ultimate purpose of the fitting procedure is to measure the coherent NC(π^0) event rate. The selected sample consists of both signal and background events. To measure the number of signal events the background event rates must be accurately estimated and subtracted from the selected sample. The fitting procedure adjusts the background MC Angle-vs-Energy distribution to match the data in the sidebands of the selected sample and the near-PID sample. The best-fit values for the fit parameters are determined by minimizing the χ^2, and are used to estimate the event rate of each class of background events across the entire selected sample. The best-fit background event rate is determined by applying the best-fit values for the fit parameters to their respective background Angle-vs-Energy distributions in a bin-by-bin fashion. Effective fit parameters scale the total number of events in a sample, and the

same factor is applied to each bin. Systematic fit parameters adjust the shape of the Angle-vs-Energy distribution, and a different scaling factor is applied to each bin. However, the systematic fit parameter scale factors in each bin are constrained by the shape changes induced by reweighting the Angle-vs-Energy spectrum to fluctuations of the systematic error sources.

The number of events from the standard MC in bin ij, from background b, is N_{ijb}^{SMC}. Each N_{ijb}^{SMC} is scaled by an effective fit parameter, n_b, which is constant for all bins, and the combined systematic scale factor, s_{ijb}. The value for each s_{ijb} factor is the product of fractional changes to the bin contents induced by the best-fit values of each of the systematic fit parameters. There is a different value of s_{ijb} for each bin of the Angle-vs-Energy histogram, and for each background category.

The predicted number of background events, N_{ij}^{Bkg}, in bin ij, is the sum of the scaled values of N_{ijb}^{SMC} over the five background categories (NC DIS, NC resonance production, CC-ν_μ DIS, CC-ν_μ resonance production, and CC-ν_e),

$$N_{ij}^{Bkg} = \sum_b (n_b)\,(s_{ijb})\,N_{ijb}^{SMC} \ . \tag{9.20}$$

The values of n_b are the same for the NC and CC-ν_μ DIS samples and for the NC and CC-ν_μ resonance production samples, but the values for s_{ijb} differ for each event class. The number of signal events in each bin is then,

$$N_{ij}^{Coh} = N_{ij}^{Data} - N_{ij}^{Bkg} = N_{ij}^{Data} - \sum_b (n_b)\,(s_{ijb})\,N_{ijb}^{SMC} \ . \tag{9.21}$$

Here N_{ij}^{Data} is the number of data events in bin ij, where the data can be mock data, or real data. The background subtraction yields a count of selected signal events per bin. To recover the total number of interactions that occurred in

the Near Detector over the neutrino exposure, the acceptance (efficiency) corrections discussed in Chapter 3.4 need to be applied. In general, the measured number of signal events in the selected sample is divided by the MC prediction for the number of selected signal events and multiplied by MC prediction for the total events rate. However, this simple correction introduces large uncertainties related to the uncertainty on the coherent model as expressed in Eq. (9.1). Instead, a series of acceptance corrections are applied that limit the reliance on the coherent model, and reduce the uncertainty propagated to the result.

The acceptance correction should be a function of the selection algorithm, not the coherent model. To remove the model dependence, the acceptance correction is applied bin-by-bin via an efficiency function,

$$\epsilon_s^{ij} = \frac{N_{sel}^{ij}}{N_{tot}^{ij}} \ , \tag{9.22}$$

where N_{sel}^{ij} is the number of coherent NC(π^0) MC events in bin ij in the selected sample and N_{tot}^{ij} is the number of coherent NC(π^0) events in bin ij in the total MC sample. The values for ϵ_s^{ij} are displayed in Fig. 9.5.

Some bins have an efficiency of zero, and their contribution to the total event rate cannot be accounted for with this method. A second overall correction efficiency, ϵ_o, is applied to the the sum of the bin-by-bin, acceptance-corrected event rates to account for bins where $\epsilon_s^{ij} = 0$. The value and associated uncertainty for ϵ_o also incorporates the detection efficiency, ϵ_o, i.e. the ratio of the number of reconstructed coherent NC(π^0) events to the total number of coherent NC(π^0) interactions in the Near Detector, as estimated by MC. The detection efficiency was found to be 1.0 with an uncertainty of -0.05%. The

overall efficiency can be expressed as

$$\epsilon_o = \epsilon_d \left(\frac{\sum_{ij}^{\epsilon_s^{ij}>0} N_{sel}^{ij}}{\sum_{ij} N_{tot}^{ij}} \right) . \tag{9.23}$$

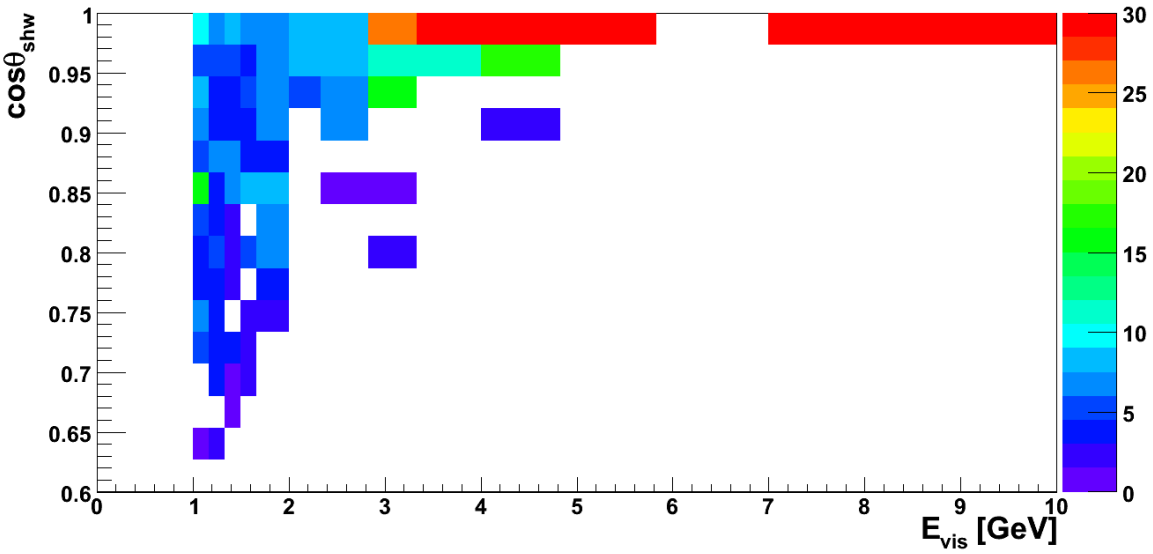

Figure 9.5: The bin-by-bin acceptance correction factors (the inverse of the bin-by-bin efficiency) as a function of Angle-vs-Energy. These correction factors are applied to bins with an Energy below 3.3 GeV. The bins above 3.3 GeV are combined into a single correction factor to reduce the associated error contribution. Bins with an acceptance (efficiency) of zero are corrected for in a similar fashion.

The uncertainty on the bin-by-bin acceptance corrections are evaluated by calculating the statistical error on each bin of ϵ_s^{ij}. The error propagated to the final result from the bin-by-bin acceptance correction for a single bin is a function of the statistical error on the efficiency in the bin, the number of measured events in the bin, and magnitude of the correction. Bins above an Energy threshold of 3.33 GeV, have relatively large uncertainties coupled with corrections of greater than 20 to 1. To reduce the total error propagated to

the result these bins are not corrected for on a bin-by-bin basis, and instead are absorbed into the overall acceptance correction. The overall acceptance correction is then redefined as

$$\epsilon_o = \epsilon_d \left(\frac{\sum_{ij}^{\epsilon_s^{ij}>0} N_{sel}^{ij} - \sum_{ij}^{i>M} N_{sel}^{ij}}{\sum_{ij} N_{tot}^{ij}} \right) , \tag{9.24}$$

where M is the value of the Energy index, i, corresponding to bins with a minimum Energy of 3.33 GeV. The acceptance corrected coherent NC(π^0) event rate is then expressed as

$$N^{Coh} = \frac{1}{\epsilon_o} \sum_{ij}^{i<M} \frac{1}{\epsilon_s^{ij}} \left(N_{ij}^{Data} - \sum_b \left(n_b\right) \left(s_{ijb}\right) N_{ijb}^{SMC} \right) . \tag{9.25}$$

The largest single contribution to the overall efficiency is from events with a final-state pion energy below 1.0 GeV. These events, which account for more than 40% of the predicted event rate, are excluded from the analysis, and thus induce a large correction. The second largest contribution is from the events at high energy, where the uncertainty from the bin-by-bin correction is large. The uncertainty on the overall acceptance corrections is evaluated by considering an alternative coherent model. The Berger-Sehgal model for coherent interactions [3] was introduced, and used to reweight the coherent NC(π^0) events sample. Details of the model and the reweighting scheme are discussed in Chapter 10.1. Studies based on the application of acceptance corrections derived from an alternate coherent model revealed several interesting aspects.

The first aspect was that the uncertainty on the number of events below 1.0 GeV is large, and when these events are included in the analysis the error

from ϵ_o propagated to the final result is roughly 20%. Excluding these events reduces the error significantly, and is necessary to attain a useful result. The analysis thus becomes a measurement of the cross section for coherent NC(π^0) interactions that produce a final-state π^0 with an energy above 1.0 GeV. An additional correction for the number of events with a true pion energy below 1.0 GeV, and a reconstructed pion energy above 1.0 GeV, and vice versa, must now also be included.

To ensure that the minimum uncertainty is propagated to the result from the acceptance correction, the contributions from the bin-by-bin statistical uncertainties, from the alternate model uncertainties from each bin of the bin-by-bin efficiency, and from the overall efficiency were considered together. Bins were moved in and out of the overall efficiency, and the total uncertainty propagated to the result was calculated for each permutation. The 3.33 GeV energy cutoff for bins to be included in the overall efficiency yielded an uncertainty of just under 5%; very close to the minimum value. The overall efficiency is 79%, and the combined acceptance correction contributes an uncertainty of 5% to the measurement of the coherent NC(π^0) event rate.

Chapter 10

Systematic Uncertainties

10.1 Sources of Systematic Uncertainty

The systematic error sources for the measurement of the coherent NC(π^0) event rate originate with the uncertainties in the physics modelling of neutrino interactions for the events in the selected MC sample, and from the modelling of the detector response to the interactions. The following section reviews in detail, the various error sources as applied to the signal and the three background categories.

Source of Uncertainty for Each Background

The selected NC event sample incurs uncertainties from several sources. The hadronization model, which determines the identity and four-momenta of the final-state particles in the hadronic shower, is known to have large uncertainties. Tables 6.2 and 6.3 imply that a large fraction of the selected MC

events include pion or nucleon absorption. This indicates that the intranuclear rescattering model (Intranuke) is frequently invoked for the generation of selected events. Consequently, uncertainties in its implementation must be taken into account. Additionally, NC cross sections are less constrained by the World's data than are those for CC events, especially for DIS interactions. Lastly, there is uncertainty in the energy scale, i.e. the conversion from the light output measured in the ND to the visible energy in GeV. This arises from calibration errors, uncertainty in assumptions in the intranuclear re-scattering model, and uncertainties in the detector response as measured by the MINOS Calibration Detector (CalDet).

The uncertainties on the selected CC-ν_μ sample arise from the same sources as the uncertainties on the selected NC sample, however the cross sections are better constrained. Additionally, the selected CC-ν_μ event rate is roughly 10% of the NC sample, and the events occupy the same region in the Angle-vs-Energy plane, so their contribution to the total uncertainty for the number of background events in the selected sample is relatively small.

The uncertainties on the selected CC-ν_e sample, as compared to the uncertainties on the NC and CC-ν_μ are relatively small; the largest due to the $\pm$20% uncertainty on the ν_e event rate. The selected sample is quasi-elastic-like so there are no visible hadronic showers, and the only detectable particle is the final-state electron. Therefore, uncertainties in the hadronization and the intranuclear rescattering models are not propagated to the selected CC-ν_e sample. As with the selected CC-ν_μ sample, the event rate is only about 10% of the NC rate. However, the CC-ν_e events occupy a distinct region of the Angle-vs-Energy plane, so uncertainties on the shape of the CC-ν_e Angle-vs-Energy distribution can have a more pronounced effect on fit results than do

uncertainties of the CC-ν_μ distribution.

The Hadronization Model

The hadronization model used in NEUGEN3 is known to have large uncertainties [37]. Most of the uncertainties stem from a lack of available data in the kinematic regions accessed by the neutrinos in the MINOS experiment. In-depth studies on the effect of these uncertainties on MC predictions were conducted by the $\nu_\mu \rightarrow \nu_e$ oscillation analysis (ν_e) Working Group [37]. The complexity of the hadronization model does not allow for an exact reweighting. Instead, a reweighting scheme developed by the ν_e Working Group determines event weights as a function of the EM shower fraction, the invariant hadronic mass (W), and the shower transverse momentum (p_t). Six sources of uncertainty for the hadronization model have been identified, and are described in brief below.

- Baryon x_f Selection (t1) - Based on Parton model arguments the KNO model in NEUGEN3 assumes that the baryon will be found in the backward hemisphere. This assumption is removed, and four-vectors are generated in the center-of-mass according to phase space decay.

- Probability of π^0 Selection (t2) - External data suggests that 30% of produced mesons will be neutral pions. A +30% variation on this quantity has been assumed changing the probability of selecting a neutral pion to 39%.

- Charged-Neutral Particle Multiplicity Correlation (t3) - The AKGY model in NEUGEN3 independently selects neutral and charged particle multiplicities. This does not reproduce the charged particle topological cross

sections. Correlations for particle multiplicity selection have been included in such a way as to improve the agreement between the hadronization model and data.

- Implementation Ambiguities (t4) - There are differences in the implementation of the hadronization model in NEUGEN3 and GENIE [11]. Here the GENIE version of the implementations are used.

- Transverse Momentum (p_t) Squeezing (t5) - A transverse momentum squeezing parameter in the remnant system decay has a default value of -3.5. This value is shifted to -1.5, resulting in broader showers.

- Isotropic Two-Body Decays (t6) - NEUGEN3 assumes that all two-body decays are isotropic. Here it is assumed that all two-body decays occur at an angle of 90° with respect to the momentum transfer direction.

The Intranuclear Re-scattering Model (Intranuke)

The intranuclear rescattering model is used to propagate interaction products through the nucleus. Several of the input parameters can be adjusted and the results propagated to the selected MC samples via a reweighting scheme [36]. These parameters can be grouped into two categories.

The first is the relative rates for the possible intranuclear processes. The numbers following each item are the ± 1 σ errors used in the studies carried out for the initial MINOS $\nu_\mu \rightarrow \nu_\tau$ oscillation analysis, and are also applied here, in the coherent NC(π^0) analysis.

- INS01 and INS02 - π Charge Exchange ($\pm 50\%$)

- INS03 and INS04 - π Elastic Scattering ($\pm$10%)
- INS05 and INS06 - π Inelastic Scattering ($\pm$40%)
- INS07 and INS08 - π Absoption ($\pm$30%)
- INS09 and INS10 - $\pi \rightarrow 2\pi$ ($\pm$20%)
- INS11 and INS12 - Nucleon Knockout ($\pm$20%)
- INS13 and INS14 - $N \rightarrow N + \pi, N \rightarrow N + 2\pi$ ($\pm$20%)

The second category of parameters relate to the cross sections for the possible intranuclear interactions.

- INS15 and INS16 - Formation Time ($\pm$50%)
- INS17 and INS18 - π Cross Section ($\pm$10%)
- INS19 and INS20 - Nucleon Cross Section ($\pm$10%)

The INSXX labels identify the Intranuke systematic error sources in the table below. The odd numbered labels refer to -1 σ fluctuations, while the even numbered labels refer to +1 σ fluctuations. The formation time determines whether or not an outgoing hadron can interact within the nucleus. As the energy of an outgoing hadron increases, so does the distance traveled before the particle emerges as a completely formed hadron having its full scattering capability. Beyond a certain energy cutoff determined by the value of the formation time, a particle will form outside the nucleus and have zero probability of intranuclear rescattering. Thus, adjustments to the formation time result in changes to the energy cutoff for invocation of the intranuclear rescattering model.

A few of the Intranuke assumptions have uncertainties for which reweighting is not feasible. These errors are propagated via the uncertainty on the energy scale [38].

The Energy Scale and Detector Model Systematics

These systematic error sources include uncertainties in the beam simulation (SKZP), in the detector simulation, in the detector calibration, and in the hadronic and the electromagnetic energy scales. Of these, only the uncertainties in the EM energy scale and uncertainties in the calibration contribute to the overall error budget. The uncertainty in the EM energy scale ($\pm 5.6\%$) results from the aforementioned assumptions made in Intranuke ($\pm 5.1\%$), and the uncertainties in the detector response to EM showers ($\pm 2.0\%$) as measured by CalDet [38].

There are several calibration error sources, described in Appendix E, that can affect the analysis. These calibration errors are difficult to reweight for, and full MC samples must be generated to study them. This approach was not feasible for the coherent NC(π^0) analysis due to the large MC sample size needed to generate a statistically significant selected sample. The calibration errors are therefore not included in the fitting package. However, based on studies done by the ν_e Working Group it was determined that, *i*) the systematic uncertainties resulting from systematic errors sources measured by the coherent NC(π^0) analysis induced similar responses in the $\nu_\mu \rightarrow \nu_e$ oscillation analysis, and that *ii*) the contributions to the uncertainty from the calibration errors were relatively small compared to the effect of uncertainties propagated from the hadronization model, and the EM energy scale [32].

Based on these points, calibration uncertainties are accounted for by adding, in quadrature, the ν_e Working Group estimates for the calibration errors to the overall uncertainty on the coherent NC(π^0) cross section. Tables of ND systematic errors ([32] p223) prepared by the ν_e Working Group show the uncertainties introduced by calibration errors propagated to the $\nu_\mu \rightarrow \nu_e$ oscillation analysis result. Table 10.1 reproduces these results for the calibration error sources that effect the Near Detector, which contribute roughly 5% to the overall error budget. To be conservative in the application of these numbers to the coherent NC(π^0) analysis the errors from these sources are assumed to be 10%. For comparison, the ν_e Working Group's evaluation of the hadronization model systematic error sources gives comparable results to the estimates carried out independently for this work, in both the absolute and relative magnitudes of the systematic uncertainties induced in the analyses. This can be seen by comparing columns 3, 4, and 5 with column 6 in Table 10.1.

Uncertainties on the MRCC correction factors are also taken into account. A systematic error reweighted sample is generated by randomly varying each of the applied MRCC correction factors within their statistical uncertainties.

Cross Section Models

The largest uncertainties in the cross section model come from the uncertainty *i*) in the axial mass used in (quasi)-elastic (M_A^{QE}) cross sections, *ii*) in the axial mass used in resonance production (M_A^{Res}) cross sections, and *iii*) in the treatment of the resonance production to DIS transition region [35]. Only the CC-ν_e sample contains (quasi)-elastic events, and changes to M_A^{QE} do not significantly effect the Angle-vs-Energy distribution for that sample. Uncertainties in M_A^{QE} are absorbed into the $\pm 20\%$ uncertainty on the ν_e event rate

	Systematic Uncertainty Source	Fractional Error (ν_e)			Fractional Error (Coherent NC(π^0))
		NC	CC-ν_μ	CC-ν_e	
Calibration	Gains	2.1%	2.2%	3.4%	-
	Attenuation	0.4%	0.2%	0.8%	-
	Strip to Strip	0.6%	0.2%	0.6%	-
	Linearity	0.2%	0.1%	0.2%	-
	Low Pulse Height Hits	1.8%	0.6%	0.4%	-
Hadronization	t1	21.3%	23.0%	2.7%	25.7%
	t2	8.5%	7.9%	0.8%	8.2%
	t3	13.7%	9.4%	1.5%	16.4%
	t4	7.0%	5.5%	0.8%	9.9%
	t5	5.7%	6.1%	0.7%	8.6%
	t6	6.1%	6.8%	1.1%	13.6%

Table 10.1: Magnitude of the fractional uncertainties on the ND event rates due to uncertainties in the calibration from the ν_e analysis. Detailed explanations of the calibration related systematic error source can be found in Appendix E. For comparison, uncertainties on the ND event rates from the hadronization model on both the ν_e analysis and the coherent NC(π^0) analysis are included. The agreement of the magnitudes of the hadronization model errors for the $\nu_\mu \rightarrow \nu_e$ oscillation analysis and the coherent NC(π^0) analysis suggests that the use of the $\nu_\mu \rightarrow \nu_e$ oscillation analysis calibration errors is sufficient.

and not included in the systematic error analysis. There is a significant fraction of resonance events in the NC and CC-ν_μ samples, especially between 1.0 to 2.0 GeV. The uncertainty on M_A^{Res} leads to sizable fluctuations in the number of events in the resonance samples. For this reason the NC and CC-ν_μ backgrounds require separate fit parameters for the resonance and DIS contributions to the event samples. The behavior of the KNO model in the transition region is controlled by a series of parameters, r_{ijk}. These parameters control the fraction of the low-multiplicity DIS cross section that needs to be removed in order to avoid double counting with the resonance production cross section, in the invariant mass regime where both processes contribute. There are 16 r_{ijk} parameters, one for each of the low multiplicity channels; $i = 1$ indicates a CC interaction while $i = 2$ refers to a NC reaction, j indicates either a neutrino or antineutrino interaction with either a proton or neutron, and k refers to a final state multiplicity of either two or three. The adjusted cross section parameters and the corresponding $\pm 1\sigma$ uncertainties suggested by the authors of NEUGEN3 are as follows:

- M_A^{Res} ($\pm 15\%$)
- r_{1j2}^{kno} ($\pm 100\%$)
- r_{2j2}^{kno} ($\pm 200\%$)
- r_{1j3}^{kno} ($\pm 100\%$)
- r_{2j3}^{kno} ($\pm 200\%$)

Uncertainties on the Coherent Model

Rein and Sehgal [5] suggest a 50% uncertainty on the cross sections calculated using their model. There is no clear experimental evidence to the contrary for interactions involving neutrino energies above a few GeV and on high A nuclei. To further constrain the coherent NC(π^0) cross section the Berger-Sehgal [3] model was introduced. The model for the coherent interaction is relatively simple, and an exact reweighting scheme is possible. Coherent events are generated without the use of the hadronization model or Intranuke, and the four-vectors of all final-state particles can be determined exactly. The Berger-Sehgal cross section for an existing MC event can be calculated based on the truth information in the stdhep record. This cross section can then be compared with the NEUGEN3 (Rein-Sehgal) cross section and an exact event weight can be calculated for each MC event. The Berger-Sehgal model has been incorporated into NEUGEN3 for use in such a reweighting scheme.

The model differences between the Berger-Sehgal model and the Rein-Sehgal model, highlighted in Chapter 1.5, can be broken out into three parts: *i*) differences in the kinematic terms and the calculation of $|t|$ arise from the Rein-Sehgal assumption of an infinitely heavy nucleus; *ii*) the pion-nucleus scattering term is calculated differently for the two models; and *iii*) the value of M_A shifts from 1.0 GeV in the Rein-Sehgal model to 0.95 GeV in the Berger-Sehgal model. The changes from the Rein-Sehgal model to the Berger-Sehgal model were implemented in a piecewise manner, and then as an entire set. Cross section weights were also calculated for a Regge model which was used by Rein and Sehgal as a comparison to their model. Finally, cross section weights were calculated for a shift in the value of M_A from 1.0 GeV to 1.2 GeV, the value used in the MC generators for the MiniBooNE and SciBooNE ex-

periments [18][19]. The change to the selected and total number of predicted coherent NC(π^0) events for the five sets of cross section weights are shown in Table 10.2.

Coherent Model	Coherent NC(π^0) Selected Events	Percent of RS Prediction	Coherent NC(π^0) Total Events	Percent of RS Prediction
Rein-Sehgal (RS)	1044	100%	13904	100%
Berger-Sehgal (BS)	1519	145%	19722	142%
Regge	971	93%	15475	111%
RS w/ BS Kin.	1279	123%	15819	114%
RS w/ BS π Scatt.	1278	122%	17615	127%
$M_A = 1.2$ GeV	1118	107%	14784	106%

Table 10.2: Predictions for the coherent NC(π^0) event rate for 2.8×10^{20} POT in the MINOS Near Detector for various coherent models as compared with the Rein-Sehgal model. The Berger-Sehgal reweighted MC predicts 45% more events than the standard MC in the selected sample.

The full implementation of the Berger-Sehgal model produces the largest change to the number of expected coherent NC(π^0) events, however that change is fairly consistent between the pre-selected and selected samples implying that the changes to the shape of the Angle-vs-Energy spectrum are relatively small. The individual changes of the kinematic and pion-nucleon scattering portion of the models produces increases of roughly 20% in the selected sample but differ from that by 5% to 10% in the total number of predicted signal events. This implies that a greater change in the shape of the Angle-vs-Energy distribution is induced by these individual model changes. As expected, increasing M_A moderately increases the cross section but does not affect the shape of the Angle-vs-Energy distribution. The Regge model changes the cross section moderately as well, but has a relatively large effect on the shape of the Angle-vs-Energy distribution.

10.2 Individual Systematic Error Studies

For each of the systematic error sources described in the previous Section, either one or two reweighted MC samples were created. The samples were created by altering a single input parameter to the MC by the $\pm 1\ \sigma$ uncertainty on that parameter. In general, this was done using a reweighting scheme, as it is not practical to regenerate the entire MC sample for each systematic error source. Standard error analysis techniques require that the measurement of the cross section be carried through using each of the reweighted MC samples, and that the uncertainty on the results be the quadrature sum of the variations in the measured cross section. For the measurement of the coherent NC(π^0) cross section the resulting error bars would be exceedingly large.

Instead, the fitting procedure attempts to reduce the error by adjusting the MC to the data. The estimate of the total systematic uncertainty is carried out through a series of mock data studies detailed in Chapter 11. First the effect of each individual systematic error source must be evaluated. To this end Angle-vs-Energy histograms from each of the reweighted MC samples were compared to the Angle-vs-Energy distribution of the standard MC to determine how each systematic can effect the measurement of the coherent NC(π^0) event rate. The most straightforward way to compare the two distributions is to fit the standard MC to the reweighted MC. In this way the reweighted MC is treated like data, and will be referred to as Single Systematic Mock Data, or SSMD. The fits to SSMD samples do not include any systematic fit parameters, nor are any penalty terms included in the χ^2 calculation. Also of note, statistical fluctuations are not included in the production of SSMD event samples.

A demonstration of the fitting procedure as applied to the M_A^{Res} $+1\ \sigma$ reweighted

SSMD is shown in Figures 10.1 through 10.4. Displayed are the Angle projections of the Angle-vs-Energy histograms that are used in the fits. The fitting procedure starts with the Angle-vs-Energy histograms of the reweighted SSMD selected sample, and the backgrounds broken out by reaction category. Figure 10.1 displays the Angle projection of the bins in the sideband region, where the fits are performed.

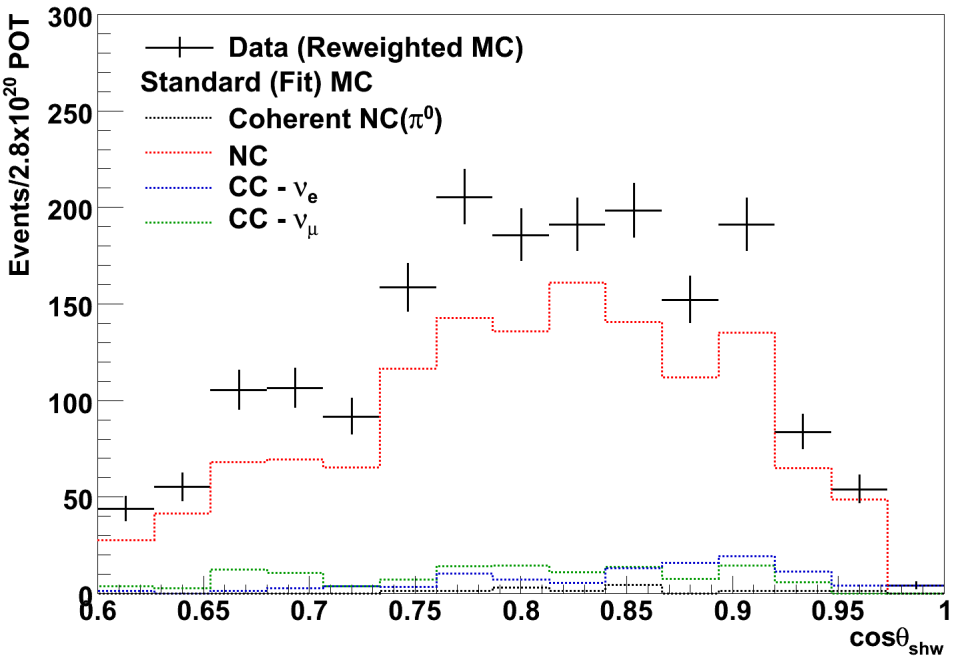

Figure 10.1: Angle projections of the sideband region of the Angle-vs-Energy histogram for the SSMD reweighted with M_A^{Res} increased by $+1\ \sigma$ and for the three standard MC backgrounds. The Angle-vs-Energy histograms are inputs to the fit.

The backgrounds are adjusted by the effective fit parameters such that the sum of the background distributions best match the SSMD distribution in the sideband. The red (NC), green (CC-ν_μ) and blue (CC-ν_e) curves in Fig. 10.2 show the best-fit backgrounds in the sideband, and the magenta curve is the sum of the three background distributions. There is only a small contribution from the signal in the sideband, and it is expected that the sum of the best-fit

backgrounds should be fairly close to the SSMD. However, the degree to which the backgrounds match the data in Fig. 10.2 is indicative of a good fit. This is reinforced by a χ^2/ndf value of 0.022. (It should be noted that there are no statistical differences between the SSMD and fit MC samples, so the reduced χ^2 should be compared with zero instead of one.)

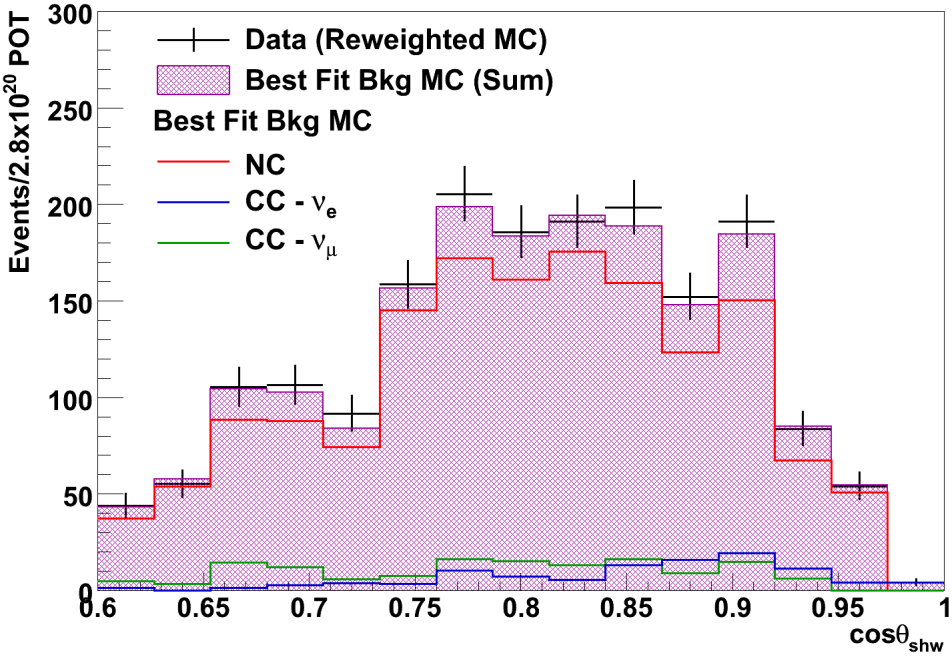

Figure 10.2: Angle projections of the sideband region of the Angle-vs-Energy histogram for the SSMD reweighted with M_A^{Res} increased by $+1$ σ, for the three best MC backgrounds, and for the sum of the best-fit MC backgrounds. The sum of the backgrounds and the SSMD sample distributions are in good agreement.

The best-fit values for the fit parameters are used to calculate the background distributions in the signal region. Fig. 10.3 displays the Angle projections over the entire Angle-vs-Energy plane. Bins in the signal region are expected to contain signal events, and the data distribution and the total MC distribution are no longer expected to match.

The difference between the SSMD and the sum of the best-fit backgrounds

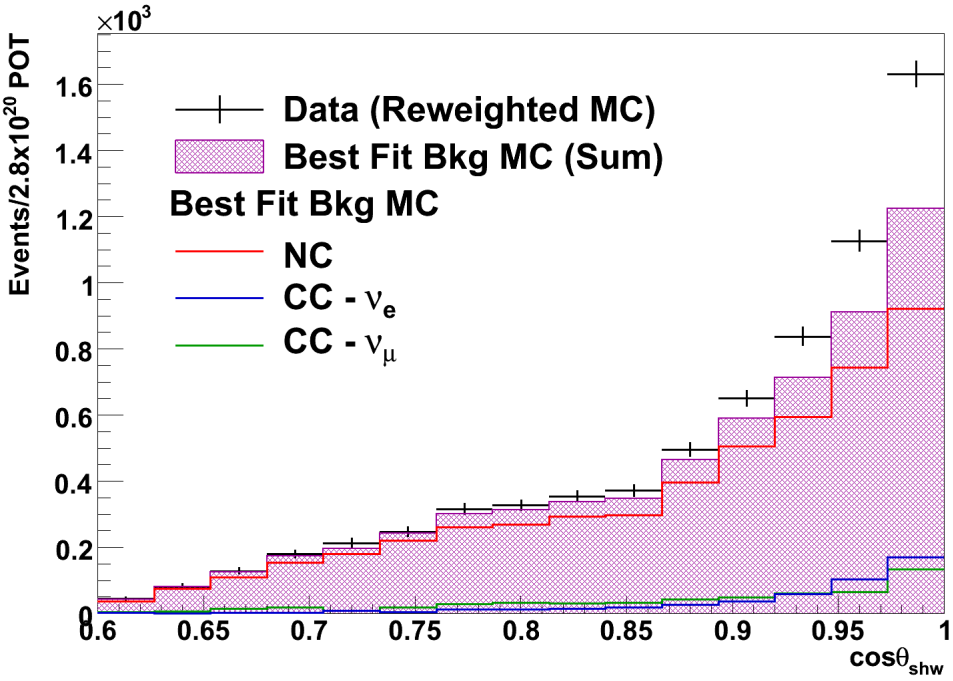

Figure 10.3: Angle projections of the Angle-vs-Energy histogram for the SSMD reweighted with M_A^{Res} increased by $+1$ σ, for the three best-fit MC backgrounds and for the sum of the best-fit MC backgrounds. The sum of the backgrounds matches the SSMD at large angles where the contribution from the signal is minimal.

is the selected sample events rate measured by the fit, and is displayed by the solid black histogram in Fig. 10.4. This can be compared with the dashed black histogram which displays the actual event rate in the SSMD. The results are very close suggesting that the effective fit parameters are able to absorb the shape changes to the Angle-vs-Energy histogram induced by +1 σ shift in M_A^{Res}.

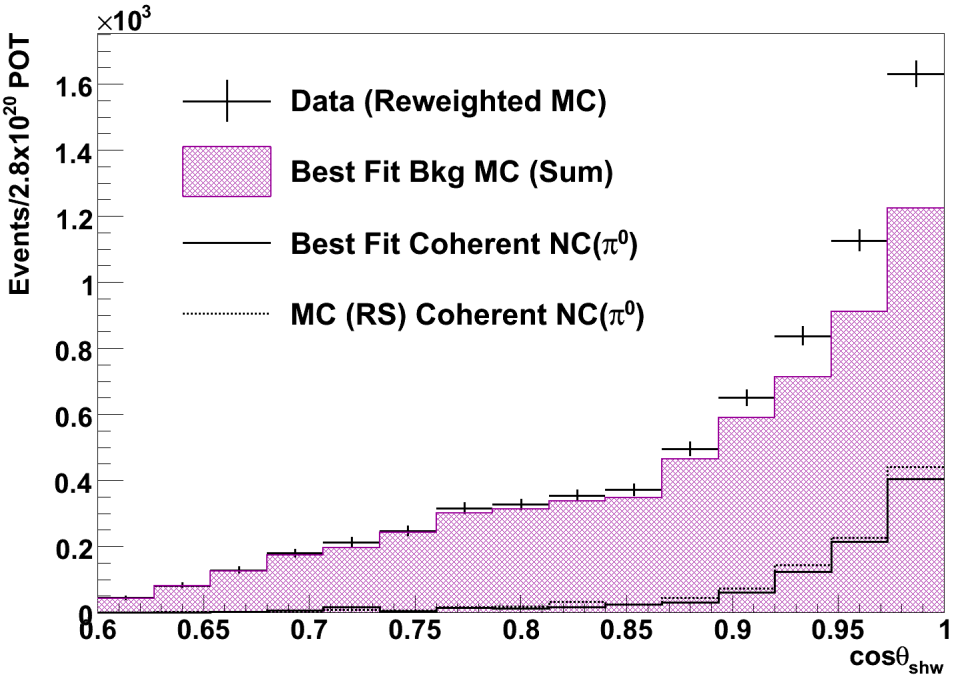

Figure 10.4: Angle projections of the Angle-vs-Energy histogram for the SSMD reweighted with M_A^{Res} increase by +1 σ and the sum of the best backgrounds. The difference between the two is the measured coherent NC(π^0) event rate (solid histogram), which can be compared to the Rein-Sehgal prediction (dashed histogram).

An example of a systematic error source that may require the addition of a systematic fit parameter to the fitting procedure is the EM energy scale. The Angle projections of the Angle-vs-Energy histogram for the SSMD sample created by shifting the EM energy scale by +1 σ along with the best-fit backgrounds and the resulting coherent NC(π^0) event rate are shown in Fig. 10.5.

The fit for the EM energy scale SSMD sample resulted in a reduced χ^2 value of 3.35, and the measured event rate does not match the number of signal events in the SSMD sample. This suggests that the EM energy scale cannot be absorbed by the effective fit parameters, and requires an additional systematic fit parameter to be included in the fitting procedure.

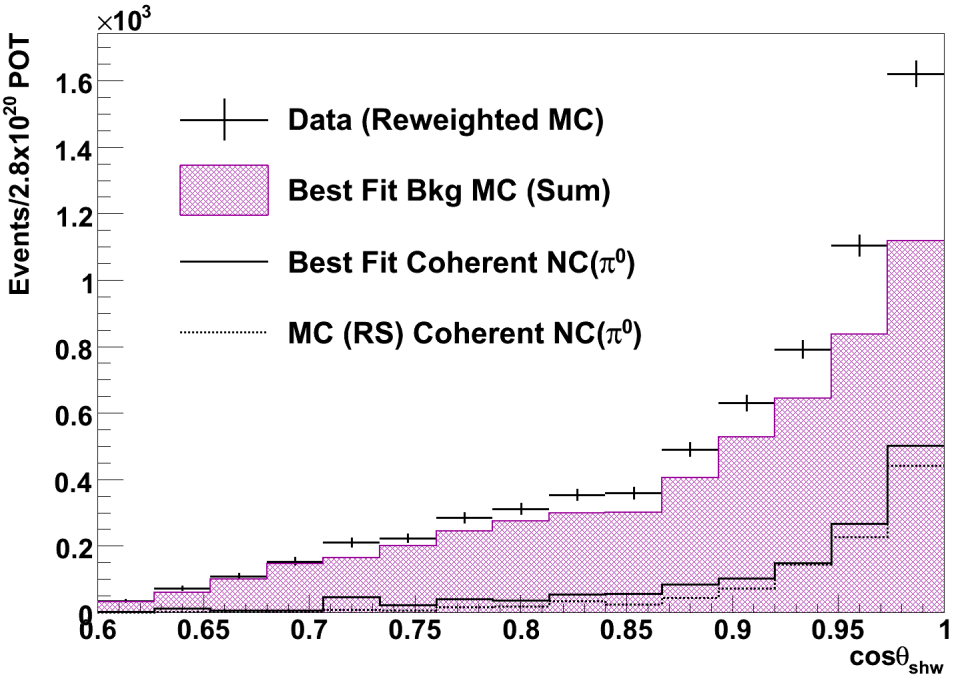

Figure 10.5: Angle projections of the Angle-vs-Energy histogram for the SSMD reweighted with the EM energy scale increase by $+1\ \sigma$ and the sum of the best background. The agreement between the measured coherent NC(π^0) event rate and the SSMD (true) event rate is poor compared to the fit to the M_A^{Res} $+1\ \sigma$ SSMD

A set of concrete criteria are necessary to evaluate the effects of each of the systematic error sources, and to decide how they should be treated in future fits. Three outputs of the fits can be used for this purpose; *i*) the goodness-of-fit via the reduced χ^2, *ii*) the best-fit values of the effective fit parameters, and *iii*) the measurement of the coherent NC(π^0) event rate. A χ^2/ndf close to zero suggests that the standard MC can be adjusted, via the effective fit pa-

rameters, to match a SSMD sample. The best-fit values for the fit parameters should have reasonable and expected values. For example changes to M_A^{Res} should induce changes in the NC/CC-ν_μ resonance fit parameter, but not the NC/CC-ν_μ DIS fit parameter, or the CC-ν_e fit parameter. Each of the systematic error sources considered in these studies can only affect the number of background events in the selected sample, and fits to the SSMD should ideally return the nominal MC value for the coherent NC(π^0) event rate.

If *i*) the best-fit χ^2/ndf is small, *ii*) the best-fit values for the effective fit parameters agree with expectations, and *iii*) the measured signal events rate is relatively close to the true value, then a systematic error source can be absorbed into the effective fit parameters. Otherwise the systematic error reweighting is assumed to change the shape of one or more of the background Angle-vs-Energy distributions and an additional systematic error source must be included in the fits to account for this systematic error source independently. The results for SSMD fit studies for each of the included systematic error sources are shown in Tables 10.3 and 10.4. The systematic error sources are ranked by the reduced χ^2. Systematic error sources with the highest ranks may require individual systematic fit parameters, while unranked systematic error sources are easily absorbed into the effective fit parameters.

In addition to providing information on how to treat each systematic error source in the fitting procedure, the fit results indicate the level to which fluctuations in the MC are reasonable given the implicit uncertainties. The results of the SSMD studies presented in Tables 10.3 and 10.4 demonstrate that the 30% data-vs-MC difference observed in Chapter 6.6 is well within the uncertainties of the MC. They also provide a way to estimate the range for reasonable best-fit values for the effective fit parameters.

Systematic Name		χ^2/ndf	Signal Ratio	NC/CC-ν_μ DIS	NC/CC-ν_μ Res	CC-ν_e	Fit Priority
Hadronization	**t1**	0.79	0.68	0.64	1.52	0.44	2
	t2	0.01	0.98	1.12	0.88	1.16	-
	t3	0.16	0.89	0.76	1.32	0.52	4
	t4	0.13	0.83	0.88	1.12	0.80	5
	t5	0.12	0.85	0.88	1.16	0.80	6
	t6	0.17	0.78	0.84	1.20	0.64	3
Cross Section	$\mathbf{M_A^{Res} + 1\sigma}$	0.02	0.84	1.04	1.72	1.00	-
	$\mathbf{M_A^{Res} - 1\sigma}$	0.00	0.96	1.00	0.88	1.00	-
	$\mathbf{r_{ij2} + 1 + 1}$	0.02	0.96	1.04	1.16	0.92	-
	$\mathbf{r_{ij2} - 1 - 1}$	0.02	0.93	0.96	0.88	1.12	-
	$\mathbf{r_{ij3} + 1 + 1}$	0.01	0.97	1.04	1.04	0.88	-
	$\mathbf{r_{ij3} - 1 - 1}$	0.01	0.92	0.96	0.96	1.12	-
Detector	$\mathbf{E_{EM} + 1}$	3.35	1.21	1.20	0.72	0.52	1
	$\mathbf{E_{EM} - 1}$	0.49	1.12	0.80	1.12	0.76	1
	skzp+1	0.00	0.97	1.04	1.04	1.08	-
	skzp-1	0.00	0.92	0.96	0.96	0.92	-
	mrcc	0.10	1.03	1.00	0.92	1.16	8

Table 10.3: Summary of systematic error sources, and the results of the corresponding SSMD studies. Each entry includes the χ^2, the signal ratio, and the best-fit values for the three effective fit parameters. The signal ratio is defined as the ratio of the measured coherent NC(π^0) event rate to the Monte Carlo prediction for the coherent NC(π^0) event rate. The last column is the "fit rank", or order in which the systematics error sources will be added to the fitting procedure. The EM energy scale and "t1" of the hadronization model produce the most prominent shape distortions to the Angle-vs-Energy distributions, as measured by the χ^2/ndf. The systematic error source related to Intranuke are included in the following table.

Systematic Name		χ^2/ndf	Signal Ratio	NC/CC-ν_μ DIS	NC/CC-ν_μ Res	CC-ν_e	Fit Priority
Intranuke	**INS01**	0.00	0.97	1.00	1.00	0.96	-
	INS02	0.00	0.92	1.00	1.00	1.04	-
	INS03	0.00	0.93	1.00	1.04	1.00	-
	INS04	0.00	0.96	1.00	0.96	1.00	-
	INS05	0.03	0.93	1.00	1.00	1.04	-
	INS06	0.03	0.96	1.00	1.00	0.96	-
	INS07	0.02	0.97	1.00	0.92	0.96	-
	INS08	0.02	0.92	1.00	1.08	1.04	-
	INS09	0.00	0.95	1.00	1.00	0.96	-
	INS10	0.00	0.94	1.00	1.00	1.04	-
	INS11	0.01	0.96	1.00	1.04	1.08	-
	INS12	0.01	0.93	1.00	0.96	0.92	-
	INS13	0.00	0.94	1.00	1.00	0.96	-
	INS14	0.00	0.95	1.00	1.00	1.04	-
	INS15	0.05	1.03	1.12	1.00	0.88	-
	INS16	0.11	0.80	0.84	1.08	0.92	7
	INS17	0.00	0.93	1.00	0.96	0.96	-
	INS18	0.00	0.95	1.00	1.04	1.04	-
	INS19	0.02	0.90	1.00	1.00	1.00	-
	INS20	0.02	0.96	1.00	1.04	1.00	-

Table 10.4: Summary of systematic error sources, and the results of the corresponding SSMD studies. Each entry includes the χ^2, the signal ratio, and the best-fit values for the three effective fit parameters. The signal ratio is defined as the ratio of the measured coherent NC(π^0) event rate to the Monte Carlo prediction for the coherent NC(π^0) event rate. The last column is the "fit rank", or order in which the systematics error sources will be added to the fitting procedure. Only ± 1 σ changes to the formation time (INS15 and INS16) produce a significant change to the MC Angle-vs-Energy distributions.

The penalty terms require nominal (mean) values and widths to define the Gaussian pdfs that constrain the fit parameters to reasonable values. The nominal values are given by the standard MC used in the fits. The external knowledge about the fit parameters that determine the widths is contained in the estimates for the $\pm 1\ \sigma$ fluctuations described in the previous Section. The fit values for systematic fit parameters are parametrized as fractions of a standard deviation, and the widths of the Gaussian pdfs are all equal to 1.0. The effective fit parameters are more complex, as they account for several systematic error sources. The SSMD studies propagate the $\pm 1\ \sigma$ fluctuations of the systematic error sources to the Angle-vs-Energy histograms, and on to the best-fit values for each fit parameter. The values of the effective fit parameters are the fractional changes to the background distribution normalizations. The width for each effective fit parameter pdf is the quadrature sum of the best-fit values for all of the systematics assumed to be absorbed by this effective fit parameter.

The widths of the pdfs to be used in the penalty terms, σ_f^2, are not necessarily symmetrical. Some of the systematic shifts only make sense in one direction, while others have non-symmetric effects. For example, shifting M_A^{Res} up by 15.0% ($+1\ \sigma$) gives a best-fit result with an 84.0% increase in the number of resonance events, while a -15.0% (-1 σ) change only produces a 4.0% reduction in the number of resonance events. Depending upon the sign of deviation of the effective fit parameter from the nominal value, δ_f, either the "positive", or the "negative" width of the pdf is used in calculating the χ^2 penalty. The

positive and negative widths are calculated separately as

$$\sigma_f^2 \;=\; \begin{cases} \sum\limits_{sys} \left(f_{sys}^{+}\right)^2 & : \delta_f > 0.0 \\ \sum\limits_{sys} \left(f_{sys}^{-}\right)^2 & : \delta_f < 0.0 \end{cases} \tag{10.1}$$

Here σ_f^2's are calculated for each effective fit parameter. The fractional changes produced by systematic, sys, where the best-fit values were greater than 1.0 are denoted by f_{sys}^{+}. Conversely, f_{sys}^{-} denote the fractional normalization changes where the best-fit values were less than 1.0. A covariance matrix is constructed from the penalty terms as indicated by Eq. (9.17), Eq. (9.18), and Eq. (9.19). Systematic error sources with individual systematic fit parameters are not included in calculating the widths for the effective fit parameter penalty terms.

Chapter 11

Estimating the Sensitivity

11.1 Mock Data Studies

Mock data studies form the basis for determining the optimal configuration of the fitting procedure and for evaluating the total systematic+statistical uncertainty on the coherent NC(π^0) event rate. Mock data samples are comprised of reweighted MC samples, where the reweighting combines contributions from each of the systematic error sources, statistical fluctuations, and fluctuations of the coherent NC(π^0) event rate. Mock data experiments are evaluated by the resulting reduced χ^2 values, and by a comparison of the measured coherent NC(π^0) event rate to the mock data (true) coherent NC(π^0) event rate. The uncertainty of the analysis is determined through the results of an ensemble of mock data experiments. Ensembles of mock data experiments are performed, each in various fit configurations; the optimal configuration yielding the lowest overall uncertainty.

The SSMD studies provide *i*) a ranked list of systematic error sources that

significantly change the shape of the background Angle-vs-Energy distribution and may require independent fit parameters, and they provide *ii*) estimates for the widths of the Gaussian pdfs used to construct the penalty terms for the three effective fit parameters. Varied amongst the fit configurations, among other things, are the number and the identity of the systematic fit parameters. Once the mock data studies have been performed, the complete analysis methodology is in hand to carry out a measurement of the coherent NC(π^0) flux-averaged, energy-averaged cross section using the MINOS ND data.

Several initial mock data studies were performed in order to elucidate the effects of fluctuations of individual inputs to the mock data. First sets of mock data were created where only the coherent NC(π^0) event rate was varied. These studies were performed for various definitions of the signal region, and for different sets of inputs to the fitting procedure. The next set of mock data experiments included statistical fluctuations. Finally, several sets of full mock data experiments were performed which included systematic fluctuations. Each ensemble of mock data experiments (i.e. mock data study) was performed with a different fit configuration, which included alterations to the number and identity of the systematic fit parameters used in the fits, substitution of the Berger-Sehgal reweighted signal MC for the signal sample of the fit MC, or use of the Berger-Sehgal reweighted signal MC to construct the mock data samples. The null hypothesis (where the signal event rate is set to zero) was also explored.

11.1.1 Mock Data Generation

The fitting procedure takes into account twenty-two systematic error sources. If the uncertainties from these error sources were taken into account in an un-

sophisticated way, the measurement would be rendered needlessly imprecise. However, by incorporating all of the systematic error sources into the fitting procedure, the combined error on the final measurement is reduced. An estimate of the overall systematic+statistical uncertainty can be obtained using an ensemble of mock data experiments. It is important that the mock data reflect all possible differences between the MINOS data and the predictions of the standard MC. There must be contributions from all the data-vs-MC differences that may arise from all of the systematic error sources as well as a contribution from random statistical fluctuations. The mock data studies can only evaluate systematics error sources for which reweighting can be performed. The resulting uncertainties from systematic error sources not included in the mock data generation procedure must be added in quadrature to the result of the mock-data-based systematic+statistical error studies.

Mock data is constructed as follows:

1) Angle-vs-Energy histograms derived from the standard MC for the signal and for each of the background reaction categories are loaded and re-binned according to the prescription detailed in Chapter 9.2.

2) The normalization of the coherent NC(π^0) event sample is varied by the application of a random scale factor to the signal Angle-vs-Energy distribution. The large uncertainty on the coherent NC(π^0) cross section requires the mock data to allow variations in the normalization of up to 50% in accordance with the uncertainty suggested in the Rein-Sehgal paper. There are, however, several measurements of this interaction and it is reasonable to conservatively assume that the normalization does not vary by more than 50% of the Rein-Sehgal prediction. There is no evidence from external data or theory to suggest that the event rate is less than 50% of the Rein-Sehgal prediction, and an ex-

perimental lower bound of 21% below the Rein-Sehgal prediction is obtained from the NOMAD measurement [17]. In addition none of the alternate coherent models investigated decrease the predicted event rate. Therefore, the normalization scale factor was taken to be a random number generated from a flat pdf between 0.5 and 1.5.

3) Similarly, to reflect the 20.0% uncertainty of the background CC-ν_e event rate, a random scale factor is generated based on a Gaussian pdf with a mean of 1.0 and a width of 0.20. This random number is used to scale the CC-ν_e Angle-vs-Energy distribution.

4) The signal and background Angle-vs-Energy histograms from each of the SSMD samples are loaded and re-binned in a process analogous to step 1.

5) Each systematic reweighted histogram set from step 4 represents a ± 1 σ fluctuation from a single systematic error source. In order to randomly adjust the level of the fluctuation for each systematic error source, a set of random numbers, r_{sys}, (one for each systematic error source) is generated using appropriate pdfs. The uncertainties on systematic error sources are well described by a Gaussian pdf with a mean of zero and width of one. Several of the systematic error sources are not well described by a Gaussian pdf. For these systematic error sources the appropriate pdf is used to generate the random number. The r_{sys} values are used in step 6.

6) Each of the resulting MC Angle-vs-Energy histograms is then reweighted, bin-by-bin, according to

$$\mathcal{N}_{ijb}^{MD} = N_{ijb}^{SMC} + \sum_{sys} r_{sys} \left(N_{ijb}^{sys} - N_{ijb}^{SMC} \right) \ . \tag{11.1}$$

Here $\mathcal{N}_{ij}^{MD}$ refers to the reweighted contents of bin ij, N_{ijb}^{SMC} is the standard MC content of bin ij in signal/background category b. N_{ij}^{sys} is the content for bin ij of the reweighted SSMD Angle-vs-Energy distribution for systematic error source, sys, and r_{sys} is the corresponding random number setting the strength in relation to a 1 σ fluctuation of the systematic error source.

7) The bin contents of the Angle-vs-Energy histograms for the signal and for the backgrounds from Eq. (11.1) are added together, bin-by-bin, via

$$\mathcal{N}_{ij}^{MD} = \sum_b \mathcal{N}_{ijb}^{MD} = \sum_b \left[N_{ijb}^{SMC} + \sum_{sys} r_{sys} \left(N_{ijb}^{sys} - N_{ijb}^{SMC} \right) \right] \ , \qquad (11.2)$$

producing a single Angle-vs-Energy histogram, which is then used as mock data.

8) Statistical fluctuations for bin ij are included as indicated by

$$N_{ij}^{MD} = P\left(\mathcal{N}_{ij}^{MD} \right) \ . \qquad (11.3)$$

Here $P\left(x, N\right)$ returns a random number, N, using the Poisson-statistics-based generating function:

$$Prob\left(x, N\right) = e^{-x} \left(\frac{x^N}{N!} \right) \ . \qquad (11.4)$$

Eq. (11.4) gives the probability of Eq. (11.3) returning the number N, based on the expectation value, x, where $N = N_{ij}^{MD}$ and $x = \mathcal{N}_{ij}^{MD}$.

For most of the systematic error sources the Angle-vs-Energy distributions are only available for the +1 σ and/or the -1 σ cases used to create the SSMD samples. Incremental changes to the Angle-vs-Energy spectra required to produce the mock data are calculated through linear interpolation and extrapolation of

each SSMD sample Angle-vs-Energy histograms. This formulation is adequate as the reweighting does not change the measured value of the Energy or the Angle of the events, only the weight. However, changes to the EM energy scale require recalculation of the event Energy and cannot be easily interpolated or extrapolated from the $\pm 1\ \sigma$ case. Instead, a series of SSMD samples are created, each with an EM energy scale shifted in increments of 0.1 σ from -2.0 σ to +2.0 σ. Random fluctuations in the EM energy scale systematic are linearly interpolated, bin-by-bin, from the two closest SSMD samples Angle-vs-Energy distributions, or extrapolated from the $\pm 2.0\ \sigma$ samples.

The mock data Angle-vs-Energy distributions are fitted using the three effective fit parameters, and between one and four systematic fit parameters. The result of a fit is a coherent NC(π^0) event rate, N_{fit}. This can be compared to the true mock data NC(π^0) event rate, N_{true}, randomly selected in step 2 of the mock data generation procedure. The fractional error on N_{fit},

$$\frac{N_{true} - N_{fit}}{N_{true}} \ , \tag{11.5}$$

is plotted for an ensemble of mock data experiments. The width of the fractional error distribution determines the $\pm 1\ \sigma$ confidence interval on the number of coherent NC(π^0) events in the MINOS Near Detector Run I + Run II data sample. The width is defined as the region about the peak of the fractional error distribution that includes 68% of the area.

Several factors may influence the result of a mock data fit, and thus the width of the fractional error distribution. These factors include *i*) the definition of the signal region, *ii*) the values and ranges of the fit parameters, *iii*) the method for introducing statistical fluctuations, and *iv*) the number and identity of the systematic fit parameters. To obtain information on each of these factors,

special mock data sets were created and a series of output measures and plots were evaluated.

11.1.2 Coherent NC(π^0) Normalization Studies

To test the fitting package, special mock data samples were generated wherein the systematic and statistical fluctuations of step 3 through step 8 of the mock data creation procedure were turned off. In these samples, only the normalization on the coherent NC(π^0) Angle-vs-Energy distribution is varied. Due to the absence of any statistical or systematic fluctuations of the background Angle-vs-Energy distributions, the fitting procedure should be able to return the input signal rate to high accuracy. Figure 11.1 shows the results of roughly 1000 of these mock data experiments. Plot a), on the left, is the number of mock data experiments as a function of N_{fit}/N_{RS}-vs-N_{true}/N_{RS}. N_{fit}/N_{RS} is the measured signal event rate as compared to the Rein-Sehgal prediction in the standard MC, and N_{true}/N_{RS} is the mock data event rate compared to the Rein-Sehgal prediction. The latter quantity is equal to the random normalization scale factor applied to the signal in creating the mock data. Plot b) displays the fractional error distribution for the same set of mock data experiments.

The slope of the line produced by the mock data experiments displayed in plot a) of Fig. 11.1 should ideally be exactly 1.0, but instead the line follows the equation $y = 0.942x + 0.058$. This is due to signal contamination in the sideband region of the selected and the near-PID samples. In essence the MC prediction is pulling the result toward the nominal value inherent in the fit (standard) MC sample. To explore how the level of signal contamination affects the slope of the (N_{fit}/N_{RS})-vs-(N_{true}/N_{RS}) line, Fig. 11.2 shows four

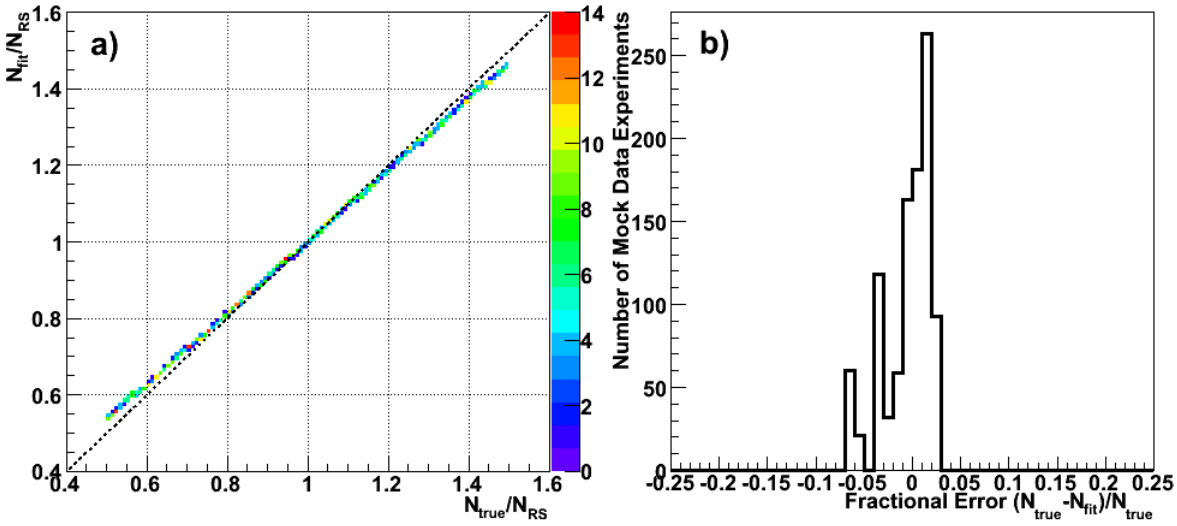

Figure 11.1: Plot a) displays the measured signal event rate, N_{fit}, versus the mock data event rate, N_{true}, for mock data experiments where only the signal event rate was varied. Both event rates are scaled by the Rein-Sehgal model prediction as implemented by NEUGEN3 in the MINOS Monte Carlo, N_{RS}. No additional variation, of either a statistical or systematic nature, was included. Plot b) displays the number of mock data experiments as a function of the fractional error for the same set of mock data experiments. The structure of the distribution is a consequence of the result-dependent bias discussed in the text.

plots each displaying a set of mock data experiments with different definitions of the signal region. Plot a) defines the signal region as the Angle-vs-Energy bins with a MC prediction for a purity, ρ, of less than 2.5%. Plot b) displays the same mock data experiments shown in Fig. 11.1 which have a purity cut of 5.0%. Plots c) and d) follow with the definition of the signal region based on a purity cut of 10% and 20%, respectively. As the purity value used to define the signal region increases the slope of the line decreases, rotating about the point (1,1), which corresponds to a mock data coherent NC(π^0) event rate, N_{true}, and a measured event rate, N_{fit}, equal to the Rein-Sehgal model MC prediction, N_{RS}.

The number of mock data experiments as a function of the fractional error is displayed in plot b) of Fig. 11.1. Without the result-dependent bias, the distribution would be peaked at 1.0, and exhibit none of the observed structure. The mock data experiments with a fractional error above 0.0 ($N_{fit} < N_{true}$) result from signal normalization scale factors (N_{true}/N_{RS}) greater than 1.0, where the result-dependent bias reduces the measured coherent NC(π^0) event rate. The denominator of the fractional error, N_{true}, is relatively large for these mock data experiments. Thus the range of the right-hand-side of the distribution is smaller than the left-hand-side, where $N_{fit} > N_{true}$, and N_{true}/N_{RS} is less than 1.0. The measured coherent NC(π^0) event rate for mock data experiments where N_{true}/N_{RS} is less than 1.0 is increased toward the Rein-Sehgal prediction by the result-dependent bias. The magnitude of the fractional error for these events is larger for a given deviation from the Rein-Sehgal prediction due to the lower number of input signal events, N_{true}, used as the denominator in calculating the fractional error. The structure of the right hand plot of Fig. 11.1 is explained by the step-wise nature observed in the left hand plot, which is described in more detail below.

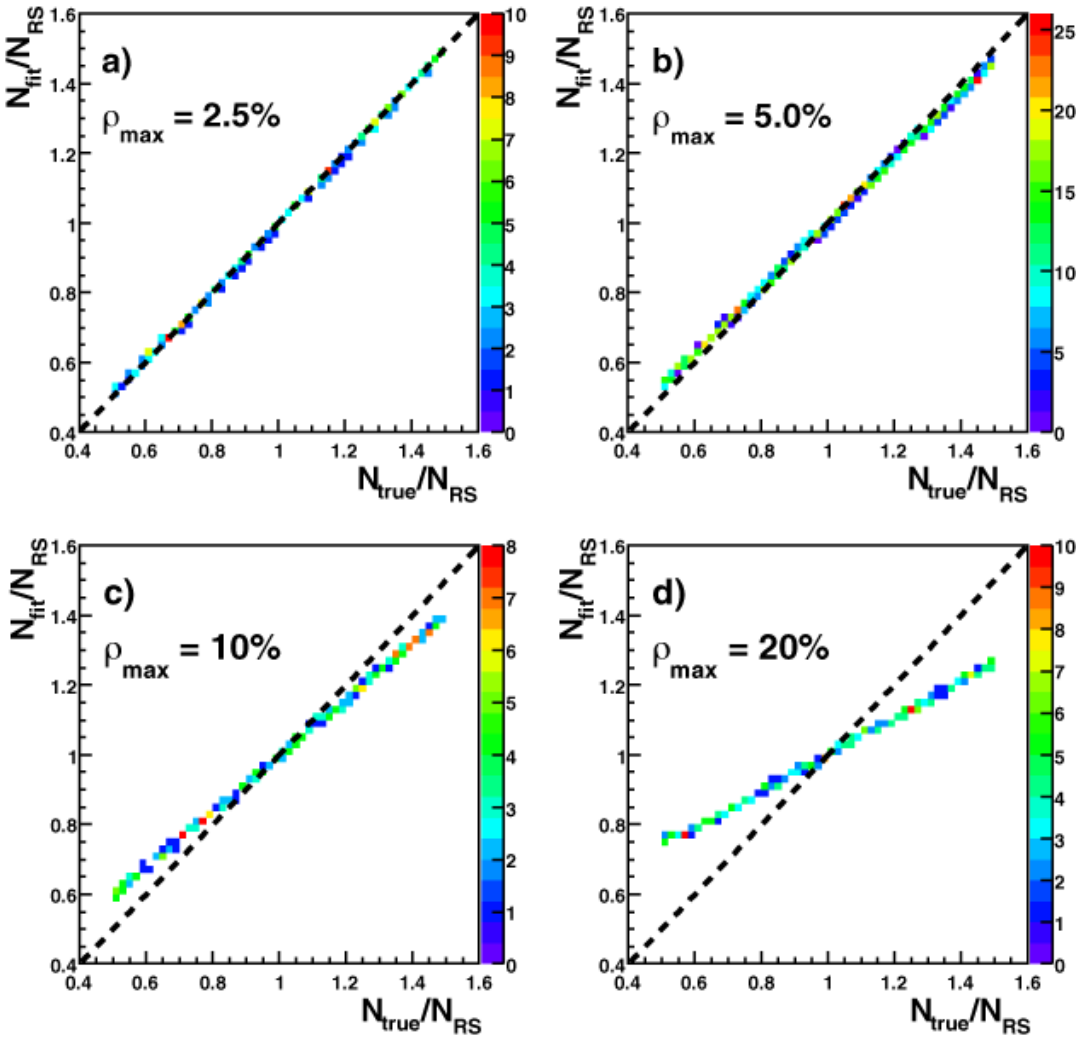

Figure 11.2: The measured signal event rate, N_{fit}, versus the mock data event rate, N_{true}, for mock data experiments where only the signal event rate was varied. Both event rates are scaled by the Rein-Sehgal model prediction as implemented by NEUGEN3 in the MINOS Monte Carlo, N_{RS}. No additional variation, of either a statistical or systematic nature, is included. The change in the observed slope is a function of the signal purity cutoff used to define the signal region, and is thus related to the signal contamination in the sideband region. The curves are rotated about the point (1,1), where $N_{fit} = N_{true} = N_{RS}$, toward a flat distribution (i.e. $N_{fit} = N_{RS}$ for all values of N_{true}).

The reason for the result-dependent bias stems from the fit parameters adjusting to the increased (or decreased) number of signal events. The magnitude of the result-dependent bias is a function of the purity cut, and the deviation of the signal normalization scale factor from unity. A reduction of the result-dependent bias is obviously preferred, however, as explained in Chapter 9.1, a harsher purity cut reduces the size of the sideband region, and thus the number of bins (and information) available to the fit. The best compromise, determined by the lowest uncertainty propagated to the measured coherent NC(π^0) event rate, is a signal region defined by a purity cut of 5.0%. The effect of the (up to) 5.0% signal contamination is a result-dependent bias of 5.8%, resulting from a slope of 0.942. The result-dependent bias will underlie all of the following mock data studies; it also sets a minimum width for the fractional error distribution as that of plot b) of Fig. 11.1.

The quantized nature of the fit parameters discussed in Chapter 8 leads to another input to the fit procedure. Shown in Fig. 11.3 are similar mock data studies where the number of fit parameter values sampled is varied. Plot a) shows the number of mock data experiments as a function of (N_{fit}/N_{RS})-vs-(N_{true}/N_{RS}) for mock data studies where the fit parameter values are sampled in steps of 0.20. Plots b) and c) show the same distribution for mock data studies done with steps of 0.10 and 0.05, respectively, in each fit parameter. Plot d) is the same distribution as shown in Fig. 11.1, where the mock data studies are performed with steps of 0.025 in the values of the fit parameters.

The stepwise nature of the plots in Fig. 11.3 can be understood by examining the corresponding best-fit values for the fit parameters of the mock data experiments.

The breaks in plots a), b) and c) correspond to shifts of one step in the CC-ν_e

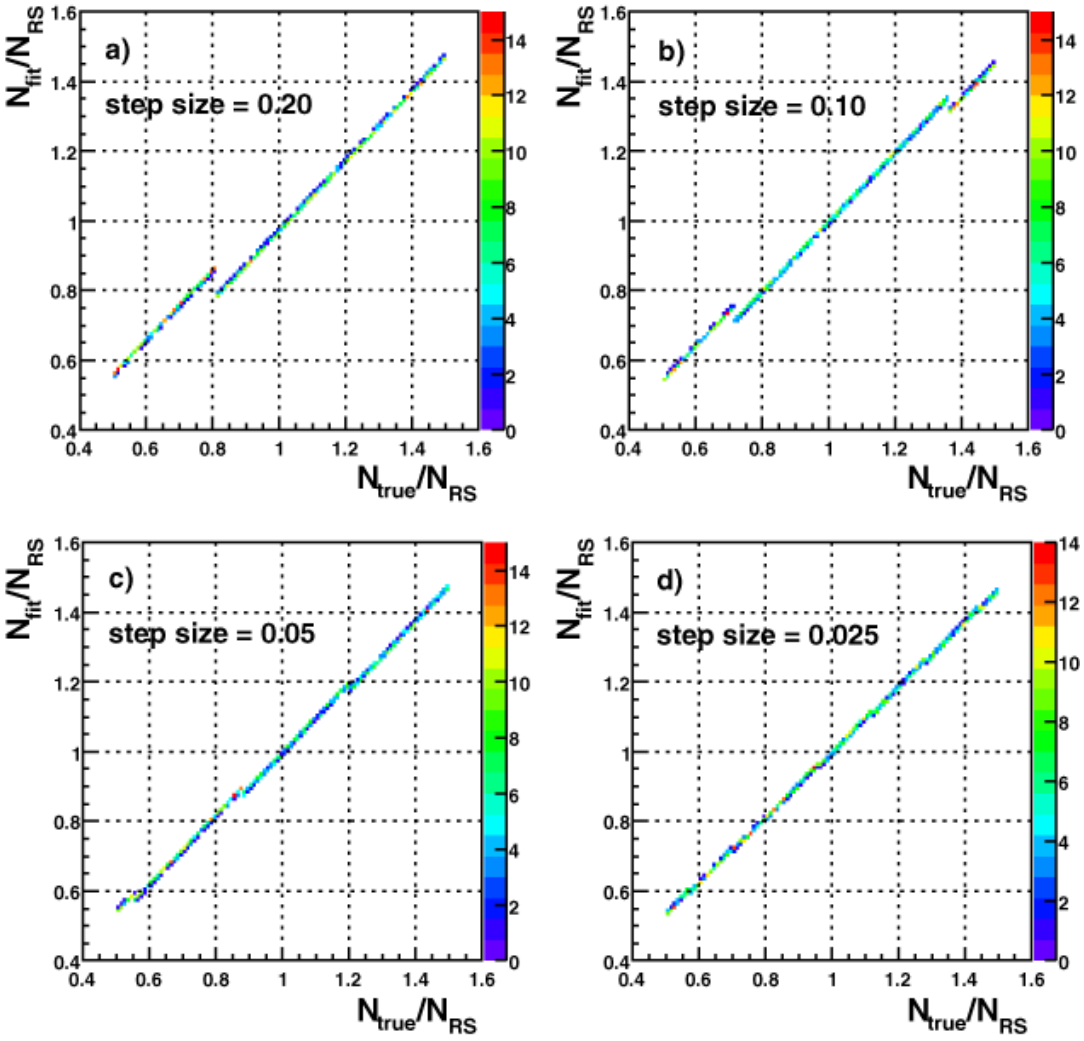

Figure 11.3: The measured signal event rate, N_{fit}, versus the mock data event rate, N_{true} (both scaled by the Rein-Sehgal model prediction as implemented by NEUGEN3 in the MINOS Monte Carlo, N_{RS}) for mock data experiments where only the signal event rate was varied. No additional variation, of either a statistical or systematic nature, is included. The "jump discontinuities" are reduced, and then eliminated upon increasing the number of fit parameter steps.

fit parameter. The fit MC is being adjusted to account for the increase (or decrease) in the number of signal events in the sideband region, and can be more finely tuned as the step size between fit parameter values decrease. This allows for the fitter to be more responsive to differences between the data and MC and for better fit results (lower χ^2 values). In plot d), where the step size is 0.025, one or more of the effective fit parameters are adjusted to describe the changes induced by the systematic reweighting. The step size of 0.025 was chosen for the remainder of the mock data experiments.

11.1.3 Statistical Error Studies

An additional dedicated set of mock data studies include random statistical fluctuations along with the random normalization scaling of the coherent NC(π^0) event rate. The standard procedure for the inclusion of statistical errors is described in step 8 of the mock data generation procedure. The fluctuations are generated independently on a bin-by-bin basis. Studies of statistically fluctuated mock data can be used to determine the statistical error that results from the fitting procedure. Figure 11.4 shows the (N_{fit}/N_{RS})-vs-(N_{true}/N_{RS}) distribution in plot a), and the fractional error distribution in plot b) for the set of statistically fluctuated mock data experiments. The width of the fractional error distribution is 12%, settting a measure of the statistical error, although this also includes the 5.8% contribution introduced by result-dependent bias, implying a statistical error of roughly 10.5%. The statistical fluctuations also induce a bias of roughly -5.4% (i.e. the average fractional error is -0.054). This is an expected consequence of statistical fluctuations based on a Poisson distribution. The integral of the Poisson probability mass function below the the expectation value is greater than the integral above the

expectation value.

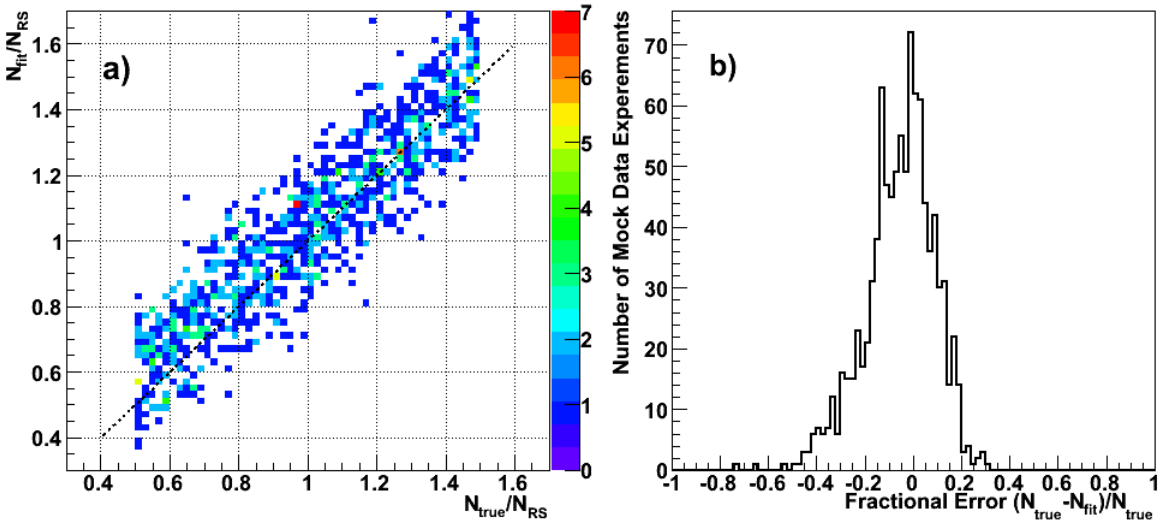

Figure 11.4: Plot a) displays the number of mock data experiments as a function of (N_{fit}/N_{RS})-vs-(N_{true}/N_{RS}) for the mock data experiments that include statistical fluctuations of the nature described in the mock data creation procedure. Plot b) displays the number of mock data experiments as a function of the fractional error for the same set of mock data experiments. The spread of the fractional error distribution in plot b) is 0.12.

Alternate schemes for including statistical fluctuations were investigated, but were eventually rejected because they introduced correlations. The first method examined involved splitting the MC sample into two subsamples using a binomial statistics-based probability. One sample was to be used for the fit MC while the other sample was to be used for mock data generation. In this method, however, the two subsamples are correlated, in that if an event is in one subsample it cannot be in the other. Therefore the statistical fluctuations seen in the Angle-vs-Energy distribution of one subsample would be mirrored in the in the Angle-vs-Energy distribution of the other subsample, in essence doubling the size of the fluctuations.

The second method that was tried and rejected involved using the MC Angle-vs-Energy distribution as pdf. The mock data sample was populated by sam-

pling the pdf N times, where N is a random number generated using Eq. (11.4), with the total number of MC events as the expectation value. In this case, if an event is chosen to be in one bin it can not be in any other bin, resulting in a bin-to-bin correlation. The correlation causes fluctuations in one bin to have an opposite effect on the contents of the other bins, overestimating the amount of statistical fluctuation.

The statistical error resulting from the size of the fit sample is also a concern. This can be tested by randomly selecting a fraction of the full MC sample to use as the fit Monte Carlo. Figure 11.5 shows the fractional error distribution for the full fit MC sample as compared with several reduced statistics samples at 95%, 85%, 70%, 60%, 50%, 40%, 20%, and 5% of the full MC sample. Negligible deleterious effect is observed until the size of the sample is reduced by 50%. As the sample size is reduced further, a bias is introduced, and as the sample size decreases the size of the bias grows. However, the direction of the bias changes as well, so the effect is not intrinsic to the reduction in sample size, but rather a reflection of the randomly selected sample. It is plausible that a reduced statistics sample, with as few as 20% of the original sample size, would return the same results as the full sample if the reduced sample was representative of the original sample Angle-vs-Energy distribution.

11.1.4 Full Mock Data Studies

Mock data generated using the full procedure includes both statistical fluctuations, and systematic shifts from the 22 reweightable sources of systematic uncertainty. The results of these "full" mock data studies set the overall combined systematic+statistical error for the coherent NC(π^0) event rate, as measured by the width of the fractional error distribution. An additional

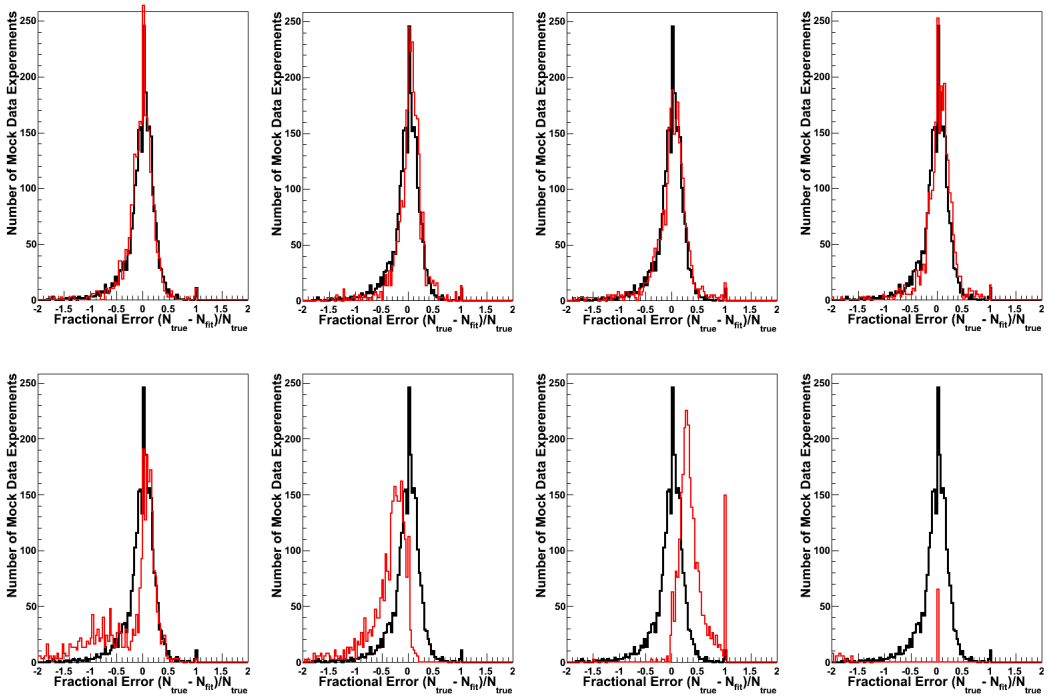

Figure 11.5: The fractional error distribution for the mock data experiments that include statistical fluctuations of the nature described in the mock data creation procedure (black). Overlaid are fractional error distributions for the mock data experiments fit with a randomly selected reduced MC set (red). Going left to right, top to bottom, the data sets include 95%, 85%, 70%, 60%, 50%, 40%, 20%, and 5% of the full MC sample. The ensembles of mock data experiments for reduced fit MC samples produce results consistent with the the full fit MC sample mock data experiments for samples with at least 60% of the standard MC events.

10% is added (in quadrature) to the mock-data-based error estimate in order to include calibration systematic error sources for which reweighting cannot be performed. The number of mock data experiments as a function of (N_{fit}/N_{RS})-vs-(N_{true}/N_{RS}) is shown in plot a) of Fig. 11.6 while plot b) displays the fractional error distribution for mock data experiments performed with the following fit configuration:

- Signal region purity cutoff: 5.0%
- Statistical fluctuations: Poisson-statistics-based/bin-by-bin
- Effective fit parameters: 3 (NC/CC-ν_μ resonance, NC/CC-ν_μ DIS, and CC-ν_e)
- Effective fit parameter step size: 0.025
- Systematic fit parameters: 2 (EM Energy Scale, Hadronization "t1")
- Systematic fit parameter step sizes: EM Energy Scale - 0.10, Hadronization "t1" - 0.05

In order to determine the number of systematic fit parameters that should be used, the systematics are ranked at the outset. The ranking is based on the results of the SSMD studies, specifically the goodness of fit (χ^2/ndf), and a comparison of the measured coherent NC(π^0) event rate, N_{fit}, to the SSMD sample coherent NC(π^0) event rate, $N_{true} = N_{RS}$. The rankings, or fit priorities, are presented in Tables 10.3 and 10.4.

Several sets of mock data experiments were performed using a single systematic fit parameter for one of the systematic error sources of highest rank.

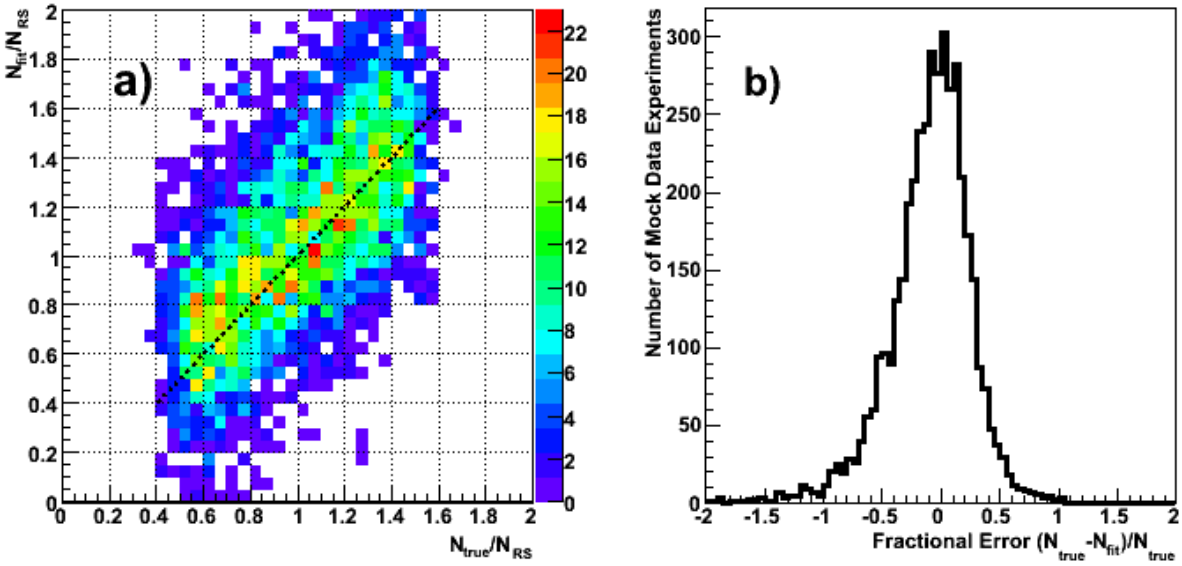

Figure 11.6: Plot a) displays the number of mock data experiments as a function of (N_{fit}/N_{RS})-vs-(N_{true}/N_{RS}). The fit is performed with the three effective fit parameters and two systematic fit parameters described in the text. Plot b) displays the number of mock data experiments as a function of the fractional error for the same set of mock data experiments. The spread about $N_{fit} = N_{true}$ is ± 0.30.

The results of these studies give the fractional errors for the single systematic fit parameters. The number of mock data experiments as a function of the fractional error for the top four ranked systematics are shown in Fig. 11.7. These can be compared with the fractional error distribution for mock data experiments fit with the effective fit parameters, and no systematic fit parameters shown in Fig. 11.8. Further mock data studies are performed which fit for a combinations of two of the systematic fit parameters, then three, and so on. Through these studies it was determined that the best combination of sensitivity and processing efficiency results from fits with two systematic fit parameters, namely, the EM energy scale, and "t1" of the hadronization model. This setup is used to fit the data, and the results of the corresponding ensemble of mock data experiments sets the systematic+statistical uncertainty on the coherent NC(π^0) event rate.

The results of the ensemble of mock data experiments performed with the fit configuration to be used to fit the data is displayed in Fig. 11.6. The width of the fractional error distribution is 30% (-35%, +25%). With the inclusion of the 10% uncertainty from the calibration systematic error sources (for which reweighting cannot be done), this translates to a total systematic+statistical error of 31.6%. There is a 12% contribution to the uncertainty from the combination of the result-dependent bias, and statistical fluctuations, which is already included in the 30% fit uncertainty. The fit uncertainty results from the quadrature sum of the individual contributions. As such the non-systematic contributions increase the total uncertainty by 2.5% ($= \sqrt{(30\%)^2 - (12\%)^2}$), suggesting that an increase to the size of the data sample would have minimal effect on the sensitivity of the measurement.

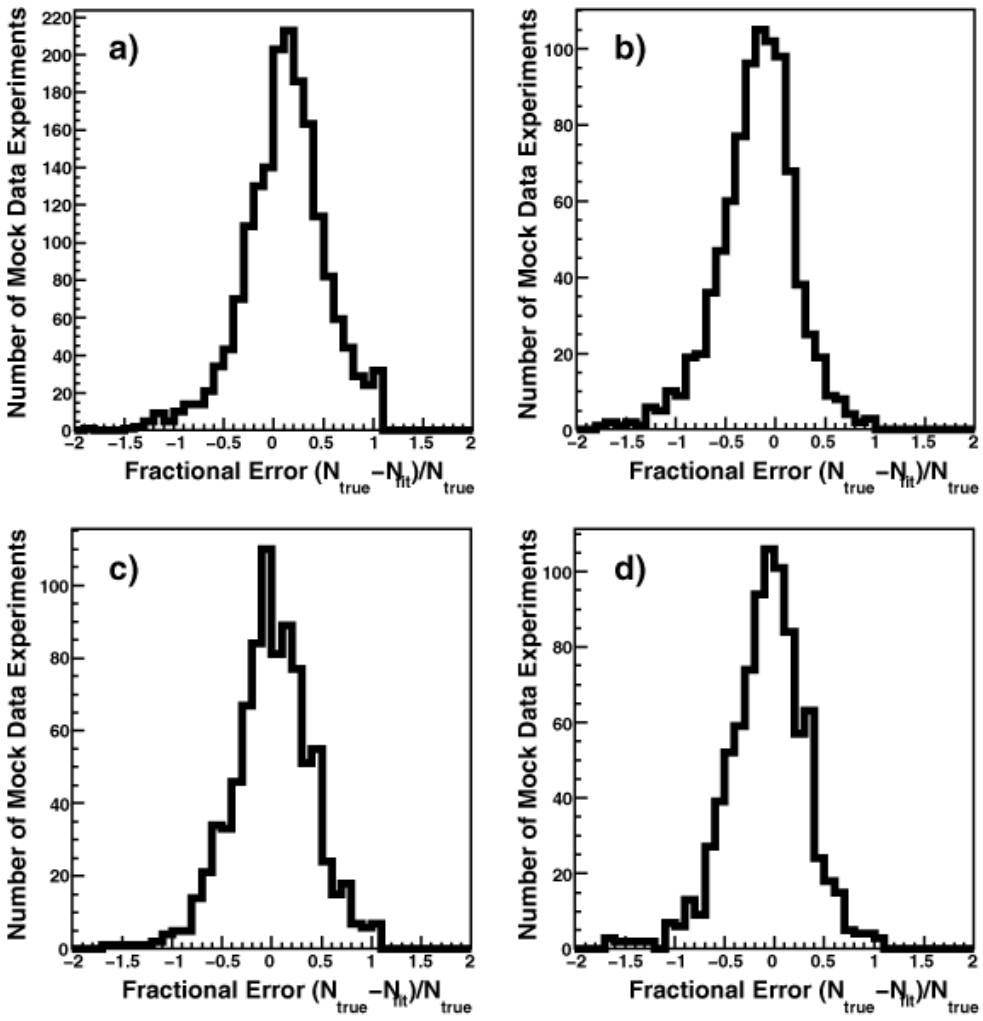

Figure 11.7: The number of the mock data experiments as a function of the fractional error for fits performed with a single systematic error fit parameter. Plot a) is for the set of mock data experiments where the systematic fit parameter is the EM energy scale. Plots b), c), and d) are for the set of mock data experiments where the systematic fit parameter is the hadronization model systematic "t1", "t3", and "t5", respectively.

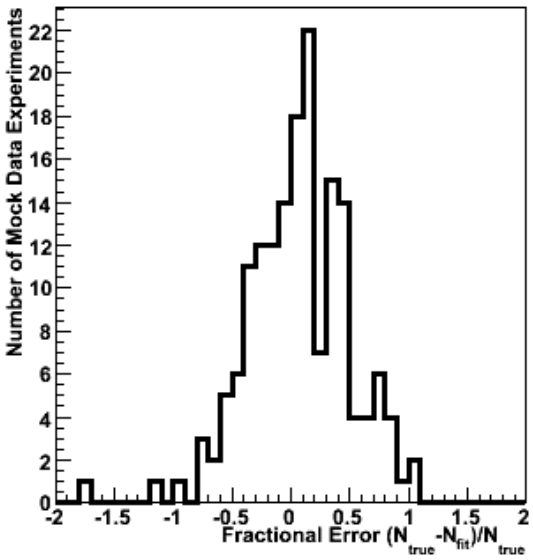

Figure 11.8: Distribution of mock data experiments as a function of the fractional error for fits performed with no systematic fit parameters.

The mock data experiment distributions, as functions of the best-fit values for the fit parameters, and the χ^2/ndf values are also of interest. They afford tests of the fit procedure, and are benchmarks for the best-fit points returned by fits to the real data. Figure 11.9 displays the best-fit values for the effective fit parameters. As expected, the best-fit values for the fit parameters distribute with a roughly Gaussian shape.

Figure 11.10 displays the best-fit values for the two systematic fit parameters: *i*) the EM energy scale in plot a) and *ii*)"t1" of the hadronization model in plot b). The EM energy scale fit parameter behaves as expected, matching the distribution of the input fluctuations fairly well. The hadronization systematic, however, is strongly peaked at 0.0, and has a long flat tail. This behavior can be explained by considering the level of systematic fluctuations in each mock data experiment. The fit parameter matches the input level of fluctuations for mock data experiments, where "t1" is the dominant systematic fluctuation. However

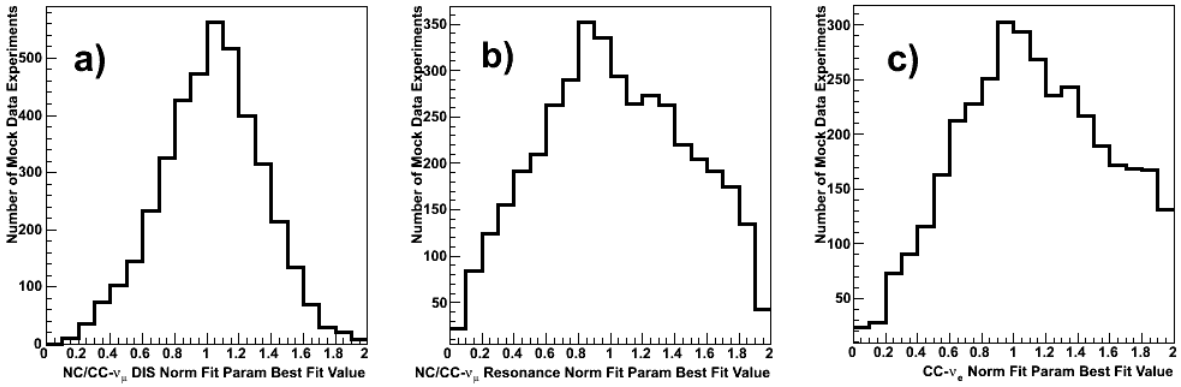

Figure 11.9: The number of mock data experiments as a function of the best-fit value for, a), the NC/CC-ν_μ DIS fit parameter, b), the NC/CC-ν_μ resonance fit parameter, and c), the CC-ν_e fit parameter for mock data experiments that also fit for the EM energy scale and the hadronization model "t1" parameters. As expected the distributions are peaked at 1.0, and have a Gaussian-like shape.

for the majority of mock data experiments there are large fluctuations in one or more of the other systematic error sources. In these cases, if possible, the shape changes produced by the "t1" systematic are exploited to help match the shape changes induced by the systematic fluctuations in the mock data sample. In this way the "t1" systematic fit parameter becomes an effective fit parameter as well.

The number of mock data experiments as a function of the reduced χ^2 is displayed in Fig. 11.11. The distribution peaks at around 0.6, and falls off linearly. There also seems to be a second peak around a χ^2/ndf value of 1.65. There is no correlation between the χ^2 value and the fractional error, however, mock data experiments that overestimate the coherent NC(π^0) event rate of the sample have a greater probability of lying in the second peak than do mock data experiments that underestimate the signal event rate.

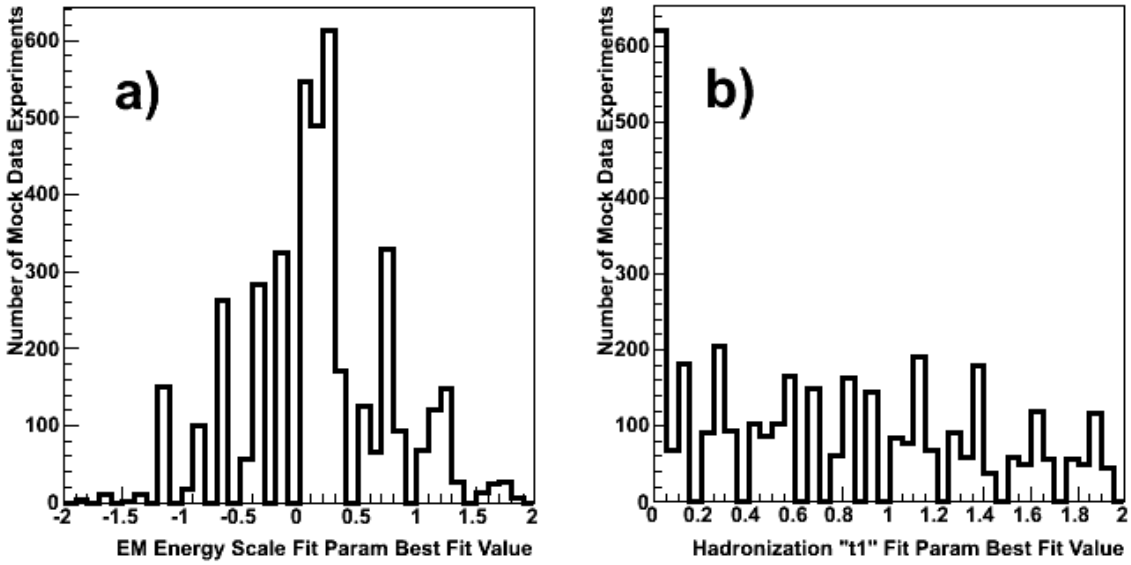

Figure 11.10: The number of mock data experiments as a function of the best-fit value for the systematic fit parameters for, a), the EM energy scale, and b), "t1" of the hadronization model. The shapes of the distributions reflect the input values for the systematic fluctuations induced by the mock data creation procedure. The systematic fit parameters scale as the number of standard deviations, σ, from the nominal value of the standard MC.

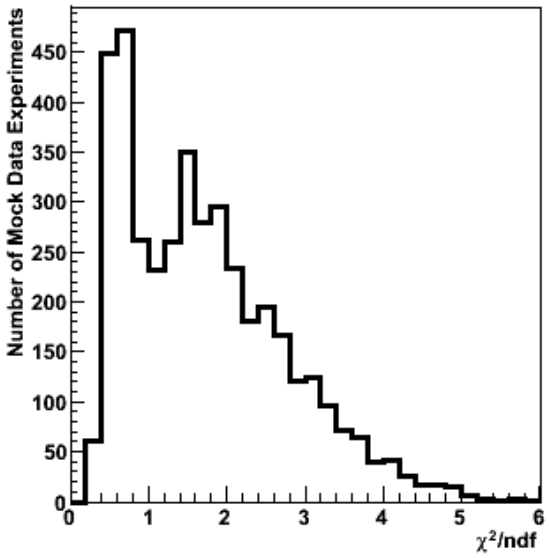

Figure 11.11: The number of mock data experiments as a function of the reduced χ^2 value peaks near 0.6, and falls off linearly. A second peak at roughly 1.6 corresponds to mock data experiments that tend to overestimate the coherent NC(π^0) event rate.

The alternate coherent models discussed in Chapter 10.1 are incorporated into mock data experiments in two ways; *i*) they are included as the signal model in the mock data or *ii*) they are used as the coherent NC(π^0) sample in the fit Monte Carlo. Figure 11.12 shows a set of mock data studies where the Berger-Sehgal model prediction for the Angle-vs-Energy distribution is used in the fit MC. There is a shift of roughly 10% to the right, and a small reduction in the width of the fractional error distribution. This is not surprising, as the Berger-Sehgal prediction for the event rate in the selected sample is 45% higher than in the standard MC, which increase the level of signal contamination in the sideband beyond 5.0%. On average the standard MC based mock data will have fewer coherent events in the sideband than the fit MC. This results in an underestimate of the background, and thus an overestimate number of coherent NC(π^0) events, enhancing the result-dependent bias. However, the

lack of any significant change between the Berger-Sehgal based fit MC mock data studies and the corresponding standard fit procedure mock data studies is evidence that the fitting is relatively insensitive to the signal model.

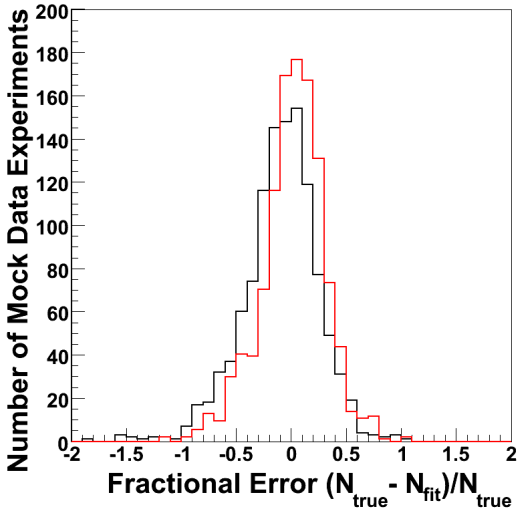

Figure 11.12: Fractional error distribution for mock data experiments including one systematic error fit parameter (black histogram), and for mock data experiments using the Berger-Sehgal coherent model reweighted MC for the fit MC (red histogram). The lack of variation between the two types of simulated experiments suggests that the fit procedure is relatively independent of the fit coherent model. The +10% shift in the fractional error is explained by an enhanced result-dependent bias.

Figure 11.13 displays the fractional error distribution and (N_{fit}/N_{RS})-vs-(N_{true}/N_{RS}) plots for mock data studies done with the alternate coherent models considered in this Thesis. All of the fractional error distributions have widths comparable to the corresponding standard fit procedure studies, and no biases are introduced. Taken all together, these studies suggest that the fit procedure is robust to changes in the coherent model.

Of over 1,000 mock data experiments only one returns a value of zero, and only ten give a result less than 30% of the Rein-Sehgal prediction. It is reasonably expected that the NC coherent(π^0) event rate in MINOS is at least 50% of the

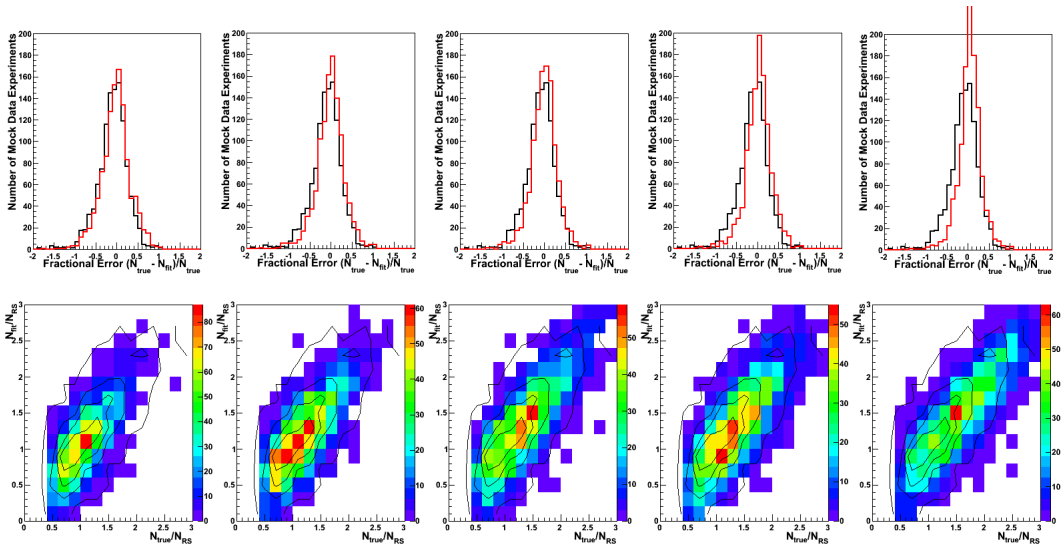

Figure 11.13: The top row displays the fractional error distribution for mock data experiments including one systematic error fit parameter (black histograms), overlaid by a mock data study performed using an alternate coherent model in the mock data (red histograms). From left to right the models are Regge, M_A =1.2 GeV, Berger-Sehgal kinematics, Berger-Sehgal pion-nucleon scattering, and the full Berger-Sehgal model. The bottom row displays (N_{fit}/N_{RS})-vs-(N_{true}/N_{RS}) for each of the corresponding plots of the top row. The overlaid contour plot displays, for comparison, the (N_{fit}/N_{RS})-vs-(N_{true}/N_{RS}) distribution for standard mock data experiments. The lack of a pronounced difference in either the width or center point of the distributions suggest that the fit procedure is performing as required to make a measurement of the signal event rate. The average signal event rate is greater for the Berger-Sehgal based sets of mock data experiments accounting for the reduced widths of the fractional error distributions.

Rein-Sehgal prediction, accounted for by the mock data generation procedure. Consequently, it is highly unlikely ($< 1\%$) that the measured signal event rate will be less than 70% of the Rein-Sehgal prediction, and even more unlikely, that the measured event rate is zero ($< 0.1\%$). A test can also be performed to see how the fitting procedure responds to the null hypothesis. A special set of mock data experiments was performed where the signal content was set to zero. Figure 11.14 shows the measured signal rate scaled by the Rein-Sehgal prediction. The distribution is sharply peaked at zero, however, the distribution has a long tail that extends out toward 1.0.

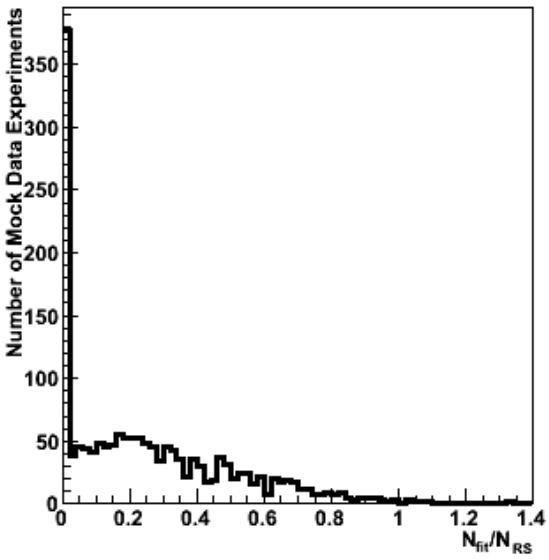

Figure 11.14: Distribution of extracted signal rate (relative to Rein-Sehgal) from mock data experiments in which the coherent NC(π^0) event rate was set to zero. A null rate is observed to be the most probable outcome.

11.2 Cross Section Measurement Sensitivity

The uncertainty on the number of coherent NC(π^0) events in the MINOS Near Detector Run I + Run II sample based on the twenty-two systematic error

sources included in the fitting procedure is ±30%. This uncertainty includes both systematic and statistical uncertainties. The statistical portion of the error is estimated by setting the random numbers, r_{sys}, from the mock data generation procedure used to set the strengths of the various systematic error sources all to zero. The width of the fractional error distribution of ±12% for the resulting mock data experiments is due to purely statistical differences between the data sets, along with the result-dependent bias.

Systematic error sources not included in the mock data studies are conservatively estimated to add an additional error of 10%, based primarily on studies done by the ν_e Working Group. Inclusion of these errors brings the overall uncertainty to ±31.6%. The systematic error contribution from the acceptance correction is 5%. The resulting combined overall uncertainty on the coherent NC(π^0) event rate is ±32.0%. For comparison with other results the cross sections are scaled to account for the events with an E_π <1.0 GeV. In these cases an added uncertainty of 20% is propagated to the result

Finally, there is uncertainty associated with converting the event rate to a cross section. The combined uncertainty on the fiducial mass, neutrino exposure, and neutrino flux of 7.9% is added in quadrature to the 32.0% uncertainty on the coherent NC(π^0) event rate. This yields a total systematic+statistical uncertainty on the Energy averaged, flux averaged coherent NC(π^0) cross section for interactions producing a final state pion with an Energy greater than 1.0 GeV of 33.0%

Chapter 12

Results and Discussion

12.1 Cross Checks and the Box Opening Procedure

Studies were carried out to ensure that each step of the fit to the data returned a reasonable result, and that the fit was robust to changes in the fitting procedure. The box opening procedure outlined the steps to be taken to insure that data samples were not unblinded until the observations of the previous step were understood. The first step was to choose the fit configuration with the best sensitivity and to complete the prerequisite studies outlined in the previous chapter. Prior to fitting the data, the sideband region of the selected data Angle-vs-Energy distribution was examined and compared with MC. The Angle projection for the Angle-vs-Energy histogram for the data in the sideband and the selected background MC in the sideband are shown in Fig. 12.1. (The corresponding Energy projection for each Angle projection shown here can be found in Appendix F.)

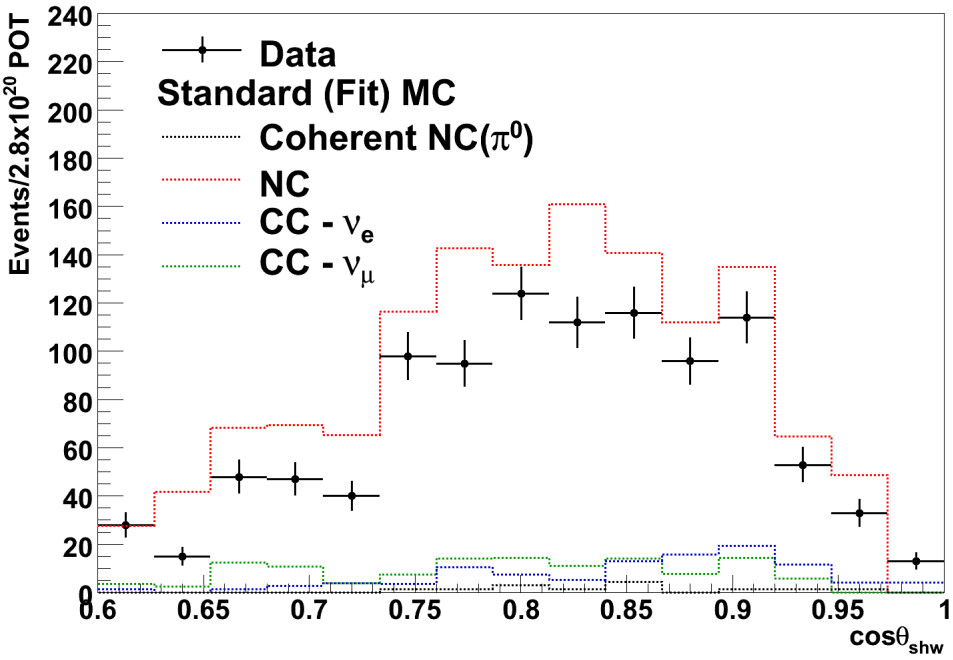

Figure 12.1: Angle projections of the sideband region of the Angle-vs-Energy histogram for the data and for the standard background MC. These represent the inputs to the fit.

The next step was to fit the selected MC background distributions in the sideband to the data in the sideband using the selected fit configuration. The resulting best-fit values for the fit parameters are:

NC/CC-ν_μ DIS: -40%

NC/CC-ν_μ Resonance: -50%

CC-ν_e: +75%

EM Energy Scale: +0.4 σ

"t1" of the Hadronization Model: +0.2 σ

The best-fit values for the effective fit parameters for the NC/CC-ν_μ DIS and resonance samples reduced the number of events in the standard (fit) MC by 40-50%, while the CC-ν_e event rate was increased by 75%. The EM energy scale was increased by 2.24%, and "t1" of the hadronization model is shifted by 0.2 σ. The effect of the adjustments to the MC samples is shown in Fig. 12.2 where the Angle projections of the best-fit background MC have been overlaid onto Fig. 12.1.

The level of agreement between the best-fit MC in the sideband and the data in the sideband can be seen in Fig. 12.3. Here, the Angle projections of the standard MC shown in Fig. 12.2 have been removed and the sum of the Angle projections of the backgrounds is now shown in magenta. The data is observed to agree with the sum of the MC backgrounds at the level of statistical uncertainties, suggesting a successful fit.

The fitting procedure performs a combined fit of the sideband regions of the selected sample and the near-PID sample. The best-fit values for the fit parameters are selected to induce the best agreement between the data and the

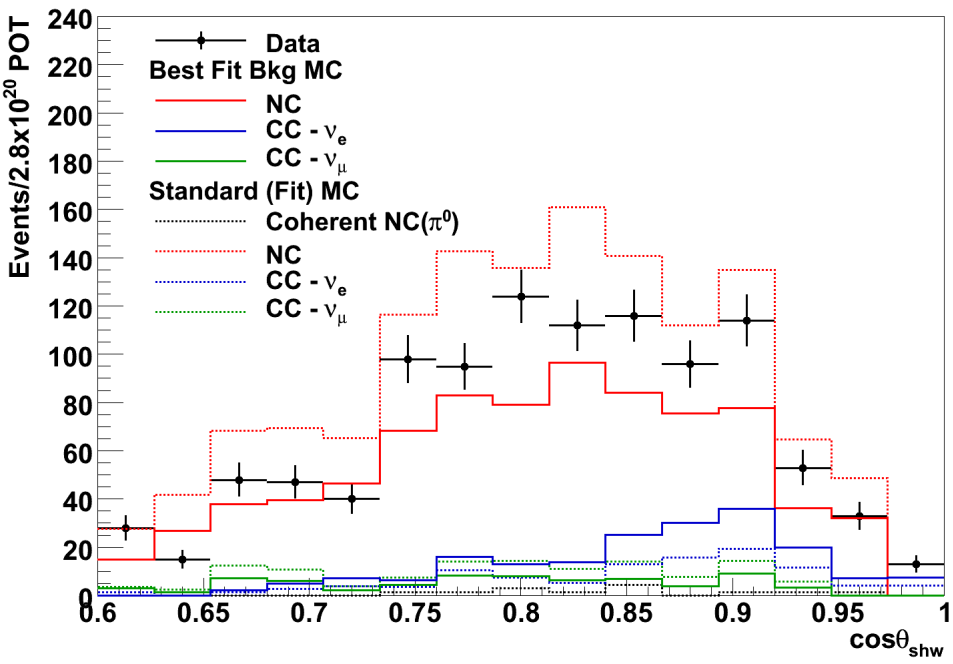

Figure 12.2: Angle projections of the sideband region of the Angle-vs-Energy histograms for the data sample, for the standard MC backgrounds, and for the best-fit MC backgrounds. The NC background is weighted down significantly to match the data.

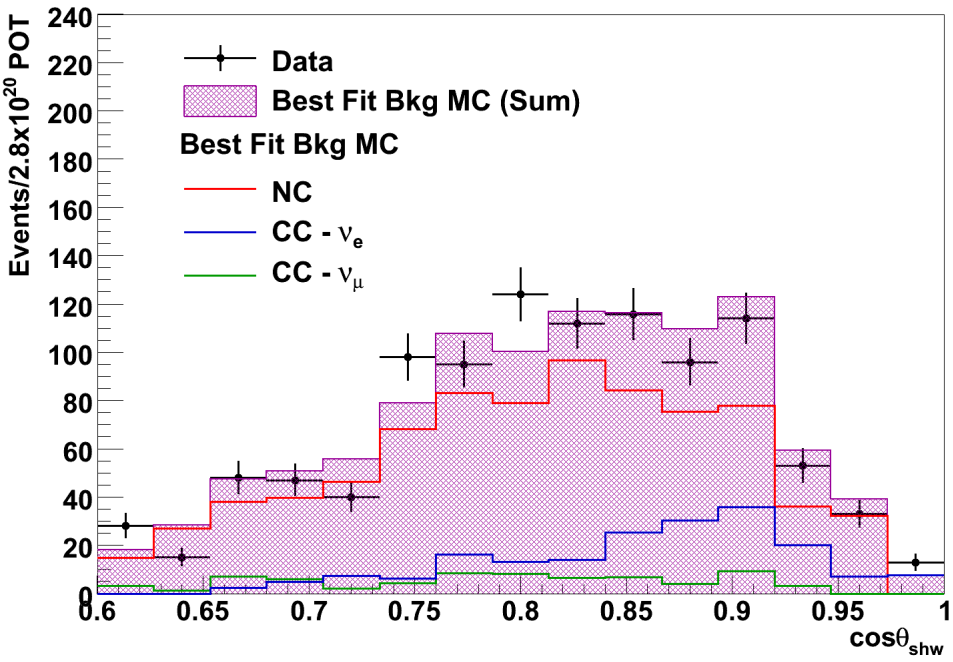

Figure 12.3: Angle projections of the sideband region of the Angle-vs-Energy histograms for the data sample, for the best-fit MC backgrounds, and for sum of the the best-fit MC backgrounds. The sum of the best-fit MC backgrounds agree with the data within statistical uncertainties.

MC in the sideband regions of both samples. As an additional cross check, the Angle projections from the sideband region of the near-PID Angle-vs-Energy histograms are also examined. Figure 12.4 displays the near-PID sideband Angle projections for each of the best-fit near-PID MC backgrounds, for the sum of the best-fit MC backgrounds, and for the data. The agreement be-

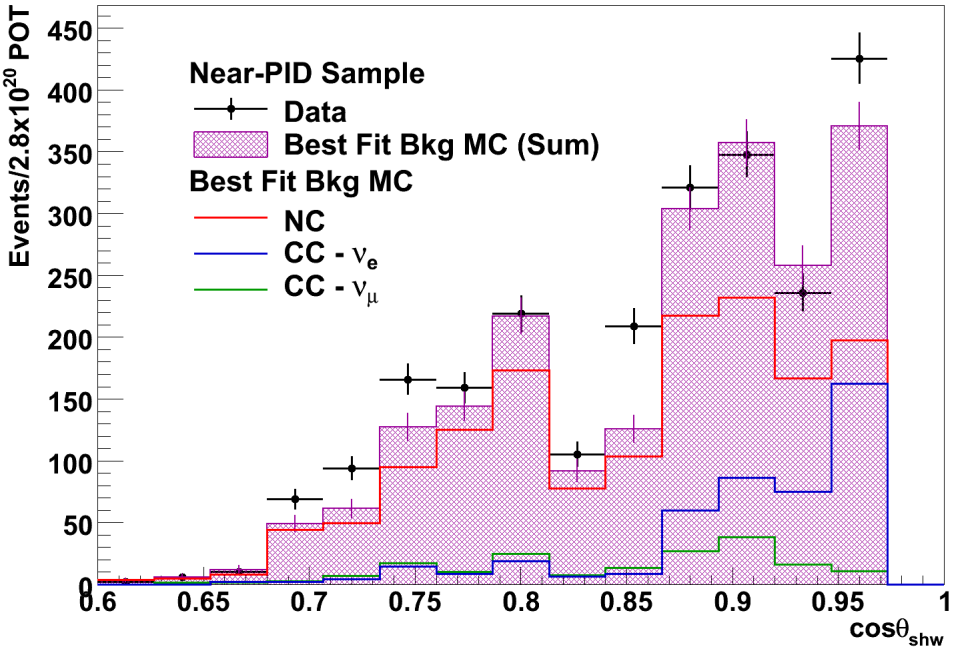

Figure 12.4: Angle projections of the sideband region of the near-PID Angle-vs-Energy histograms for the data sample, for the best-fit near-PID MC backgrounds, and for sum of the the best-fit near-PID MC backgrounds. The sum of the best-fit near-PID MC backgrounds roughly agree with the data within the combined statistical uncertainties on the data and the MC.

tween the best-fit near-PID background MC and the near-PID data is, for the most part, within statistical uncertainties. However, the agreement is near the limit of the combined statistical uncertainties of the MC and the data, and the fit to the near-PID sample is marginally acceptable. Taken together with the fit to the sideband of the selected sample the overall fit is successful. The data-vs-MC agreement for the best-fit backgrounds in the sideband regions of

the selected sample and the near-PID sample are reflected by the value of the reduced χ^2, which is discussed discussed in the context of the corresponding mock data experiments below.

The best-fit values of the fit parameters from fitting the MC to the data are compared with the distributions of the number of mock data experiments as a function of the best-fit values for full mock data experiments performed with the same fit configuration in Fig. 12.5 (effective fit parameters) and Fig. 12.6 (systematic fit parameters). The best-fit values for the fit parameters are

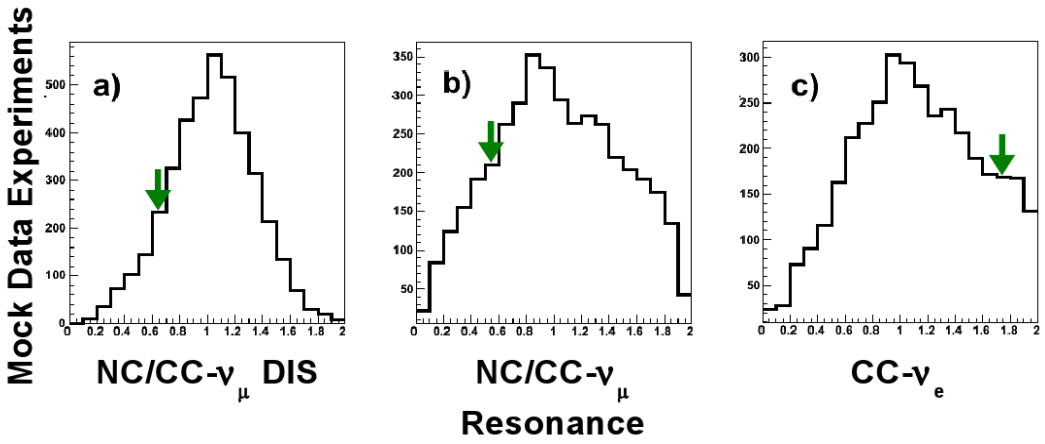

Figure 12.5: The number of mock data experiments as a function of the best-fit value for; a) the NC/CC-ν_μ DIS, b) the NC/CC-ν_μ resonance, and c) the CC-ν_e, fit parameter for an ensemble of mock data experiments. The fit configuration used for these mock data experiments, which also includes systematic fit parameters for the EM energy scale and "t1" of the hadronization model, is also used to fit the data. Arrows indicate the best-fit points for the fit to the data.

well within the limits set by the mock data experiments. This is evidence that the mock data was able to replicate the data, and thus the data and the standard MC agree within systematic errors. It is also an indication that the best-fit values for the fit parameters are within reason, and the next step in the analysis can be executed.

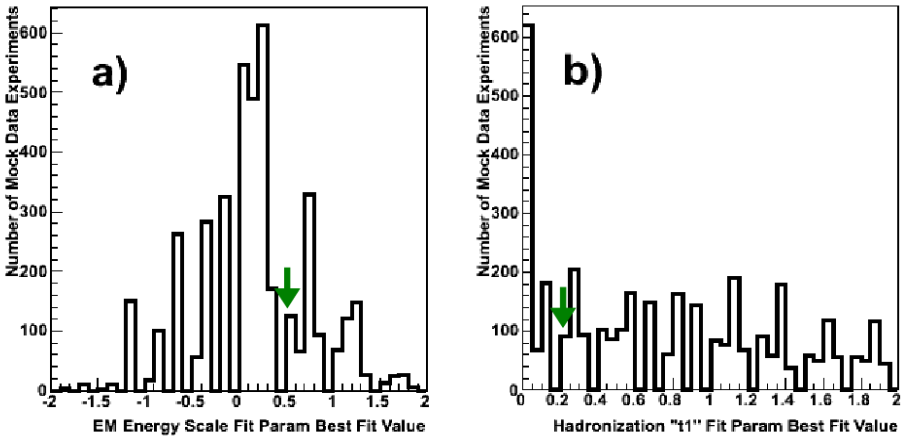

Figure 12.6: The number of mock data experiments as a function of the best-fit value for the systematic fit parameters for: a) the EM energy scale, and b) "t1" of the hadronization model. The shapes of the distributions reflect the input values for the systematic fluctuations induced by the mock data creation procedure. The systematic fit parameters scale as the number of standard deviations, σ, from the nominal value used in the standard MC. Arrows indicate the best-fit points for the fit to the data.

The reduced χ^2 for two statistically different samples is usually compared with 1.0 to determine the goodness-of-fit. In this case the χ^2 formulation is based on Poisson statistics, and not the usual Gaussian formulation, and the comparison to 1.0 is not necessarily valid. Instead, it is better to compare the χ^2/ndf resulting from the fit to the data to the distribution of the number of relevant mock data experiments as a function of χ^2/ndf. The fit to the data returned a reduced χ^2 of 1.76 which is also compared with the χ^2/ndf values resulting from the relevant ensemble of mock data experiments in Fig. 12.7. The best-fit values for the fit parameters, and the reduced χ^2 from the fit to the data appear reasonable when compared with the results obtained with the corresponding ensemble of mock data experiments.

The initial fit was performed using the χ^2/ndf minimization algorithm. As a cross check, the fits were repeated using a grid search over a limited range of

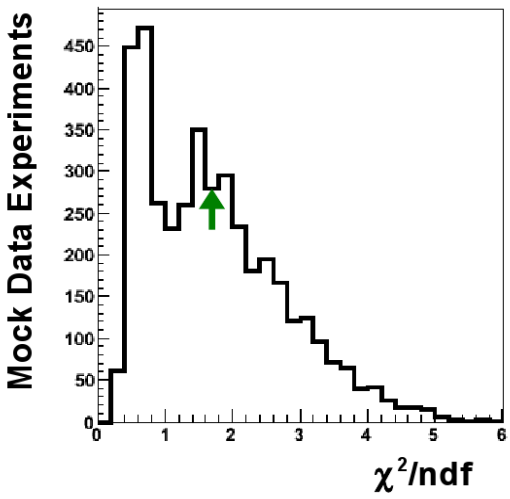

Figure 12.7: The number of mock data experiments as a function of the reduced χ^2 value peaks near 0.6, and falls off linearly. The arrow indicates the χ^2/ndf for the fit to the data.

fit parameter values. The results of the second fit confirmed the results of the initial fit, returning the same fit parameter values and χ^2. The grid search yielded a set of $\Delta\chi^2$ contours and surfaces, which are displayed in Fig. 12.8. Each plot displays $\Delta\chi^2$ for either one or two parameters. The parameters that are not displayed in each of the plots are treated as nuisance parameters and are marginalized.

Each of the single fit parameter plots displayed along the diagonal of Fig. 12.8 contains a dashed line. These lines represent a $\Delta\chi^2$ value of 1.0, and the points of intersection with the $\Delta\chi^2$ contour denote the 68% confidence interval for that fit parameter. The two-dimensional, off-diagonal plots display the covariance between pairs of fit parameters. The black contours enclose the 68%, 90%, and 99% confidence contours in each pair of fit parameters.

As a cross check the fits were performed with other fit configurations to examine the sensitivity to the fit configuration. The fractional difference between the the primary fit result and the result from these alternative fit configura-

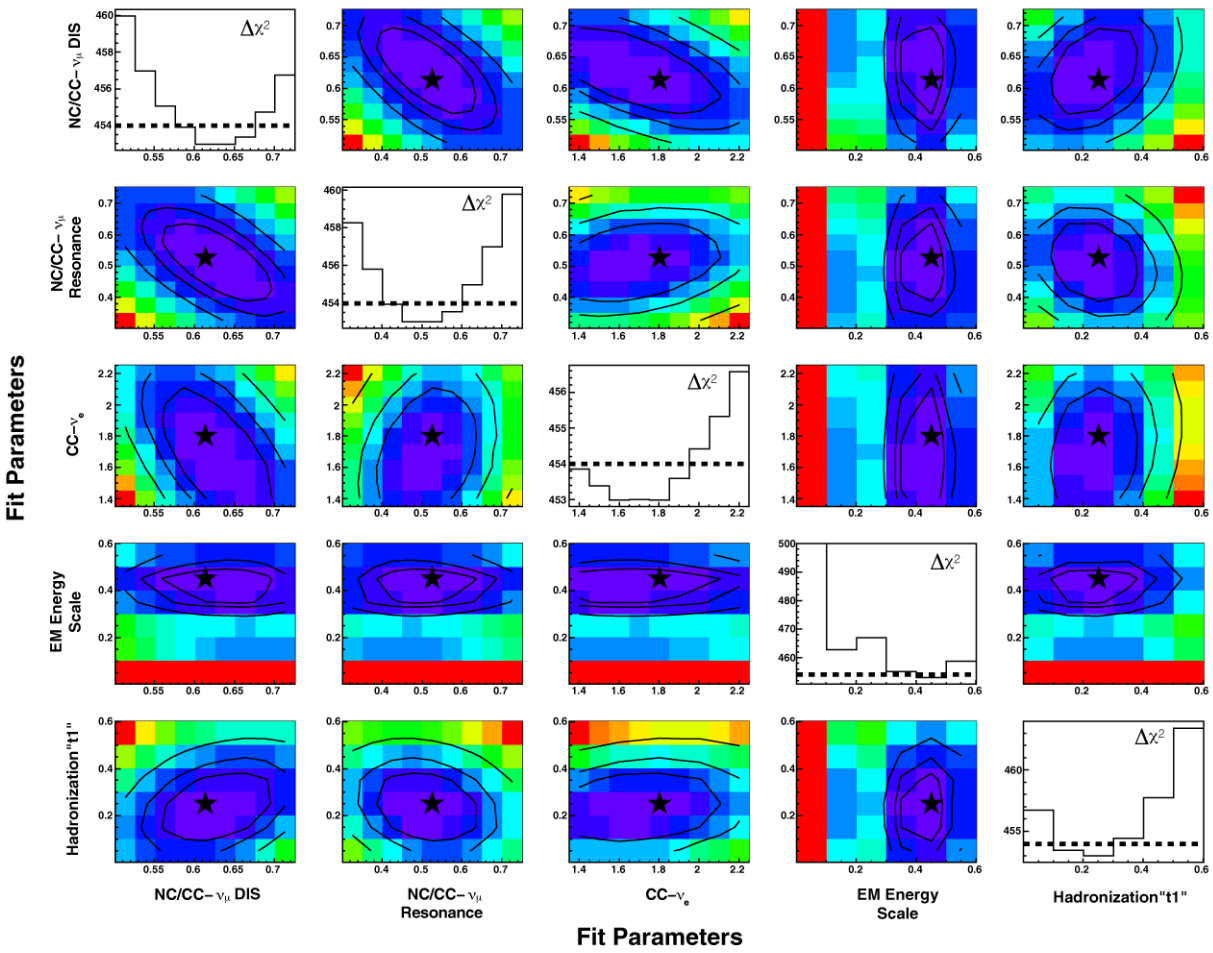

Figure 12.8: The $\Delta\chi^2$ contours and surfaces resulting from the fit to the data. The contours along the diagonal show the χ^2 for individual fit parameters; the other fit parameters are treated as nuisance parameters, and are marginalized. The horizontal dotted lines denote a $\Delta\chi^2$ of 1.0, and the points of intersection between the χ^2 distributions and the dashed lines correspond to the 68% confidence intervals for the best-fit values of the fit parameters. The off-diagonal plots display the $\Delta\chi^2$ (color axes), and best-fit points (stars) for combinations of two fit parameters. The solid lines denote the 68%, 90%, and 99% confidence level contours corresponding to $\Delta\chi^2$ values of 2.41, 4.61, and 9.21, respectively. The level of covariance between the fit parameters can be deduced from the shape of the confidence level contours. For example, an increase of the NC/CC-ν_μ DIS fit parameter would induce a decrease in both the NC/CC-ν_μ resonance and the CC-ν_e fit parameters.

tions, which include *i*) fits performed with other (combinations of) systematic fit parameters, *ii*) fits performed with fit MC where the MRCC reweighting had not been applied, and *iii*) fits performed using only half of the bins in the sideband. For the former the Angle-vs-Energy histogram was divided into two groups in a "checkerboard" pattern. The fits was performed with one group of bins, and then repeated using the other group. All of the considered fit configurations returned an event rate within $\pm 3\%$ of the primary result. All of the cross checks possible without unblinding the data yielded satisfactory results. Subsequently data in the signal region was unblinded so that the remainder of the fitting procedure could be completed.

12.2 Results

The fit to the data yielded a good match between the data and the background MC in the sideband as measured by the reduced χ^2, and as confirmed by visual inspection. The resulting best-fit values for the fit parameters are within the range of reasonable values from mock data experiments, and the fit results are robust to reasonable changes in the fit configuration. At this point the best-fit values for the fit parameters are used to extrapolate the background Angle-vs-Energy distributions into the signal region. Fig. 12.9 shows the Angle projections of the entire Angle-vs-Energy histograms for the data, the best-fit MC backgrounds, and the sum of the best-fit MC backgrounds. The difference between the data and the sum of the backgrounds is the measured number of coherent events in the selected sample. In Fig. 12.10 the individual backgrounds are removed and the difference between the data and the best-fit MC backgrounds is displayed in the solid black histogram. The

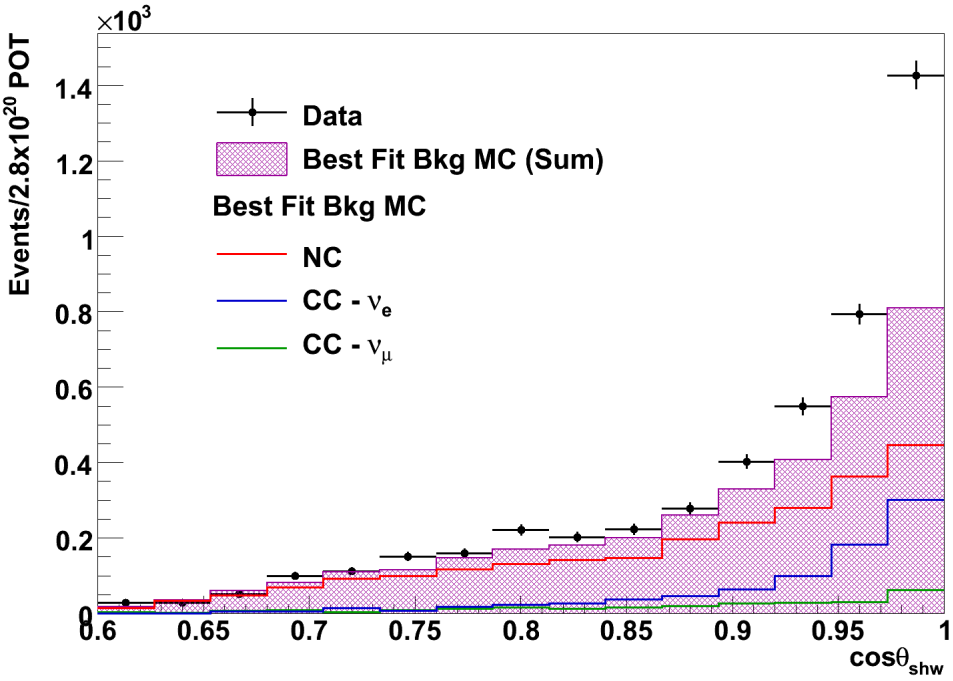

Figure 12.9: Angle projections of the entire Angle-vs-Energy histograms for the data sample, for the best-fit MC backgrounds, and for sum of the the best-fit MC backgrounds. The data and the sum of the best-fit MC backgrounds agree for small values of Angle, where a limited contribution from the signal is expected.

measured event rate in the selected sample is compared with the Rein-Sehgal prediction displayed in the dashed black histogram.

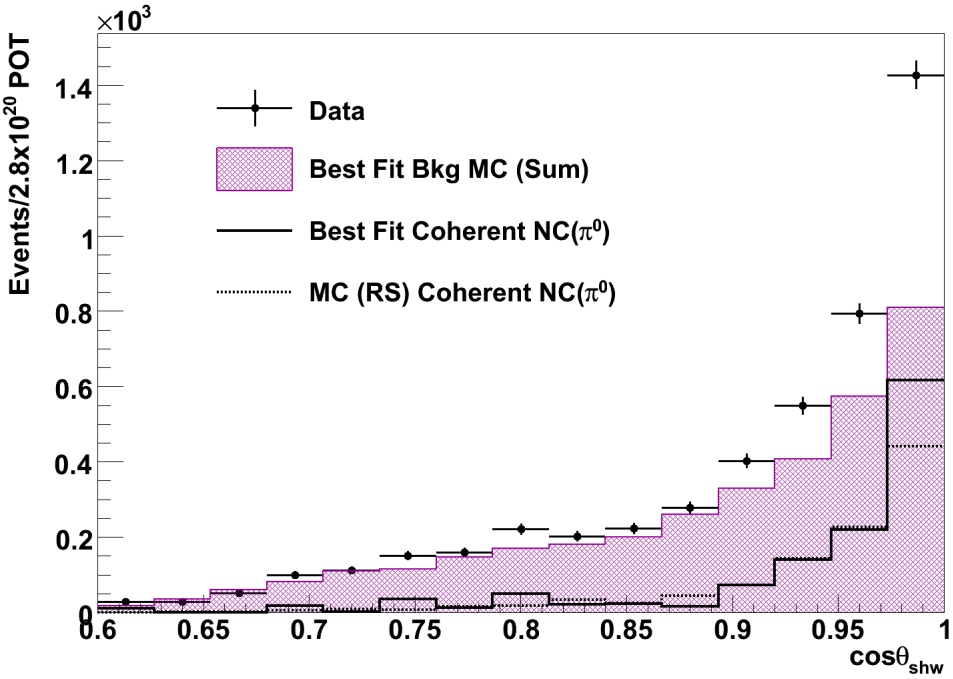

Figure 12.10: Angle projections of the entire Angle-vs-Energy histograms for the data sample, and for the sum of the the best-fit MC backgrounds. The difference between the two histograms is the measured selected signal event rate (solid black). This can be compared to the MC prediction (dashed black). The measured signal event rate and the Rein-Sehgal prediction agree for most values of Angle. However, an excess of signal events is measured for small opening angles.

Again, the near-PID sample can be used as a cross check. In Fig. 12.11 the Angle projection of the entire Angle-vs-Energy histogram for the near-PID sample is shown. The sum of the best-fit MC backgrounds (magenta) is subtracted from the data (circles). The result is the measured number of coherent NC(π^0) events in the near-PID sample (solid), which can be compared with the corresponding MC prediction (dashed). The measured number of coherent NC(π^0) events in the near-PID sample is in good agreement with the MC prediction, except at large values of Angle, where an excess is observed. This

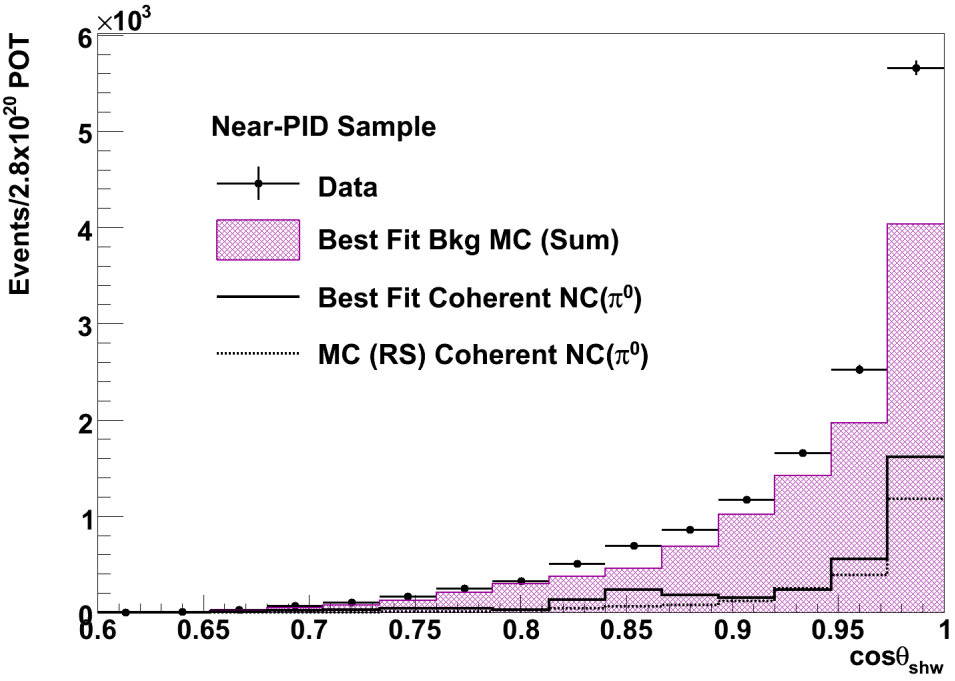

Figure 12.11: Angle projections of the entire near-PID Angle-vs-Energy histograms for the data sample (circles), and for the sum of the the best-fit MC backgrounds (magenta). The difference between the two histograms is the measured near-PID signal event rate (solid). This can be compared to the MC prediction (dashed). The measured signal event rate and the Rein-Sehgal prediction agree for most values of Angle. However, an excess of signal events is measured for small opening angles, which is in agreement with what is observed in the selected sample.

trend is in agreement with what is observed in the selected sample. A small excess is also seen between Angle values of 0.8 and 0.9, but can be accounted for by a statistical fluctuation. The signal to background ratio in the near-PID sample, as shown in Fig. 12.11, is less than the signal to background ratio in the selected sample, as shown in Fig. 12.10. The lower signal to background ratio increases the uncertainty on the measured signal content of the near-PID sample, and incorporation the information displayed in Fig. 12.11 into the signal extraction would increase the total uncertainty on the measured event rate, and the measured cross section. However, inclusion of the sideband region of the near-PID sample in the fits decreased the uncertainty, by providing more information to the fit, and the use of the near-PID region as a cross check has increased confidence in the result.

The number of events in the the selected sample best-fit MC, the selected data sample, and the measured number of selected coherent NC(π^0) events can also be displayed as a function of η. Figure 12.12 shows the best-fit backgrounds and their sum. The error bars on the sum reflect the 68% confidence intervals from the single fit parameter $\Delta\chi^2$ contours of Fig. 12.8 propagated to each background. Shown in Fig. 12.13 is the sum of the best-fit background MC of Fig. 12.8 compared with the selected data sample, both as functions of η. The difference between the two histograms is the selected coherent NC(π^0) sample, displayed as the solid black histogram, which can be compared to the Rein-Sehgal prediction of the standard MC displayed as the dashed black histogram. The errors on the measured coherent NC(π^0) sample are quadrature sum propagated from the statistical uncertainty on the data and the fit errors on the sum of the backgrounds. The measured number of coherent NC(π^0) events is consistent with the MC, within the fit uncertainties, for all but the first two bins in η. Below $\eta = 0.1$ however, there is an excess of roughly 2 σ

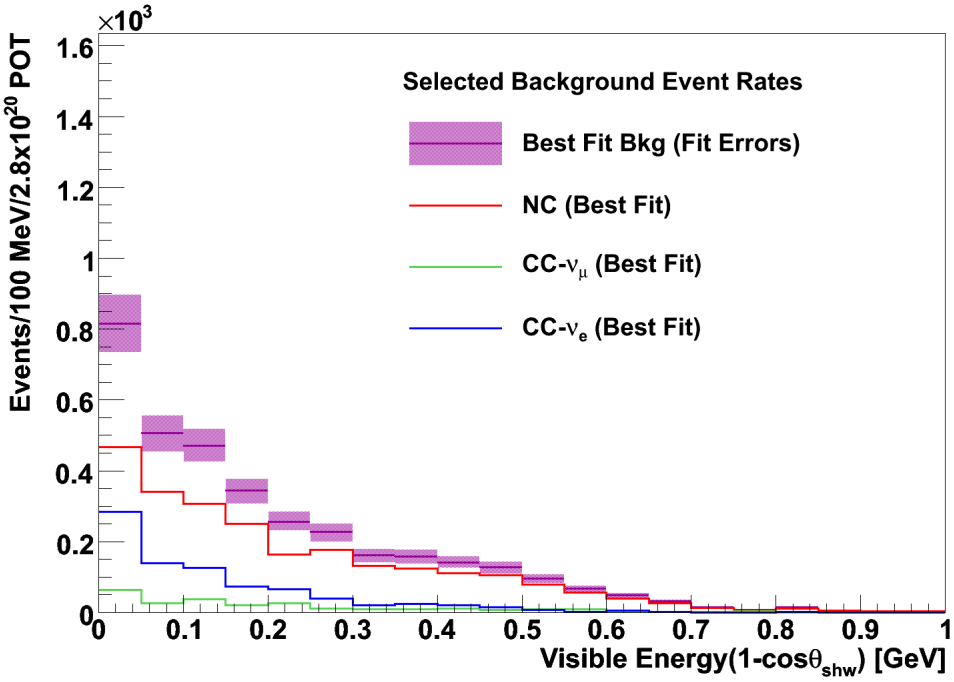

Figure 12.12: The η distribution for the best-fit MC backgrounds, and their sum. The errors on the sum of the backgrounds are assigned based on the 68% confidence intervals of the fits parameters calculated from the plots along the diagonal of Fig. 12.8.

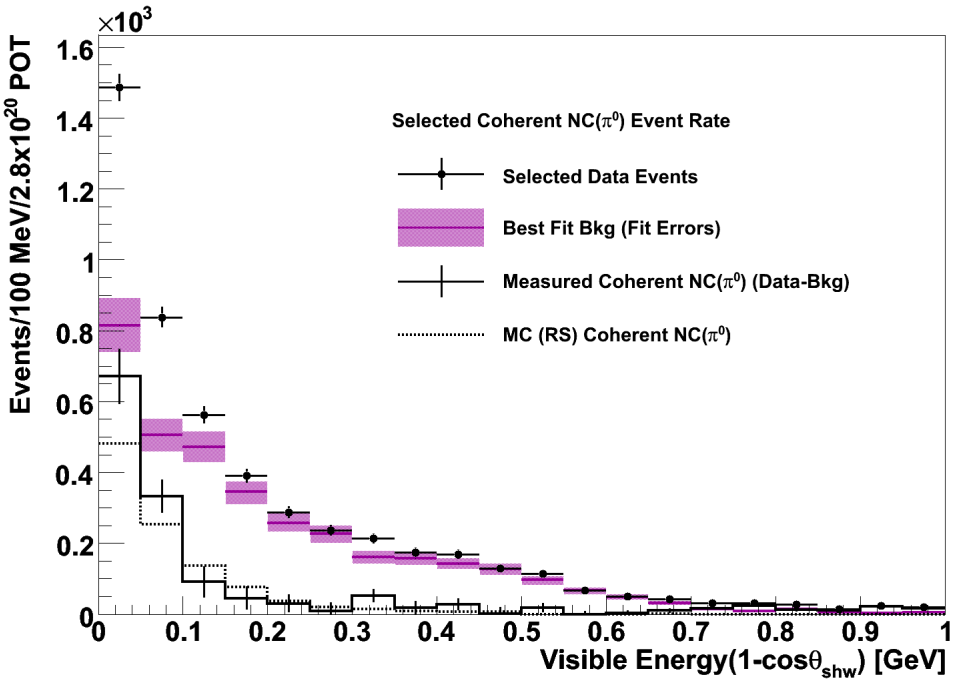

Figure 12.13: The η distribution for the data and for the sum of the best-fit MC backgrounds. The difference between the two distributions is the measured coherent NC(π^0) event rate for the selected sample (solid black histogram). The signal events rate can be compared the the MC prediction (dashed black histogram). The errors on the measured coherent NC(π^0) event rate of the selected sample are propagated from the fit errors assigned to the backgrounds plus the statistical errors on the data.

above the MC estimate which is based upon the Rein-Sehgal model. To recover the total coherent NC(π^0) events rate the acceptance corrections must be applied. Figure 12.14 shows the acceptance corrected measured coherent NC(π^0) event rate as a function of η (black crosses). The error bars shown are

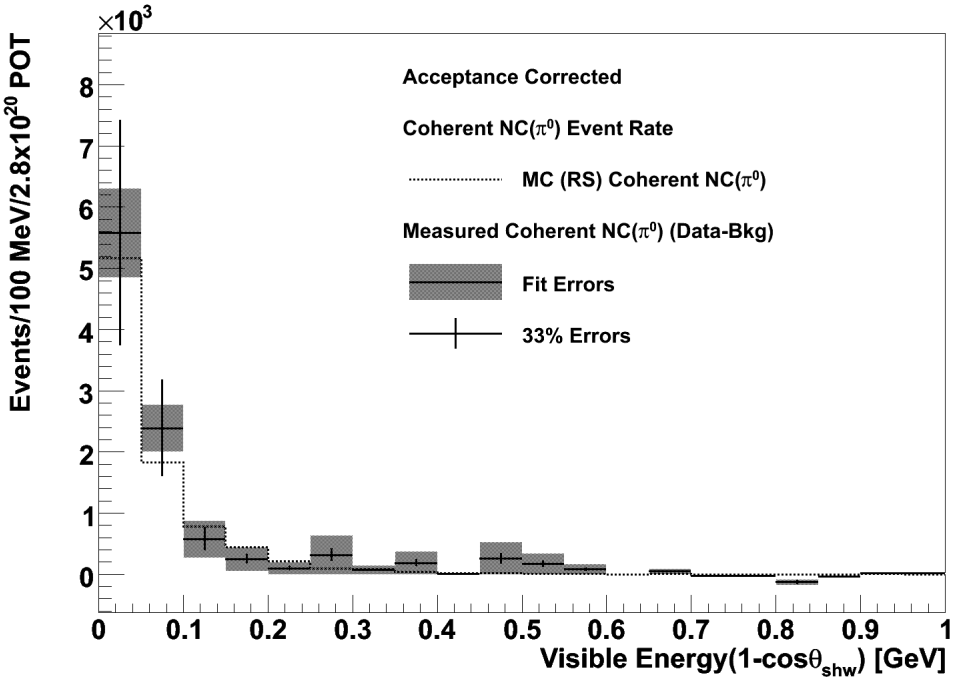

Figure 12.14: The η distribution for the acceptance corrected coherent NC(π^0) event rate, and the total MC signal event rate. The solid gray error bars on the measured coherent NC(π^0) event rate of the selected sample are propagated from the fit errors assigned to the backgrounds, the statistical errors on the data, and the acceptance correction. The black line error bars display the 33% uncertainty assigned to the cross section measurement.

the propagated fit errors combined with the additional uncertainty from the acceptance correction. The solid error bars represent the 33% uncertainty to be applied to the cross section measurement. In the first two bins of η, the mock data uncertainties are roughly double the fit uncertainties. However, the fit uncertainties are larger than 33% for the rest of the bins. The total uncertainty based on the fit errors is 29% which agrees well with the 30% uncertainty determined from the individual errors on thousands of mock data

experiments. Also displayed is the coherent NC(π^0) event rate for the entire MC sample (dashed black histogram). Again, there is an excess in the first two bins, while the two distributions are well matched for $\eta > 0.10$

The acceptance-corrected Angle projection for the Angle-vs-Energy histogram is shown in Fig. 12.15, along with the corresponding MC prediction. The

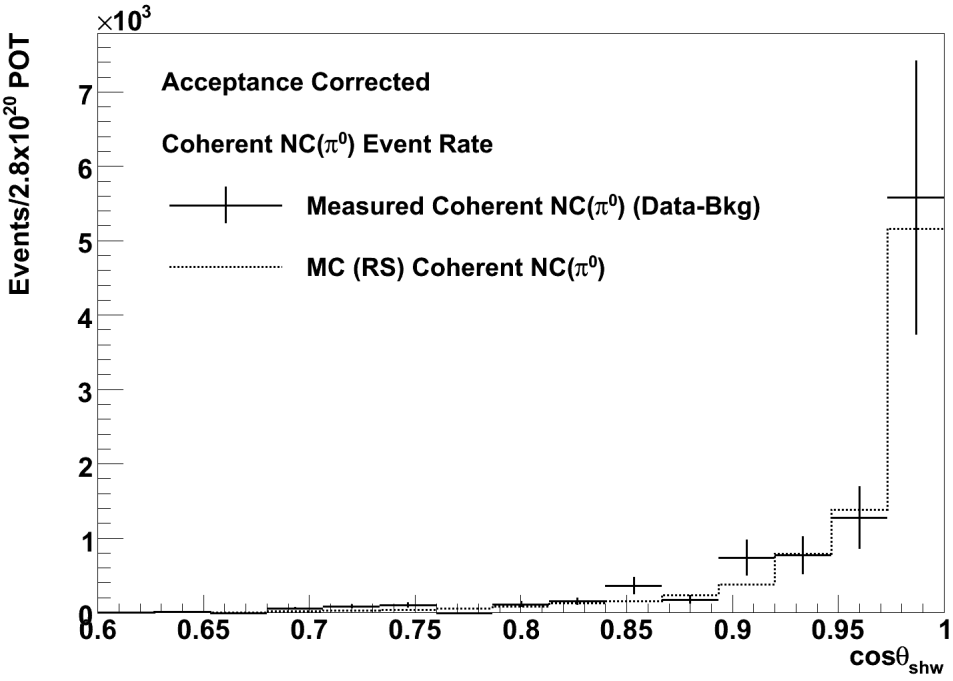

Figure 12.15: The Angle projection of the Angle-vs-Energy distribution with the bin-by-bin acceptance correction applied. The error bars display the 33% uncertainty assigned to the cross section measurement. The dashed histogram is the Angle distribution for the MC prediction for the total coherent NC(π^0) event rate.

error bars reflect the 33% uncertainty on the cross section. The excess seen in the η distributions is reflected in the far right Angle bin. A similar plot for the Energy projection is shown in Appendix F. The final step is to apply the overall acceptance correction to the bin-by-bin acceptance-corrected coherent NC(π^0) event rate shown in the previous two plots. The result is the measured total coherent NC(π^0) event rate in the MINOS Near Detector Run I + Run II

data sample. For events producing pions with an energy greater than 1.0 GeV, $N^{Coh} = 9241 \pm 2957$ events. This is an excess of 16% above the Rein-Sehgal prediction of 7971 events. The procedure outlined in Chapter 3.4 is used to convert the event rate to a cross section via

$$\langle \sigma \rangle = \frac{N^{Coh}}{\mathcal{E}\mathcal{M}_T \Phi} \tag{12.1}$$

where the integrated flux, Φ, is $2.93 \times 10^{-8} \nu/\text{cm}^2/\text{POT}$, the neutrino exposure is 2.8×10^{20} POT, and the number of nuclei in the fiducial mass is 3.57×10^{29} nuclei. The nuclei are comprised of roughly 80% iron, and 20% carbon, yielding an average nuclear mass of 48, corresponding to the atomic weight of titanium. The cross section on a titanium-like nucleus is therefore

$$\begin{aligned} \langle \sigma \rangle &= \frac{9241 \pm 2957}{(2.8 \times 10^{20}) \times (3.57 \times 10^{29}) \times (2.93 \times 10^{-8})} \\ &= (31.6 \pm 10.5) \times 10^{-40} \text{cm}^2/\text{Ti}^{48}\text{nucleus} \ . \end{aligned} \tag{12.2}$$

The average neutrino energy is 4.9 GeV, and 68% of the total neutrino flux occurs between the energies of 2.4 GeV and 9.0 GeV. The NEUGEN3 prediction for the coherent NC(π^0) cross section on titanium at a neutrino energy of 4.9 GeV is 27.9×10^{-40} cm^2/Ti^{48} nucleus. This cross section calculation only includes interactions that produce pions of at least 1.0 GeV by setting the appropriate limits of integration over ν, the energy transfer to the hadronic system. The average nucleus assumption can be checked by comparing the cross section on titanium with the average cross section of iron and carbon, weighted to the relative number of nuclei: 26.8×10^{-40} cm^2/nucleus, according to NEUGEN3. As expected the cross section calculated using the average nucleus is a slight over-estimate of the average cross section because the cross section does not scale linearly with A. The NEUGEN3 predictions are also

consistent with the cross section determined from the MC event rate of 7971, which yields

$$\begin{aligned}\langle\sigma\rangle &= \frac{7971}{(2.8\times10^{20})\times(3.57\times10^{29})\times(2.93\times10^{-8})} \\ &= 27.2\times10^{-40}\text{cm}^2/\text{nucleus}\ .\end{aligned} \tag{12.3}$$

In order to determine the coherent NC(π^0) cross section on iron (and carbon) an estimate for the relative cross sections must be used to determine which fraction of the coherent NC(π^0) interactions took place on iron, which corresponding event rate fraction for carbon. To first order this ratio should be model independent, but the nuclear models of competing theories of the coherent interaction predict different A dependencies. The ratio of the coherent NC(π^0) on iron to the coherent NC(π^0) cross section on carbon for a neutrino energy of 4.9 GeV, as determined by NEUGEN3, is 2.18. The uncertainty on the cross section ratio is estimated from comparisons with competing models to be 20%. Again, this uncertainty results from the different A dependencies of the nuclear models.

The cross section ratio at 4.9 GeV, combined with the number of iron nuclei (2.89×10^{29}), and the number of carbon nuclei (6.57×10^{28}) can be used to calculate the relative fraction on interactions on iron and carbon. Interactions on iron account for 90.6% the total event rate, while the other 9.4% of coherent NC(π^0) neutrino interactions occur with carbon nuclei. Using the corrected event rate and the number of iron nuclei the measured cross section on iron is

$$\begin{aligned}\langle\sigma\rangle &= \frac{(9241\pm2957)\times(0.906\pm0.015}{(2.8\times10^{20})\times(2.89\times10^{29})\times(2.93\times10^{-8})} \\ &= (35.3\pm12.4)\times10^{-40}\text{cm}^2/\text{Fe}^{56}\text{nucleus}\ .\end{aligned} \tag{12.4}$$

The error bars include propagation of the 20% error assigned to the iron-

to-carbon cross section ratio, plus the 33% error from conversion of event rate to cross section. Calculation of the cross section on iron from the MC event rate of 7971 events yields a value of 30.5×10^{-40} cm^2/Fe^{56} nucleus. The NEUGEN3 prediction of for the cross section on iron at 4.9 GeV is 30.3×10^{-40} cm^2/Fe^{56} nucleus. A similar calculation for the fraction of interactions on carbon yields

$$\begin{aligned}\langle\sigma\rangle &= \frac{(9241 \pm 2957) \times (0.094 \pm 0.015)}{(2.8 \times 10^{20}) \times (6.57 \times 10^{28}) \times (2.93 \times 10^{-8})} \\ &= (16.1 \pm 8.5) \times 10^{-40}\text{cm}^2/\text{C}^{12}\text{nucleus}\ .\end{aligned} \tag{12.5}$$

Again, the uncertainty includes the propagation of the 20% error on the cross section ratio. The MC cross section implied by the event rate is 13.9×10^{-40} cm^2/C^{12} nucleus, which agree with the NEUGEN3 cross section on carbon at 4.9 GeV of 13.9×10^{-40} cm^2/C^{12} nucleus.

12.3 Discussion

A signal for neutrino-induced NC(π^0) production is observed in the relevant kinematic regime as an excess of events of three standard deviations above background. The reaction cross section, averaged over a ±1 σ energy window of $2.4 \leqslant E_\nu \leqslant 9.0$ GeV is determined to be $(31.6\pm10.5)\times10^{-40}$ cm^2/nucleus. The result is the first evidence obtained for neutrino-nucleus coherent NC(π^0) scattering on iron, and is the first measurement for an average nuclear target above $A = 30$. The cross section is in agreement with NEUGEN3 implementation of the model by Rein and Sehgal which is motivated by the PCAC hypothesis. The result is also consistent with the more recent Berger-Sehgal model, which incorporates the Rein-Sehgal model and several improvements

that provide better agreement with data.

The shapes of the distributions of the measured coherent NC(π^0) event rate as functions of Angle, Energy, and η are consistent with theory. The MINOS data however, suggests an excess event rate at low energies and small angles compared to that predicted by the original Rein-Sehgal model. The kinematic signature of the excess events is in agreement with the Berger-Sehgal model which predicts similar event rate distributions as functions of the relevant variables. The PCAC hypothesis has been called into question since its inception. The success of the PCAC-based coherent models in describing the data suggest the theory is valid within appropriate kinematic regimes, and can be trusted in other applications.

Table 2.1 and Fig. 2.1 have been updated to include the MINOS results. The revised Table displays the MINOS cross section result and the corresponding MC prediction for the cross section on a titanium-like nucleus, on iron nuclei, and on carbon nuclei. The NOMAD collaboration reports a cross section on a carbon-like nucleus ($A = 12.8$) at an average $E_\nu = 24.8$ GeV of $(72.6\pm10.6)\times10^{-40}$ cm^2/C$^{12.8}$ nucleus. They compare their measurement to 78×10^{-40} cm^2/C$^{12.8}$ nucleus, the prediction of their MC, which is based upon the Berger-Sehgal model. NEUGEN3 predicts a corresponding cross section of 52×10^{-40} cm^2/C$^{12.8}$ nucleus. The NOMAD MC prediction for the cross section is roughly 50% greater than the MINOS MC prediction. This is not surprising given that evaluation of the Berger-Sehgal model on iron for this Thesis showed that it predicts 45% more events than the MINOS MC. Most of the data, including the MINOS result, are compatible with the larger cross sections predicted by the Berger-Sehgal model.

NEUGEN3 cross sections and estimates of the Berger-Sehgal cross sections cal-

Experiment	Year	Average Neutrino Energy, $\bar{E}_\nu$ [GeV]	Average Nucleus $\mathcal{A}$ [nucleons]	Minimum π^0 Energy, $E_{\pi^0}^{min}$ [GeV]	Coherent Cross Section, σ^{coh} $\nu/(\bar{\nu})$ $[10^{-40}\text{cm}^2/A]$	Rein-Sehgal (NEUGEN3) Cross Section $[10^{-40}\text{cm}^2/A]$
Aachen-Padova [12]	1983	2	Aluminum 27	0.0	29±10 (25±7)	19.0
Gargamelle [13]	1984	2	Freon CF_3Br - 30	0.0	31±20 (45±24)	27.7
CHARM [14]	1985	31 24	Marble $CaCO_3$ - 20	6.0	96±42 (79±26)	84.5
SKAT [15]	1986	7	Freon CF_3Br - 30	0.0	52±19	44.5
15' BC [16]	1986	20	Neon NeH_2 - 20	2.0	RSx0.98±0.24	66.0
MiniBooNE [18]	2008	0.8	Mineral Oil C_XH_Y - 12	0.0	RSx0.65±0.14 RSx0.65±0.14	4.4
NOMAD [17]	2009	24.8	Carbon+ 12.8	0.5	72.6±10.6	52.1
SciBooNE [19]	2010	0.8	Polystyrene C_8H_8 - 12	0.0	RSx0.96±0.20	4.4
MINOS	2010	4.9	Iron & Carbon - 48	1.0	31.6±10.5	26.8
MINOS	2010	4.9	Iron 56	1.0	35.3±12.4	30.3
MINOS	2010	4.9	Carbon 12	1.0	16.1±8.5	13.9

Table 12.1: Summary of coherent NC(π^0) searches, including the MINOS result. Several experiments only provide a ratio to the Rein-Sehgal prediction for the coherent NC(π^0) cross section. These results are displayed as RSx the fractional cross section. Coherent scattering off hydrogen is not defined, as a single nucleon cannot be in a coherent state. Hydrogen nuclei, therefore, do not contribute to the event rate, and are not included in the calculation of A.

culated for events that produce single π^0 mesons of energies exceeding 1.0 GeV are displayed as a function of E_ν in Fig. 12.16. The cross sections are drawn for nuclei of $A = 12$, $A = 48$, and $A = 56$, corresponding to the three coherent NC(π^0) cross sections calculated from the MINOS data, which are also displayed. The three points correspond to an E_ν of 4.9 GeV, and are shifted for display purposes.

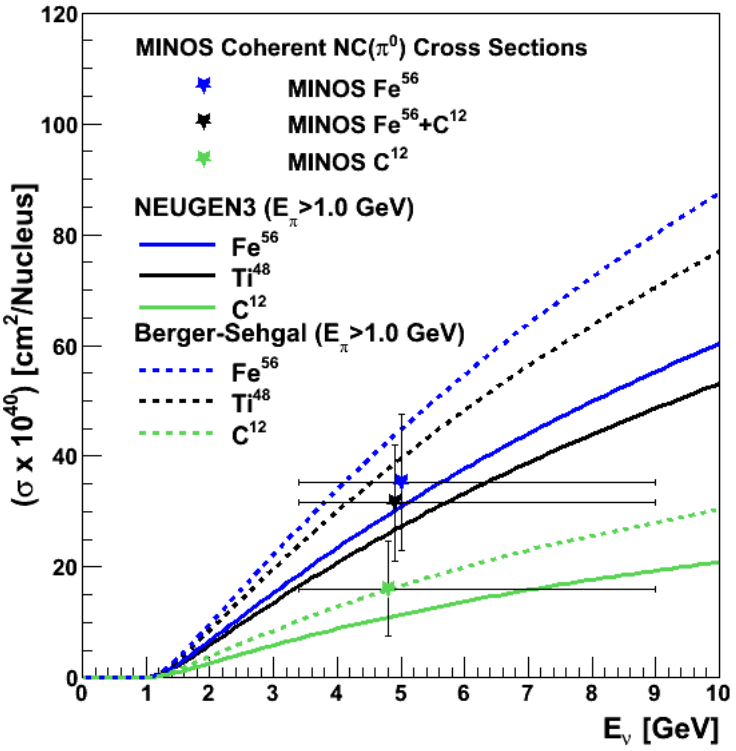

Figure 12.16: Measurements of the coherent NC(π^0) cross section from MINOS data. Accompanying cross section curves as a function of neutrino energy from NEUGEN3, and from estimates of the Berger-Sehgal model, are shown for comparison. The cross section curves are calculated from interactions that produce pions with an energy exceeding 1.0 GeV. The MINOS measurements are consistent with both models. Horizontal error bars denote the ± 1 σ energy range of the NuMI neutrino flux. The measurements are all at 4.9 GeV, and the points are shifted horizontally for display purposes.

Figure 12.17 shows the NEUGEN3 cross section as a function of neutrino energy. An estimate of the Berger-Sehgal cross section calculated by scaling the

NEUGEN3 cross section up by 45% is also displayed. The scaled Berger-Sehgal cross section agrees with the reweighed MINOS MC, and with the reported NOMAD MC cross section for A =12.8 and E_ν =24.8 GeV. It also agrees with with the cross section on Aluminum at E_ν =2.0 GeV of 33×10^{-40} cm^2/Al^{27} nucleus reported in the original paper by Rein and Sehgal corresponding to the Aachen-Padova measurement. The plot also shows the results from all published papers on coherent NC(π^0) interactions. The measurements from the 15-ft. Bubble Chamber, MiniBooNE, and SciBooNE are given as a fraction of the Rein-Sehgal cross section. These data points, displayed by green symbols, are scaled to the NEUGEN3 cross section. The MINOS data point has been scaled up to account for events that produce pions with an energy less than 1.0 GeV. The additional uncertainty from this correction has been propagated to the error bars.

The cross section measurements can also be plotted as a function of mass of the target nuclei, A. Figure 12.18 displays the NEUGEN3 and Berger-Sehgal cross sections for 4.9 GeV as functions of A. As previously, these curves display the cross section for interactions that produce a pion with an energy of at least 1.0 GeV to be compared with the MINOS result. Three points are displayed for MINOS, one for each target nucleus. The cross section on the titanium-like target has the smallest fractional uncertainty, at 33%. The cross section on iron has a fractional uncertainty of 35%, and the cross section on carbon has a fractional uncertainty of 53%. A larger error is incurred by propagation of the added uncertainty on the NEUGEN3 cross section ratio used in the calculations.

Figure 12.19 displays the full NEUGEN3 and Berger-Sehgal cross sections as functions of A. Superimposed are the results of all previous experiments which

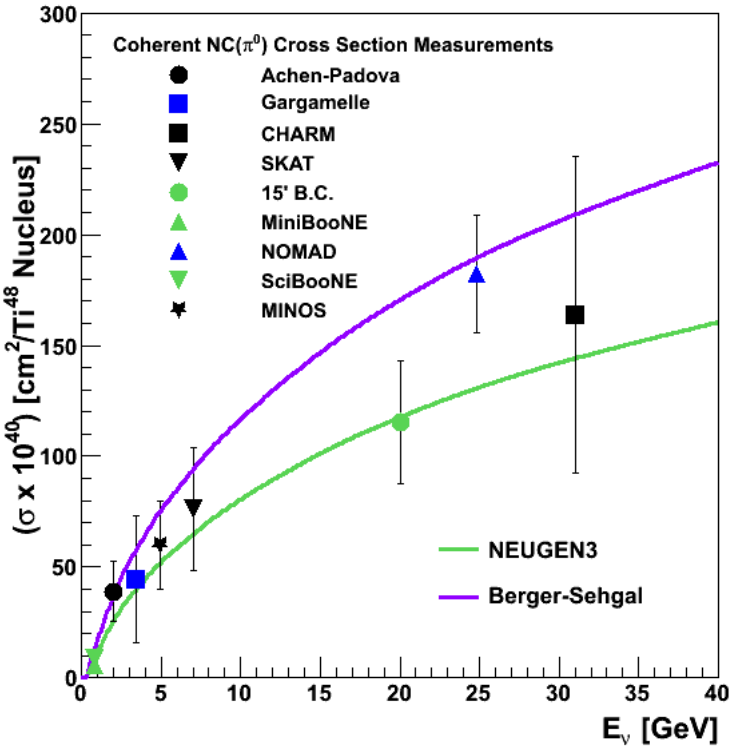

Figure 12.17: Selected cross section measurements for neutrino coherent NC(π^0) scattering scaled to titanium as a function of neutrino energy. The solid (green) line is the NEUGEN3 prediction for the neutrino-carbon coherent NC(π^0) scattering cross section as a function of neutrino energy. The MiniBooNE, SciBooNE, and the 15-ft. Bubble Chamber results have been scaled to the NEUGEN3 cross section prediction. The MINOS result (solid star) is compared with the cross section for interactions that produce a pion with an energy greater than 1.0 GeV. The MINOS measurement (solid star) appears slightly above the NEUGEN3 prediction.

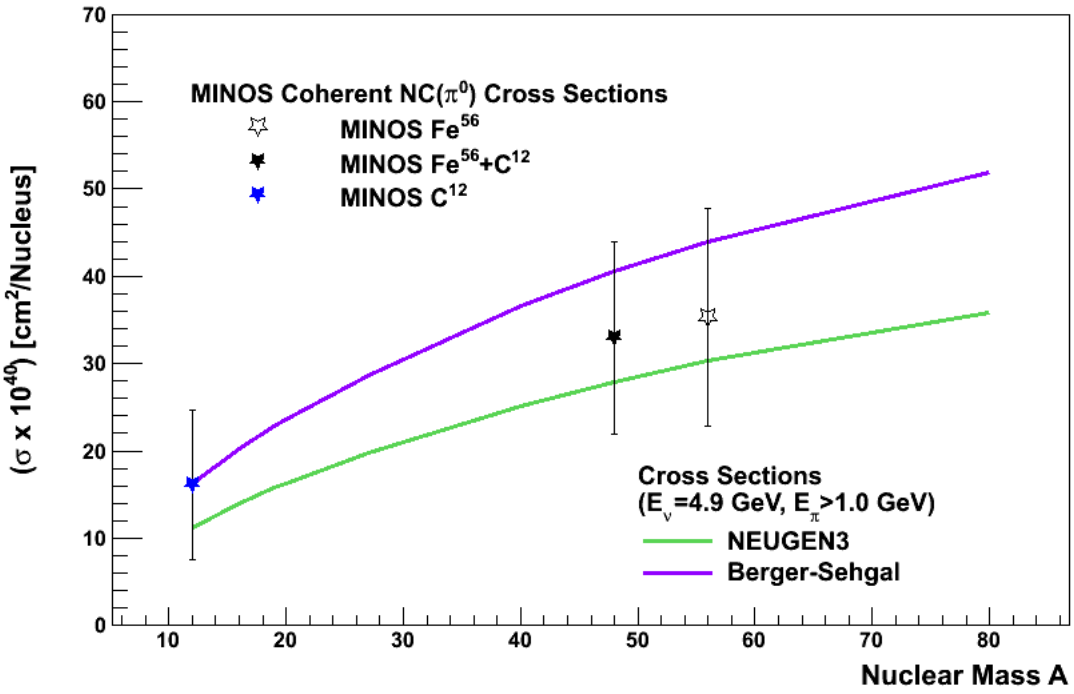

Figure 12.18: MINOS cross section measurements for neutrino coherent NC(π^0) scattering at 4.9 GeV, the average MINOS neutrino energy. The solid (green) line is the NEUGEN3 prediction for the neutrino-carbon coherent NC(π^0) scattering cross section, as a function of nuclear mass, A, for events that produce π^0 mesons with $E_\pi > 1.0$ GeV. The measured MINOS cross sections on titanium-like nuclei, iron nuclei, and carbon nuclei, plotted here are consistent with both NEUGEN3 cross sections and the corresponding estimated Berger-Sehgal cross sections (purple).

measured the coherent NC(π^0) cross section. The previous measurements that were provided as a fraction of their respective MC are again scaled to the corresponding NEUGEN3 values. The three MINOS data points have been scaled to the total cross section based on the MC event rate ratio of total number of coherent NC(π^0) events to the number of events having E_π >1.0 GeV.

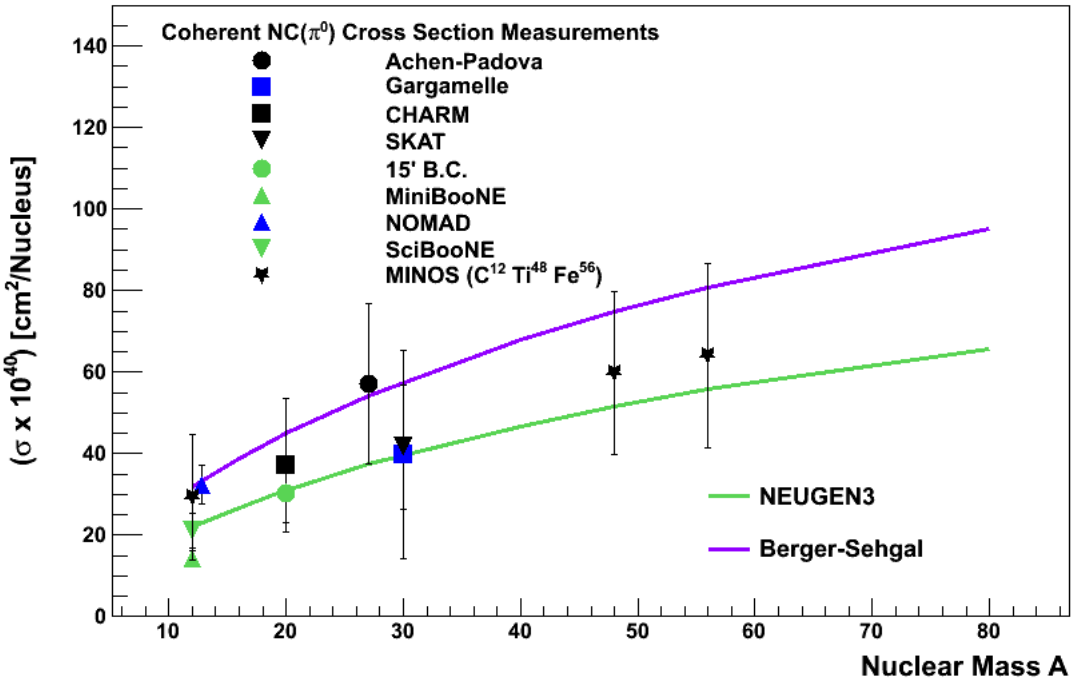

Figure 12.19: World cross section measurements for neutrino-induced coherent NC(π^0) scattering scaled to 4.9 GeV, the average MINOS neutrino energy. The solid (green) line is the NEUGEN3 prediction for the neutrino-carbon coherent NC(π^0) scattering cross section, as a function of nuclear mass, A. The purple curve is the estimated Berger-Sehgal cross section. The measured MINOS cross sections on titanium-like nuclei, iron nuclei, and carbon nuclei are scaled to the total cross section by the total coherent NC(π^0) relative to the $E_\pi > 1.0$ GeV event rate.

The observation of a coherent NC(π^0) signal in MINOS represents the first instance of a MINOS analysis using electromagnetic shower events to measure a positive signal. The $\nu_\mu \rightarrow \nu_e$ oscillation search has established limits, but has not observed a signal. The coherent NC(π^0) cross section measurement demon-

strates that there is enough information contained in the shower topologies of MINOS Detector interactions to extract a physics result. The coherent NC(π^0) process represents an irreducible background for $\nu_\mu \rightarrow \nu_e$ oscillation searches. For small values of the oscillation parameter θ_{13} this background, and its associated uncertainty become important, especially for wideband beam long baseline experiments, where the NC backgrounds are large. Additional data helps to constrain possible models and to reduce the uncertainty on the cross sections, thereby increasing the sensitivity of future measurements.

The coherent cross section is expected to be the same for antineutrino-induced interactions as it is for neutrino-induced interactions. As such, a measurement with the MINOS reversed horn current data (RHC), which focuses the negative mesons produced at the target that decay into antineutrinos, should observe a similar coherent NC(π^0) event rate, with a reduced background sample. The resulting sample of signal-like events might enable a measurement with lower backgrounds, and in turn small uncertainties. Such an analysis would again test the PCAC basis for the coherent model, both at the level of the cross section and the supposition that the neutrino and antineutrino cross sections are equivalent. The analysis procedures described in this Thesis, together with the software tools that have been developed, providea n excellent foundation for a subsequent, future MINOS measurement using antineutrinos.

Appendices

Appendix A

SVM Input Attributes

Shower Size Variables:

shwfit.contPlaneCount200:	Number of continuous planes with a pulse height (PH) > 200 mips.
shwfit.contPlaneCount015:	Number of continuous planes with a PH > 15 mips.
fracvars.fract_2_planes:	Fraction of event PH in the two planes with the highest PH.
fracvars.fract_4_planes:	Fraction of event PH in the four planes with the highest PH.
fracvars.fract_6_planes:	Fraction of event PH in the six planes with the highest PH.
fracvars.fract_4_counters:	Fraction of event PH in the four strips with the highest PH.
fracvars.fract_8_counters:	Fraction of event PH in the eight strips with the highest PH.

fracvars.fract_12_counters: Fraction of event PH in the twelve strips with the highest PH.

srshower.planes: Total number of planes in the shower.

Shower Shape Variables:

shwfit.uv_molrad_vert_9s_2pe: Moliere radius from the shower vertex.

shwfit.uv_molrad_peak_9s_2pe: Moliere radius from the shower peak.

shwfit.uv_rms_9s_2pe: Shower RMS in coordinate.

shwfit.pos_E_split: Longitudinal distance between shower vertex and point at which the shower has deposited half of its energy.

shwfit.n_ratio_half: Ratio of energy deposited in first (longitudinal) half of the shower to energy deposited in second half of the shower

mstvars.ewtot+ mstvars.owtot: Sum of the weights in a minimal spanning tree formed of the total pulse heights in mips.

mstvars.eeprob+ mstvars.oeprob: Sum (u and v) of the probability that, based on fits to a minimal spanning tree, an event has an EM shower.

mstvars.ealpha+ mstvars.oalpha: Sum (u and v) of a fit parameter for a minimal spanning tree fit to the shower.

fracvars.fract_road: Fraction of the event PH in a "narrow road" along the shower centroid.

srshower.stripRatio: Number of shower strips divided by total number of strips in the event.

Shower Fits Variables:

shwfit.trans_u_sigma+
shwfit.trans_v_sigma: Sum of the spreads of Gaussian fits to the transverse shower profiles in u and v.

shwfit.trans_u_chisq+
shwfit.trans_v_chisq: Sum of the χ^2 values for the transverse shower profile fits for u and v.

shwfit.Beta_Maxwell: Fit parameter for a Maxwell distribution fit to the longitudinal shower profile.

shwfit.chisq_Maxwell: χ^2 value for the Maxwell distribution fit to the longitudinal shower profile.

shwfit.par_b: Fit parameter describing the falling edge of a Landau distribution fit to a longitudinal shower energy profile

Hadronic Activity Variables:

shwfit.vtxEnergy: Energy deposited near the event vertex.

shwfit.energyPlane1: Energy deposited in 1st plane after vertex plane.

shwfit.energyPlane2: Energy deposited in 2nd plane after vertex plane.

angcluster.weightedPH1: Sum of weighted strip PH, where the weight is a function of distance from shower highest PH strip.

angcluster.weightedPH2: Sum of weighted strip PH, where the weight is a (2nd) function of distance from shower highest PH strip.

Track Variables:

srtrack.sigmaQoverP: Measure of the track curvature.

srtrack.length: Length of the longest track in the event.

Appendix B

SVM Training and Optimization

An initial set of studies were carried out to identify a set of attributes and to evaluate the relative performace of several machine learning multivariate analysis techniques. The Weka software package [41] was used. Weka provides a large sample of easily configurable machine-learning multivariate analysis techniques; these are made accessible through a convenient GUI. Candidate attribute values and true class information for a representative event sample were extracted from MINOS root ntuples to a Weka readable format. Weka keeps the entire data sample in memory, thereby providing quick access to the training and testing samples, thus allowing relatively quick evaluation of a variety of MVAs and attribute combinations. A list of 30 attributes was selected. A brief description of each attribute is given in Appendix A. Several MVA techniques were investigated, and SVMs with the radial basis function (rbf) kernel were ultimately chosen. Although Weka works well for evaluating various MVA techniques and combinations of attributes it is not well suited for integration into minossoft because it is written in Java.

LibSVM [42] is an intergated support vector machine software package written

in the C computer language. The package includes programs for training and testing SVMs. The inputs to the training program are *i*) a list of attributes, *ii*) the identity of a kernel function and related parameters, and *iii*) parameters that define relative event weights for classes, and the strength of the penalty for misclassified events. In addition, there are data structures that contain the training data. For each event there is a list of attributes followed by a true class identifier. The training program produces an SVM "model" file which contains a function that calculates the distance from a point in attribute space to the nearest SVM border. The testing program takes the SVM model file as an input, along with a test sample. The format of the data structure for the test sample is identical to that of the training sample, except that the true class in not specified. The measured class is calculated as a function of the distance from the test point to the nearest SVM border. Events on opposing sides of a border are considered by the SVM to be of different classes. These two programs were incorporated into the minossoft coherent NC(π^0) analysis software package.

To incorporate the libSVM programs into minossoft, large pieces of code were copied and altered to read ROOT [43] ntuples, to accept arguments passed from other minossoft class, and to return quantities useful to the coherent NC(π^0) analysis. The minossoft classes that call the libSVM altered programs extract attribute and class information from ROOT ntuples and package it into libSVM data structures, which are passed to the training and testing programs. Also passed to the training programs are the values required to define the SVM kernel function. The standard output of the libSVM testing program is the measured class of each event. The program was altered to return the distance to the nearest border so that classification could be determined later based on the distance information. The sample selected by the SVM is too inclusive

and contain to high a proportion of signal-like background events. Instead, the distance information is used to choose a more selective sample which, according to MC, includes a higher proportion of true signal events.

The original training samples were derived from a randomly selected sample of the Daikon04 MINOS MC corresponding to roughly half of the total sample. There is an irreducible background sample in the MC, in which background events produce a topological signature identical to signal events, and therefore have a signal-like set of attributes. Since the SVM cannot distinguish between the signal and the irreducible backgrounds, the true class was determined by the value of the true EM shower fraction as opposed to the physics interaction category. Studies of shower topologies and SVM response determined that use of an EM shower fraction value of 0.90 provided the best distinction between signal-like and background-like events.

The distribution shapes and ranges of attributes vary widely, resulting is some attributes having more influence in the SVM training calculations. To avoid this effect, attribute values are usually scaled so as to be between two common values, such as zero and one. Effective scaling may require the tails of distributions to be cut off so as not to concentrate the majority of events contained in the distribution peak into a small fraction of the attribute range. Great care must be taken in these procedures, and they must be performed on an attribute by attribute basis.

The problem of missing attribute values is common amongst machine learning algorithms. In most cases, including SVMs, substitute values are employed as placeholders. For the analysis presented here the types of missing values were placed into one of four categories to determine the substitute value to be used. The first class of missing values are for attributes that cannot be

filled for a large fraction of the training class. For example, attributes related to reconstructed event tracks cannot be filled for events that do not contain a reconstructed track. Missing values for track attributes, or other attributes of this type, were assigned a value of minus one. This separates the training sample into two distinct populations; events with tracks will occupy different regions of attribute space from events without tracks. Events may have missing attribute values for a variety of other reasons. If the reason is indicative of a true class of signal-like events, then the missing value is assigned the average attribute value for signal-like event sample. The same holds true for background-like events. If the fact that there is a missing value does not provide any class information, the attribute is assigned the average value for that attribute across the entire sample.

Several kernel functions were investigated and studies showed that the radial basis function (rbf) kernel, which has the functional form of a Gaussian, provided the best performing SVMs. The input parameters to the SVM are the width parameter of the rbf kernel function, γ, the penalty for a misclassified event, C, and the relative weight, w, of the signal-like event class to the background-like event class. The parameter C should roughly scale inversely with number of training points, w should scale with the relative number of training events in each class, and γ should scale as the multiplicative inverse of the number of attributes. However, it is impossible to know a priori what parameter values will generate the best performing SVM for a given training sample. The common practice is to train a multitude of SVMs each with a different pair of parameters, varying the values of C and γ over many orders of magnitude. Successive grid searches converge on the values of C and γ that provide the best performing SVM.

Evaluation of the SVM performance consisted of three parts. First the SVM model was used to process the entire test sample. Next, the resulting distribution of test events as a function of the distance to the nearest SVM border was used to select samples. Event samples were selected based on the position of the events in the distance distribution with respect to a set of cut values. The purity and efficiency of each sample were used to calculate the analysis sensitivity based on Eq. (9.2). The SVM performance was taken to be the highest sensitivity that could be produced for a minimum efficiency of 10%.

The number of events in the background-like class far exceed the number of signal-like events in the standard MC, and most of the events in the background-like class are easily separated from the signal-like events. The inclusion of events that are of obvious class does not provide much benefit to the training procedure, and the cpu time involved in training an SVM increases linearly with the sample size. Support Vector Machines draw borders in the regions where both classes occupy the same volume in attribute space, and rely on the events in that volume to determine the optimal positions for the borders. Having a high density of points in these regions of "ambiguous class" will result in the best possible SVM model for separating the classes. Support Vector Machines trained using the original training samples did not produce favorable results, and improvements to the training samples were required.

A coherent NC(π^0) event enhanced MC sample was generated to increase the population of signal events in the regions of ambiguous class. Creating a coherent NC(π^0)-enhanced sample, a relatively simple task, requires restricting the event generator to a single physical process namely coherent NC(π^0) interactions. Creating a useful background-enhanced sample was more difficult because the MC does not allow for the selection of specific final states. Only a

small fraction of events from each physics process will have the attributes of an event in the ambiguous class region of attribute space. Initially, an enhanced MC sample that only included events that would pass the pre-selections cuts, based on detector position (fiducial volume) and muon momentum, was generated [44]. Next, the background-enhanced sample was classified by the best performing SVMs from the first round of training, and events with a clear background-like class were discarded. The remaining background-enhanced event sample consisted of events that were likely to be of ambiguous class. The samples used in the second round of SVM training consisted of the original MC training sample plus additional events from the enhanced signal sample and the likely-ambiguous-class subset of the enhanced background sample. For the second round of fits the w parameter was set to one, and the relative number of signal-like and background-like training events were varied instead. The SVMs produced by the second round of training performed much better than did SVMs produced in the first round of training.

The support vector machine used in the analysis was generated with $C = 6.0$, $\gamma = 0.075$, and $w = 1.0$. Several models with similar input parameters performed equally well. This particular model was chosen because the parameter values were amongst the central values of the parameter ranges that produced the high performing SVMs. Figure 6.1 displays the number of events as a function of the distance to the nearest SVM border for the data, the total MC, and the MC broken out by physics reaction category.

Appendix C

Comparison of the Signal Region of the Selected Sample with the Sideband Region

The plots of Figures C.1 through C.3 display a comparison of event rate distributions as functions of kinematic variables for the signal and sideband regions of the selected sample. The kinematic variables used are the invariant mass of the hadronic system (W^2), and the Bjorken scaling variables x and y. The implications of these distributions are discussed in the text of Chapter 6.5 where the distribution of the event rate as a function of Q^2 is also discussed.

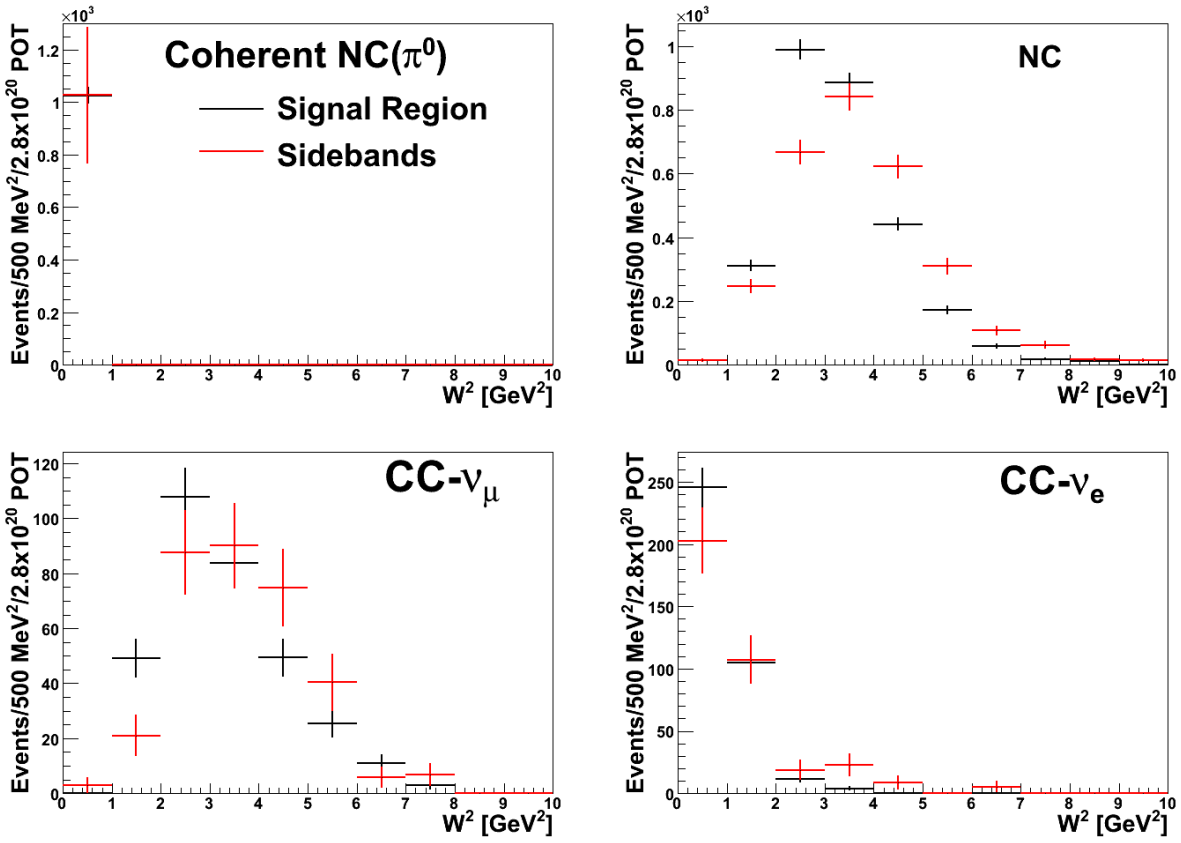

Figure C.1: The event rate distribution as a function of true W^2 for selected MC events. The plots show the number of events in the signal region (black) area-normalized to the number of events in the sideband region (red). The background distributions are peaked at higher values of W^2 in the sideband as compared with the signal region. All coherent events are assigned a W^2 value of 0.0, and the two distributions for the signal are identical.

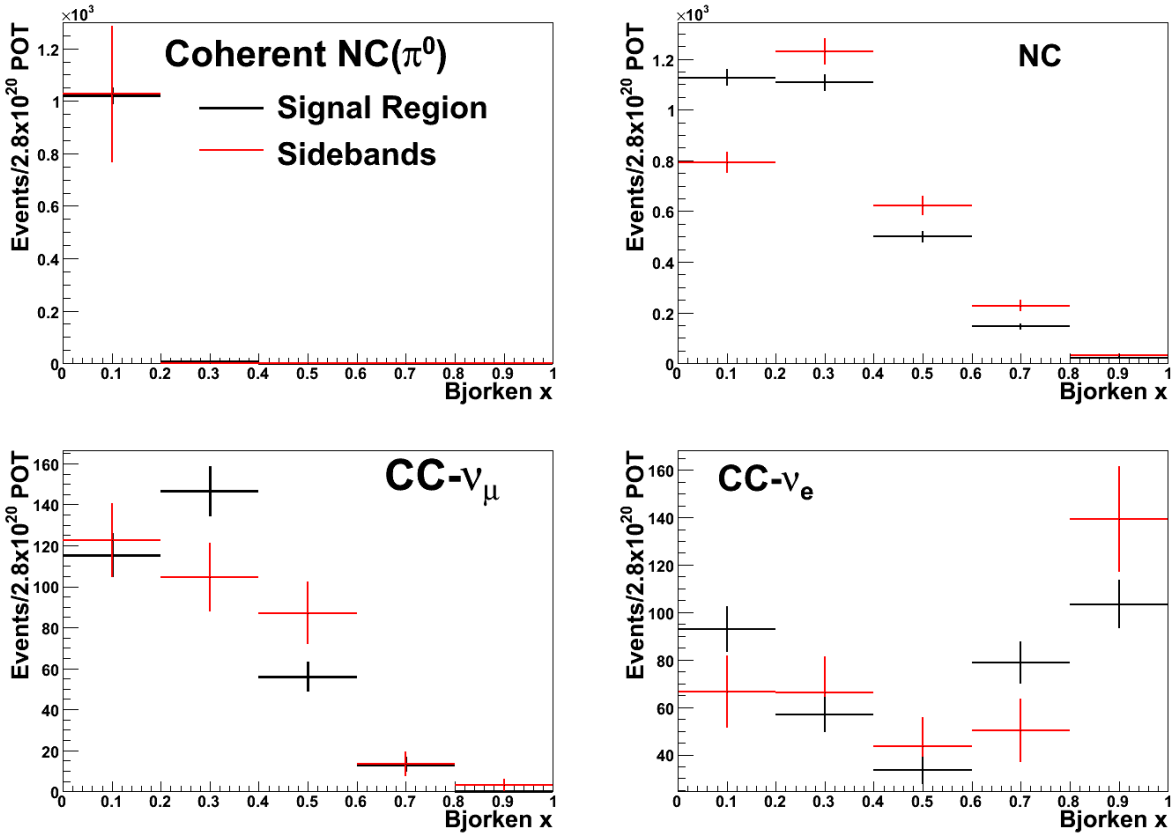

Figure C.2: The event rate distribution as a function of true Bjorken x for selected MC events. The plots show the number of events in the signal region (black) area-normalized to the number of events in the sideband region (red). The sideband region, generally peaks at higher values of x, following the Q^2 distribution, although the convolution with the corresponding y distributions softens the trend for the CC-ν_μ and CC-ν_e backgrounds.

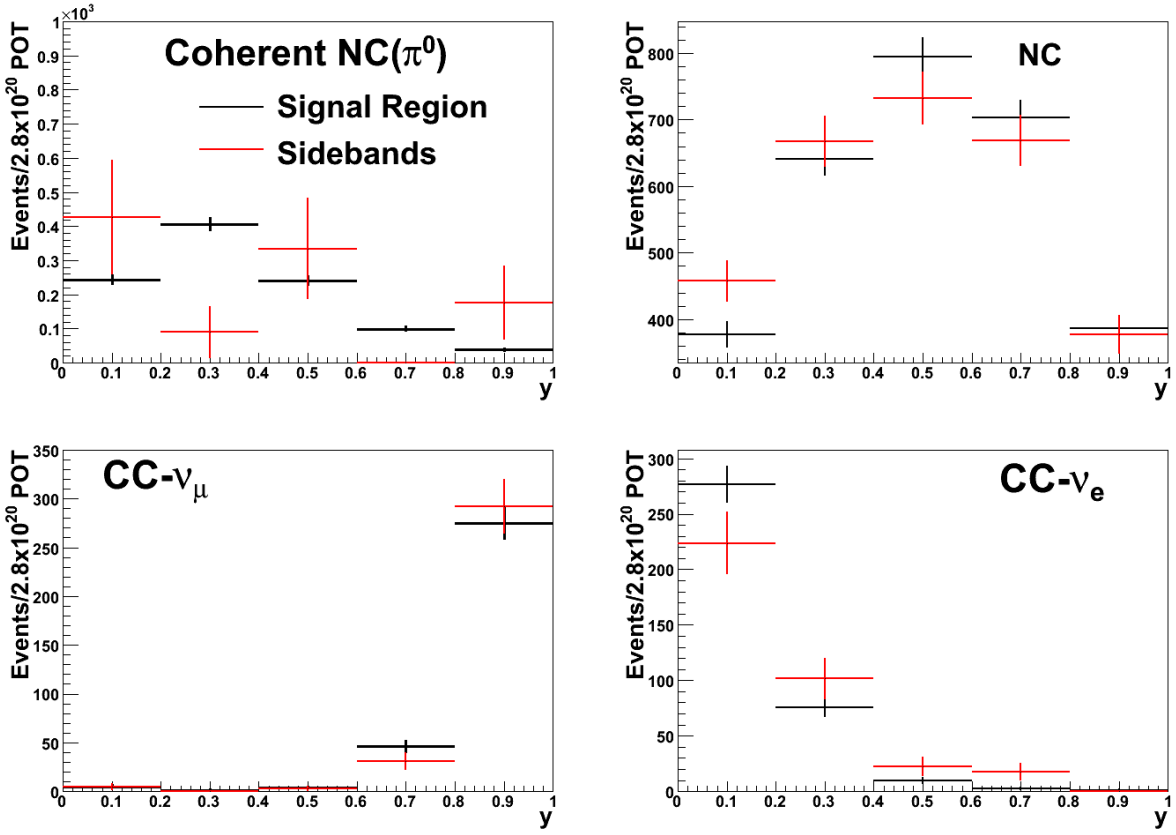

Figure C.3: The event rate distribution as a function of true y for selected MC events. The plots show the number of events in the signal region (black), area-normalized to the number of events in the sideband region (red). The sideband contains a higher fraction of low-y NC events compared to the signal region. On the other hand, the sideband has a larger contribution from high-y events from the CC background classes.

Appendix D

Comparison of the Selected Sample with the Near-PID Sample

The plots of Figures D.1 through D.3 provide comparisons of event rate distributions as functions of kinematic variables for the number of signal and background events in the selected sample and the near-PID sample. The kinematic variables used are the invariant mass of the hadronic system (W^2), and the Bjorken scaling variables x and y. The implications of these distributions are discussed in the text of Chapter 6.5.

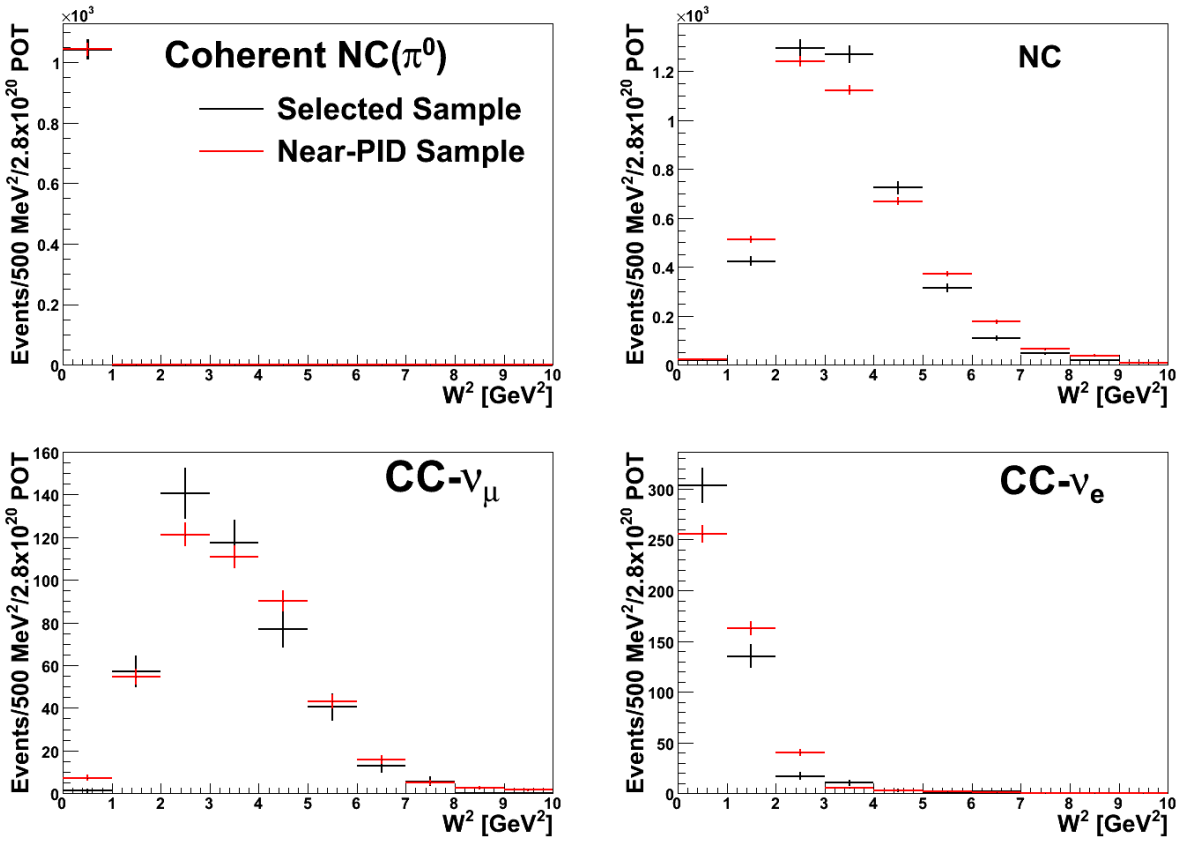

Figure D.1: The event rate distribution as a function of true W^2 for selected sample (black) and near-PID sample (red) MC events. The plots show the number of events in the signal region area-normalized to the number of events in the near-PID sample. The background distributions are peaked at higher values of W^2 in the sideband as compared with the signal region. All coherent events are assigned a W^2 value of 0.0, and the two distributions are identical.

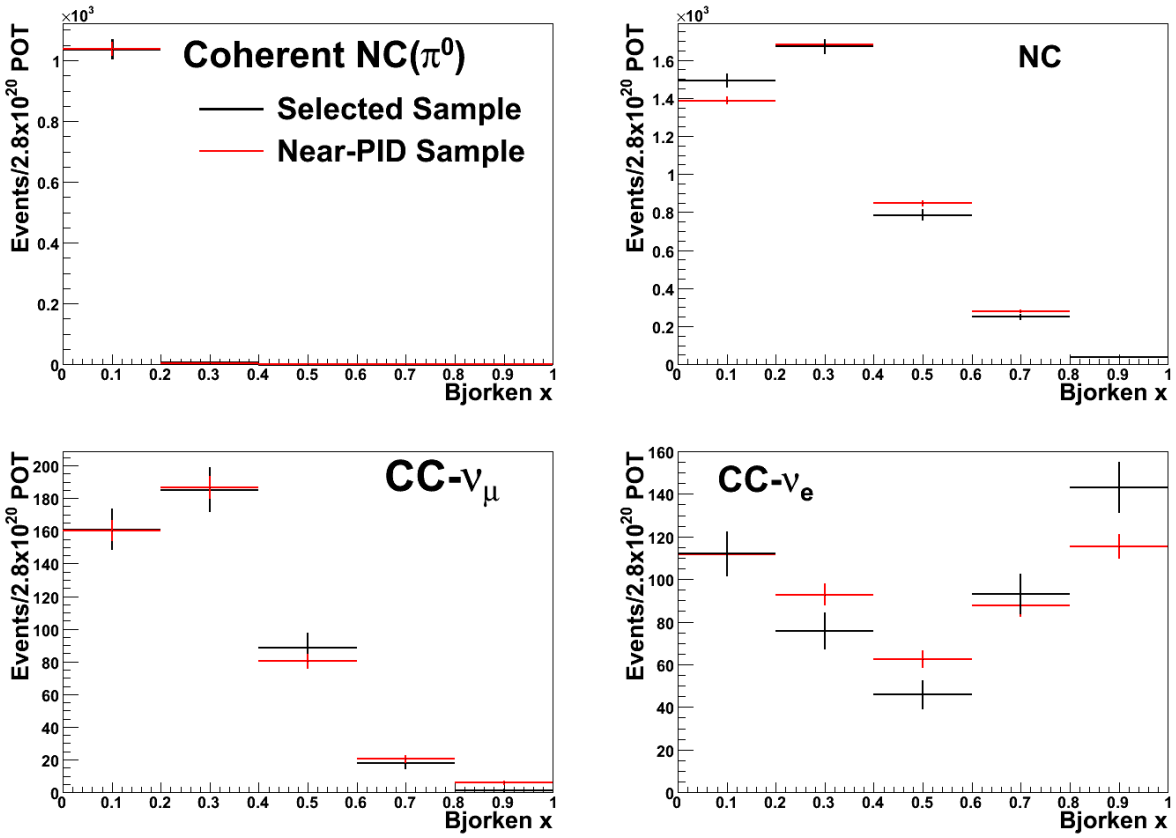

Figure D.2: The event rate distribution as a function of true Bjorken x for the selected sample (black) and near-PID sample (red) MC events. The plots show the number of events in the signal region area-normalized to the number of events in the near-PID sample. The sideband regions, for the most part peak at higher values of x, following the Q^2 distribution, although the convolution with the corresponding y distributions weakens the trend for the CC-ν_μ and CC-ν_e backgrounds.

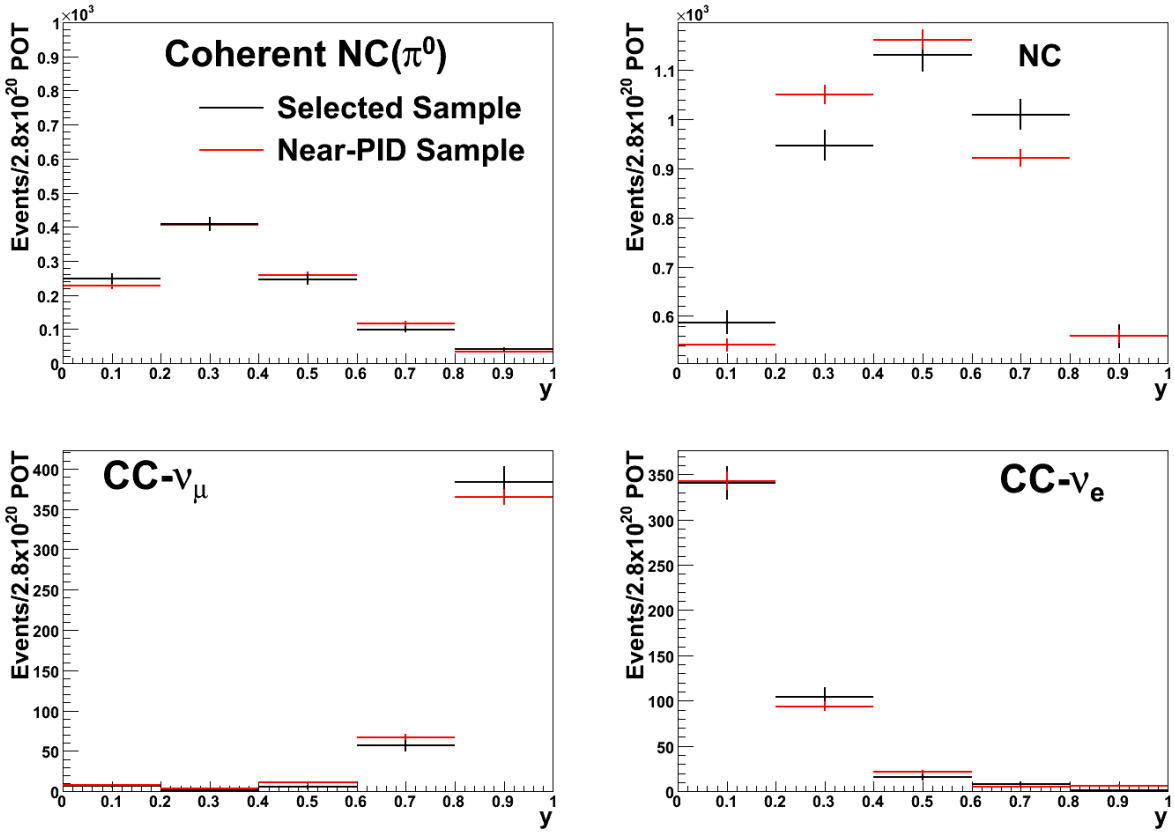

Figure D.3: The event rate distribution as a function of true y for the selected sample (black) and the near-PID sample (red) for MC events. The plots show the number of events in the signal region area-normalized to the number of events in the near-PID sample. The sideband consists of a higher fraction of low y NC events as compared with the signal region. On the other hand, the sideband has a larger contribution from high y events from the CC background classes.

Appendix E

Calibration Error Sources

The following descriptions are excerpted from a thesis on the $\nu_\mu \rightarrow \nu_e$ oscillation analysis [32].

Gains

"The gain calibration is not part of the [energy scale] calibration at the reconstruction level; however, gains are used in the conversion from the observed number of ADCs into PEs which are then used as input into the PE cut used to remove strips and as input into the LEM process. The gains for each detector are known to within a systematic shift of $\pm 5\%$ and to within random channel-to-channel variation of 7%. To evaluate the uncertainties due to imperfections in the gain calibration, two sets of MC samples where generated by shifting the value of the gains for every channel up and down by 5%. On top of this 5% systematic shift, a 7% random variation is independently applied to each channel according to a Gaussian distribution."

Attenuation

"The attenuation calibration normalizes the mean response along the position of each strip to be equal to the response in the middle of the strip. This correction is validated using the stopping muon calibration. Even after the correction there still are residual differences in the mean response along the strip on the order of 1%. The MC response as a function of position is rescaled to match the data response."

Strip to Strip

"The strip to strip calibration normalizes the mean response of each strip to be equal. The mean variation in strip to strip response after calibration should be less than 0.5%. In order to simulate the effect of imperfect strip to strip calibration at the 0.5% level, MC samples are produced in which the value of [the correct strip pulse height] in each strip is independently varied according to a Gaussian distribution with a 0.5% width."

Linearity

"This systematic error corresponds to how accurately the data are corrected for the effect of non-linearity in the detector response. In order to evaluate the effect of this calibration uncertainty, MC samples are produced in which the value of [the correct strip pulse height] in each strip is independently varied by a Gaussian distribution. The width of the distribution is set to the uncertainty on the [the correct strip pulse height] value that is calculated by default in the

linearity calibration framework. The value of this error is calculated using the uncertainties on the linearity fits stored in the calibration database."

Low Pulse Height Hits

"To evaluate the reconstruction uncertainties associated with the mismodeling of the low pulse height hits, a special MC sample was generated where the sub 2 PE hits were removed at reconstruction time. The change in the [ν_e] PID assigned to a given event may be determined on an event by event basis. The difference between these samples is defined as the systematic error associated with the low pulse height cut."

Appendix F

Energy Projection Plots from Fits to the Data

The main text presents the step-by-step fit procedure through Angle projections of the Angle-vs-Energy histograms used in the fits. The following plots provide the corresponding Energy projections.

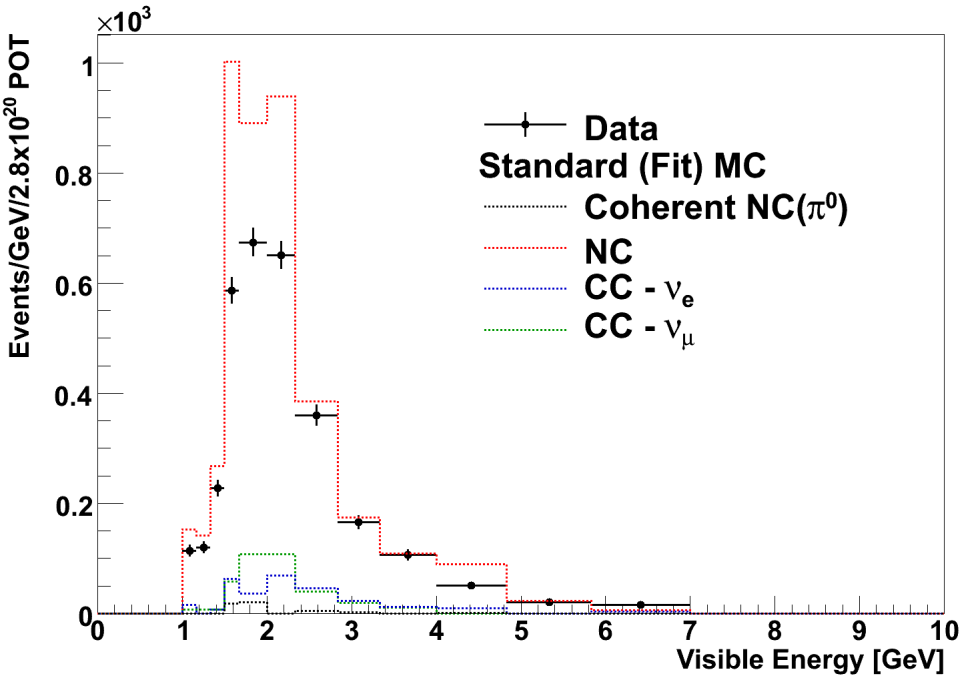

Figure F.1: Energy projections of the sideband region of the Angle-vs-Energy histogram for the data and for the standard MC prediction for the backgrounds.

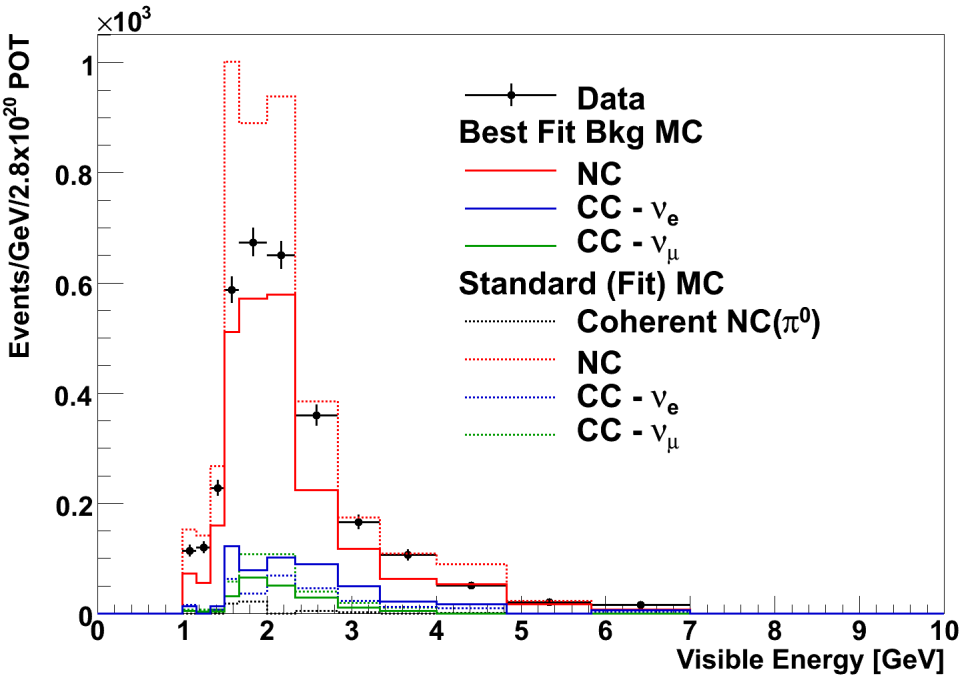

Figure F.2: Energy projections of the sideband region of the Angle-vs-Energy histograms for the data sample, for the standard MC backgrounds, and for the best-fit MC backgrounds.

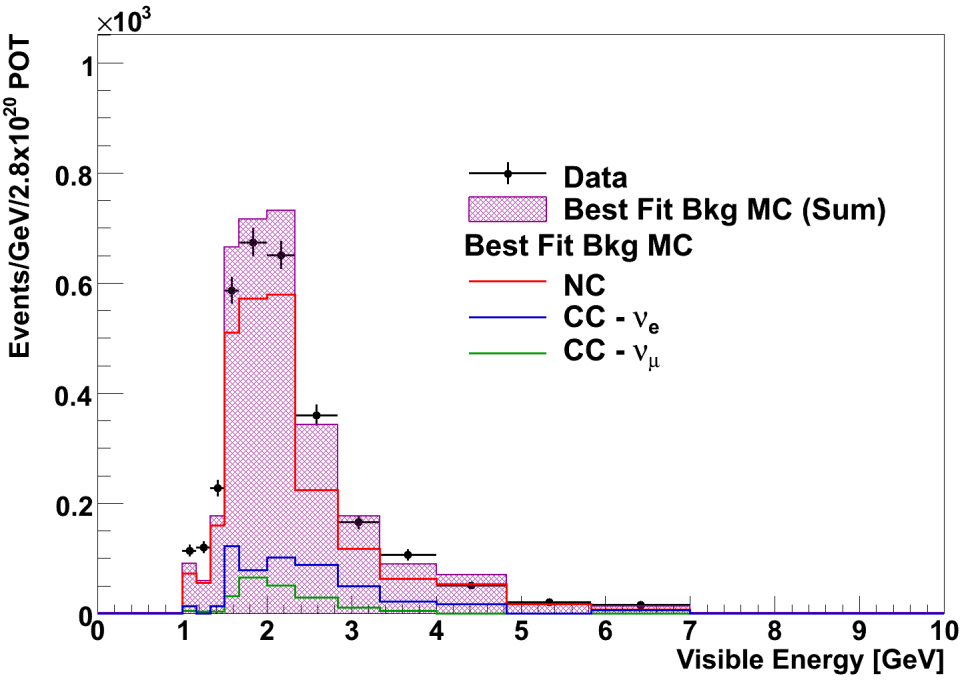

Figure F.3: Energy projections of the sideband region of the Angle-vs-Energy histograms for the data sample, for the best-fit MC backgrounds, and for the sum of the the best-fit MC backgrounds.

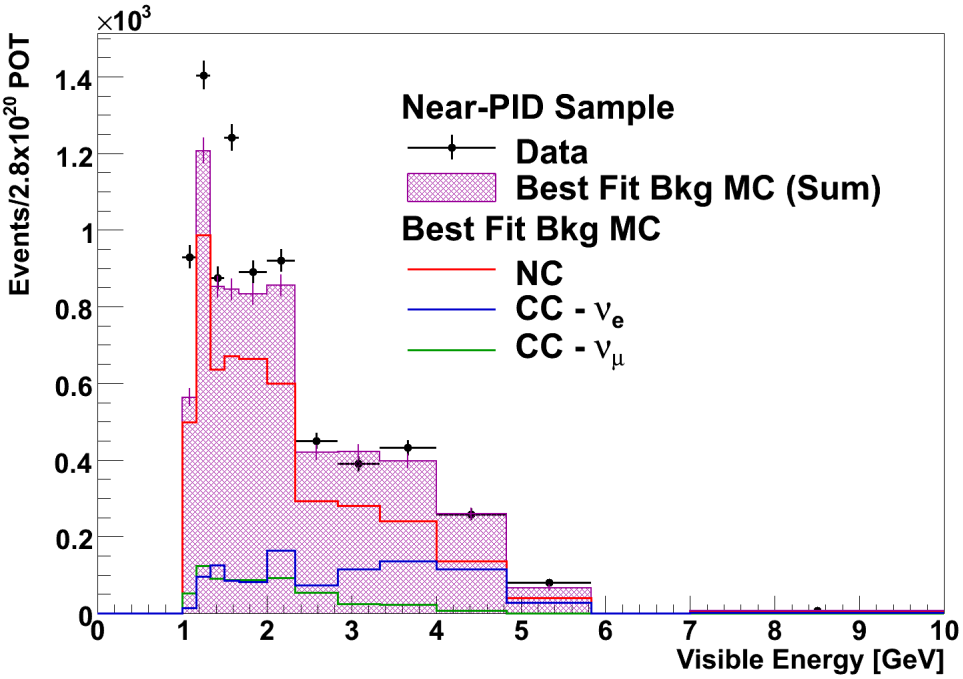

Figure F.4: Energy projections of the sideband region of the near-PID Angle-vs-Energy histograms for the data sample, for the best-fit MC backgrounds, and for the sum of the the best-fit MC backgrounds. The data and the best-fit MC agree at higher energies, although there is an excess in the data at lower energies as compared with the best-fit MC.

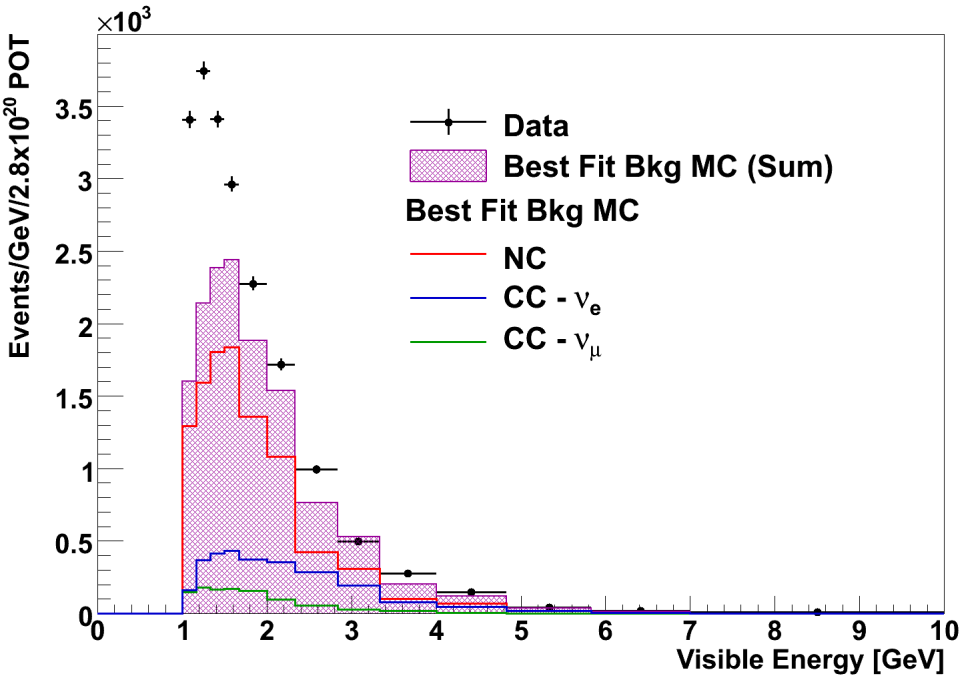

Figure F.5: Energy projections of the entire Angle-vs-Energy histograms for the data sample, for the best-fit MC backgrounds, and for the sum of the the best-fit MC backgrounds.

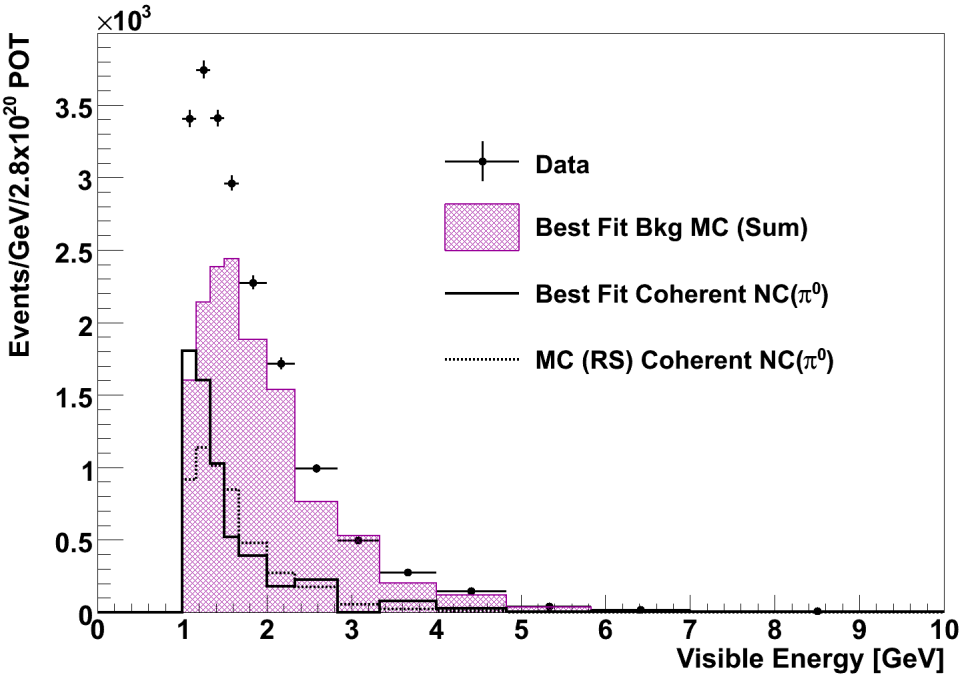

Figure F.6: Energy projections of the entire Angle-vs-Energy histograms for the data sample, for sum of the the best-fit MC backgrounds. The difference between the two histograms is the measured selected signal event rate (solid black). This can be compared to the MC prediction (dashed black).

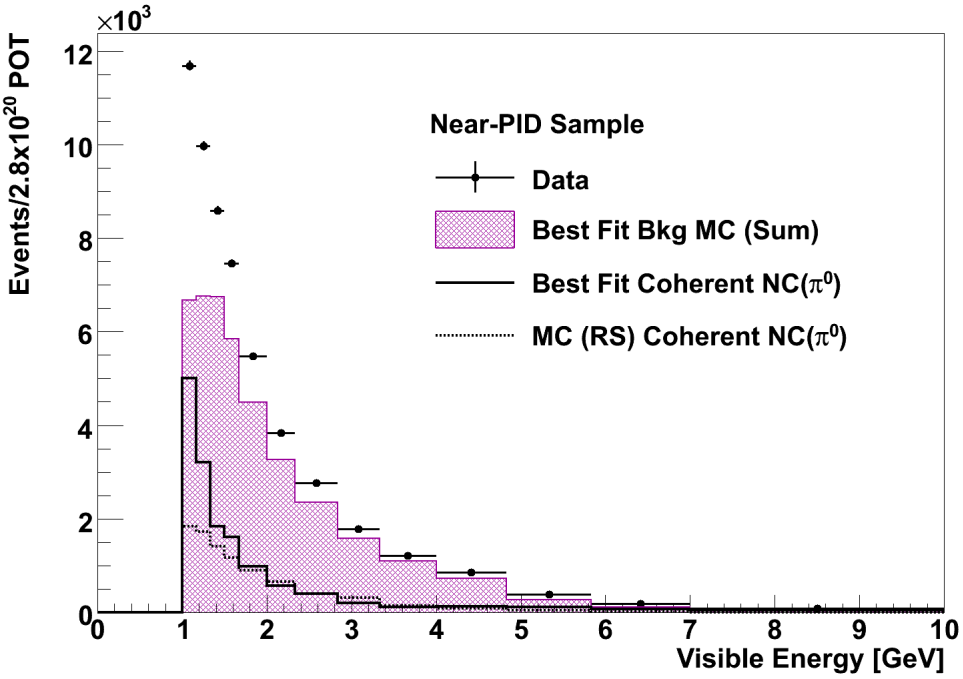

Figure F.7: Energy projections of the entire near-PID Angle-vs-Energy histograms for the data sample (circles), for sum of the the best-fit MC backgrounds (magenta). The difference between the two histograms is the measured near-PID signal event rate (solid). This can be compared to the MC prediction (dashed). The measured signal event rate and the MC prediction agree at higher Energies, however at lower Energies, an excess is observed. This excess is in agreement with the trend observed in the Energy projections of the selected sample.

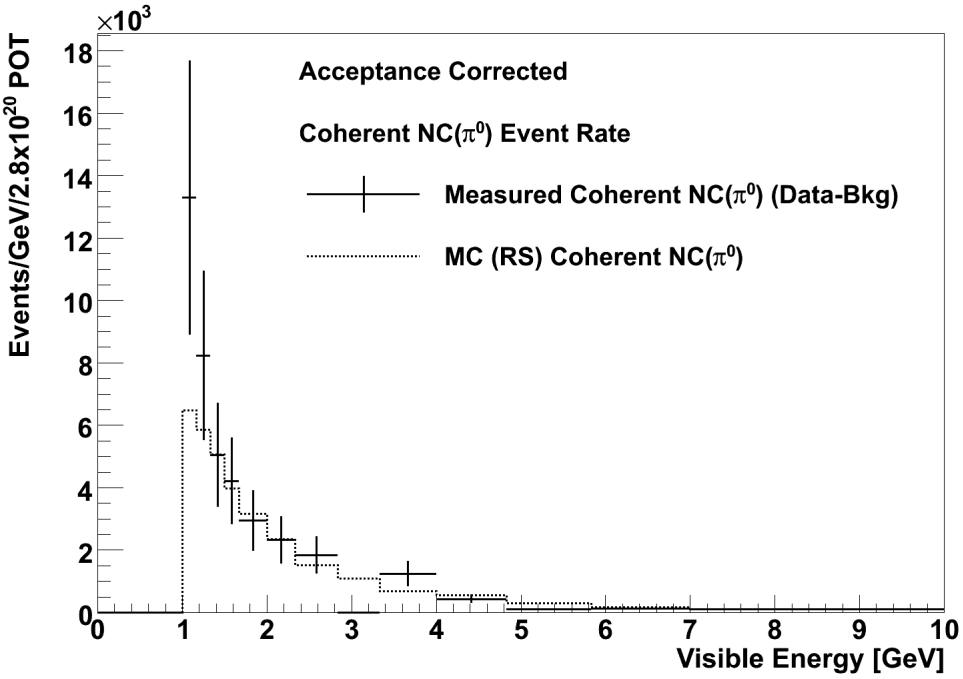

Figure F.8: The Energy projection of the Angle-vs-Energy distribution with the bin-by-bin acceptance correction applied. The error bars display the 33% uncertainty assigned to the cross section measurement. The dashed histogram is the Energy distribution for the MC prediction for the total coherent NC(π^0) event rate.

Bibliography

[1] B. Z. Kopeliovich and P. Marage, Int. J. Mod. Phys. **A8**, 1513 (1993).

[2] S. Willocq, *Coherent Production of Pions and Rho Mesons in Neutrino Charged Current Interactions on Neon Nuclei at the Fermilab Tevatron*, PhD thesis, Tufts University, 1992.

[3] C. Berger and L. M. Sehgal, Phys. Rev. **D79**, 053003 (2009), 0812.2653.

[4] W.-M. Yao *et al.*, Journal of Physics **G 33** (2006).

[5] D. Rein and L. M. Sehgal, Nucl. Phys. **B223**, 29 (1983).

[6] H. Gallagher, Nuclear Physics B - Proceedings Supplements **112**, 188 (2002).

[7] E. A. Paschos, A. Kartavtsev, and G. J. Gounaris, Phys. Rev. **D74**, 054007 (2006), hep-ph/0512139.

[8] E. Hernández, J. Nieves, and M. J. V. Vacas, Phys. Rev. **D80**, 013003 (2009).

[9] D. Rein and L. M. Sehgal, Phys. Lett. **B657**, 207 (2007), hep-ph/0606185.

[10] S. Boyd, S. Dytman, E. Hernandez, J. Sobczyk, and R. Tacik, AIP Conf. Proc. **1189**, 60 (2009).

[11] C. Andreopoulos *et al.*, Nucl. Instrum. Meth. **A614**, 87 (2010), 0905.2517.

[12] Achen-Padova, H. Faissner *et al.*, Phys. Lett. **B125**, 230 (1983).

[13] Gargamelle, E. Isiksal *et al.*, Phys. Rev. Lett. **52**, 1096 (1984).

[14] CHARM, F. Bergsma *et al.*, Phys. Lett. **B157**, 469 (1985).

[15] SKAT, H. J. Grabosch *et al.*, Z. Phys. **C31**, 203 (1986).

[16] 15' BC, C. Baltay *et al.*, Phys. Rev. Lett. **57**, 2629 (1986).

[17] NOMAD, C. T. Kullenberg *et al.*, Phys. Lett. **B682**, 177 (2009), 0910.0062.

[18] MiniBooNE, A. A. Aguilar-Arevalo *et al.*, Phys. Rev. **D81**, 013005 (2010), 0911.2063.

[19] SciBooNE, Y. Kurimoto *et al.*, Phys. Rev. **D81**, 033004 (2010).

[20] K2K, F. Sanchez, Nucl. Phys. Proc. Suppl. **155**, 239 (2006).

[21] K2K, M. Hasegawa *et al.*, Phys. Rev. Lett. **95**, 252301 (2005), hep-ex/0506008.

[22] MiniBooNE, M. O. Wascko, Nucl. Phys. Proc. Suppl. **159**, 50 (2006), hep-ex/0602050.

[23] L. Loiacono, *Measurement of the Muon Neutrino Inclusive Charged Current Cross Section on Iron Using the MINOS Detector*, PhD thesis, University of Texas at Austin, 2010.

[24] MINOS, P. Adamson *et al.*, Phys. Rev. **D81**, 072002 (2010), 0910.2201.

[25] P. Adamson *et al.*, Measuring the Number of Protons-on-Target (POT) in the NuMI Beamline, MINOS-doc-1491-v1.

[26] MINOS, P. Adamson *et al.*, Phys. Rev. Lett. **101**, 131802 (2008), 0806.2237.

[27] P. L. Vahle, (2004), FERMILAB-THESIS-2004-35.

[28] MINOS, D. G. Michael *et al.*, Nucl. Instrum. Meth. **A596**, 190 (2008), 0805.3170.

[29] MINOS, P. Adamson *et al.*, Phys. Rev. Lett. **103**, 261802 (2009), 0909.4996.

[30] P. Adamson, Accelerator Status Report, MINOS-doc-4428-v1.

[31] Z. Pavlovich, *Observation of Disappearance of Muon Neutrinos in the NuMI Beam*, PhD thesis, University of Texas at Austin, 2008.

[32] J. A. A. Boehm, *A Measurement of Electron Neutrino Appearance with the MINOS Experiment*, PhD thesis, Harvard University, 2009.

[33] *The Elements of Statistical Learning: Data Mining, Inference, and Prediction* (Springer, 2001).

[34] MINOS ν_e Analysis Group, Overview of the MINOS ν_e Appearance Analysis, MINOS-doc-5388-v11.

[35] C. Andreopoulos *et al.*, Updated Cross Section Model Uncertainties for the Charged Current Analysis, MINOS-doc-1276-v4.

[36] M. Kordosky, A Prodcedure to Re-weight Events to Account for Uncertainties in Sinal State Interactions, MINOS-doc-3449-v2.

[37] J. Boehm, H. Gallagher, and T. Yang, Hadronization Model Uncertainties for the ν_e Analysis, MINOS-doc-5392-v1.

[38] S. Dytman, H. Gallagher, and M. Kordosky, Shower Energy Scale Uncertainties For Run I+II CC Analysis, MINOS-doc-3362-v2.

[39] G. Cowan *et al.*, Phys. Rev. **B667**, 320 (2008).

[40] R. J. Barlow and C. Beeston, Comput. Phys. Commun. **77**, 219 (1993).

[41] M. Hall *et al.*, SIGKDD Explorations **11** (2009).

[42] C.-C. Chang and C.-J. Lin, *LIBSVM: a library for support vector machines*, 2001, Software available at `http://www.csie.ntu.edu.tw/~cjlin/libsvm`.

[43] R. Brun and F. Rademakers, Nucl. Inst. Meth. in Phys. Res. **A389**, 81 (1997).

[44] D. Cherdack, Proposal for the Generation of Additional Background Monte Carlo for the Analysis of Coherent π^0 Production, MINOS-doc-4945-v2.